RgF RÉFÉRENTIEL GÉOLOGIQUE DE LA FRANCE

UGA Université Grenoble Alpes

THÈSE

Pour obtenir le grade de

DOCTEUR DE L'UNIVERSITÉ GRENOBLE ALPES

Spécialité : **Sciences de la Terre et de l'Univers et de l'Environnement**

Arrêté ministériel : 01 Septembre 2019

Présentée par

Ahmed Nouibat

Thèse dirigée par **Romain Brossier**
et codirigée par **Laurent Stehly**

préparée au sein de **l'institut des Sciences de la Terre**
dans **l'École doctorale Terre, Univers, Environnement**

Bayesian inversion and wave-equation tomography using ambient noise records from dense seismological networks: 3-D lithospheric models of the Alps and the Ligurian sea

Thèse soutenue publiquement le **15 décembre 2022**,
devant le jury composé de :

Yann Capdeville
Directeur de recherche, CNRS, Nantes Université, Rapporteur
Jérôme Vergne
Physicien, Université de Strasbourg, Rapporteur
Helle Pedersen
Physicienne, Université Grenoble Alpes, Présidente
Stéphanie Durand
Chargée de recherche, CNRS, Université Claude Bernard Lyon 1, Examinatrice
Romain Brossier
Maître de conférences, Université Grenoble Alpes, Directeur de thèse
Laurent Stehly
Physicien adjoint, Université Grenoble Alpes, Co-Directeur de thèse
Philippe Calcagno
Ingénieur chercheur, BRGM, Invité

Abstract

In the complex tectonic setting of the western Mediterranean region, the deep dynamic processes involved in the orogenesis of the western Alps and the opening of the Ligurian-Provence back-arc basin remain not fully understood. Although these regions have been probed by a broad spectrum of geological and geophysical studies, there is still a gap in precision between the knowledge of the surface geology and the knowledge of the three-dimensional lithospheric structure – crucial for describing the deep dynamics. The availability of the European permanent networks, the dense AlpArray temporary network, and other temporary experiments, gives a unique opportunity for large-scale, high-resolution 3-D seismic imaging to further constrain the crust and upper mantle structures beneath the western Alps and the Ligurian-Provence basin.

Taking advantage of this exceptional seismic coverage, we construct high-resolution ambient-noise 3-D shear-wave velocity models using innovative imaging approaches. First, we perform a full data-driven probabilistic inversion in the framework of the two-step 'classical' ambient-noise tomography (ANT): (i) we compute 2-D Rayleigh-wave group-velocity maps and their uncertainties in the period band 4-150 s using a transdimensional Bayesian inversion; (ii) using a 1-D probabilistic inversion that accounts for uncertainties in the local dispersion curve, we estimate at each location, at each depth, the probability density on shear-wave velocities and on the presence of interfaces. The probabilistic V_s model is further refined using a linear inversion. The resulting model provides a high-resolution image of the European lithosphere subduction and presents a striking fit with receiver-function cross-sections in the western Alps.

The offshore part of the ANT V_s model, the Ligurian sea, is constructed after a specific processing of the OBS data: (i) we enhance the long-period content of the OBS noise records by correcting for transients and seabed-induced noises; (ii) we optimize the path coverage in the Ligurian sea by computing OBS-OBS iterative correlations, involving onshore stations of AlpArray and permanent networks. The obtained 3-D V_s model presents a striking fit with controlled-source seismic data along the basin axis and provides new insights on the lithology and petrological nature of the Ligurian oceanic crust.

The second step consists in refining the crust and uppermost mantle parts of the ANT model in the Alps and the Ligurian sea. To achieve this, we perform a wave-equation tomography (WET) based on numerical modelling of 3-D elastic and acoustic-elastic surface-wave propagation. The velocity model is iteratively updated by minimizing the phase traveltime differences between the observed and synthetic waveforms in the period band 5-85 s. We apply a fluid-solid coupling for waveform simulations in the 5-20 s period band to fully account for the water-layer effect on 3-D propagation of Rayleigh-Scholte waves in the Ligurian-Provence basin and its conjugate margins. The resulted 3-D V_s model is of higher resolution, exhibiting new features and stronger velocity contrasts. We extract an onshore-offshore 3-D Moho map, higher-resolution than the previous Moho maps in the Alps and Ligurian sea.

Résumé

Dans le contexte tectonique complexe de la région ouest méditerranéenne, les processus dynamiques profonds impliqués dans l'orogenèse des Alpes occidentales et l'ouverture du bassin d'arrière-arc liguro-provençal ne sont pas encore entièrement compris. Bien que ces régions aient été sondées par un large éventail d'études géologiques et géophysiques, il existe toujours un fossé en termes de précision entre la connaissance de la géologie de surface et la connaissance de la structure lithosphérique tridimensionnelle – cruciale pour décrire la dynamique profonde. La disponibilité des réseaux permanents européens, du réseau temporaire dense AlpArray, et d'autres réseaux temporaires, donne une opportunité unique pour réaliser des imageries sismiques 3-D haute-résolution à grande échelle afin de mieux contraindre les structures de la croûte et du manteau supérieur sous les Alpes occidentales et sous le bassin Liguro-Provençal.

En tirant profit de cette couverture sismologique exceptionnelle, nous construisons des modèles 3-D haute-résolution de vitesse d'ondes de cisaillement à partir du bruit ambiant en utilisant des approches d'imagerie innovantes. Tout d'abord, nous réalisons une inversion probabiliste complète dans le cadre de la tomographie bruit ambiant 'classique' à deux étapes (ANT) : (i) nous calculons des cartes 2-D de vitesse de groupe d'onde de Rayleigh et leurs incertitudes dans la bande de période 4-150 s en utilisant une inversion Bayésienne transdimensionnelle; (ii) en utilisant une inversion probabiliste 1-D qui tient compte des incertitudes dans la courbe de dispersion locale, nous estimons à chaque localisation, à chaque profondeur, la densité de probabilité sur les vitesses d'ondes de cisaillement et sur la présence d'interfaces. Le modèle probabiliste V_s est ensuite affiné par une inversion linéaire. Le modèle obtenu fournit une image à haute résolution de la subduction de la lithosphère européenne et présente un remarquable accord avec les coupes transversales de fonction récepteur dans les Alpes occidentales.

La partie marine du modèle ANT V_s, à savoir la mer Ligure, est construite après un traitement spécifique des données de stations OBS : (i) nous améliorons le contenu longue période des enregistrements bruts des OBS en éliminant les bruits électroniques et les bruits du fond marin; (ii) nous optimisons la couverture des trajets dans la mer Ligure en calculant des corrélations itératives OBS-OBS, impliquant des stations terrestres des réseaux AlpArray et permanents. Le modèle 3-D V_s obtenu présente un remarquable accord avec les données de la sismique active le long de l'axe du bassin et apporte de nouvelles informations sur la lithologie et la nature pétrologique de la croûte océanique sous le bassin Liguro-Provençal.

La deuxième étape consiste à affiner la croûte et le manteau supérieur du modèle ANT sous les Alpes et la mer Ligure. Pour ce faire, nous réalisons une tomographie par équation d'onde (WET) basée sur la modélisation numérique de la propagation élastiques et élasto-acoustiques 3-D d'ondes de surface. Le modèle V_s est mis à jour itérativement en minimisant les différences de temps de phase entre les formes d'onde observées et synthétiques dans la bande de période 5-85 s. Nous appliquons un couplage fluide-solide dans la bande de période 5-20 s afin de tenir compte de l'effet de la couche d'eau sur la propagation 3-D des ondes de Rayleigh-Scholte dans le bassin Liguro-Provençal et à travers ses marges conjuguées. Le modèle 3-D V_s obtenu est de meilleure résolution, présentant de plus forts contrastes de vitesse et de nouvelles structures. Nous extrayons du modèle obtenu une carte de Moho terre-mer 3-D, dont la résolution est supérieure à celle des cartes de Moho précédentes dans les Alpes et la mer Ligure.

Contents

Chapter 1

Introduction

Contents

The study of the deep Earth's interior – inaccessible to direct measurements – is fundamental to understand the geodynamic processes at the origin of the geological objects observed on the Earth's surface, e.g, mountain ranges, ocean ridges, volcanoes. Exploring the structure of the Earth is at the heart of internal geophysics, a broad study domain grouping a number of disciplines (geodesy, geomagnetism, seismology, etc.) that seek to 'probe' the Earth's interior using indirect investigation methods involving different types of physics and observables.

Seismology – the study of earthquakes and seismic waves – is at the origin of major findings on the Earth structure. In 1909, Mohorovičić discovered the crust-mantle boundary (known today as the Moho) from seismogram analysis for local earthquakes, demonstrating that the physical properties of the structures in the Earth's interior can be deduced from travel times of seismic waves. This simulated further important discoveries, e.g, depth of the boundary of the Earth's core by Gutenberg in 1914 (who also discovered the asthenosphere in 1926) and the discovery of Earth's solid inner core by Lehmann in 1936 (Fig. 1.1). Knowledge of the Earth structure has been further refined with the advent of computers and emergence of radial models describing the evolution at depth of the main physical proprieties (P-, S-wave velocity, density) and discontinuities, e.g, PEM-A (Dziewonski et al., 1975), PREM (Dziewonski and Anderson, 1981, Fig. 1.1b).

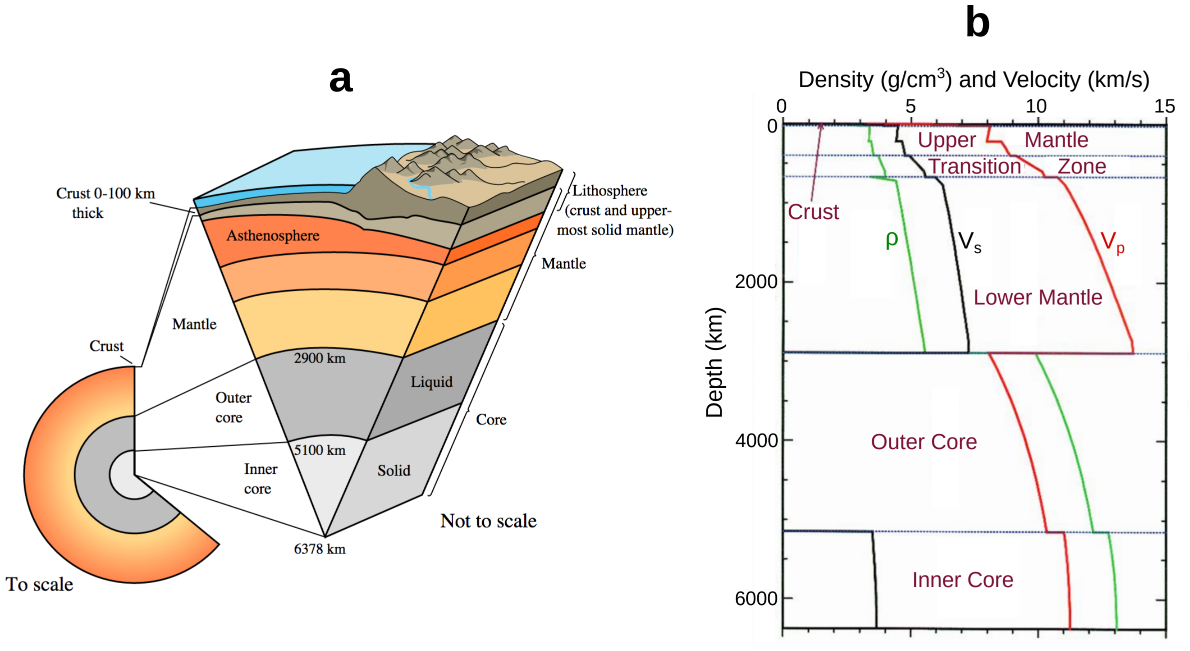

Figure 1.1: Internal structure of the Earth and the radial Earth model PREM (Preliminary Reference Earth Model; Dziewonski and Anderson, 1981). (a) Cutaway views showing the Earth's radial structure (source: USGS website). (b) Evolution of P-, S-wave propagation velocity and density ρ as a function of depth according to the PREM.

1.1 Seismic imaging of 3-D structures in the Earth's interior

The knowledge of the three-dimensional structure of the Earth's interior has been achieved with the advent of seismic tomography, simulated by advances in electronics, computing resources and theoretical developments in seismology. Seismic tomography is a powerful imaging method that exploits the information contained in seismic records to derive 3-D models of seismic velocity variations at depth, i.e, the Earth's interior is represented by 3-D structures with different seismic velocities that translate the variations of physical properties at depth. Seismic tomography applications cover a wide range of observation scales, from the first few meters of the subsurface to the entire Earth.

Since the introduction of seismic tomography in Seismology by Aki et al. (1977), many tomographic studies have been conducted on regional and global scales. The earliest 3-D tomographic studies were conducted in the 1970s, e.g, in Central California (Aki and Lee, 1976); in Southeastern Norway (Aki et al., 1977), using traveltime of body waves recorded by short-period seismometers. Then, on larger areas, notably to infer subduction slabs, e.g, in Western Europe (e.g., Spakman, 1986, 1988), in Caribbean region (e.g., Grand, 1987; Van der Hilst et al., 1990), with lateral resolution of ~ 100 to 200 km. With the development of global networks of broadband seismic stations, global models of the Earth have been derived using either body-wave travel times (e.g., Romanowicz, 1991; Ritzwoller and Lavely, 1995), surface-wave dispersion measurements (e.g., Nataf et al., 1986), or fundamental-mode free-oscillation measurements (e.g., Masters et al., 1982; Davis, 1987), with lateral resolution of ~ 2000 to 4000 km. Since the 2000s, with increasing computational resources leading to considering more complete observables (e.g., signal waveform), and other passive sources (e.g., seismic ambient noise) in large-scale tomography, aided by the deployment of dense regional seismic arrays (USAarray, AlpArray, etc.), the seismic tomography has entered a new era towards increasingly higher resolution, in the order of tens of kilometres, and higher robustness. Nowadays, it is undoubtedly the most widely used geophysical method for exploring the deep Earth's interior.

1.1.1 Seismic tomography: an inverse problem

Seismic tomography is an inverse problem – based on seismic data observed on the Earth's surface, conclude about the physical properties of structures in the Earth's interior through which the seismic waves have travelled. The determination of the Moho depth by Mohorovičić (1909) is one of the first inverse problems in seismology. By analyzing phase arrival times for Pokupsko earthquake (Croatia) and other local earthquakes recorded by the European seismological centers in the period 1904-1905, Mohorovičić (1909) explained the arrival times of P, S direct and refracted waves by the presence of a major discontinuity – the crust-mantle boundary at 54 km estimated depth (Fig. 1.2).

Seismic tomography uses the same principle to recover the velocity structures at depth in three dimensions. In a general form, given a model $\mathbf{m}$ of physical parameters (velocity, density, etc.), one can predict seismic data $\mathbf{d}$ using the following relation: $\mathbf{d} = g(\mathbf{m})$, that is $\mathbf{d}$ can be considered as a projection of the model $\mathbf{m}$ through the operator g, which represents the physics associated with the forward problem of the seismic tomography. The inverse problem of seismic tomography seeks to find the model $\mathbf{m}$ such that $\mathbf{d}$ explains the observed data $\mathbf{d}_{obs}$. However, in most of cases, this problem is 'ill-posed' and non-linear, i.e, its solution is non-unique.

It is often difficult to image both long-wavelength variations and small-scale heterogeneities in the same tomographic model, as different types of seismic data (arrival time, the signal's waveform), seismic sources (natural sources, controlled seismic sources) and seismic waves (body waves, surface waves) are often treated separately in the inversion framework. Furthermore, seismic waves have different sensitivity to the same physical parameters and different resolution capacities. A body wave is more sensitive to sharp contrasts of the physical parameters and therefore more sensitive to interfaces, while a surface wave is more sensitive to the 3-D lateral variations. This with the presence of noise in data, and the common issue of the spatial distribution of sources and recording sensors leads inevitably to increase ill-posedness and non-linearity of the inverse problem, so that, most often, these issues are mitigated by introducing 'a priori' constrains on the model parameters and linearizing the inverse problem.

1.1.2 Tomography of the lithosphere: a variety of methods

3-D seismic tomography is key to understand the structure, dynamics and evolution of the lithosphere. With the deployment of the first regional-scale seismic networks and the emergence of traveltime tomography methods, the 3-D structure of the lithosphere has become increasingly well constrained, making it possible to confirm or refute geodynamic scenarios and structural models. Initially relying on earthquakes, traveltime tomography had to deal with of the event spatial-distribution and occurrence issues. Thus, other types of sources were exploited, such as seismic ambient noise, which has the advantage of being better distributed and continuous. In the meantime, other methods have been designed to exploit the complete waveform, i.e. the entire signal recorded by the stations, rather than only the travel time, which is moreover affected by estimation errors. In the following, we will briefly present the principles of these three imaging methods and highlight their strengths and limitations.

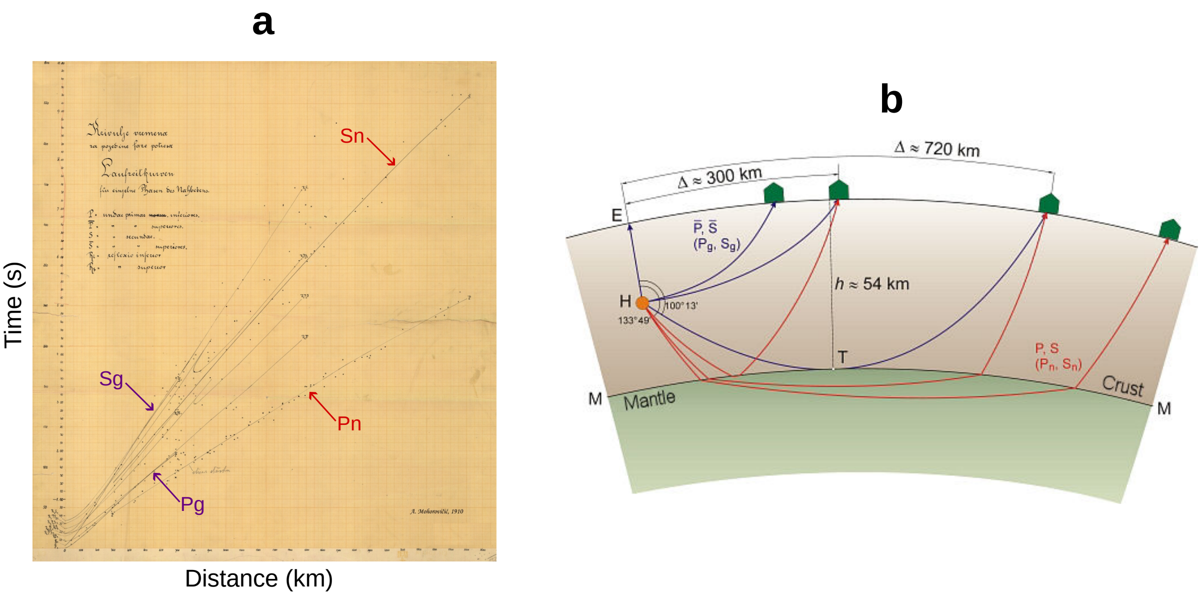

Figure 1.2: Discovery of the Mohorovičić discontinuity (Moho). (a) Travel-time curves – seismic arrival times as a function of epicentral distance – for the local earthquakes used by Mohorovičić. We observe different phases of P, S waves. Pn, Sn: refracted waves – P, S waves bottoming in the uppermost mantle; Pg, Sg: direct waves – upgoing P, S waves in the crust. (b) A simple two-layer crust-mantle model showing the seismic ray paths of direct and refracted P, S waves generated by a crustal earthquake (epicentre indicated by H), and recorded by four stations on the surface. The problem tackled by Mohorovičić is why the direct phases (Pg, Sg) do not reach stations at distances greater than 720 km (critical distance). Mohorovičić (1909) concluded that the Earth is not homogeneous and is composed by two layers having different elastic proprieties – the crust and the mantle – separated by a surface discontinuity where the seismic velocity suddenly increases. Modified from Herak (2005).

Local earthquake tomography (LET)

The LET is a traveltime imaging method that aims to determine 3-D velocity anomalies of the crust based on records of body waves emitted by local earthquakes. Aki and Lee (1976) first apply this method to image the 3-D structure of the crustal beneath California. The principle of traveltime tomography is simple: based on ray theory (e.g., Cerveny, 2003; Cerveny et al., 2007), determine the velocity perturbations of the medium that explain the differences between observed travel times (in general, the first arrival) and travel times computed in a reference model. In a medium descritized into 3-D blocks (generally rectangular; e.g., Spakman and Bijwaard, 1998) of homogeneous velocity, in which rays are straight lines, the forward problem (i.e., computation of the wave-propagation times) is solved by integrating the slowness field (inverse of the velocity) along the ray paths between source-receiver pairs

$$t_i = \sum_{j=1}^{M} \frac{L_{ij}}{v_j} \tag{1.1}$$

where L_{ij} is the length of the ith ray across the block j of slowness $s_j = 1/v_j$.

Assuming stationary wave-ray paths, the difference in traveltime of the ith ray is expressed as a function of perturbations to the slowness distribution in the medium: $\delta t_i = \sum_{j=1}^{M} \delta s_j L_{ij}$, where M in the number of model parameters. For N observations, this linear system takes the matrix form

$$\mathbf{d} = \mathbf{G}\mathbf{m} \tag{1.2}$$

where $\mathbf{d}$ is a N-vector which contains the differences between the observed travel times and the computed travel times. $\mathbf{G}$ is a $N \times M$-matrix that contain for each path the segment length within each block, and $\mathbf{m}$ is M-vector of model slowness perturbations.

The inverse problem consists in determining the model $\mathbf{m}$ of slowness perturbations minimizing the error (or objective function) between the predicted and observed traveltime delays. Usually, the system 1.2 is overdetermined – much more data than model parameters ($N > M$). The standard procedure for solving it is to approximate the solution in a least squares sense: $\mathbf{m} = \tilde{\mathbf{m}} \Longleftrightarrow \|\mathbf{d} - \mathbf{d}_{obs}\|^2 = min$, where the least squares solution $\tilde{\mathbf{m}}$ is the exact solution of the system (e.g., Trefethen and Bau, 1997): $\mathbf{G}^T\mathbf{G}\mathbf{m} = \mathbf{G}^T\mathbf{d}$, and has the form

$$\tilde{\mathbf{m}} = \left(\mathbf{G}^T\mathbf{G}\right)^{-1}\mathbf{G}^T\mathbf{d} \tag{1.3}$$

In large-scale tomography problems, $\mathbf{G}^T\mathbf{G}$ is usually close to being singular – (1.3) is an 'ill-conditioned' problem. Explicit regularization – a priori constrains – is often used to stabilize the solution by simply adding extra systems in the original problem. These additional systems contain the requirements to the solution (norm, roughness). The weight of this regularization on the least square solution is usually controlled by a 'damping parameter' $\lambda > 0$. Finally, the damped least-square solution of the obtained 'nearby' well-conditioned problem is usually derived using iterative algorithms (e.g., LSQR; Paige and Saunders, 1982).

In spite of its simplicity, LET has proven to be robust in constraining at first order the 3-D structure of the crust. However, this method has two main limitations. First, the use of the ray theory in the forward problem. Although the forward problem involves a proportionality between slowness and traveltime, the geometry of the ray is affected by variations in seismic velocities, so that the LET problem is in fact non-linear or at least poorly linear. The use of the ray theory implies that the traveltime is only sensitive to the ray path (i.e, to the structure over the zero-width source-receiver path). This is only valid in the high-frequency case where the scale of velocity structures is much larger than the seismic wavelength (see Fig. 1.3; e.g., Snieder, 1986; Cerveny, 2003). The other limitation is the use of an explicit regularization to solve the inverse problem, for which the choice of 'optimal' damping parameters can be challenging as it requires a good knowledge of the uncertainty in the data and uncertainty in the model itself. Methodological efforts have been made to overcome these limitations, in particular the high-frequency assumption, by the use of finite-frequency tomography. However, it remains that traveltime tomography has a limited resolution capacity as it only uses the information contained in the arrival time, unlike FWI for instance.

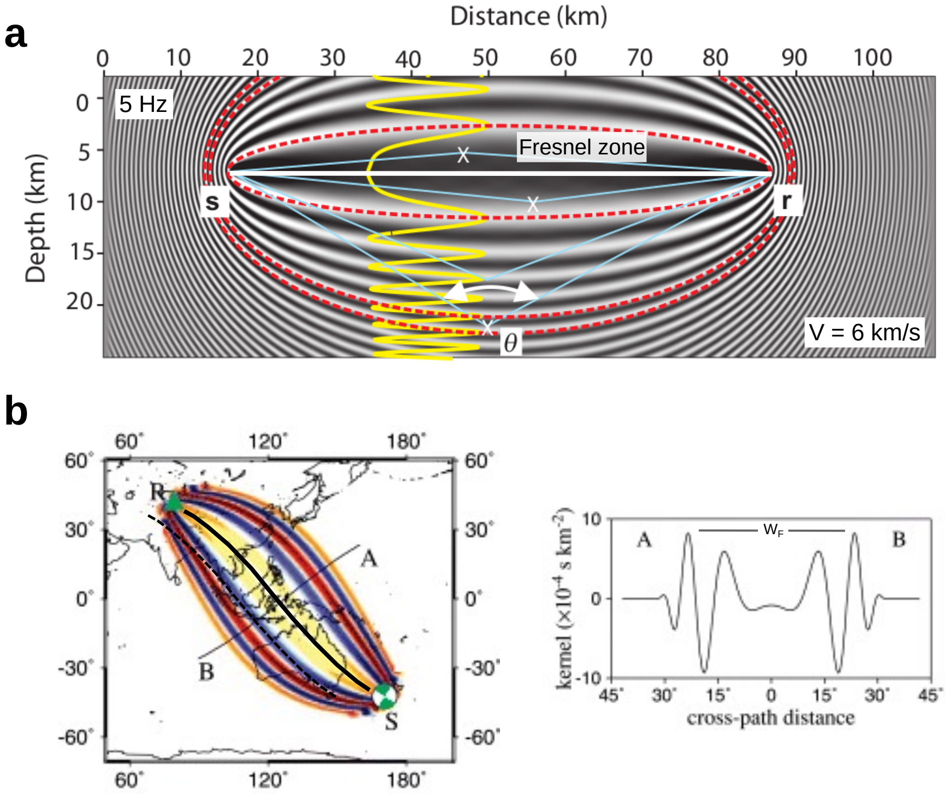

Figure 1.3: Sensitivity kernel (Banana Doughnut). (a) Kernel for a point-source monochromatic Green's function propagating in a 3-D homogeneous medium. The yellow line corresponds to a vertical section across the sensitivity kernel. The width of the Fresnel zone is $\sqrt{\lambda D_{sr}}$, where λ is the wavelength and D_{sr} the source-receiver distance. The white line indicates the straight ray path between the source and the receiver in the high-frequency assumption. In such case, the kernel would be zero everywhere except along the ray-path geometry (modified from Virieux and Operto, 2009). (b) 2-D finite-frequency sensitivity kernel of a 10-mHz surface wave, showing the Fresnel zone (W_F) in the great-circle sidebands. The black line indicates the unperturbed great-circle ray path in the high-frequency assumption (modified from Dahlen and Zhou, 2006).

Ambient noise tomography (ANT)

The ANT is a surface wave-based tomography method that infer the medium properties using group or phase velocity dispersion of surface waves reconstructed from cross-correlation of ambient seismic noise. The first attempt was made by Shapiro et al. (2005) who successfully used surface waves from ambient noise correlations to the Californian region, revealing their potential in recovering 3-D velocity structures at depth. Since that, ANT has been extensively employed as well as for sub-surface and lithosphere imaging. Nowadays, it is probably the most widely used method for imaging the crust and uppermost mantle.

From ambient noise to Green's function

It has been shown theoretically and experimentally that the cross-correlation of seismic noise recorded over a long time by two receivers can be used to reconstruct the Green's function for the surface wave propagating from one receiver to another. This is valid under assumptions of equipartition of noise sources in a homogeneous medium or anisotropic distribution of sources in a medium sufficiently heterogeneous to produce a diffuse wavefield (e.g., Lobkis and Weaver, 2001; Derode et al., 2003b,a; Wapenaar, 2004; Snieder, 2004; Gouedard et al., 2008).

In 3-D homogeneous acoustic medium, the scalar wave equation can be written as follows

$$\Delta u\left(\vec{r},t\right) - \frac{1}{c^2}\frac{\partial^2 u\left(\vec{r},t\right)}{\partial t^2} = f\left(\vec{r},t\right) \tag{1.4}$$

where $u\left(\vec{r},t\right)$ is the displacement at position $\vec{r}$ and time t, c is the velocity in the medium, and $f\left(\vec{r},t\right)$ is the source term.

The Green's function $G(\vec{r_1},\vec{r_2};t)$ between two receivers R_1 and R_2 is the impulse response of the medium between those two receiver positions $\vec{r_1}$ and $\vec{r_2}$, i.e, the signal that R_1 would record at time t if R_2 is a source emitting a Dirac $\delta(\vec{r_1}-\vec{r_2})\delta(t-t')$ at time t'. $G(\vec{r_1},\vec{r_2};t)$ is therefore a particular solution of the wave equation (1.4) where $f\left(\vec{r},t\right) = \delta(\vec{r_1}-\vec{r_2})\delta(t-t')$.

In the time domain, the expression of the Green's function between R_1 and R_2 takes the form

$$G(\vec{r_1},\vec{r_2};t) = \frac{1}{4\pi r/c}\delta(t-r/c) \tag{1.5}$$

where $r = |\vec{r_1}-\vec{r_2}|$ is the distance between the two receivers and $k=\omega/c$ is the wavenumber.

It can be shown that in case of isotropic noise field of uncorrelated plane waves in a free-space medium (e.g., Cox, 1973; Campillo et al., 2014), the normalized cross-spectral density $C(\vec{r_1},\vec{r_2};\omega)$ between R_1 and R_2 can be expressed as

$$C(\vec{r_1},\vec{r_2};\omega) = \frac{sin(kr)}{kr} \tag{1.6}$$

The cross-correlation function in the time domain is simply obtained from the inverse Fourier transform of $C(\vec{r_1},\vec{r_2};\omega)$

$$\begin{aligned} C(\vec{r_1},\vec{r_2};t) &= \frac{1}{2\pi}\int_{-\infty}^{+\infty} C(\vec{r_1},\vec{r_2};\omega)\exp(i\omega t)\,d\omega \\ &= \frac{1}{4\pi}\int_{-\infty}^{+\infty}\frac{\exp\left[i\omega(t+r/c)\right]}{ikr}d\omega - \frac{1}{4\pi}\int_{-\infty}^{+\infty}\frac{\exp\left[i\omega(t-r/c)\right]}{ikr}d\omega \end{aligned} \tag{1.7}$$

Finally, by expressing the time-derivative of the cross-correlation function, we obtain the relation

$$\begin{aligned} \frac{dC(\vec{r_1},\vec{r_2},t)}{dt} &= \frac{1}{4\pi r/c}\left[\delta(t+r/c)-\delta(t-r/c)\right] \\ &= G(\vec{r_1},\vec{r_2};-t) - G(\vec{r_1},\vec{r_2};t) \end{aligned} \tag{1.8}$$

where $G(\vec{r_1},\vec{r_2};t)$ and $G(\vec{r_1},\vec{r_2};-t)$ are the causal and acausal sides of the Green's function between the two receivers.

The relation (1.8) states that the correlation of the ambient-noise wavefields recorded by two receivers is proportional to the Green's function between those receiver positions. This demonstration can be generalized to any arbitrary 3-D heterogeneous medium with anisotropic noise-source distribution. Following the approach of Wapenaar (2004) and Campillo et al. (2014), we start from the Helmholtz equation

$$\Delta G(\vec{r},\vec{x};\omega) + k^2 G(\vec{r},\vec{x};\omega) = \delta(\vec{x}-\vec{r}) \tag{1.9}$$

which is the expression in the frequency domain of the wave equation (1.4) for an impulse source located at $\vec{x}$. $G(\vec{r},\vec{x};\omega)$ is simply the frequency domain Green's function for position $\vec{r}$. For simplicity, we consider no attenuation in the medium.

For two receiver positions $\vec{r_1}, \vec{r_2}$ in a locally heterogeneous medium, we can define the flux of the Poynting vector through an arbitrarily closed surface S in a homogeneous far-field

$$I = \oint_S \left[G(\vec{r_1},\vec{x};\omega)\vec{\nabla}G(\vec{r_2},\vec{x};\omega)^* - \vec{\nabla}G(\vec{r_1},\vec{x};\omega)G(\vec{r_2},\vec{x};\omega)^* \right] d\vec{S} \tag{1.10}$$

where $G(\vec{r_1},\vec{x};\omega)$ and $G(\vec{r_2},\vec{x};\omega)$ are the Green's functions at $\vec{r_1}$ and $\vec{r_2}$ to the noise source $\vec{x}$ located on S. Their complex conjugates are denoted by the asterisk $(*)$ while $\vec{\nabla}$ denotes the divergence operator.

The flux integral (1.10) can be transformed to a volume integral using the divergence theorem

$$\begin{aligned} I &= \int_V \vec{\nabla} \left[G(\vec{r_1},\vec{x};\omega)\vec{\nabla}G(\vec{r_2},\vec{x};\omega)^* - \vec{\nabla}G(\vec{r_1},\vec{x};\omega)G(\vec{r_2},\vec{x};\omega)^* \right] dV \\ &= \int_V \left[G(\vec{r_1},\vec{x};\omega)\Delta G(\vec{r_2},\vec{x};\omega)^* - \Delta G(\vec{r_1},\vec{x};\omega)G(\vec{r_2},\vec{x};\omega)^* \right] dV \end{aligned} \tag{1.11}$$

From equation (1.9), we have $\Delta G(\vec{r_1},\vec{x};\omega) = \delta(\vec{x}-\vec{r_1}) - k^2 G(\vec{r_1},\vec{x};\omega)$ and $\Delta G(\vec{r_2},\vec{x};\omega)^* = \delta(\vec{x}-\vec{r_2}) - k^2 G(\vec{r_2},\vec{x};\omega)^*$. By substituting these two expressions in (1.11), we obtain

$$I = G(\vec{r_1},\vec{r_2};\omega) - G(\vec{r_2},\vec{r_1};\omega)^* \tag{1.12}$$

By combining this equation with (1.10), and using the reciprocity theorem which states that $G(\vec{r_1},\vec{r_2};\omega) = G(\vec{r_2},\vec{r_1};\omega)$, it follows that

$$G(\vec{r_1},\vec{r_2};\omega) - G(\vec{r_1},\vec{r_2};\omega)^* = \oint_S \left[G(\vec{r_1},\vec{x};\omega)\vec{\nabla}G(\vec{r_2},\vec{x};\omega)^* - \vec{\nabla}G(\vec{r_1},\vec{x};\omega)G(\vec{r_2},\vec{x};\omega)^* \right] d\vec{S} \tag{1.13}$$

where the left-hand side corresponds to the causal and acausal sides of the Green's function between the two receivers. Since we consider the surface S in the far-field of the medium heterogeneities, we have

$$G(\vec{r_1},\vec{x};\omega) \approx \frac{1}{4\pi|\vec{r_1}-\vec{x}|} \exp(-ik|\vec{r_1}-\vec{x}|), \text{ and } \vec{\nabla}G(\vec{r_1},\vec{x};\omega) \approx i\vec{k}G(\vec{r_1},\vec{x};\omega) \tag{1.14}$$

By expressing $G(\vec{r_2},\vec{x};\omega)^*$ and $\vec{\nabla}G(\vec{r_2},\vec{x};\omega)^*$ in the same way and subtitling in the (1.13), we finally obtain the relation

$$G(\vec{r_1},\vec{r_2};\omega) - G(\vec{r_1},\vec{r_2};\omega)^* = -2ik \oint_S G(\vec{r_1},\vec{x};\omega)G(\vec{r_2},\vec{x};\omega)^* \, d\vec{S} \tag{1.15}$$

where the right hand-side refers to the time-derivative of the cross-correlation function of wavefields recorded at the receiver positions for sources on the closed surface S. As previously, this last relation states that the Green's function between two receivers can be reconstructed by performing a cross-correlation of the ambient noise recorded by those receivers.

In practice, the full surface-wave Green's tensors is reconstructed by combining vertical, radial and transverse components in cross-correlations. Rayleigh waves extracted from vertical-component correlations are the most commonly used for crustal and uppermost mantle tomography. This is usually done by exploiting the dispersion of group velocities and their depth-sensitivity kernels to the 1-D medium (see Fig. 1.4). Different approaches are used to measure group velocities, for example, multiple filter analysis (MFA, Dziewonski et al., 1969a; Herrmann, 1973; Stehly et al., 2009) based on time-domain detection of local maxima of the signal envelope on the causal and acausal parts of correlations. Dispersion curves for each station pair are derived by assembling group-velocity measurements at M measured periods (example in Fig. 1.5). A careful selection is applied to keep the most relevant measurements, according to SNR, symmetry, inter-station distance and other criteria.

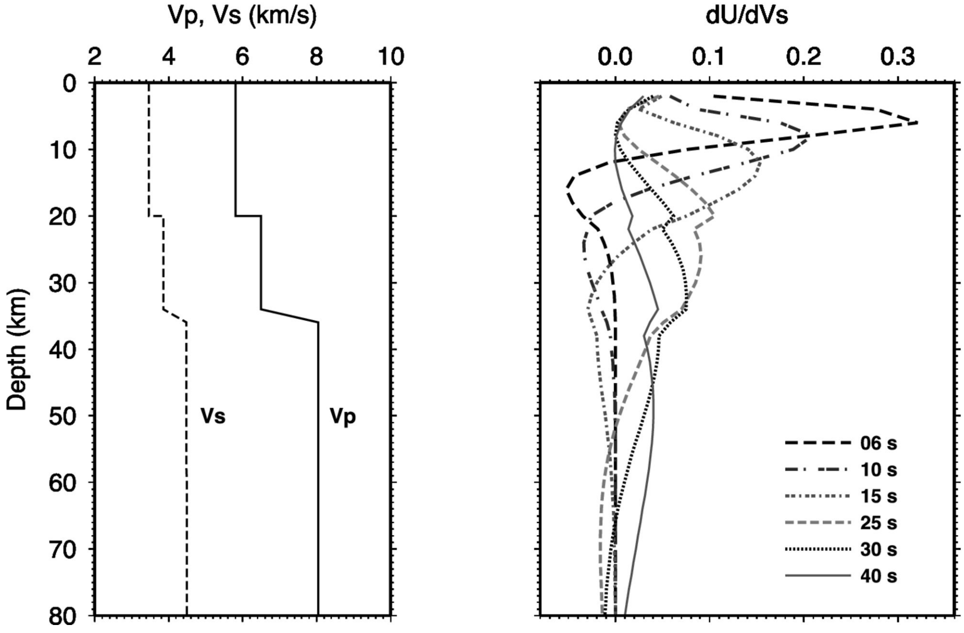

Figure 1.4: 1-D depth sensitivity kernels to V_s for the fundamental mode Rayleigh wave group velocity. The Kernels are computed using the velocity model in the left-hand side. From Ren et al. (2013).

.

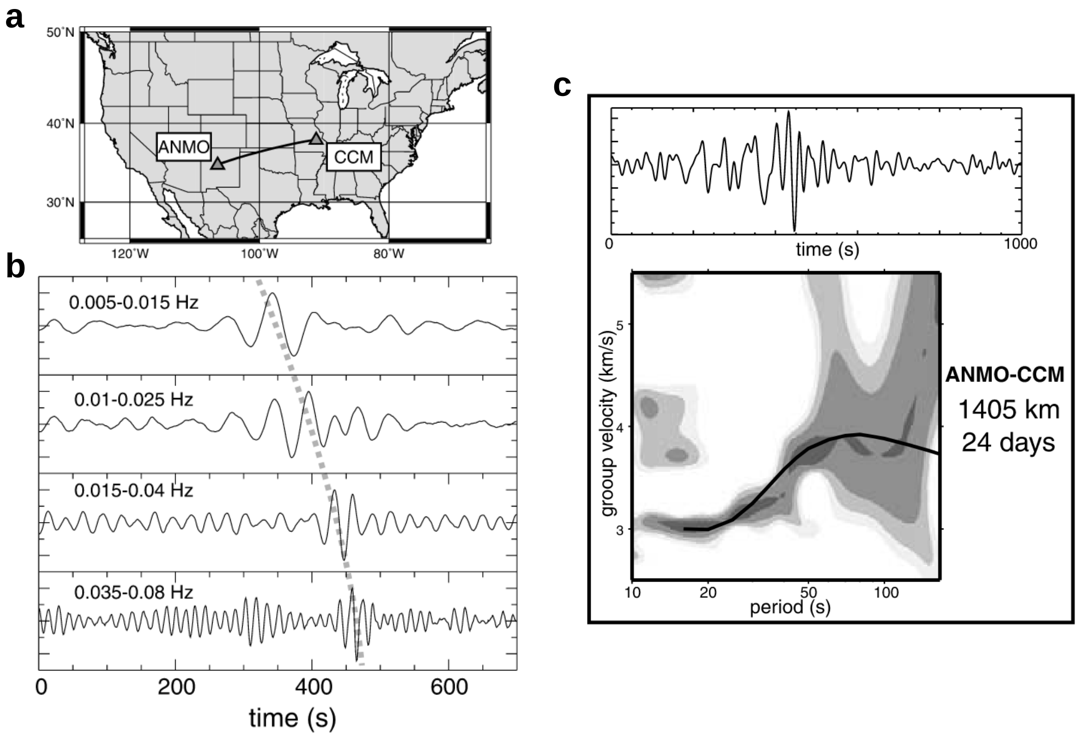

Figure 1.5: Cross-correlation results from 24 days of continuous vertical-component ambient noise recorded by a station pair from the USArray (1405 km inter-station distance). (a) Map showing the location of the station pair. (b) The causal part of the vertical-component correlation filtered in four frequency bands. Emergent Rayleigh waves are emphasized by the gray dashed line. (c) Top: the broadband cross-correlation signal; Bottom: the gray area show the frequency-time analysis of the broadband signal while the black line indicate the dispersion curve for the same couple, predicted from group-velocity maps of a global tomographic model. From Shapiro and Campillo (2004).

The construction of 3-D isotropic shear-wave velocity models based on ambient-noise Rayleigh-wave group velocities is conducted on two steps:

From dispersion curves to 2-D group-velocity maps

This first step, also called 'regionalisation' uses individual group-velocity dispersion curves involving N station pairs to build independently, isotropic 2-D maps of lateral velocity variations (see the example in Fig. 1.6). This is usually done by performing a group-velocity traveltime inversion at each period. Similar to the LET witch uses the ray theory for 3-D propagation of body waves, this tomography employs the ray theory for 2-D propagation of Rayleigh waves. The velocity field is usually discritized by means of fixed-size or adaptive structured mesh grids based on rectangular cells (e.g., Kustowski et al., 2008; Schaefer et al., 2011), or unstructured mesh grids based on Delauney or Voronoi cells (e.g., Curtis and Snieder, 1997; Sambridge et al., 2005; Bodin et al., 2012).

The forward problem is similar to (1.1) for a Rayleigh-wave propagating on 2-D along the great circle from one station considered as a 'virtual source' to a given receiver. The inverse problem, which consists on determining the velocity distribution in the medium explaining the

Rayleigh-wave traveltime can be tackled by two approaches:

- **Standard linearized inversion:** treats the analogue of the matrix-based linear inverse problem in (1.2) for a 2-D problem. Generally solved in least squares sens for a unique solution model, this approach is the most commonly used.

- **Bayesian inversion:** treats the inverse problem in a probabilistic way, i.e, the solution is represented by a posterior probability density function $p(\mathbf{m}|\mathbf{d})$ representing the probability of the model parameters $\mathbf{m}$, given a set of observed group velocities $\mathbf{d}$. According to Bayes theorem

  $$p(\mathbf{m}|\mathbf{d}) \propto p(\mathbf{d}|\mathbf{m})p(\mathbf{m}) \tag{1.16}$$

  where $p(\mathbf{d}|\mathbf{m})$ is the likelihood function, i.e, the probability of observing $\mathbf{d}$ given a model parameters $\mathbf{m}$. $p(\mathbf{m})$ is an 'a priori' probability density distribution on $\mathbf{m}$, i.e, what we know about the model independently of the data. Generally, $p(\mathbf{d}|\mathbf{m})$ is expressed with the Gaussian form (e.g., Bodin et al., 2012)

  $$p(\mathbf{d}|\mathbf{m}) = \frac{1}{\sqrt{(2\pi)^N|\mathbf{C}|}} \times \exp\left(\frac{-\phi(\mathbf{m})}{2}\right) \tag{1.17}$$

  where $\mathbf{C}$ is the covariance matrix of data errors and $\phi(\mathbf{m})$ is a L_2-norm misfit function between the candidate synthetic set of group velocities and $\mathbf{d}$.

  In this case, the velocity structures in the medium are no longer represented by a unique solution but by an ensemble of potential solutions, which is more in line with the non-unicity of the solution of the inverse problem. In addition, this method provides 'a posteriori' statistics on the model that can be useful in the interpretation, such as the uncertainties.

From local dispersion curves to S-wave velocities

The second step of the ANT procedure uses local dispersion curves extracted at each cell from the set of group-velocity maps to build local 1-D V_s models, that are usually interpolated in a 'quasi-3-D' model. This step requires performing a point-to-point 1-D inversion at depth. The forward problem is the 1-D modeling of the dispersion curve given a model $\mathbf{m}$. The inverse problem – determining the S-wave velocity distribution at depth that explains the dispersion curve – is non-linear, but as the LET problem, it is usually linearized and tackled by iterative standard LSQR-based procedures (e.g., Herrmann, 2013) that provide a unique solution, starting from a reference model. Other techniques has been deployed to mitigate the non-uniqueness of the solution, e.g, grid search (e.g., Stehly et al., 2009; Macquet et al., 2014), direct-search stochastic inversion (e.g., Mordret et al., 2014; Molinari et al., 2015) with Neighbourhood Algorithm (NA; Sambridge, 1999; Wathelet, 2008), grid-search-based probabilistic inversion (e.g., Lu et al., 2018; Brives, 2020), or transdimensional Bayesian inversion (e.g., Yuan and Bodin, 2018; Alder et al., 2021). For instance, the Bayesian approach uses a similar formulation as in (1.17) for a 1-D problem. In this case $\mathbf{d}$ represent the observed dispersion curve at a given location, N the number of group-velocity measurements in $\mathbf{d}$, and $\phi(\mathbf{m})$ is the misfit between $\mathbf{d}$ and the synthetic dispersion curve computed in a given candidate model $\mathbf{m}$ using well-established routines (e.g., Herrmann, 2013). The inverse problem and its formulation in a Bayesian framework is further discussed in Chapter 2 of the manuscript.

The densification of seismological networks has resulted in widespread application of ANT, demonstrating its ability to provide spatially continuous 3-D velocity models of the crust and upper mantle. However, ANT is limited by assumptions used in the two steps of the inversion procedure: (i) the high-frequency assumption used in the forward modeling of the 2-D inversion for group-velocity maps, and (ii) the V_s model is not constrained as a whole because of the 1-D point-to-point character of the inversion assuming later homogeneity of the medium. Moreover, ANT relies on surface waves that, by virtue of their propagation physics, are more sensitive to lateral variations. In contrast to body waves, they tend to smooth intracrustal variations and structural interfaces. Finally, the frequency content of the ambient noise (up to $\sim$ 3-5 s period) does not make possible to recover very small-scale structures and discontinuities.

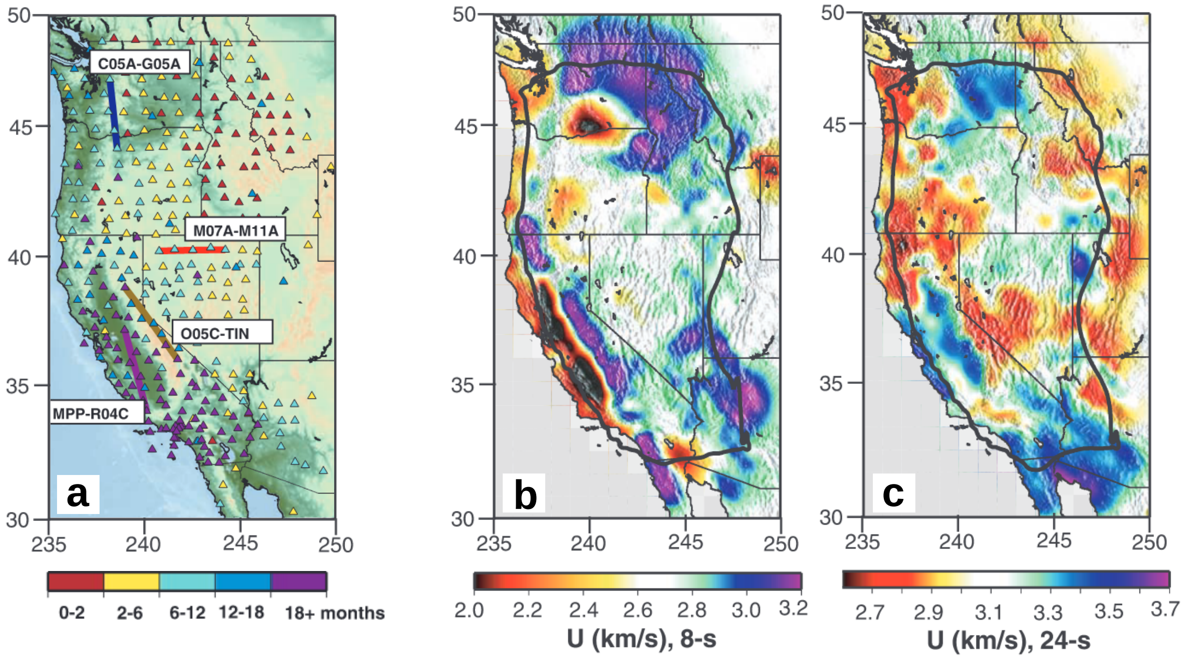

Figure 1.6: Results of a Rayleigh-wave group-velocity tomography using the USArray. (a) Map showing the location of the seismological stations used in the tomography. (b) and (c) show the 8-s velocity map (sensitive to the 5-10 km depth range) and the 24 s velocity map (sensitive to upper and lower crust depths), respectively. Modified from Moschetti et al. (2010).

Full-waveform inversion (FWI)

FWI is an iterative imaging procedure proposed by Lailly and Bednar (1983) and Tarantola (1984) in the 1980s, to exploit the full information contained in the seismic record (all the phases and all the amplitudes), with a potential resolution of up to half the wavelength. The inverse problem consists in minimizing residuals (data-to-data) between observed and synthetic seismograms. The forward problem – the 3-D modeling of wave-propagation – requires solving the wave equation.

Forward problem

Given a model parameters $\mathbf{m}$, the general form of the wave equation can be written as follows: $\mathcal{F}(\mathbf{m})\mathbf{u} = \mathbf{S}$, where $\mathcal{F}$ is the forward propagator on the model parameters – the physics of the wave propagation – $\mathbf{u}$ is the seismic wavefield computed by $\mathcal{F}$, and $\mathbf{S}$ is the source term. In a solid domain, the complete form of the second-order elastic-wave equation of the displacement field can be written as

$$\begin{cases} \rho(\mathbf{x})\partial_{tt}u_i(\mathbf{x},t) = \partial j\sigma_{ij}(\mathbf{x},t) + f_i(\mathbf{x},t) \\ \sigma_{ij}(\mathbf{x},t) = c_{ijkl}(\mathbf{x})\varepsilon_{kl}(\mathbf{x},t) + \Gamma_{ij}(\mathbf{x},t) \end{cases} \tag{1.18}$$

where ρ is the density, u the displacement field, f the external force term, σ and ε are the stress and strain tensor respectively, c_{ijkl} is the elastic stiffness coefficient and Γ is the stress failure related to moment-tensor source. ε is given by spatial derivatives of displacement through: $\varepsilon_{kl} = \frac{1}{2}\left(\partial_k u_l + \partial_l u_k\right)$.

Following the Voigt indexing (11 → 1, 22 → 2, 33 → 3, 23 or 32 → 4, 13 or 31 → 5, 12 or 21 → 6) and matrix notation, (1.18) can be written in the discrete form

$$\rho\partial_{tt}\mathbf{u} = DCD^T\mathbf{u} + \mathbf{S} \tag{1.19}$$

where C is the stiffness tensor which in the isotropic case is reduced to

$$C = \begin{pmatrix} \lambda+2\mu & \lambda & \lambda & 0 & 0 & 0 \\ \lambda & \lambda+2\mu & \lambda & 0 & 0 & 0 \\ \lambda & \lambda & \lambda+2\mu & 0 & 0 & 0 \\ 0 & 0 & 0 & 2\mu & 0 & 0 \\ 0 & 0 & 0 & 0 & 2\mu & 0 \\ 0 & 0 & 0 & 0 & 0 & 2\mu \end{pmatrix} \tag{1.20}$$

and $\mathbf{S}$ the source term. D denote the spatial derivative operator in the Cartesian domain

$$D = \begin{pmatrix} \partial_1 & 0 & 0 & 0 & \partial_3 & \partial_2 \\ 0 & \partial_2 & 0 & \partial_3 & 0 & \partial_1 \\ 0 & 0 & \partial_3 & \partial_2 & \partial_1 & 0 \end{pmatrix} \tag{1.21}$$

Different approach can be used for numerical solving of this 3-D partial differential equation (PDE): finite-difference (FD), finite element method (FEM; e.g., Graves, 1996; Operto et al., 2007) or spectral element method (SEM; e.g., Komatitsch and Vilotte, 1998; Komatitsch and Tromp, 1999). However, SEM methods, generally based on hexahedral elements, have been proven to provide an accurate representation of complex 3-D geological structures in crustal-scale imaging topics.

SEM methods usually approximate the solutions by means of Lagrange polynomials of high degrees, using Gauss-Lobatto-Legendre (GLL) points for spatial interpolation and numerical integration. The physical domain ($\Omega \subset \mathbb{R}^3$) is descritized to a set of deformed hexahedral elements $\{\Omega_e : \mathbf{x} = (x, y, z) \in \mathbb{R}^3\}$. Each element is composed of $(N+1)^3$ GLL points $\mathbf{x}_{ijk}$; N refers to the interpolation order, and i, j, k are the indexing of the GLL points in z, x and y dimensions, respectively. The hexahedral elements being isomorphic to a cube, one can find a unique Jacobian matrix $\mathbf{J}(\boldsymbol{\xi})$ that allows the transformation (or mapping) of a mesh element Ω_e into a reference cube element $\{\boldsymbol{\xi} = (\xi, \eta, \zeta) \in [-1, 1]^3\}$

$$\mathbf{J}(\boldsymbol{\xi}) = \begin{bmatrix} \partial_\xi z & \partial_\eta z & \partial_\zeta z \\ \partial_\xi x & \partial_\eta x & \partial_\zeta x \\ \partial_\xi y & \partial_\eta y & \partial_\zeta y \end{bmatrix} \tag{1.22}$$

An element of volume $dxdydz$ in the physical domain is associated to a volume $d\xi d\eta d\zeta$ in the reference domain through: $dzdxdy = J_d d\xi d\eta d\zeta$, where J_d is the Jacobian determinant, i.e. the determinant of $\mathbf{J}(\boldsymbol{\xi})$. The mapping between the reference cube and the hexahedral element Ω_e can be written as follows

$$\mathbf{x}(\boldsymbol{\xi}) = \sum_{i,j,k=0}^{N} N_{ijk}(\boldsymbol{\xi}) \mathbf{x}_{ijk} \tag{1.23}$$

where $\mathbf{x}_{ijk} = \mathbf{x}(\boldsymbol{\xi}_{ijk})$; $\boldsymbol{\xi}_{ijk} = (\xi_i, \eta_j, \zeta_k)$ are the GLL points in the reference domain. N_{ijk} is the basis function (or shape function) defined by triple products of Lagrange polynomials of degree N: $N_{ijk}(\boldsymbol{\xi}) = L_i(\xi) L_j(\eta) L_k(\zeta)$, where the polynomial $L_l(x)$ can be written as follows

$$L_l(x) = \prod_{m=0, m \neq l}^{N} \frac{x - x_m}{x_l - x_m} \tag{1.24}$$

Thus, a vector $\mathbf{u}$ can be approximated on the element Ω_e in the physical domain using the relation

$$\mathbf{u}\left(\mathbf{x}(\boldsymbol{\xi})\right) \approx \sum_{i,j,k=0}^{N} N_{ijk}(\boldsymbol{\xi}) \mathbf{u}(\xi_{ijk}) = \sum_{i,j,k=0}^{N} N_{ijk}(\boldsymbol{\xi}) \mathbf{u}_{ijk} \tag{1.25}$$

Similarly, the gradient of $\mathbf{u}$ can be approximated using the derivatives of the Lagrange polynomials. Using the GLL quadrature and the property of Lagrange polynomials, the global system (or variational formulation) of (1.19) takes the weak discrete form (e.g., Trinh et al., 2019)

$$\mathbf{M} \partial_{tt} \mathbf{u} = -\mathbf{K}\mathbf{u} + \mathbf{F} + \mathbf{B} \tag{1.26}$$

where $\mathbf{M}$ and $\mathbf{K}$ are the global mass and stiffness matrices respectively, and $\mathbf{F}$ is the source term. $\mathbf{M}$ and $\mathbf{F}$ are given by: $M_{\hat{k}\hat{k}} = w_{\hat{k}} \rho(\boldsymbol{\xi}_{\hat{k}}) J_d(\boldsymbol{\xi}_{\hat{k}})$, and $F_{\hat{k}\hat{k}} = w_{\hat{k}} J_d(\boldsymbol{\xi}_{\hat{k}}) S_{\hat{k}}$. In these expressions, $\hat{k}$ stands for the triple indexes i,j,k, and w corresponds to the quadrature weight associated with the GLL points $\boldsymbol{\xi}_{\hat{k}}$ in the reference domain. The stiffness matrix is given by the spatial derivative matrices through $\mathbf{K} = \mathbf{D}^w C \mathbf{D}$, where $\cdot^w$ denotes the GLL weighting. Finally, the matrix $\mathbf{B}$ represent the boundary term – the absorbing conditions at edges of the numerical model used to attenuate the outgoing wavefield.

The PDE (1.26) and its adjoint system (for the adjoint wavefield $\bar{\mathbf{u}}$) are usually solved in time domain using Newmark scheme (e.g., Komatitsch and Tromp, 1999) which gives a good numerical accuracy and reasonable convergence when the courant-Friedrichs-Lewy (CFL) stability condition is satisfied.

Inverse problem

The inverse problem consists in minimizing a misfit function (also called objective function) $\chi(\mathbf{m})$ between synthetic waveforms $\mathbf{d_{cal}}$ obtained from the numerical resolution of (1.26) given a model parameters $\mathbf{m}$, and the observed waveforms $\mathbf{d}$. The least-square norm (or $L2$-norm for short) is usually used as a default misfit function for real data application as it takes use of the complete information of the signal, and presents other advantages, such us the simplicity of its adjoint source (difference in time between $\mathbf{d}_{cal}$ and $\mathbf{d}$) – straightforward to implement and computationally inexpensive. The $L2$-norm misfit function takes the form

$$\chi(\mathbf{m}) = \frac{1}{2}\|\mathbf{d}_{cal}(\mathbf{m}) - \mathbf{d}\|^2 \tag{1.27}$$

The $L2$-norm distance is a non-convex function as it is intrinsically affected by the cycle skipping issue – a phase-ambiguity problem occurring when the time shift between observed and synthetic signals is larger than half a period (e.g., Virieux and Operto, 2009; Pladys et al., 2021) – as illustrated in Figure 1.7. Obviously, the non-convexity of this type of misfit function makes the FWI problem being strongly non-linear, meaning that a wrong kinematic (i.e., the inversion fits wrong phases of the data), results in a convergence of the model solution towards a local minimum. Nevertheless, it remains challenging to find convenient convex functions for the FWI real-data application – reason why the conventional $L2$-norm is still widely used nowadays.

The minimization of the misfit function in (1.27) can be tackled either by global and semi-global methods (e.g., Metropolis and Ulam, 1949; Kirkpatrick et al., 1983; Sen and Stoffa, 1995) or by local optimization methods (e.g., Nocedal and Wright, 2006). Global and semi-global approaches seek to search for the global minimum of the misfit function by sampling the model space, without any 'a priori' knowledge. These methods are hardly applicable in practice as they require performing a large number of forward simulations – computationally expensive – and dense sampling of the model parameters space – necessity of big storage capacity. Local optimization strategies are usually used as an alternative to global strategies, as they are designed to iteratively converge to the global minimum while considering a larger number of model parameters. However, theses methods require the use of a relatively 'good' initial model – a starting point that is within the global minimum basin of attraction. Starting from the initial model $\mathbf{m}_0$, at each iteration k, the minimization process of local optimization methods will search for an updated model $\mathbf{m}_{k+1}$ in the vicinity of the starting point, so that the misfit function χ decreases. The updated model can be expressed as the sum of the actual model $\mathbf{m}_k$ and a model update (or perturbation model) $\Delta\mathbf{m}_k$

$$\mathbf{m}_{k+1} = \mathbf{m}_k + \Delta\mathbf{m}_k \tag{1.28}$$

Assuming small perturbation model $\Delta\mathbf{m}_k$, the Taylor expansion of the first-order misfit gradients to the model parameters is given by: $\nabla\chi(\mathbf{m}_{k+1}) \approx \nabla\chi(\mathbf{m}_k) + H_k\Delta\mathbf{m}_k$, where H_k is the Hessian matrix, i.e. second-order derivatives of the misfit function. The local optimization strategies generally rely on the linearization of the inverse problem, so that the misfit function $\chi(\mathbf{m})$ can be approximated locally by a quadratic function of a minimum corresponding to

$\nabla\chi(\mathbf{m}_{k+1}) = 0$. Consequently, the model update can be estimated from the misfit gradients $\nabla\chi(\mathbf{m}_k)$ and their inverse derivatives (e.g., Virieux and Operto, 2009; Trinh et al., 2017)

$$\Delta\mathbf{m}_k = -{H_k}^{-1}\nabla\chi(\mathbf{m}_k) \tag{1.29}$$

The gradients are usually computed from the zero-lag correlations of incident and adjoint wavefields. In the elastic case, misfit gradients with respect to the solid parameters (ρ_s, C_{IJ}) are given by

$$\frac{\partial\chi\left(\mathbf{m}\right)}{\partial\rho} = \left(\bar{\mathbf{u}}, \partial_{tt}\mathbf{u}\right)_{\Omega,t}; \quad \frac{\partial\chi\left(\mathbf{m}\right)}{\partial C_{IJ}} = \left(\bar{\varepsilon}, \frac{\partial\mathbf{C}}{\partial C_{IJ}}\boldsymbol{\varepsilon}\right)_{\Omega,t} \tag{1.30}$$

where $\bar{\mathbf{u}}$ is the adjoint displacement wavefield associated with $\mathbf{u}$, and $\bar{\varepsilon}$ is the adjoint of the strain field $\boldsymbol{\varepsilon}$ for model sets Ω.

In practice, accessing the full Hessian matrix is unfeasible because of its large size, meaning that the optimal model update can not be achieved. Several approaches has been designed to tackle this issue by approximating the Hessian, such as the limited memory quasi-Newton method (l-BFGS) that approximates the inverse Hessian using a limited number of gradients and models from the previous iterations (Byrd et al., 1995; Nocedal, 1980).

Other wave-equation-based imaging methods are used for large-scale imaging. Called WET (for wave equation tomography), these approaches use misfit functions of arrival-time differences (Luo and Schuster, 1991), thus representing a more sophisticated alternative to conventional traveltime tomography methods, such as LET or ANT (see an example in Fig. 1.8). The wave equation tomography, in line with physics of the wave-propagation, has been proven to provide robust 3-D velocity models at the scale of the crust and upper mantle (e.g., Fichtner et al., 2009; Tape et al., 2010; Zhu et al., 2012; Yuan et al., 2014; Fichtner and Villaseñor, 2015; Beller et al., 2018; Lu et al., 2020; Wang et al., 2021). However, it is worth recalling that these methods, usually involving local optimization strategies, have two main limitations: (i) they are sensitive to the initial model, and (ii) their computational cost that rapidly increases when it comes to applying them with large volume of data.

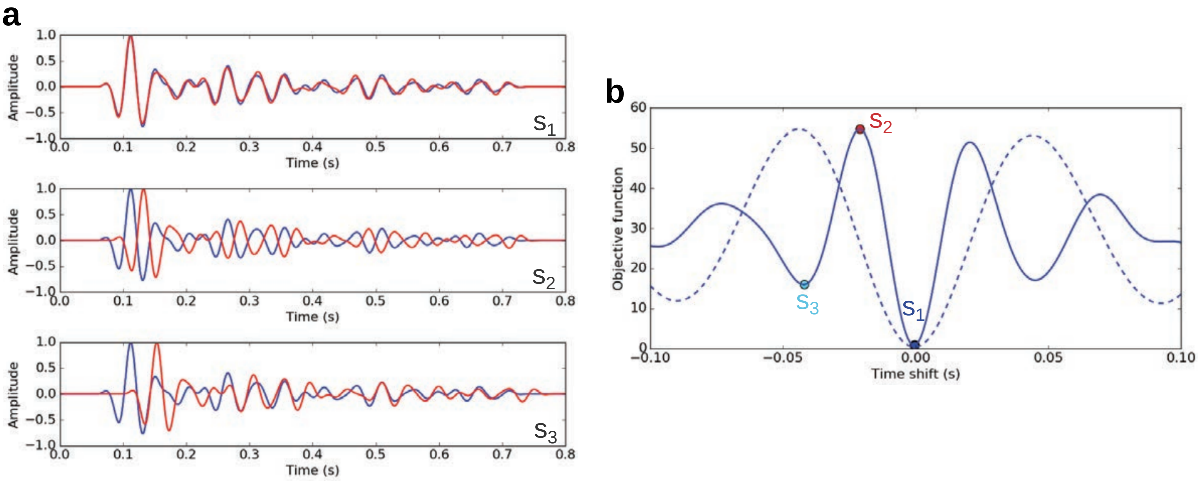

Figure 1.7: Numerical synthetic illustration of the cycle-skipping effect on the shape of the misfit function. (a) Observed signal (blue) and synthetic signal (red) for three different time shifts (s_1, zero-shift; s_2, half a period shift; s_3, period shift). The shape of the $L2$-norm misfit function. The dots are associated with each time-shift value. The zero-shift value (s_1) corresponds to the global minimum while s_2 and s_3 result on local maximum and minimum, respectively. The dashed curve is the misfit function obtained for the central-frequency divided by two. Modified from Chauris (2021).

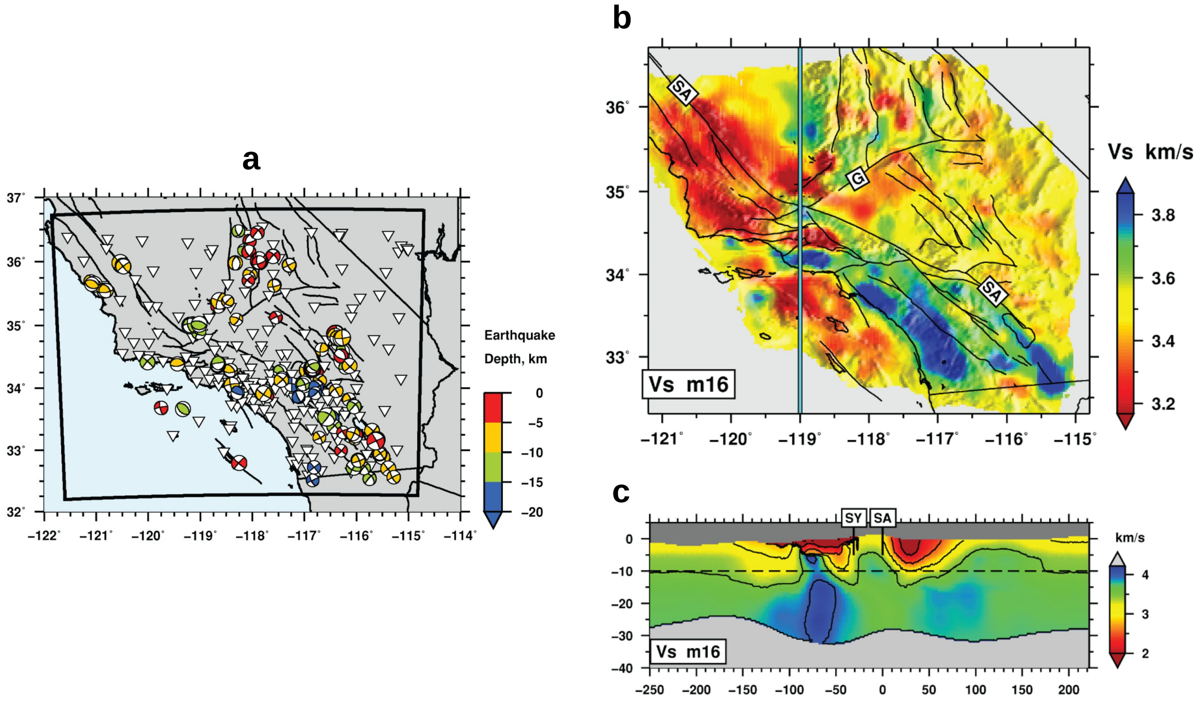

Figure 1.8: Results of a 3-D SEM-based wave-equation tomography in southern California using body and surface waves from regional earthquakes. (a) Map showing the earthquakes and the seismological stations used in the tomography. (b) 10-km depth slice in the final V_s model. (c) A north-south 2-D cross-section in the final V_s model. Modified from Tape et al. (2010).

1.2 Context: Western Alps and Ligurian-Provence basin

This section places our tomographic study, which focuses on the western Alps and the Ligurian-Provence basin, in a more global geodynamic context, that is the western Mediterranean region. We briefly present the tectonic evolution of the Alps and the Ligurian basin leading to their present-day structural architecture and describe their main geological domains and units. We point out the major geodynamic, structural and petrological concerns that stimulated 3-D tomography studies and the expansion of seismological surveys. Thus, we will present the AlpArray seismic network and overview the 3-D tomographic models in the region and their main insights and limitations. Finally, we highlight the remaining concerns that require further progress in the accuracy and consistency of tomographic models at this scale, which is precisely what motivates our study.

1.2.1 Geodynamic setting

The geodynamic evolution in Mediterranean region occurs in a context of plate reorganization, dominated since the Late Cretaceous by the convergence between Europe and Africa plates, and involves the Adria and Iberia micro-plates. The relative long-term motion of Africa with respect to Europe (about 6-3 mm/yr; e.g., Macchiavelli et al., 2017) resulted in the orogenesis of the Alps and other peri-Mediterranean mountain ranges (Pyrenees, Dinarides, Apennines, etc.) and also caused the opening of the western Cenozoic rift system. In this context the opening of the Mediterranean back-arc oceanic domains (Ligurian, Algerian, and Tyrrhenian basins) is mainly driven by the dynamics of subduction of the old and dense Tethyan oceanic slab (Fig. 1.9, Faccenna et al., 2014).

Western Alps orogenesis

In this slow plate convergence context, the western Alps result from three successive tectonic episodes involving Europe, the Adria micro-plate and the Tethyan oceanic domain (Tethys) in between: (i) closure of the oceanic domain by subduction from Late Cretaceous to Early Eocene (e.g., Handy et al., 2010). (ii) continental subduction of the European margin beneath Adria during the Late Eocene (e.g., Chopin, 1984; Duchêne et al., 1997; Guillot et al., 2009; Zhao et al., 2015), and (iii) continental collision from Oligocene onwards (e.g., Polino et al., 1990; Dumont et al., 2012). This later change of dynamics from subduction to collision was accompanied by a change in the Adria-Europe convergence direction, from N-S to E-W at about 35 Ma. This multiphase evolution led to a complex present-day arcuate architecture of Western Alps, where different units are involved: (1) to the west, the European continental domain (or European foreland) corresponding to the lower plate (Fig. 1.9b); (2) to the east, the Adria continental domain (or Adriatic foreland) corresponding to the upper plate (Fig. 1.9b); (3) the Eocene subduction wedge (or accretionary prism) in between, bounded by two major crustal-scale faults: to the west, the Frontal Pennine Fault (FPF; Fig. 1.9b) and to the east, the dextral strike-slip Insubric Fault (IF). The European domain is composed of different units: Meso-Cenozoic sedimentary cover overlying a Paleozoic crystalline basement corresponding to the French External Crystalline massifs (Aa, Aar; Ar, Argentera; Be, Belledonne; Go, Gotthard; GP, Gran Paradiso; MB, Mont Blanc; Pe, Pelvoux, Fig. 1.9b). The Adriatic domain is composed of thick sedimentary series including the Po plain and the Piedmont tertiary basin, overlying a basement of metamorphic units (IV, Ivrea-Verbano; La, Lanzo; Se, Sesia-Lanzo, Fig. 1.9b). The Eocene subduction wedge recorded high-pressure metamorphic facies related to the subduction dynamics. This zone is developed by stacking of oceanic lithosphere and sediments slices with crustal units originating from the European continental margin such as GP: Gran Paradiso, MR: Monte Rosa, and DM: Dora Maira (Fig. 1.9b). Dora Maira hosts exhumed rocks of UHP (Ultra-HP) minerals (e.g. coesite), which were first observed by Chopin (1984) as an evidence of the subduction of the European continental crust (e.g., Agard, 2021).

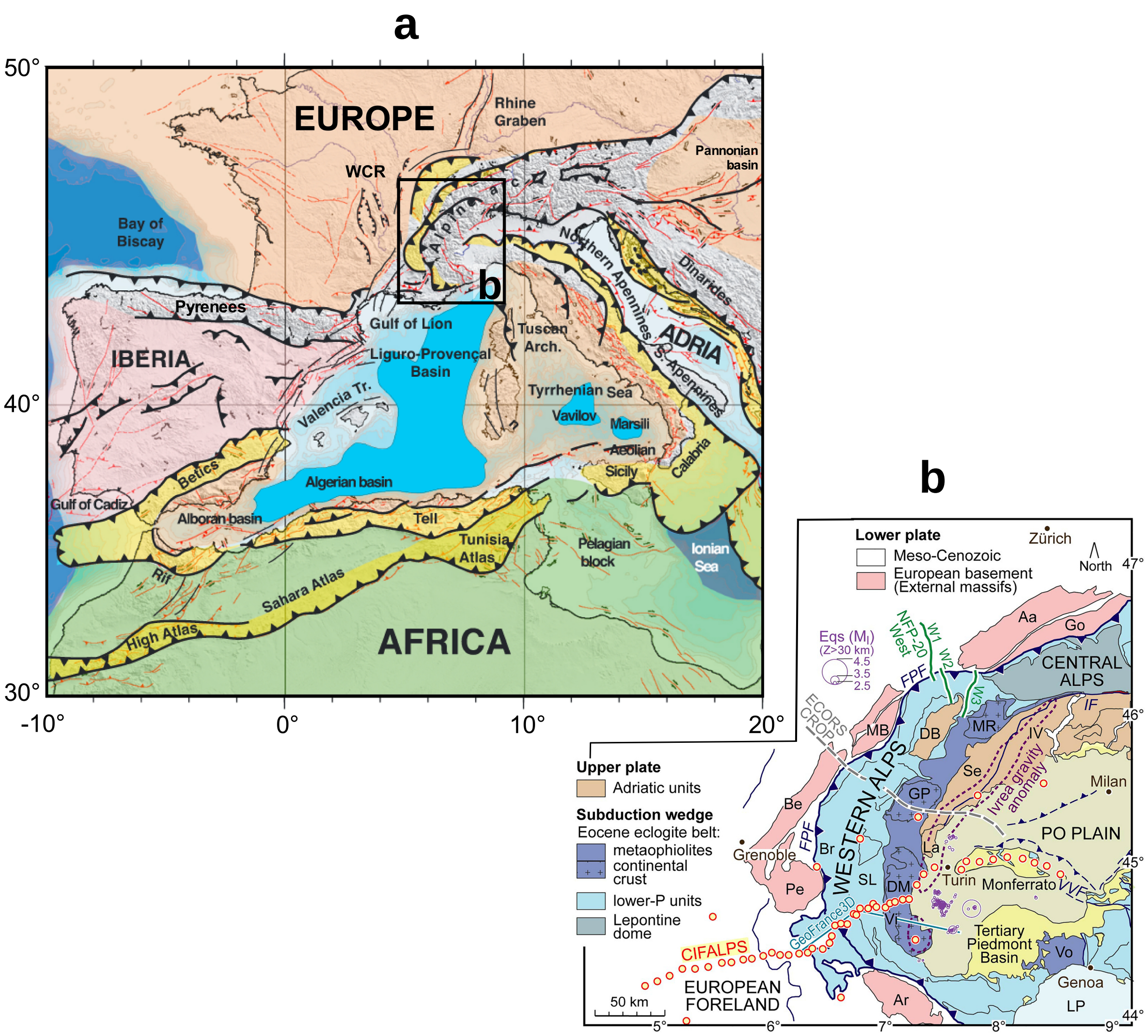

Figure 1.9: Tectonic setting in the western Mediterranean region. (a) Tectonic map showing plates and micro-plates implicated in the tectonic evolution in the area, as well as the associated mountain belts and oceanic basins (modifed from Faccenna et al., 2014). The acronym WCR refers to the Western Cenozoic Rift System. (b) Geological map presenting the main structural domains of the western Alps [black frame in (a)], and some reference geophysical transects. Acronyms: Aa, Aar; Ar, Argentera; Be, Belledonne; Br, Briançonnais; DB, Dent Blanche; DM, Dora-Maira; FPF, Frontal Pennine Fault; Go, Gotthard; GP, Gran Paradiso; IF, Insubric Fault; IV, Ivrea-Verbano; La, Lanzo; LP, Ligurian-Provence domain; MB, Mont Blanc; MR, Monte Rosa; Pe, Pelvoux; Se, Sesia-Lanzo; SL, Schistes lustrés; TY, Tyrrhenian; Vi, Viso; Vo, Voltri; VVF, Villalvernia-Varzi Fault. Modified from Malusà et al. (2021).

Opening of the Ligurian-Provence basin

During Miocene and Pliocene Epochs, the opening of back-arc extensional basins occurred at the back of the Adria northwest-dipping subduction zone (e.g. Gueguen et al., 1998; Jolivet et al., 2020). This extension started along the Provence region leading to the Ligurian-Provence basin, and has further spread from east to west and south, resulting in the opening of the Algerian basin, and later, of the Tyrrhenian basin (e.g., Rollet et al., 2002; Séranne, 1999). The opening of the Ligurian basin initiated at 35 Ma by a rifting phase between Europe and the Corsica-Sardinia block (Fig. 1.10a). The main driving process of this opening is not the convergence between Europe and Adria/Africa, but a pull of an old and dense Tethyan oceanic slab, which remained to be subducted in this domain (e.g., Jolivet and Faccenna, 2000). The progressive south-eastward roll-back and retreat of the Adria slab below the Corsica-Sardinia domain led to Oligocene stretching of the continental crust followed by continental break-up during the early Miocene, and to the genesis of an oceanic crust between 15 and 11 Ma at a pace of up to 3 cm/yr (Fig. 1.10a; Séranne, 1999; Jolivet and Faccenna, 2000). As a result, three principal domains, mainly identified from active seismic data, describe the present-day geological setting of the Ligurian-Provence basin (Fig. 1.10b): (i) two thinned conjugate continental passive margins corresponding to the Ligurian-Provence margin to the north and Corsican margin to the south; (ii) an oceanic domain in between, described as an 'atypical oceanic crust' by Rollet et al. (2002) because it is thinner than normal oceanic crust; (iii) two transitional domains separating the margins and the oceanic domain, likely made up of a very thin continental crust overlying a thick rift-related corner of magmatic underplating (e.g., Séranne, 1999). The entire region is characterized by magnetic anomalies, and by the presence of magmatic bodies identified from seismic reflection data.

Major geologic concerns

The western Alps display strong geological variations, across and along-strike, as reflected by their complex architecture. Since the 1990s, the structure of the lithosphere beneath the western Alps and the Ligurian-Provence basin has been probed by a broad spectrum of 2-D imaging techniques, through controlled-source seismic (CSS) surveys or passive seismic experiments (e.g., receiver function analysis). In the western Alps, the ECORS-CROP normal-incidence and wide-angle reflection survey (Nicolas et al., 1990, location in Fig. 1.9b) has provided a high-resolution image of the reflectivity of the crust in the northwestern Alps, and receiver functions along the Cifalps profile (see location in Fig. 1.9b) has evidenced the European continental subduction by detecting a 75-km Moho depth beneath Dora Maira (Zhao et al., 2015). In the Ligurian sea, numerous active seismic surveys provided high-resolution images of the reflectivity in the three domains (e.g., Makris et al., 1999; Contrucci et al., 2001; Rollet et al., 2002; Dannowski et al., 2020). In such a complex tectonic setting as the one of the western Mediterranean region, the interpretation of the underlying geodynamic processes remains under debate. Thus, 3-D seismic imaging is critically needed to complement the 2-D seismological observations by constraining the deep 3-D structures, especially since the region benefits from a fairly wide coverage of seismological stations, including the newly deployed AlpArray land-sea network.

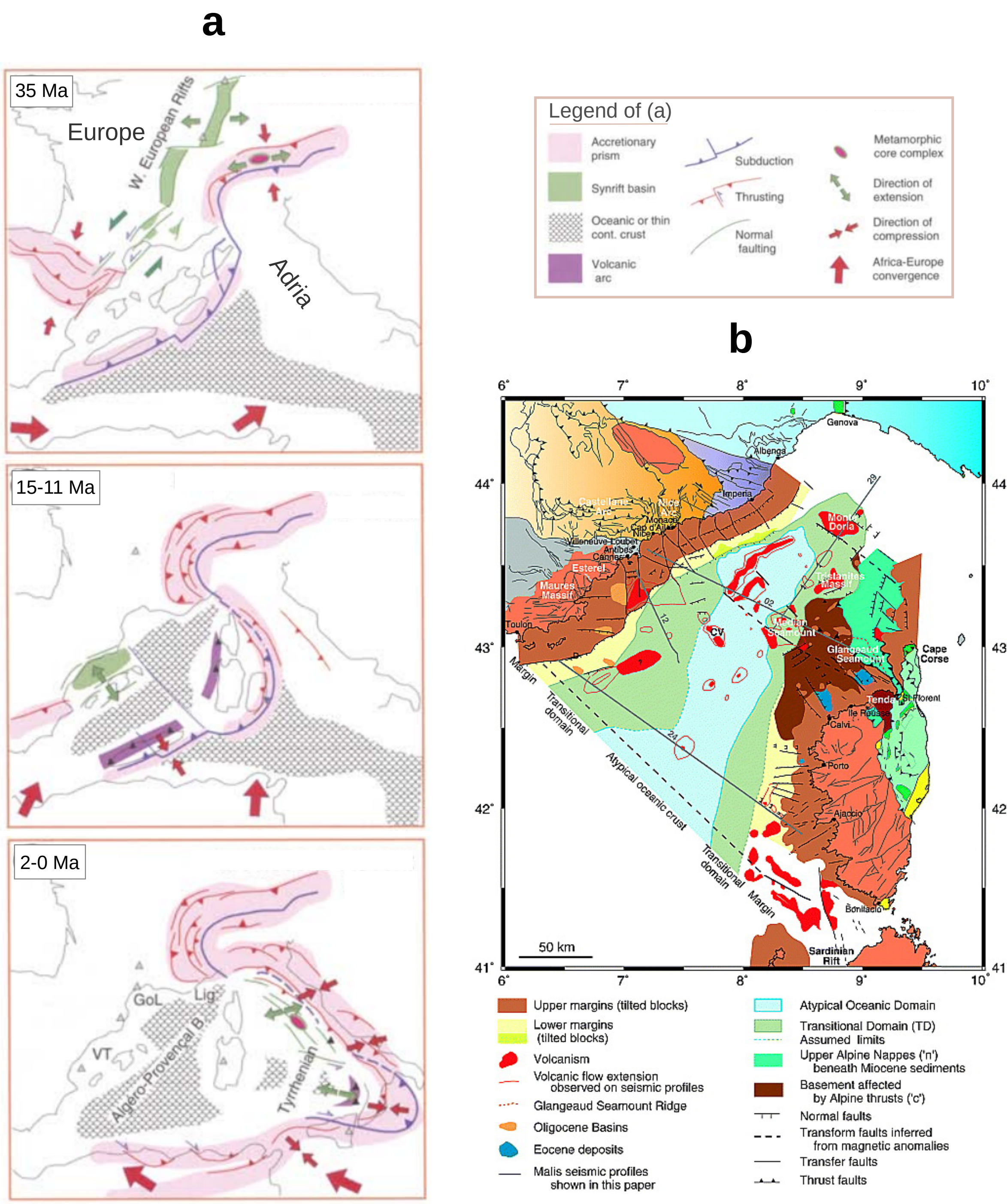

Figure 1.10: Tectonic setting of the western Mediterranean domain. (a) Sketch of the geodynamic evolution of the NW-Mediterranean domain since the Eocene (modified from Séranne, 1999). (b) Geological map showing the three main crustal domains of the Ligurian-Provence basin: continental margins, transitional domains and the central oceanic crust (modified from Rollet et al., 2002).

1.2.2 AlpArray seismic network

By developing the AlpArray Seismic Network (AASN), the principal interest of the AlpArray project, a European consortium involving 36 institutions from 11 countries, is to deepen understanding of the orogenesis in the Alps–Apennines–Carpathians–Dinarides system and its relationship to mantle dynamics, plate reorganizations, surface processes and seismic hazard (Hetényi et al., 2018). Composed of 600 broadband station spacing at less than 52 km, the AASN is one of the few dense seismic networks consisting of both onshore and offshore stations (Fig. 1.11). The onshore component of the AASN was operated for 2–4 years in the period 2015-2019 and covered the Greater Alpine. Another interest of the AASN is to further investigate the 3-D structure beneath the Ligurian-Provence basin and its margins. For that aim, the offshore part of the AASN was deployed in the northwestern Mediterranean sea with 29 Franco-German ocean bottom seismometers (OBS) that operated for 8-10 months in the period 2017-2018.

The AASN complements other temporary experiments and permanent networks by filling gaps in station coverage in Western Europe, thus providing ideal conditions for multiple 3-D seismic-imaging methods of the lithosphere. Although parts of the onshore component of the AASN have been used in lithospheric imaging, mainly by ambient noise tomography, at large-scale (Lu et al., 2018, 2020), or at regional-scale (e.g., Schippkus et al., 2018; Sadeghi-Bagherabadi et al., 2021), the entire AASN, onshore and offshore, for the entire recording period, has not yet been exploited as a hole for large-scale imaging.

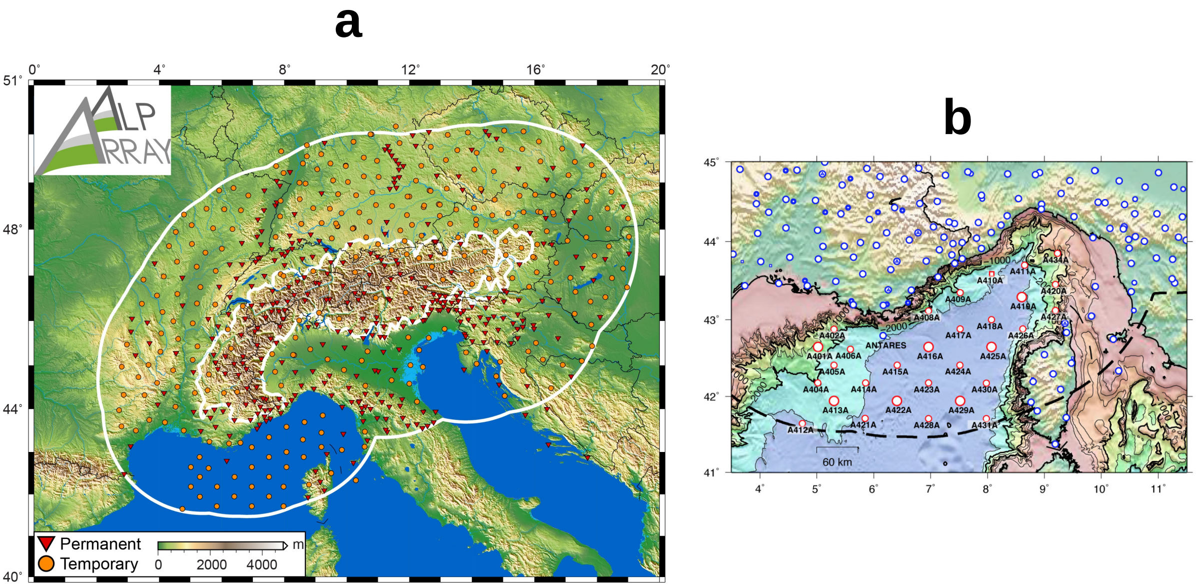

Figure 1.11: AlpArray seismic network (Hetényi et al., 2018). (a) Location map of seismological stations belonging to the AlpArray network (orange circles). Red triangles: stations from European permanent networks. (b) The AlpArray OBS network in the Ligurian sea. Large red circles: French OBSs; smaller red circles: German OBSs, blue circles: onshore stations.

1.2.3 Overview of existing 3-D tomographic models

In this section, we present a synthesis of 3-D tomography studies of the crust and upper mantle in the Alpine region and in the Ligurian-Provence basin. Two types of 3-D imaging of the crust and upper mantle have been applied in these regions. First, local earthquake tomography using essentially stations of the permanent networks, before the deployment of AlpArray. Then, with the densification of the permanent networks and the evolution of AlpArray, a number of ambient noise tomographies have been carried out. We will compare different available tomographic models, highlighting the constraints they have added into the Moho 3-D depth mapping during its evolution from the first reference map. As our study does not focus on the lower mantle structure beneath Europe, we will not discuss teleseismic tomographies. An overview of the ensemble of the seismological knowledge (active seismic, passive seismic, tomography, etc.) in the western Alps can be found in Paul (2022).

$\mathbf{V_s}$ ***models in the Alps from ambient-noise tomography***

Since the first application of ambient noise tomography (ANT) for crustal imaging of the Alps by Stehly et al. (2009), who used 150 permanent stations in Western and Central Alps, various V_s models involving different inversion approaches have been developed during the evolution of the European seismic networks. An extended model than that of Stehly et al. (2009) was constructed by Molinari et al. (2015) who used the same set of stations in the Alpine side and included more stations in Italy to cover the Adriatic crust. This model was derived using a regularized linear inversion (with LSQR) for Rayleigh-wave group- and phase-velocity maps with a fixed grid-size parameterization, and a 1-D stochastic inversion at depth for V_s. They used a similar parameterization at depth than that used for EPcrust (Molinari and Morelli, 2011), including 3 crustal layers and two 25 km-thick mantle layers. Their 3-D Moho depth map (Fig. 1.12) is a higher resolution version of Spada et al. (2013)'s smooth map, showing more details on the depth variations of the European Moho along the Alpine arc. Although their crustal model was more constrained than the model by Stehly et al. (2009), its lateral resolution ($\sim$ 100 km), far from that of LET models in the region, was insufficient to provide new insights into the small-scale crustal structures.

Combining surface waves from ambient-noise correlations, regional and telesismic earthquakes, Kästle et al. (2018) derived a large-scale V_s model of the crust and upper mantle. They used a larger number of permanent stations, resulting in a rather better coverage of the Alpine arc. Kästle et al. (2018) used a similar inversion approach than Molinari et al. (2015): a linearized inversion for phase-velocity maps, followed by a stochastic inversion at depth for V_s, exploring $28,000$ 1-D 8-layer models (sediments, upper-crust, lower-crust and a mantle composed of 5 layers over a half-space). Their model exhibits a higher resolution ($\sim$ 50 km in the crust and $\sim$ 100 km in the mantle) than the previous ANT models, allowing a better recovering of small velocity structures such as the Ivrea Body fast-velocity anomaly in the western Alps (Fig. 1.12) that was already imaged by LET models (e.g., Diehl et al., 2009; Solarino et al., 2018). Their 3-D depth map of Moho proxy shows a progressive deepening of the European Moho up to 55 km beneath the western Alps and 45-50 km depth beneath the central-eastern Alps.

With an even larger number of seismological stations (1300), including 6 months of the temporary AlpArray, Lu et al. (2018) derived a new large-scale ANT model of Western Europe. Similar to the previous ANT studies, they also derived their 2-D maps (for vertical-component Rayleigh-wave group velocities) using linearized inversion. However, they used a non-uniform grid parameterization that adapts to the path density and they estimated lateral resolutions of 30 km in the upper-, middle-crust and $\sim$ 90 km at lower-crust and upper mantle. Lu et al. (2018) performed a probabilistic inversion based on a grid search over 8×10^6 4-layer 1-D models (sediments, upper-, lower-crust and half-space Mantle). This model was the first to map in 3-D, a NE-SW 8-10-km Moho step beneath the French External Massifs. Their Moho proxy depth map (4.2 km/s iso-velocity) exhibits significant variations in the maximum depth of the European Moho along the Alpine arc (between $\sim$ 40 to $\sim$ 55 km) and finer constrains on the geometry of the Adriatic Moho than the previous maps (Fig. 1.12). Lu et al. (2020) further refined this V_s model by performing an SEM-based elastic wave-equation tomography (WET) for Rayleigh-wave phase dispersion using the dataset of Lu et al. (2018). Their WET improved the shape and contrast of the 3-D velocity anomalies and further refined the model resolution, resulting on a higher resolution Moho depth map (Fig. 1.12). This V_s model is the most up-to-date of the Alpine region.

More regional ANT models have also been developed to provide insights into specific structural and petrophysical issues, for example, in Vienna basin (Schippkus et al., 2020), in Western Alps (Zhao et al., 2020), in South-Eastern Alps (Sadeghi-Bagherabadi et al., 2021) and in Bohemian Massif (Kvapil et al., 2021). Zhao et al. (2020) who used the group-velocity maps of Lu et al. (2018) in a 1-D transdimensional inversion for V_s, provided a well-resolved image of the European subduction in the southwestern Alps.

$\mathbf{V_p}$ ***models in the Alps from local-earthquake tomography***

Numerous V_p models of the Alpine region were derived from local earthquake tomography (LET), e.g, in the western Alps and Italy by Di Stefano et al. (2009); in the central and western Alps and Po basin by Diehl et al. (2009); in the western Alps by Potin (2016) and Solarino et al. (2018). The models of Diehl et al. (2009) and Di Stefano et al. (2009) were used to complement the CSS (controlled-source seismic) data and verify the RF-detected Moho depths, for constraining the central and western Alps and Italy parts of the Spada et al. (2013)'s Moho depth map. The model by Solarino et al. (2018) provided an improved image of the structure in the subduction complex, giving additional constrains on geological models of the Dora-Maira (U)HP (Ultra-High-Pressure) units exhumation during the subduction of the European continental crust in the western Alps. The most up-to-date high-resolution V_p model of the western Alps is the one by Potin (2016) who used $791,000$ arrival times of P and S waves emitted from more than $36,000$ local earthquakes and recorded by 375 stations. Their Moho depth map, estimated from the strongest vertical-gradient shows two differentiated blocks in the Ivrea body high-velocity anomaly (IB in Fig. 1.12). However, apart from the well-covered central area, this model did not provide new information in the external areas of the Alps as these parts of their Moho map were filled in by previous models, already smooth in these areas. Thus, like the previous LET models, it failed to image the Moho jump under the French External Massifs that the ANT had been able to detect (Lu et al., 2018). Furthermore, none of these LET models were able to image the deepening of the Moho along the subduction of the European crust in the western Alps (detected down to 75 km by the RFs; Zhao et al., 2015), because of the limited seismic coverage at large depths given the few deep earthquakes in the region.

$\mathbf{V_s}$ ***models in the Ligurian-Provence basin from ANT***

In contrast to the Alpine area which has been extensively explored by 3-D tomography studies, the only two available 3-D velocity models of the crust and upper mantle beneath the

Ligurian-Provence basin are very recent and have both been derived by ANT. Until 2021, this area has only been imaged in 2-D by means of marine active-seismic surveys along irregularly distributed lines (e.g., Makris et al., 1999; Contrucci et al., 2001; Rollet et al., 2002; Dannowski et al., 2020). This gap is mainly due to the poor coverage in the Ligurian sea, as the AlpArray OBSs were only deployed in 2017 and recovered in 2018. The first attempt was made by Wolf et al. (2021) who used 22 OBSs and 23 onshore stations nearby the basin to derive an ANT model covering the Ligurian-Provence basin. Although they estimated local Moho depths, their model was nevertheless affected by small-scale irregularities, preventing the extraction of a coherent 3-D Moho map. Indeed, they pointed out the difficulty of using OBS noise data in crustal imaging. Magrini et al. (2022) derived a larger ANT, extending over the Tyrrhenian sea, but without using the AlpArray OBSs. Similarly to Wolf et al. (2021), they derived their dispersion maps from a linearized inversion. They used a stochastic approach for V_s and derived a Moho proxy by interpolating the bottom depths of the lower-crustal layers from the 1-D local V_s models. Their Moho map (Fig. 1.12) shows depths that vary between 15 km and 18 km along the Ligurian basin axis, too deep compared to the 12-km depth Moho detected by active-seismic data (Dannowski et al., 2020). Furthermore, this Moho map is too smooth to provide new constraints on the crustal architecture of the Ligurian domain.

Intermediate conclusion

These tomographic 3-D models have provided first-order constraints on the three-dimensional structure of the crust and upper mantle. However, their spatial resolution is still insufficient to discern small-size intracrustal units and deep features, partly because none of them has exploited the entire AlpArray, and also because of the simplifying assumptions made in their construction framework. Furthermore, the lack of accurate and quantitative estimate of uncertainty in theses models may bias the geological interpretation. This makes challenging the correlation of crustal-velocity structures with geological units mapped at the surface, and therefore the elaboration of large-scale self-consistent geological models – key to answer major questions about the deep geodynamics. In the western Alps, while the depth of the European Moho along the subduction of the European crust is constrained in 2-D along reference profiles by receiver functions (RFs), its 3-D geometry and along-strike variations are poorly constrained. This is a major limitation to a 3-D description of the deep dynamics, as there is no sufficiently robust 3-D model to validate the RF observations first, and subsequently make it possible to extrapolate their 2-D geological interpretations. In the Ligurian domain, the resolution and robustness of the ANT models were not sufficient to provide any additional input into the still-debated thickness and petrological-lithological nature of the oceanic crust.

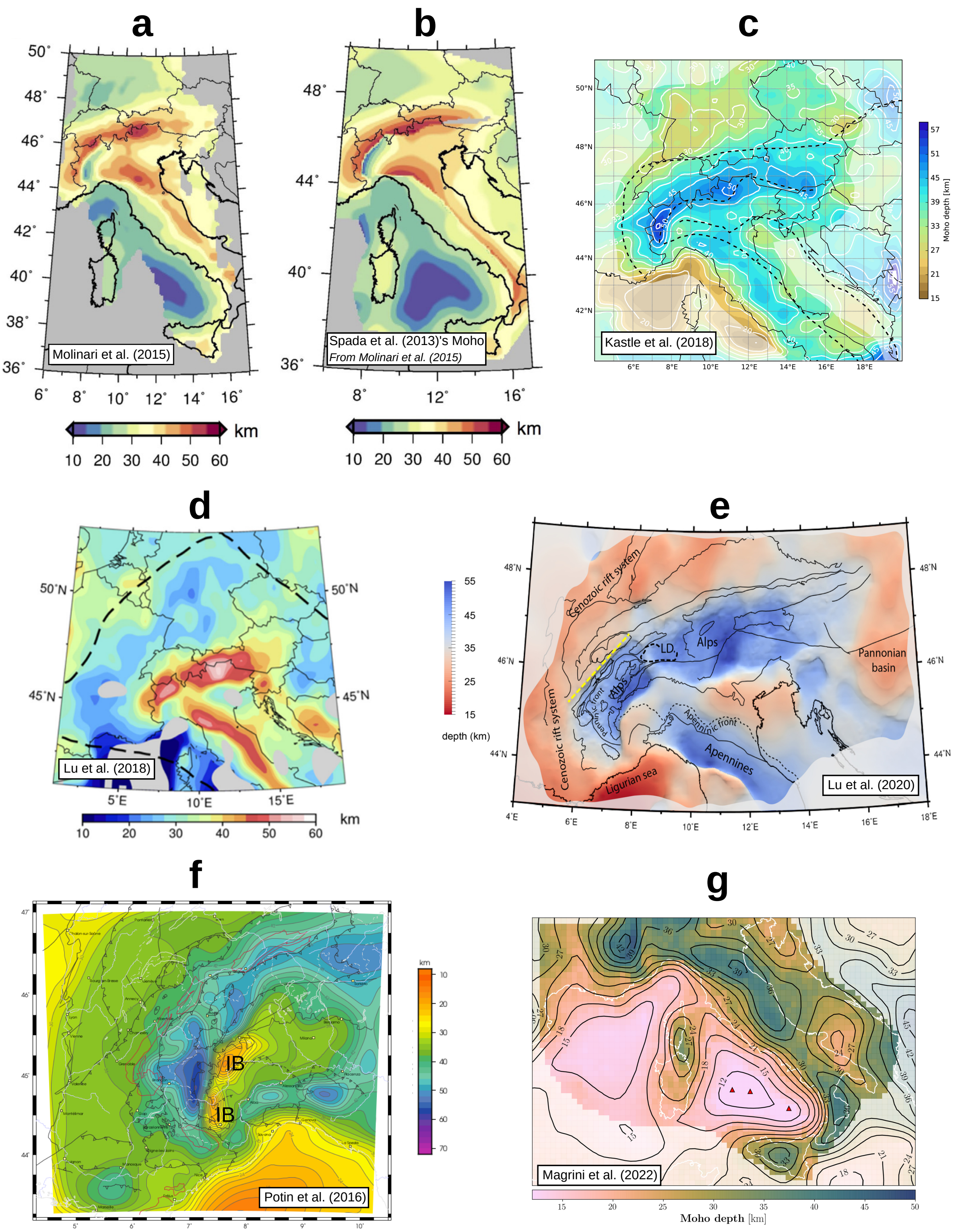

Figure 1.12: Moho depth maps, or Moho proxies from 3-D tomography studies in the Alps and Ligurian sea. Modifed from: a-b-Molinari et al. (2015); c-Kästle et al. (2018); d-e-Lu et al. (2018), Lu et al. (2020); f-Potin (2016); g-Magrini et al. (2022).

1.3 Thesis objectives and manuscript structure

To go a step further in the knowledge of the 3-D lithospheric structures beneath the Alps and the Ligurian sea, it is needed to design a new generation of high-resolution seismological models. Such models would, on the one hand, exploit the entire seismological coverage, including AlpArray, and on the other hand, rely on a more sophisticated inversion (e.g. full data-driven inversion or full-waveform inversion) that would take an optimal advantage of this coverage to gain in resolution and consistency. In line with the previous tomographic studies, our study will attempt to face those technical challenges and go one step further in the 3-D investigation of the geological objects involved.

Our long term objective is to build a high-resolution 3-D V_p, V_s model of the western Alps and the Ligurian-Provence basin using noise-correlation surface waves, local-earthquake body waves and full-waveform inversion. This model is intended to be used as a self-consistent seismological data to constrain an integrated geological-geophysical 3-D model of the lithosphere beneath the western Alps and the Ligurian sea. The first step to that aim is to build a robust 3-D shear-wave velocity model using ambient-noise data from all available seismic networks, the entire AlpArray included. This V_s model is intended to provide new constraints on the 3-D structures of the crust and upper mantle, by achieving a higher resolution and consistency than previously obtained V_s models from ambient noise tomography (ANT). In this thesis manuscript, we present the methodological developments of our ANT, the results of its application to the Alps and the Ligurian sea and their geological implications.

We build a large-scale onshore-offshore 3-D shear-wave velocity model, using 4 years (2015-2019) of seismic-noise recordings, from the densest seismological coverage of Europe, made up of 1600 broadband seismological stations including 23 OBS. This 3-D model is built in two main steps:

(1) First, we perform a full data-driven probabilistic ambient-noise tomography (ANT) in two steps:

  - inversion of Rayleigh-wave group-velocity dispersion measurements to compute 2-D dispersion maps in the period band 4-150 s. To achieve this, we perform a transdimensional Bayesian approach that treats the data noise-level and the model parameterization as parts of the inversion problem, and estimates the uncertainties on the resulting 2-D maps. The offshore part of the model (i.e., Ligurian-Provence basin) is built after a specific pre-processing applied to the OBS recordings for cleaning them from instrumental and oceanic noises.
  - inversion of local dispersion curves to compute a quasi 3-D V_s model. To achieve this, we perform a 1-D probabilistic inversion at depth that provides probability distributions of shear-wave velocities and of presence of interfaces, taking into account the uncertainties on the local dispersion curves. In the offshore locations, we derive shear-wave velocities at depth by considering the presence of the water column.

(2) In the second step, we further refine the ANT V_s model (obtained in step 1) by performing a wave-equation tomography (WET). To achieve this, we iteratively update the V_s model by minimizing the phase-traveltime differences between the observed and simulated waveforms in the period band 5-85 s. The synthetic waveforms are computed by performing 3-D elastic modelling for Rayleigh-wave propagation in the period band

20-40 s, and 3-D acoustic-elastic modelling for Rayleigh-Scholte wave propagation in the period band 5-20 s, applying fluid-solid coupling along the Ligurian-Provence basin and its margins.

This manuscript contains six chapters. In Chapter one (this Chapter), we first presented an overview of 3-D tomography methods for the lithosphere. Then, we developed the context of the thesis, its motivation and objectives. In the second Chapter, we describe our probabilistic inversion strategy for the ambient noise tomography (ANT) and its application to the western Europe region. In Chapter three, we present a validation of the ANT V_s model through a comparison with two recent receiver-function sections in the western Alps. In the fourth Chapter, we describe our specific processing of OBS records and the use of iterative noise correlations in the context of ambient-noise tomography of the Ligurian sea. In Chapter five, we present our onshore-offshore wave-equation tomography of the Alps and Ligurian-Provence basin and highlight the importance of considering the effect of the water layer in ambient-noise 3-D imaging for offshore and onshore-offshore applications. Then, we show how the wave-equation tomography improves the results obtained from the 2-step ANT inversion approach. Finally, in Chapter six, we conclude on the results of the thesis and present the future perspectives.

Chapter 2

Transdimensional Ambient-Noise Tomography of Western Europe

This Chapter is a published paper in *Geophysical Journal International.* Citation: Nouibat, A., Stehly, L., Paul, A., Schwartz, S., Bodin, T., Dumont, T., Rolland, Y., Brossier, R., Team, C., and AlpArray Working Group (2022). Lithospheric transdimensional ambient-noise tomography of W-Europe: implications for crustal-scale geometry of the W-Alps, *Geophysical Journal International*, 229(2), 862–879, `https://doi.org/10.1093/gji/ggab520`.

The first step in building the 3-D shear-wave velocity model is to perform a two-step ambient-noise group-velocity tomography (ANT). We first perform a 2-D inversion of Rayleigh-wave group-velocity measurements to derive dispersion maps in the period band 4-150 s. Then, we perform a 1-D inversion of local group-velocity dispersion curves to derive shear-wave velocities at depth. We use ambient-noise correlations from all available seismological stations in Western Europe in the period 2015-2019.

Estimating and accounting for the uncertainty of data to be inverted – dispersion measurements between station pairs and local dispersion curves – is crucial to provide more realistic constraints on the shear-wave velocity model and its uncertainty. The issue of the data and model uncertainty - not quantitatively addressed in the context of ambient noise imaging in the Alps and the Ligurian sea – is at the core of our inversion methodology. In this Chapter, we present a full data-driven Bayesian procedure. The specificity of this work consists in using, in a probabilistic inversion scheme, both the group velocities and their uncertainties to constrain the shear-wave velocities at depth. The group velocities and their uncertainties are themselves derived from a transdimentional Bayesian inversion that treats the data errors and the model parameterization as parameters to invert for. This full probabilistic procedure is applied successfully at the scale of Western Europe, for the crust and upper-mantle, using the densest seismic coverage to date. The V_s model, validated by a receiver function (RF) cross-section along a reference profile, provides a high-resolution image of the European lithosphere subduction in the western Alps.

Summary

A full understanding of the dynamics of mountain ranges such as the Alps requires the integration of available geological and geophysical knowledge into a lithospheric-scale three-dimensional geological model. As a first stage in the construction of this geo-model, we derive a new 3-D shear-wave velocity model of the Alpine region, with a spatial resolution of a few tens of kilometers, making it possible to compare with geological maps. We use four years of continuous vertical-component seismic noise records to compute noise correlations between more than 950 permanent broadband stations complemented by ~ 600 temporary stations from the AlpArray sea-land seismic network and the Cifalps and EASI linear arrays. A specific pre-processing is applied to records of ocean-bottom seismometers in the Liguro-Provençal basin to clean them from instrumental and oceanic noises. We first perform a 2-D transdimensional inversion of the travel times of Rayleigh waves to compute group-velocity maps from 4 to 150 s. The data noise level treated as an unknown parameter is determined with a Hierarchical Bayes method. A Fast Marching Eikonal solver is used to update raypath geometries during the inversion. We use next the group-velocity maps and their uncertainties to derive a 3-D probabilistic V_s model. The probability distributions of V_s at depth and the probability of presence of an interface are estimated at each location by exploring a set of 130 million synthetic four-layer 1-D V_s models. The obtained probabilistic model is refined using a linearized inversion. Throughout the inversion for V_s, we include the water column where necessary. Our V_s model highlights strong along-strike changes of the lithospheric structure, particularly in the subduction complex between the European and Adriatic plates. In the South-Western Alps, our model confirms the existence of a low-velocity structure at $50 - 80$ km depth in the continuation of the European continental crust beneath the subduction wedge. This deep low-velocity anomaly progressively disappears towards the North-Western and Central Alps. The European crust includes lower crustal low-velocity zones and a Moho jump of $\sim 8 - 12$ km beneath the western boundary of the External Crystalline Massifs of the North-Western Alps. The striking fit between our V_s model and the receiver function migrated depth section along the Cifalps profile documents the reliability of the V_s model. In light of this reliability and with the aim to building a 3-D geological model, we re-examine the geological structures highlighted along the Cifalps profile.

Keywords: Seismic tomography, Surface waves and free oscillations, Seismic noise, Crustal structure, Europe

Contents

2.1 Introduction

Since the Late Cretaceous, the geodynamic evolution of Western Europe has been dominated by convergence between the European and African plates. This long-term motion resulted in the formation of the Alps and other peri-Mediterranean mountain ranges (Pyrenees, Dinarides, Apennines, Carpathians, etc.) and also caused the opening of the Western European Cenozoic Rift System and of Mediterranean back-arc oceanic domains (Fig. 2.1a) (Faccenna et al., 2014). In the Alps, convergence resulted in oceanic subduction from Late Cretaceous to Early Eocene (e.g., Handy et al., 2010), later on followed by continental subduction of the European margin (e.g., Chopin, 1984; Duchêne et al., 1997; Guillot et al., 2009; Zhao et al., 2015). From Oligocene onwards, continental collision resulted in thrusting of the subduction wedge towards the European foreland, marked by the development of the Penninic Frontal Thrust (PFT) (Simon-Labric et al., 2009).

The objective of this study is to improve the resolution of seismic models of the lithospheric structure of Western Europe in order to better constrain 3-D geological structures, particularly in the Alpine mountain belt and its forelands. For this, we build a new 3-D high-resolution shear-wave velocity model using ambient-noise records of an exceptional array of seismic stations (Fig. 2.1b). To assess the robustness and the geological significance of our 3-D V_s model, we focus its geological interpretation on the Western Alps where the near-surface geology is well-documented and a number of high-resolution geophysical investigations have been carried out recently (see review in Malusà et al., 2021).

In the internal zones of the Western Alps, the continental subduction of the European crust beneath the Adriatic lithosphere was first highlighted by the observation of preserved UHP minerals (e.g. coesite) in the outcropping subduction wedge (Chopin, 1984). Recently, receiver functions of the Cifalps experiment have imaged the continuity of the subducted European continental crust down to $75-80$ km depth (Zhao et al., 2015). In this context, the combination of tectonics, petrophysics and numerical thermodynamics has provided conceptual models that are consistent with the formation of a subduction wedge during plate convergence (Burov et al., 2014; Liao et al., 2018), and with the involvement of serpentinites in the burial/exhumation processes (Schwartz et al., 2001; Guillot et al., 2009). However, despite the geological structure of the Western Alps having been studied for more than a century, correlating geological units mapped at the surface with geophysical images of the crust remains challenging. This is due to the limited resolution of these images, the lack of accurate uncertainty estimates, and the non-unicity of their geological interpretations regarding lithology, thermicity, fluids and deformation. Moreover, some first order questions remain controversial, such as the nature of the geophysical Ivrea body (e.g., Schmid et al., 2017; Solarino et al., 2018), and the precise geometry of the Adria mantle wedge and its role in the partitioning of the present-day strain field (Lardeaux et al., 2006; Eva et al., 2020).

Since the 1990's, the structure of the lithosphere beneath the Western Alps has been probed by a broad spectrum of geophysical techniques. The ECORS-CROP normal-incidence and wide-angle reflection controlled-source seismic survey (CSS) has provided a very high-resolution image of the reflectivity of the crust in the North-Western Alps (Nicolas et al., 1990). Local earthquake tomography (LET) studies have yielded local or regional 3-D P-wave velocity models of the crust (e.g., Paul et al., 2001; Diehl et al., 2009; Solarino et al., 2018). Receiver functions (RF) have been used to map Moho depth as a complement to the 2-D CSS profiles and 3-D LET models (e.g., Spada et al., 2013; Zhao et al., 2015). These geophysical data have lower resolution than surface geological data. They were however of great help to constrain to the first order the 3-D geometry of the crustal structure under the Western Alps. In particular, they highlighted the underthrusting of the European plate beneath the Adria micro-plate, with a maximum Moho depth locally reaching 55 km (ECORS-CROP Deep Seismic Sounding Group, 1989; Thouvenot et al., 2007).

In the last decade, seismic imaging of the Alpine lithosphere has improved thanks to the densification of permanent broadband seismological networks and the multiplication of temporary experiments (e.g., Cifalps-2, Liu et al., 2022; AlpArray, Hetényi et al., 2018). New passive imaging methods have been introduced that make optimal use of these dense station arrays and are independent of earthquake or active source illumination. Paul & Campillo (2003) and Shapiro & Campillo (2004) have shown that the cross-correlation of long time series of diffuse wavefields including ambient noise recorded at two seismic stations leads to the reconstruction of the surface waves propagating between the two stations as if a virtual seismic source is placed at one station with the emitted signal being recorded at the second station. Shapiro et al. (2005) have further shown that ambient-noise tomography (ANT) from continuous noise recordings over dense networks provides high resolution images of the crust and upper mantle. Since then, several s-wave velocity models have been derived from ANT to probe the crustal structure under the Alpine arc (e.g., Stehly et al., 2009; Verbeke et al., 2012; Molinari et al., 2015).

Taking advantage of the ever-increasing amount of available data, Kästle et al. (2018) used a stochastic inversion of travel times of surface waves from noise correlations, regional and teleseismic earthquakes to construct a 3-D V_s model of the entire Alpine region. Lu et al. (2018) used ambient-noise records of 1293 broadband stations, including the first six months of the AlpArray network, to derive a high-resolution 3-D V_s model of the European crust from ANT using a Bayesian inversion. This model was further refined in the Alpine region by Lu et al. (2020) using wave equation tomography (WET) of Rayleigh-wave phase dispersion data derived from noise correlations. Zhao et al. (2020) used Bayesian transdimensional inversion of the group-velocity dataset of Lu et al. (2020) to derive a shear-wave velocity model of the Western Alps that provides a particularly well-resolved image of the subduction. These new approaches highlighted major intra-crustal units confirmed by field observations, such as the subduction complex in the internal zone of the Alps, which is either located beneath a mantle wedge in the Western Alps or covered by Adriatic crustal units in the Central and Eastern Alps. Since the works by Lu et al. (2018, 2020) and Zhao et al. (2020), more data have been recorded, in particular in the Western Alps, that should contribute to improving the resolution of ambient-noise tomography.

In the present work, we generate a new 3-D shear-wave velocity model of Western Europe by combining ambient-noise tomography with probabilistic inversion. We use four years of continuous seismic noise records at all available broadband seismic stations including permanent networks, the Cifalps and Cifalps-2 profiles and the AlpArray network (see Fig. 2.1a, and section 2). We also include data of the AlpArray ocean-bottom seismometers to image the transition between the Ligurian sea and the Alpine region. This dataset gives a unique opportunity to image the crust and upper mantle below the Alpine belt and its forelands at an unprecedented resolution. The originality of our approach lies in the use of a transdimensional inversion to compute 2-D group-velocity maps and their uncertainties, which are then used to obtain a 3-D probabilistic shear-wave velocity model from a Bayesian inversion (sections 3 and 4). This model provides a probability distribution of V_s as well as the probability of presence of an interface at each depth and location. This approach was chosen specifically to image sharp lateral discontinuities, which is crucial in the Western Alps. To the best of our knowledge, this is the first time that a fully probabilistic approach is used at this scale to image the lithosphere. In section 5, we further assess the model robustness along the Cifalps profile (South-Western Alps) by comparing our results with a receiver-function depth section. Finally, we propose an updated crustal-scale interpretative geological cross-section based on previous geophysical-geological works (reviewed in Malusà et al., 2021), on our V_s model and the receiver-function section along the Cifalps profile. This comparison illustrates the potential contribution of our V_s model to the development of a 3-D geological model of the Alpine chain and its forelands.

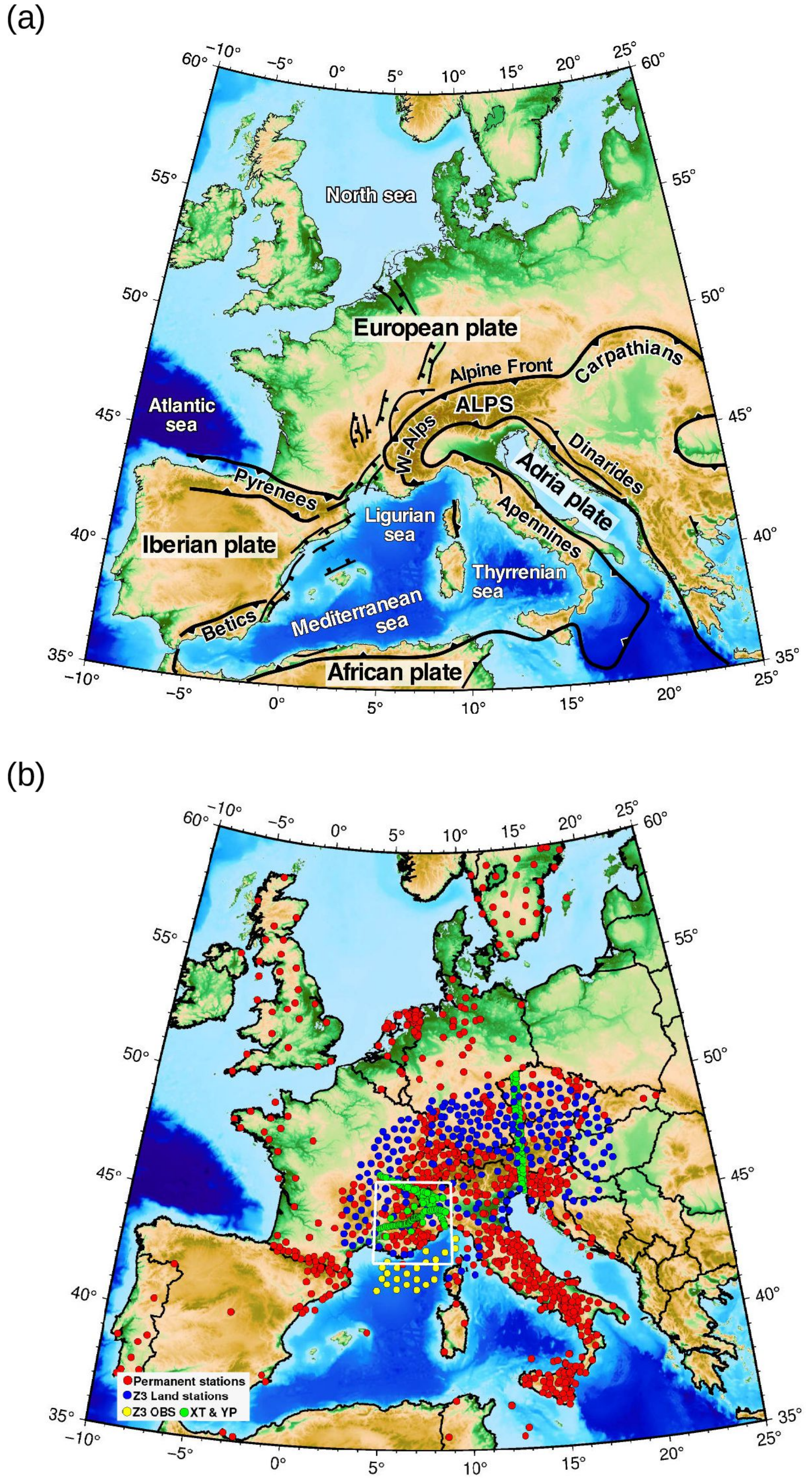

Figure 2.1: (a) Topographic map showing the regions, plates and main geological boundaries discussed in the text (modified from Faccenna et al., 2014). Black lines with triangles correspond to main thrusts and subduction zones. Black lines with squares represent extensional faults associated with development of the Western European Cenozoic Rift System. (b) Location map of the broadband seismic networks used in this study. The white frame which includes most of the Western Alps indicates the main focus area of this work.

2.2 Ambient-noise dataset

2.2.1 Station coverage

Our dataset consists of four years of vertical-component, daily seismic noise records (2015-2019) of more than 950 permanent broadband seismic stations located in and around the Greater Alpine region, complemented by 490 temporary stations from the AlpArray (Z3 network, AlpArray Seismic Network, 2015), Cifalps (YP network, Zhao et al., 2016b, and XT network, Zhao et al., 2018) and EASI experiments (XT network, AlpArray seismic network, 2014) (Fig. 2.1b). The average inter-station distance is ~ 50 km in the Greater Alpine region.

The on-land component of the AlpArray seismic network was operated for 2 to 4 years and covered the Greater Alpine area (Hetényi et al., 2018). We also used data from 23 broadband ocean-bottom seismometers (OBS) that were deployed during $8-10$ months $(2017-2018)$ in the Ligurian Sea as part of the AlpArray Seismic Network (AASN) (Hetényi et al., 2018). The OBS component of the AASN was operated within the framework of a French-German cooperation that aimed at imaging the lithospheric structure of the Ligurian basin and the transition between the Alps and the Apennines. OBS records are merged into the Z3 dataset, which means that data and metadata are archived in the same standard (FDSN) format as data recorded by on-land stations, and they are distributed by the RESIF and GEOFON nodes of the European Integrated Data Archive (EIDA) using the same procedures as on-land data. This integration of data recorded at sea-bottom and on land greatly facilitates their use in massive data processing such as that presented here.

In addition to the AASN, we also used data of the dense $(7-10$ km spacing) Cifalps (China-Italy-France Alps seismic survey) and Cifalps-2 linear arrays that operated for $14-15$ months in the Western Alps in $2012-2013$ and $2018-2019$, respectively. They provide a very dense coverage of the Western Alps, which are the main focus of this work (Fig. 2.1b).

2.2.2 Data processing and correlation

Before computing the correlations for each station pair, we pre-processed the noise records in two main steps. First, we applied a generic pre-processing scheme where each daily record was band-pass filtered between 2.5 s and 300 s, corrected for the instrumental response, decimated to 1 Hz sampling frequency and split into 4-hrs segments. Second, we decreased the contribution of earthquakes and other transient signals by (1) removing signals with amplitude 4 times greater than the standard deviation and (2) removing segments with RMS greater than 1.5 times the daily mean RMS (Boué et al., 2014). Then, each daily record was filtered into several period bands $(3-5,\ 5-10,\ 10-20,\ 20-40,\ 40-80$ and $80-200$ seconds) and normalized by its envelope. Finally, the six filtered and normalized signals were stacked. We thus obtained a broadband signal with amplitude normalized in several period bands. This processing is similar to the one used by Soergel et al. (2020).

In addition, we used a specific processing for the data of the 23 OBS in order to reduce the tilt and the compliance effects using frequency-dependent response functions (Crawford & Webb, 2000). We also corrected the records of 8 OBS that were affected by periodic glitches of electronic origin. This was achieved using a template matching algorithm (Deen et al., 2017).

For each of the 1.1 million station pairs, we computed the cross-correlations of up to 4 years of vertical component continuous noise records by segments of 4 hours. The resulting cross-correlations were then normalized and stacked. Supplementary Fig. 2.10 shows distance-time sections of cross-correlations in the $5 - 10$ s, $10 - 20$ s and $20 - 40$ s period bands. We used a specific computation scheme for correlations between ocean-bottom stations in order to enhance the signal-to-noise ratio. It was indeed poorer for OBS pairs than for on-land station pairs or mixed pairs of on-land and ocean-bottom stations. We took advantage of the large number of on-land stations and their high quality by using them as virtual sources for the OBS-OBS correlations. For each OBS pair, we correlated the ballistic Rayleigh waves of the noise correlations between each OBS and a large number of selected on-land stations, and stacked them to obtain the OBS-OBS correlation. This process is known as 'C2' (for correlation of correlation) which is a variant that uses the ballistic waves rather than the coda (Stehly et al., 2008). Another publication will be dedicated to the processing of OBS records.

2.2.3 Group-velocity measurements

Once cross-correlations were computed for the entire dataset, we derived, for each pair of stations, the group-velocity dispersion curves of positive and negative correlation times by using multiple filter analysis (*MFA*, Dziewonski et al., 1969a; Herrmann, 1973). Similarly to Lu et al. (2018), we adapted the width of the filter to the inter-station distance to accommodate the trade-off in resolution between the time and frequency domains (Levshin et al., 1989). We also corrected our group-velocity measurements for the systematic error that occurs with the *MFA* technique due to the strong amplitude decrease of the noise spectrum at periods > 20 s (Shapiro & Singh, 1999).

Careful selection of group-velocity measurements prior to group-velocity tomography is essential to prevent biases induced by the heterogeneous distribution of noise sources, by interferences of Rayleigh waves in the causal and acausal times and by instrumental problems. To that aim, for each station pair and period, we selected the group-velocity measurements with a signal-to-noise ratio > 3 and the group-velocity difference between causal and acausal Rayleigh waves < 0.2 km/s. Furthermore, we only kept paths with length of 2 to 40 wavelengths at each period. By combining these criteria, we keep only the reliable travel time measurements for the subsequent 2-D group-velocity maps.

2.3 Inversion for 2-D group-velocity maps

Our aim is to derive a 3-D probabilistic V_s model of the Alpine crust and upper mantle. As a first step towards this goal, we compute 2-D group-velocity maps and associated uncertainties using a transdimensional algorithm at discrete periods from 4 s to 150 s.

Probabilistic group-velocity maps are derived by exploring millions of 2-D models with different parameterizations using the reversible-jump Markov-chain Monte-Carlo method (*rj-McMC*), first applied in a seismic tomography context by Bodin et al. (2012). The parameterization of the model is treated as part of the inversion without any explicit regularization. This allows the local resolution to self-adapt to the path density and to the variability of the information contained in group-velocity measurements. The model complexity required to fit the data is controlled by the noise level, which is treated as an extra parameter of the inversion and determined within a hierarchical Bayes formalism (Malinverno & Brigg, 2004).

Moreover, since the Alpine crust is strongly heterogeneous and displays sharp group-velocity contrasts, the non-linearity of the forward problem is accounted for by iteratively updating the raypath geometry using the fast marching method (*FMM*, Rawlinson & Sambridge, 2004). Ray bending is more sensitive to phase-velocity changes than to group-velocity changes. However, accounting for ray bending in group-velocity *rj-McMC* tomography has proven to be substantially more accurate in a heterogeneous medium than the straight ray assumption (e.g., Galetti et al., 2015).

2.3.1 Method

The 2-D velocity field is parameterized with a set of Voronoi cells with variable number and geometries. The velocity field is described by a vector of model parameters **m** giving the position and group velocity associated with each Voronoi cell.

The inverse problem is treated in a Bayesian framework, where the solution is represented by the posterior probability density function representing the probability of the model **m**, given a set of observed data **d**. The posterior solution is expressed according to Bayes's theorem (Bodin et al., 2012)

$$p(\mathbf{m}|\mathbf{d}) \propto p(\mathbf{d}|\mathbf{m})p(\mathbf{m}) \tag{2.1}$$

where $p(\mathbf{m})$ is the *a priori* probability density of the model parameters **m**, i.e. what we know about the velocity field independently of the data. The term $p(\mathbf{d}|\mathbf{m})$ is the likelihood function and represents the probability of observing **d** given a model **m**, and given the statistics of data errors. Assuming normally distributed uncorrelated data errors, $p(\mathbf{d}|\mathbf{m})$ can be expressed with the general Gaussian form

$$p(\mathbf{d}|\mathbf{m}) = \frac{1}{\prod\limits_{i=1}^{N} \sqrt{2\pi}\sigma_{d_i}} \times \exp\left(\frac{-\phi(\mathbf{m})}{2}\right) \tag{2.2}$$

where σ_{d_i} is the standard deviation of data errors on the *ith* observation, N is the number of observations, and $\phi(\mathbf{m})$ is the misfit function for the model **m**

$$\phi(\mathbf{m}) = \sum_{i=1}^{N} \left[\frac{(g(\mathbf{m}) - \mathbf{d})^2}{\boldsymbol{\sigma}_{\boldsymbol{d}}^2}\right]_i \tag{2.3}$$

The term $g_i(\mathbf{m})$ represents data computed by the forward problem, i.e. the travel time of the *ith* ray predicted by the model **m**, and computed from

$$g_i(\mathbf{m}) = \sum_{j=1}^{n} \frac{L_{ij}}{v_j} \tag{2.4}$$

where L_{ij} is the length of the *ith* ray across the Voronoi cell j of velocity v_j.

The posterior probability distribution can be estimated with the reversible-jump *McMC* algorithm, which produces a large ensemble of models, whose distribution approximates the posterior solution. The algorithm is based on a Markov-chain Monte-Carlo sampler where at each iteration, a new velocity model is proposed by perturbing the current model (e.g. perturb the geometry of the Voronoi discretization, change the velocity within one Voronoi cell). The proposed model is then either accepted or rejected in the ensemble depending on an acceptance criteria based on the ratio of posterior values of the current and proposed model. Once the algorithm has been run for enough iterations, statistics can be extracted from the ensemble solution for interpretation. For example, at any geographical location, the mean and standard deviation of velocities can be used to produce a group-velocity map, with associated error estimates. We refer the reader to Bodin et al. (2012), for more details.

2.3.2 2-D group-velocity maps

We performed the *rj-McMC* tomography to derive group-velocity maps for periods between 4 s and 150 s. For each period, 64 Markov chains were run in parallel to explore independently the model space. Each individual process was run for 180×10^3 steps in total. Once the convergence was achieved, the ensemble of sampled models was averaged to produce a smooth average solution, that can be interpreted as the mean of the posterior solution. We used this average model to update ray path geometry and recalculate traveltimes using the *FMM*. The global scheme was run for 2 iterations, resulting in the group-velocity maps shown in Figures 3.1 and 2.3.

At 8 s period (mainly sensitive to $\sim 5-8$ km depth; Fig. 3.1a), the clearest features of the group-velocity map are low-velocity anomalies associated with thick sedimentary basins: the Po basin (labeled PB in Fig. 3.1a) and the North-Adriatic basin (NAB), the Liguro-Provençal basin (LPB), the Southeast-France basin (SFB), the Vienna basin (VB) in the easternmost part of our study area and part of the North-Sea basin in Northern Germany (NSB). The Southern Apennines (SAp) and the Sicily fold-and-thrust belt (SiB) are also characterized by low velocities. The highest velocities (> 3.2 km/s) are observed in the Variscan massifs of France such as the Western Massif Central (McF) and the Armorican Massif (ArM), and in the Marsili back-arc basin (MaB) of the Tyrrhenian Sea. Supplementary Fig. 2.11a shows the main sedimentary basins on the 8-s group-velocity map.

At 25 s (sensitive to $\sim 15-30$ km depth; Fig. 3.1b), the Liguro-Provençal basin (LPB in Fig. 3.1b) has velocities > 3.5 km/s due to the thin crust of the basin. Similar high-velocity anomalies are observed in the Tyrrhenian Sea (TyS) and to the west and north of the Alpine front in the Western and Central Alps. The very thick Po basin (PB) is still characterized by very low velocities (< 2.3 km/s), while slightly higher velocities ($\sim 2.5-2.6$ km/s) prevail in the Apenninic belt and moderately low velocities ($\sim 2.7-3.0$ km/s) in the Alpine belt. The strong high-velocity anomaly associated with the shallow mantle flake known as the Ivrea geophysical body is observed between the Po basin and the Western Alps (IB in Fig. 3.1b) in spite of its small size ($\sim 10-15$ km width). This gives a first insight into the good lateral resolution of our 2-D tomography. Supplementary Fig. 2.11b shows the comparison between the 25-s map and the reference Moho depth model of Spada et al. (2013).

At 60 s (sensitive to $\sim 50-100$ km depth; Fig. 3.1c), the upper mantle appears as heterogeneous as for shorter periods with low-velocity anomalies beneath the Po basin (PB) and the central Apennines (CAp), the Liguro-Provençal basin (LPB), the south of the French Massif Central (McF) and the South-Western Alps (SWA). High-velocity anomalies are observed beneath the Adriatic Sea (AdS) and in the northwest of the model.

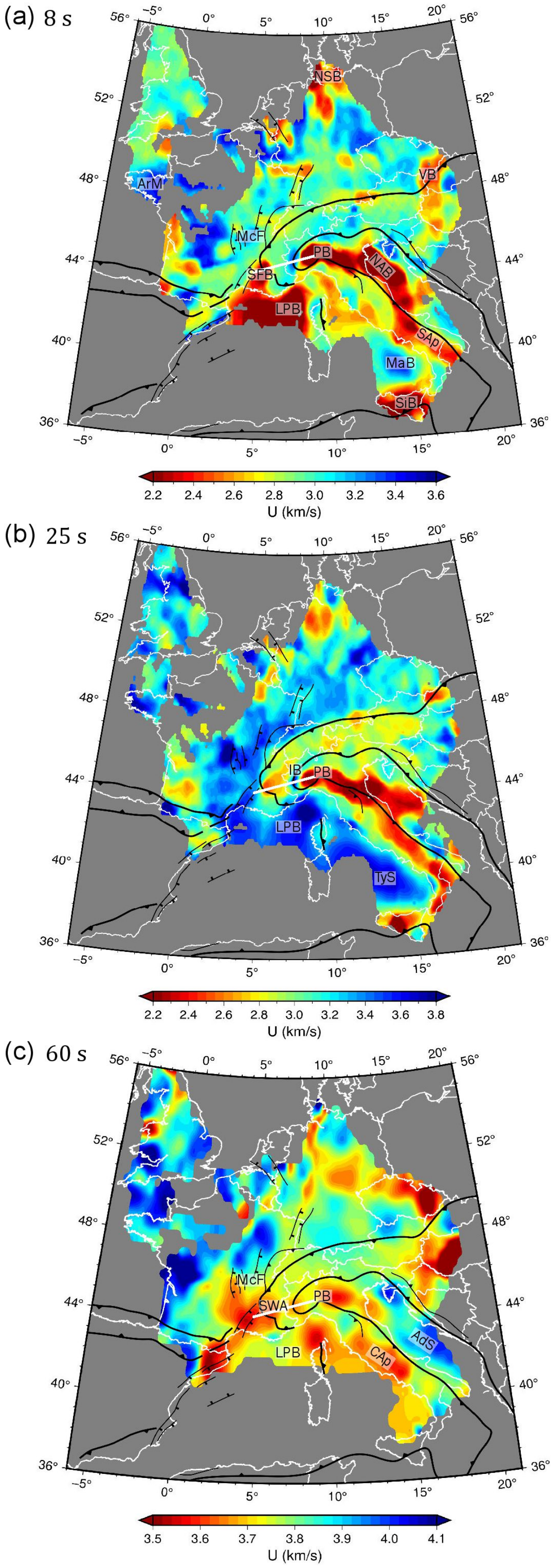

Figure 2.2: Group-velocity maps (average solutions) at (a) 8 s, (b) 25 s and (c) 60 s periods, obtained with the Hierarchical Bayes reversible-jump algorithm. Only areas with uncertainty lower than 0.5 km/s are shown. Black lines show the main geological boundaries as defined in Fig. 2.1a. The white line shows the Cifalps profile discussed in section 5. ArM: Armorican Massif, IB: Ivrea geophysical body, LPB: Liguro-Provençal basin, MaB: Marsili back-arc basin, McF: Eastern Massif Central, NAB: North-Adriatic basin, NSB: North-Sea basin, PB: Po basin, CAp: Central Apennines, SAp: Southern Apennines, SWA: South-Western Alps, SFB: Southeast-France basin, SiB: Sicily fold-and-thrust belt, TyS: Tyrrhenian Sea, VB: Vienna basin, AdS: Adriatic Sea.

2.3.3 Uncertainty estimates

At each geographical location i, we extracted posterior uncertainties from the variance of the ensemble of sampled velocities. This uncertainty is given by

$$\sigma_i = \sqrt{\frac{1}{M}\sum_{j=1}^{M}\left(v(m_j) - \overline{v}\right)_i^2} \tag{2.5}$$

where M is the total number of models in the Markov-chain ensemble and $\overline{v}$ the average solution model. This uncertainty is primarily related to the complexity of the velocity structure, but also depends on the reliability of the observations and on raypath coverage.

The uncertainty map displayed in Fig. 2.3b for 15 s period shows that our group-velocity model (Fig. 2.3a) is better constrained in the Greater Alpine region and in the Italian peninsula (uncertainty $< 0.15-0.2$ km/s) than in the Ligurian Sea (uncertainty $\sim 0.25-0.4$ km/s). This difference is certainly due to a less dense path coverage but also to relatively poorer data quality and the complexity of the medium.

A comparison of Fig. 2.3b and Fig. 2.3c shows that although uncertainty is generally low where ray coverage is good, a few areas have high uncertainty in spite of good coverage. This happens in areas of strong velocity contrast, for example along the boundaries of the low-velocity anomaly of the Po basin (PB in Fig. 2.3a). Galetti et al. (2015) attributed such loop-like structures in the error maps to the non-linearity of the forward model. Here instead, we interpret these features as due to the presence of sharp lateral discontinuities in the group-velocity maps. These typical structures in error maps are useful to identify velocity anomalies with uncertain location but well-constrained amplitude.

2.3.4 Benefits of the transdimensional inversion

The inversion scheme that we used to derive the 2-D group-velocity maps is similar to the one used by Bodin et al. (2012). This procedure has been successfully adapted to our study region despite its large size and the high volume dataset. The dynamic parameterization with Voronoi cells with variable geometries allowed the inversion process to accommodate the irregular distribution of data.

As shown in Supplementary Fig. 2.12, the 2-D transdimensional inversion outperforms commonly used linearized and regularized inversions. First, this approach allows the computation of group-velocity maps together with their posterior uncertainties that are required to constrain the 3-D V_s model. Second, linearized inversions require explicit parameterization and regularization that often rely on subjective choices. Such a regularization stabilizes the solution in poorly resolved areas, but tends to smooth lateral discontinuities and to bias the resulting solution. These problems do not arise within a Bayesian framework since the degree of smoothing and damping of the solution is naturally driven by the data noise level as well as the heterogeneity of the medium.

The number of Voronoi cells self-adapts to the level of structure present in the data. We show in Supplementary Fig. 2.13 the posterior distribution on the number of Voronoi cells. We also show the evolution of the model misfit function along the Markov chain and the posterior distribution of the traveltime misfit (Supplementary Fig. 2.14). We further assess the resolution power of the method by showing results from a synthetic checkerboard test (Supplementary Fig. 2.15).

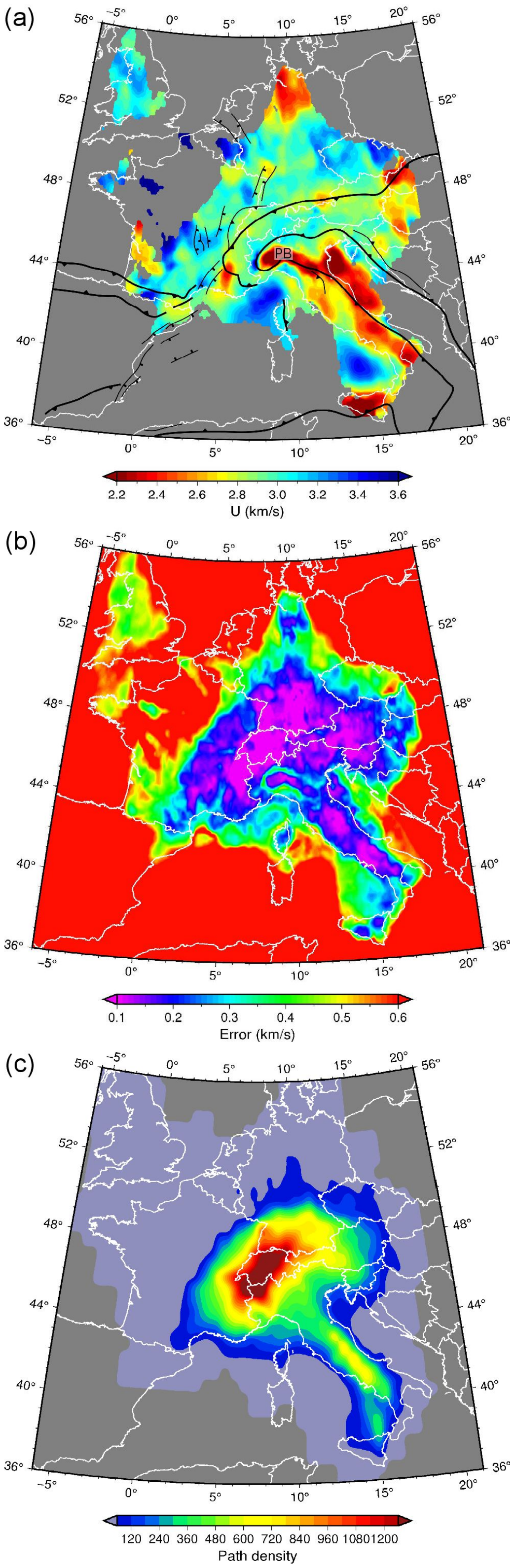

Figure 2.3: (a) Group-velocity map (average solution) obtained from the *rj-McMC* tomography at 15 s period, showing regions with error < 0.5 km/s. (b) Estimated error map (standard deviation of the ensemble of sampled velocities). (c) Corresponding path density map (number of paths crossing each 0.15° × 0.15° cell).

2.4 Inversion for shear-wave velocity

We used 2-D group-velocity maps and their uncertainties to build a 3-D V_s model of the crust and upper mantle of the Greater Alpine region in two steps. We first computed a 3-D probabilistic V_s solution that gives at each location the probability distribution of V_s and the probability of having an interface as a function of depth. Second, we computed the final V_s model (with a single V_s value at each depth) by refining the probabilistic model using a linear inversion at each pixel, as initially introduced by Macquet et al. (2014). This is particularly useful in areas with complex structures such as the Ivrea Body region, where the mean probabilistic model (obtained with an overly simple parameterization) does not fully explain the local dispersion curve.

2.4.1 Construction of the 3-D probabilistic $\mathrm{V_s}$ model

To build the 3-D probabilistic model V_s, we first extracted at each location the local Rayleigh-wave group-velocity dispersion curve from the group-velocity maps presented in the previous section. As discussed further, each of these local dispersion curves is inverted from 4 to 65 s for a local 1-D probabilistic V_s depth profile that provides at each depth the probability distribution of the shear-wave velocity and the probability of presence of an interface. This is done using an exhaustive grid search over a set $\sim$ 130 million of four-layer synthetic models. Each individual model is described with a simple parameterization that includes a sedimentary layer, an upper crust, a lower crust and a half-space representing the uppermost mantle. We assume *PREM* Earth model velocities from the Moho depth to 400 km (Dziewonski & Anderson, 1981). Each layer is parameterized by its thickness and s-wave velocity. P-wave velocities and densities are converted from V_s using Brocher's empirical formula (Brocher, 2005). As shown in Table 2.1, we choose to explore a wide range of four-layer models that allows for slow velocity layers. As discussed in section 4.2, a Bayesian solution (posterior mean) is then extracted by averaging the ensemble of models weighted by their posterior probability. The 1-D inversion problem is also cast in a Bayesian framework, and we evaluate the probability that each synthetic model $\mathbf{m}$ explains the measured local dispersion curve $\mathbf{d}$ using the Gaussian likelihood function

$$p(\mathbf{d}|\mathbf{m}) = \frac{1}{\sqrt{(2\pi)^N|\mathbf{C}|}} \times \exp\left(\frac{-\phi(\mathbf{m})}{2}\right) \tag{2.6}$$

where N is the total number of measured periods, $\mathbf{C}$ the covariance matrix of data errors and $\phi(\mathbf{m})$ the misfit function. We assume that uncertainties at different periods of the local dispersion curve are uncorrelated. In that case $\mathbf{C}$ has a diagonal form

$$\mathbf{C} = \begin{bmatrix} {\sigma_1}^2 & 0 & 0 \\ 0 & ... & 0 \\ 0 & 0 & {\sigma_N}^2 \end{bmatrix} \tag{2.7}$$

where σ_i is the posterior uncertainty on the group velocity at period i, estimated from the transdimensional group-velocity inversion (see section 3.3).

The misfit $\phi(\mathbf{m})$ between the candidate synthetic dispersion curve $g(\mathbf{m})$ and the local observed dispersion curve is estimated according to the Euclidean distance

$$\phi(\mathbf{m}) = (g(\mathbf{m}) - \mathbf{d})^T\mathbf{C}^{-1}(g(\mathbf{m}) - \mathbf{d}) \tag{2.8}$$

By substituting (2.7) and (2.8) into (2.6), we obtain the discrete form

$$p(\mathbf{d}|\mathbf{m}) = \frac{1}{\prod_{i=1}^{N} \sqrt{2\pi}\sigma_i} \times \exp\left(\sum_{i=1}^{N} \frac{-(g_i(\mathbf{m}) - d_i)^2}{2{\sigma_i}^2}\right) \tag{2.9}$$

This likelihood function gives the probability of observing the data given a 1-D profile. Here we assume all tested models are equally probable *a priori* (uniform prior distribution), which makes $p(\mathbf{m})$ a constant and allows us to write

$$p(\mathbf{m}|\mathbf{d}) \propto p(\mathbf{d}|\mathbf{m}) \tag{2.10}$$

At each depth, we therefore estimate the posterior probability of shear-wave velocities by simply weighting each of the tested models by its likelihood value $p(\mathbf{d}|\mathbf{m})$. Since we perform a uniform grid search in a multidimensional space, a large majority of models are not fitting the data, and have a very low posterior value. For practical reasons, we only used the 100×10^3 best fitting models in the ensemble, and assigned a 0 posterior value to the rest. We verified that this way of approximating the Bayesian solution does not modify the mean and variance of the posterior solution.

This allows us to get for each depth the probability distribution of V_s. In the same way, the probability of presence of an interface can be derived from the ensemble of sampled models and their associated likelihood value.

2.4.2 Construction of the 3-D final $\mathrm{V_s}$ model

The ambient-noise Bayesian scheme described above was applied up to 65 s period to better constrain the crustal part of the model while remaining consistent with the four-layer assumption. To improve the fit to the observed dispersion curve and better constrain the upper mantle part of the model, at each location we averaged the ensemble of selected models weighted by their likelihood values to build a deterministic 3-D V_s model that gives a single value of V_s at each location and depth. This is preferable to only getting the most probable V_s value, since this may introduce sharp discontinuities related to the four-layer assumption. This deterministic V_s model was then used as initial model to perform a linearized inversion (Herrmann, 2013). Three iterations were computed in the $4\ s - 150$ s frequency band, taking into account the errors on the observed dispersion curves.

This approach has been modified for the marine parts of the model. We used the same probabilistic inversion as for the on-land pixels and we added a surface layer representing the water column to the initial model of the linear inversion. The thickness of the water layer equals the water depth at the given pixel. We kept the parameters of the water layer fixed during the inversion (ρ, V_s and V_p).

Layer	Thickness (km)	V_s (km/s)
Sediments	$0 - 16$	$1.6 - 2.9$
Upper crust	$0 - 24$	$2.6 - 3.8$
Lower crust	$2 - 42$	$3.3 - 4.3$
Mantle	inf	$3.7 - 4.7$

Table 2.1: Ranges of layer thickness and shear-wave velocity used to build the set of four-layer models for the grid search. P-wave velocity and density are derived from V_s using Brocher's empirical relationship (Brocher, 2005).

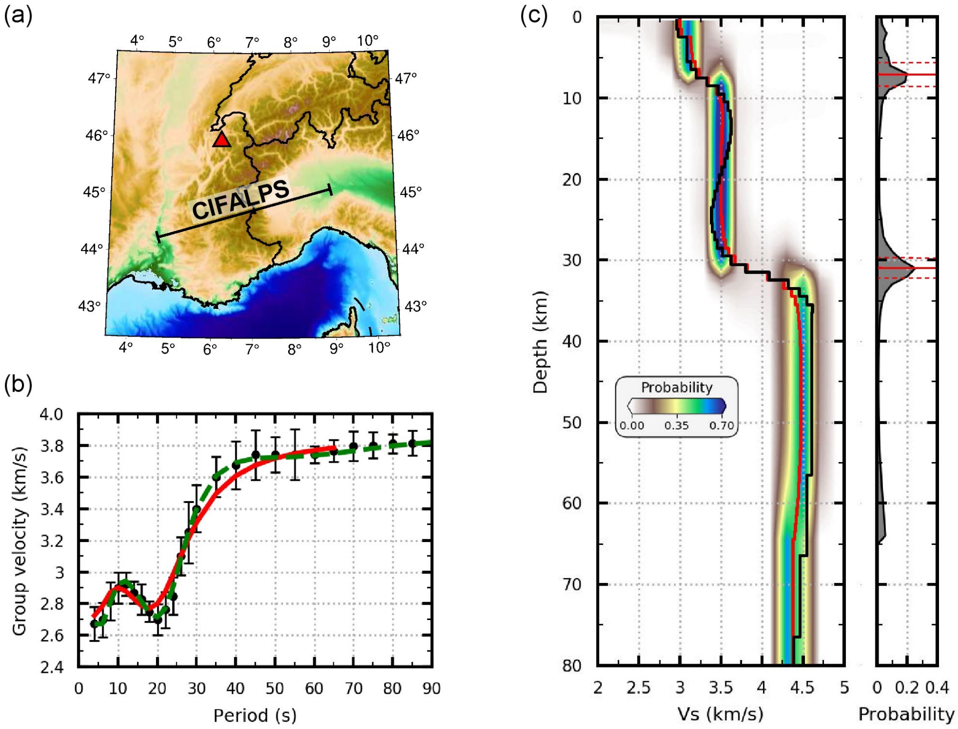

Figure 2.4: Example of the inversion process for V_s. (a) Location map of the selected grid point (red triangle); For reference, the black line shows the Cifalps profile discussed in section 5. (b) group-velocity dispersion curve of Rayleigh waves (fundamental mode) for the selected grid point; Black: observed dispersion curve with its uncertainties; Red: predicted dispersion curve for the average Bayesian model; Green: predicted dispersion curve after the subsequent linear inversion. (c) Resulting velocity models; Left: posterior probability distribution on shear-wave velocity from the Bayesian inversion (background colors), weighted average solution model (posterior mean) predicted from the probabilistic scheme (red line) and final solution model predicted from the linear inversion (black line). Right: posterior probability distribution on layer boundaries resulting from the Bayesian inversion. The two peaks outlined by red horizontal bars at $7 - 8$ km and $31 - 32$ km depths correspond to the sediment basement and to Moho; The dashed red bars indicate the uncertainty on the boundary depth estimate approximated by the 1σ width.

2.4.3 Strengths of the inversion method for $\mathbf{V_s}$

The inversion scheme that we used to derive the 3-D probabilistic V_s model is similar to that used by Lu et al. (2018), but with two significant improvements. First, rather than using a set of 8 million 1-D V_s models at each location, we explored a broader set of 130 million models that allow for velocity inversions at depth. Second, we did not consider the uncertainties of the local dispersion curves σ to be the same at all periods, nor did we consider them as a parameter of the inversion. Instead, σ was evaluated during the 2-D transdimensional group-velocity inversion. Hence, we formulated the likelihood function so that the uncertainties on group velocities σ were taken into account when computing the misfit $\phi(\mathbf{m})$ between the local dispersion curve and the dispersion curves associated to each of the 130 million of synthetic V_s models. Indeed, an underestimation of the noise level contained in the data would limit the range of 1-D V_s model considered as probable since the algorithm would try to fit the observed local dispersion curve too closely. On the other hand, overestimating the noise level would lead to considering irrelevant 1-D V_s models as probable, hence widening the probability distribution of V_s.

Figure 2.4 presents an example of a 1-D inversion at a pixel located in the Western Alps (Fig. 2.4a). In Fig. 2.4b, the local dispersion curve (black points) and its uncertainties are compared with the dispersion curves associated with the Bayesian average model obtained from the probabilistic inversion (red line) and the final V_s model obtained with an additional linear inversion (green line). The probability distribution of V_s and the probability of presence of an interface are shown on the left and right panels of Fig. 2.4c respectively. The Bayesian solution (weighted average of the best fitting models, see section 4.2) and the final model obtained after a linear inversion are shown with red and black lines respectively.

We observe a rather sharp V_s probability distribution over the whole depth range that we investigated (width $\leqslant 0.2$ km/s for probability > 50 %). The probability that an interface is present has two main peaks that correspond to the boundary between the sediment layer and the upper crust at $7-8$ km and to the Moho at $31-32$ km. This results in a multimodal distribution on V_s, with a very high standard deviation (same effect as the 'loops' in 2-D, see section 3.3).

The dispersion curve associated with the probabilistic average model (red curve) fits well the observed dispersion curve (black points in Fig. 2.4b) at periods less than 30 s and greater than 50 s. However, between 30 s and 50 s where the Rayleigh waves are mostly sensitive to the Moho depth, the posterior mean solution does not completely explain the data, even if it is still compatible with the observed dispersion curve when taking into account the uncertainties. This highlights that in the most complex areas, using a grid search over a library of 130 million four-layer models is insufficient to completely describe the complexity of the medium.

However, in this case, the reference probabilistic model is a relevant initial model for the linear inversion: as shown on Figure 2.4b, the dispersion curve associated with the final model obtained after a linear inversion fits well with the observed dispersion curve in the whole $4-90$ s period range.

2.4.4 Results: 3-D V_s model

We have derived a quasi-3-D shear-wave velocity model by assembling all 1-D individual models. This new large-scale model has a particularly good resolution over the Greater Alpine region where the density of stations is highest. We have evaluated the reliability of the V_s model by computing the data misfit reduction for each pixel.

Figure 2.5 presents depth slices at 6, 15, 30 and 60 km in the final 3-D V_s model. The 6-km depth slice in Fig. 2.5a is consistent with the geological map. We retrieve the main anomalies that we previously discussed on the 8 s map of Fig. 3.1a, in particular the thick sedimentary basins with velocities lower than 2.7 km/s (Po and North-Adriatic basins, Liguro-Provençal basin, Southeast-France basin and Vienna basin).

At 15-km depth (Fig. 2.5b), the Ivrea Body is visible as a high-velocity anomaly with V_s in the range $4 - 4.1$ km/s. The Liguro-Provençal basin is associated with high velocities greater than 4 km/s, indicating a shallow Moho. Another striking feature is that at this depth the Adriatic crust exhibits lower velocities ($3.1 - 3.2$ km/s) than European upper crust ($3.3 - 3.5$ km/s).

The 30-km depth slice (Fig. 2.5c) underlines the variations in crustal thickness, with low velocities (3.5 km/s) in the mountain belts such as the Alps and Apennines. The 60-km depth slice shows a strong low-velocity anomaly ($V_s < 4$ km/s) at the location of the Ivrea Body (IB), in sharp contrast to the shallower high-velocity anomaly. The Apennines, the Northern Adriatic and Sicily have higher velocities ($V_s > 4.6$ km/s) than the Alpine belt and its surrounding regions to the north and west. The Liguro-Provençal basin and the Tyrrhenian Sea have rather low velocities of $4.1 - 4.3$ km/s. The low velocities ($4 - 4.2$ km/s) beneath the volcanic regions and the grabens of the French Massif Central (McF) are probably related to high temperature anomalies in the uppermost mantle.

Supplementary Fig. 2.16 shows three depth sections in our shear-wave velocity model, along the Cifalps and ECORS-CROP reference profiles in the Western Alps, and the alpine segment of the EASI profile in the Eastern Alps (Hetényi et al., 2018b). These sections document strong along-strike variations in the internal structure of the crust and the Moho geometry.

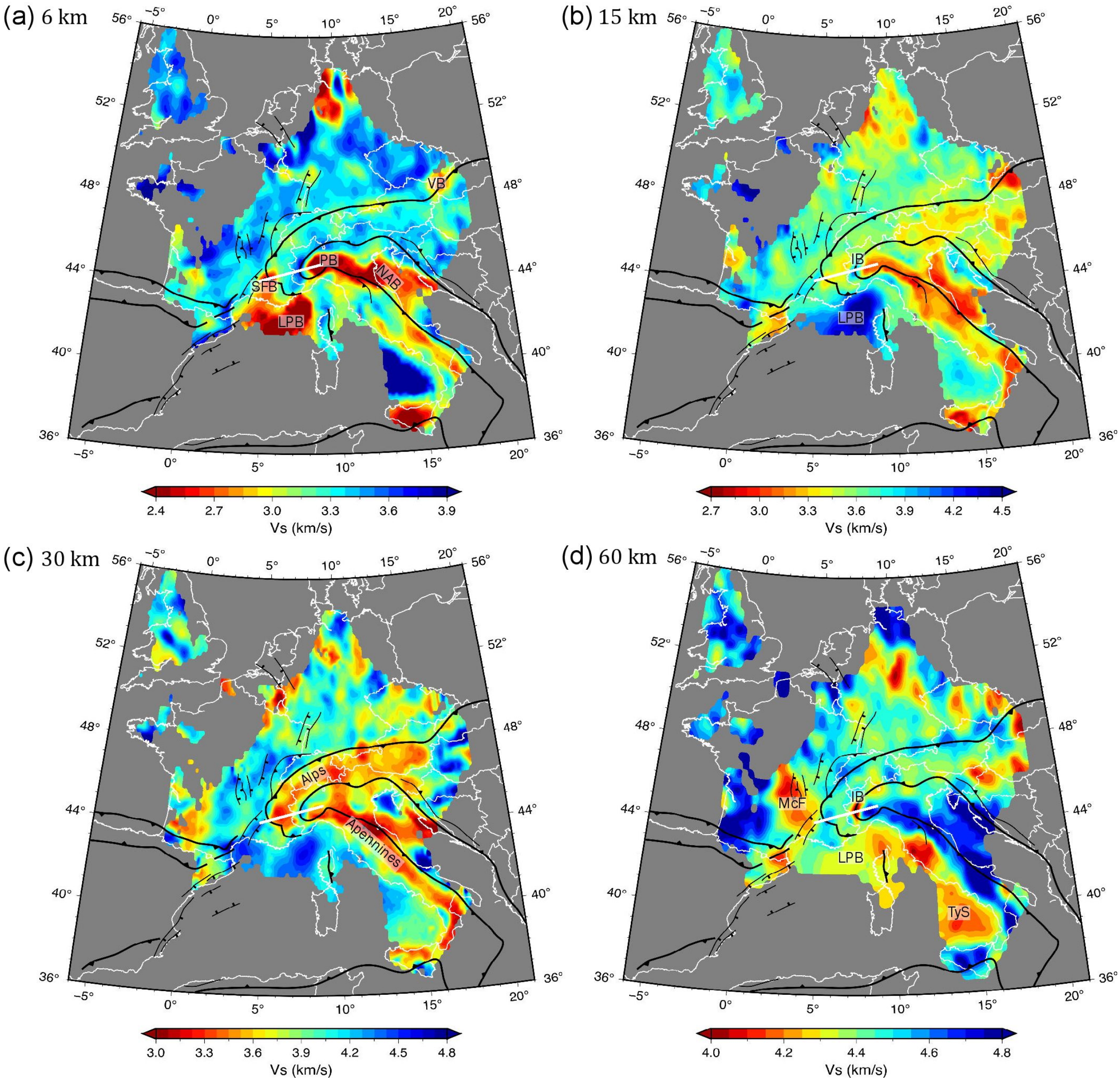

Figure 2.5: Depth slices in the final V_s model at 6, 15, 30 and 60 km. Only regions with 1σ error < 8 % are shown. Black lines show the main geological boundaries as defined in Fig. 2.1a. The white line shows the Cifalps profile discussed in section 5. IB: Ivrea geophysical body, LPB: Liguro-Provençal basin, McF: Massif Central, NAB: North-Adriatic basin, PB: Po basin, SFB: Southeast-France basin, TyS: Tyrrhenian Sea, VB: Vienna basin.

2.5 Discussion: focus on the Cifalps transect

This discussion is focused on the Cifalps cross-section in the South-Western Alps (location in Fig. 2.4a), which has been the target of a number of joint geophysical-geological studies in the last few years. The Cifalps transect is therefore a perfect case study to assess the reliability of our new crustal-scale model and to document its potential in terms of geological interpretation.

The Cifalps temporary seismic experiment ($2012-2013$) aimed at imaging the lithospheric structure of a part of the Alpine arc that had not been previously investigated by major geophysical studies (Zhao et al., 2015). It involved a dense quasi-linear profile of 46 broadband stations ($5-10$ km spacing) and 10 off-line stations (Zhao et al., 2016b). The dataset has been used in a number of seismic tomography and seismotectonic studies, which results have been interpreted in combination with gravity, tectonic, petrological and petrophysical data (see review in Malusà et al., 2021). The resulting lithospheric-scale geological-geophysical cross-section has therefore become one of the best-documented sections across the Alps. Based on P receiver functions (RF), Zhao et al. (2015) provided the first seismological evidence of continental subduction in the Alps, with the detection of P-to-s converted waves at the European Moho at $75-80$ km depth beneath the westernmost Po plain. Zhao et al. (2015) proposed an interpretative geological cross-section that was later refined based on the P-wave velocity model of Solarino et al. (2018) and on the s-wave velocity model of Zhao et al. (2020). The latter imaged a deep low-velocity anomaly at $50-70$ km depth in agreement with the deep P-to-s conversion in RF data.

2.5.1 Model robustness

2.5.1.1 Data fit and uncertainty assessment

Figures 2.6a-b show sections of group velocity (as a function of period) and shear-wave velocity (as a function of depth) along the Cifalps profile. In the western part of the cross-section ($40-140$ km distance range), the European continental crust is marked by low group velocities at $5-25$ s period that result in low s-wave velocities over the entire crust, including a low-velocity zone (LVZ) in the lower part of the crust (white star in Fig. 2.6b). By contrast, the $180-270$ km distance range is featured by anomalously high values both in group velocity ($U > 3$ km/s in a broad period range) and in s-wave velocity (4.0 km/s at 10 km depth). These anomalies correspond to the Ivrea high-velocity high-density body (IB) that was discovered in the early 1960's (Closs and Labrouste, 1963). Our V_s model of the Ivrea body region is similar to the one computed by Zhao et al. (2020) using a different transdimensional inversion scheme. It also exhibits a deep LVZ with $V_s \leqslant 3.9$ km/s at $50-80$ km depth, as an extension of the lower part of the European continental crust (black star in Fig. 2.6b). The step geometry of the velocity contours on the eastern flank of the Ivrea body that may correspond to back-thrusts of the collision belt is however a new feature that did not appear in the model of Zhao et al. (2020). This may indicate that our model is better resolved. Figure 2.6c shows the probability densities for an interface to be present. The basements of the Southeast basin of France in the WSW and of the Po basin in the ESE are marked by strong velocity gradients, hence strong probability that an interface is present. This is also the case for most of the European Moho at $25-40$ km depth, and for the very shallow Moho on top of the Ivrea mantle body that extends towards the ENE to the normal Adriatic Moho at a depth of ~ 35 km beneath the Po basin.

As shown in Fig. 2.6d, the misfit reduction between the observed dispersion curves and the dispersion curves computed from the final V_s model (dashed red line) is everywhere higher than the misfit reduction computed for the Bayesian model, used as initial model for the linearized inversion (solid red line). The misfit reduction is strongest in the Ivrea body region (distance $170-240$ km), where the uncertainty on the Bayesian V_s model is strongest at large depth ($50-80$ km). Fig. 2.6d also shows that sedimentary basins exhibit the largest uncertainties of $\sim$ 7-8 %, while the smallest uncertainties are observed along the Adriatic Moho. A similar small uncertainty is observed along the European Moho up to 180 km distance where the Moho dip increases abruptly. These lateral changes in model uncertainty and misfit differences between the Bayesian and the final V_s model indicate that in the most complex areas none of the 130 million four-layer models that have been explored during the probabilistic inversion can explain completely the observed dispersion curve. In this case the linearized inversion is required to refine the V_s model.

To further investigate the robustness of our final model and its lateral variations, we analyze in Fig. 2.7 the outputs of 1-D inversions for V_s at three representative locations labelled (1), (2) and (3) in Figures 2.6a-b. Figure 2.7 shows first of all that dispersion curves computed from the final models (green curves) match observations well. The gain with respect to the results of the Bayesian inversion (red curves) is higher at pixels (1) and (2) (Fig. 2.7a-b), which have a complex crustal structure that deviates more from the three-layer crust assumption than pixel (3) (Fig. 2.7c).

At pixel (1), the linearized inversion results in a low-velocity zone at $15-30$ km depth that better explains low group velocities at $15-25$ s period. Pixel (2) is located in the westernmost Po plain on the eastern flank of the Ivrea high-velocity body. Compared to the average probabilistic model (red curve), the linearized inversion leads to slightly higher velocities of 4.0 km/s at $\sim$ 10 km, even higher velocities at $25-45$ km depth (4.4 km/s) and lower velocities (3.8 km/s) at $52-77$ km depth. The final modeled dispersion curve (green curve in Fig. 2.7b top) fits the observations better than the dispersion curve computed from the average probabilistic model (red curve). The example pixels (1) and (2) further confirm that the Bayesian inversion and its four-layer model assumption fail to explain such complex group-velocity data, while the final step of linearized inversion does a better job thanks to its fair initial model.

Such strong differences between the average probabilistic model and the final model are not observed at pixel (3) because its V_s model has a 'normal' layered structure with a positive velocity gradient (Fig. 2.7c). The very low velocities ($\leqslant$ 2.2 km/s) from 0 to $7-8$ km depth are the signature of the thick Po basin.

2.5.1.2 Benefits of our hybrid inversion scheme

Unlike Lu et al. (2018) and most ambient-noise tomographies, we used a 2-D transdimensional inversion for group-velocity maps to avoid biases arising from explicit regularisation. The Bayesian nature of this inversion also allows for a robust quantification of the uncertainties on group velocities and hence local dispersion curves. Unlike Zhao et al. (2020) who used a full transdimensional approach in the inversion for V_s, we performed an exhaustive grid search over all possible 4-layer models, followed by a linear inversion. This hybrid methodology limits the complexity of resulting V_s model while giving enough freedom to the inversion to actually fit the data. It also provides uncertainties on V_s and the probability of having an interface at given depths. To document the benefits of our approach, supplementary Fig. 2.17 and its comments compare our model to the one by Zhao et al. (2020) on depth sections along the Cifalps and ECORS-CROP reference profiles. The two models exhibit differences that can be attributed to the improved data coverage in the western part of the study region, or to the inversion scheme. The results of our inversion is more in line with previous geophysical data. Moreover, the hybrid character of our inversion makes it much less computationally expensive than pure transdimensional inversion. Therefore, we could compute a robust 3-D V_s model at the scale of Western Europe from such a large volume of data using reasonable computational resources.

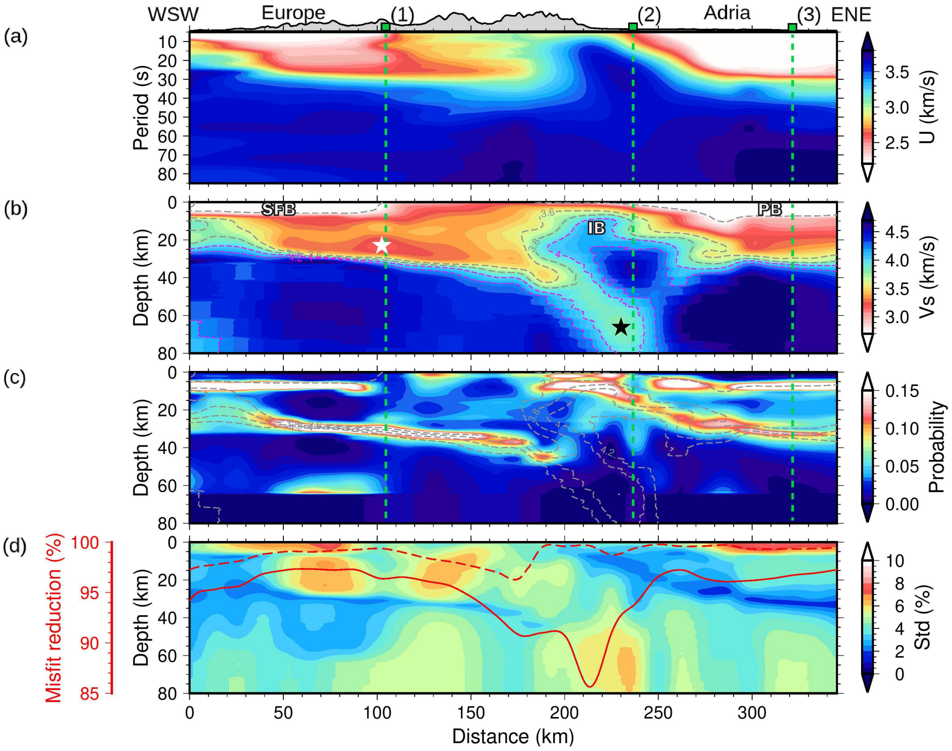

Figure 2.6: Depth sections of observations and inversion results along the Cifalps WSW-ENE profile (location in Fig. 2.4a). (a) Rayleigh-wave group velocities obtained from the Hierarchical Bayes reversible-jump tomography at grid points located along the profile. Green vertical dashed lines indicate locations of pixels (1), (2) and (3) discussed in the text. (b) Final shear-wave velocity section. The $2.7, 3.6$ and 3.8 km/s velocity contours are shown as gray dashed lines while the pink dashed lines indicate the 4.0 and 4.2 km/s velocity contours. The white and black stars mark low-velocity anomalies discussed in the text. (c) Posterior probability density of presence of a layer boundary obtained from the Bayesian inversion. The dashed lines show the same velocity contours as in (b). (d) Color map: model uncertainties approximated for each location and at each depth by the 1σ value of the ensemble of most probable models normalized by the V_s value at this grid point/depth. The thick red line indicates the total misfit reduction after the Bayesian inversion while the red dashed line indicates the total misfit reduction after the linearized inversion. IB: Ivrea geophysical Body, PB: Po basin, SFB: Southeast-France basin.

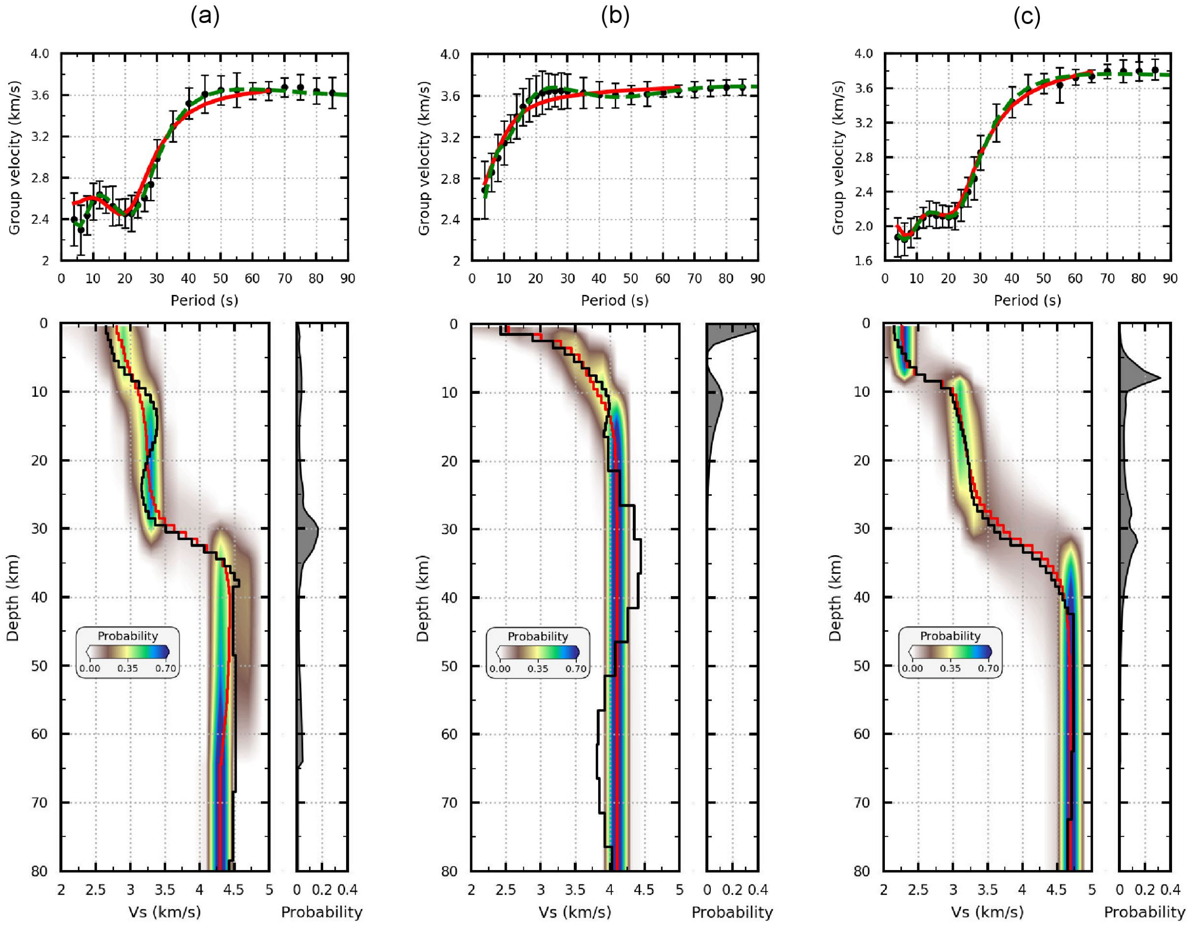

Figure 2.7: Results of the inversion for V_s at pixels 1 (panels a), 2 (panels b) and 3 (panels c). Pixel locations are indicated in Fig. 2.6a). The top panels show observed (black) and predicted dispersion curves (red: from the Bayesian inversion; green: from the linear inversion). The bottom panels show: (left) probability density of V_s (color map) and predicted V_s models (red: probabilistic average model; black: final model); (right) probability density of interface presence.

2.5.2 Comparison with other geophysical data

In Figure 2.8, we compare the depth section through our V_s model along the Cifalps profile with the Bouguer anomaly (Fig. 2.8a) and the receiver-function CCP migrated depth section (common conversion point; Zhu, 2000) computed from the Cifalps dataset (Zhao et al., 2015) and migrated using our V_s model (Fig. 2.8b).

A receiver-function section displays teleseismic P-to-s converted waves (P_s) at velocity discontinuities beneath the stations, with positive amplitudes indicative of velocity increase with depth, and negative polarities indicative of velocity decrease with depth (Vinnik, 1977). Unlike Zhao et al. (2015) who used a four-segment 1-D migration model, we used the 2-D V_s model derived from our ambient-noise tomography (shown as velocity contours in Fig. 2.8b) to perform the time-to-depth CCP migration of receiver functions.

The maximum of the Ivrea gravity anomaly (positive Bouguer anomaly in Fig. 2.8a) coincides well with the top of the high-V_s anomaly (3.8 and 4.1 km/s contours in Fig. 2.8b). The consistency between the V_s model and the CCP section is outstanding, considering that the sensitivity of surface waves to sharp velocity boundaries is rather weak. The $4.2-4.3$ km/s velocity contours are fairly consistent with the European Moho, which is characterized by a clear P_s phase of positive polarity at distances $0-200$ km. The agreement is not that good at $200-250$ km distance where the $4.2-4.3$ km/s contours are deeper than the deepest P_s phases at $70-80$ km depth that were interpreted by Zhao et al. (2015) as evidence of continental subduction of Europe beneath Adria. The *RF* data quality is poorer under the Po basin, making comparison with V_s contours difficult. In addition, the 3.6 and 3.8 km/s contours match the negative polarity P_s phases observed above the European Moho at distances $180-250$ km, which were interpreted by Zhao et al. (2015) as traces of an 'inverted' Moho between the Ivrea mantle body on top and the European crust below. We conclude from the match of the $4.2-4.3$ km/s velocity contours with the European Moho that these contours are an accurate proxy of the autochthonous Moho, while the 3.8 or 4.0 km/s contours are more adequate to characterize the Moho at the top of the serpentinized Ivrea body.

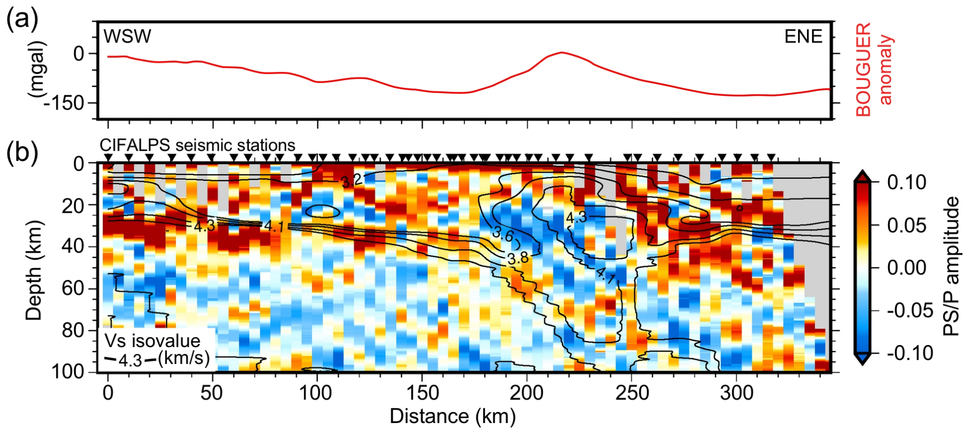

Figure 2.8: Comparison of our V_s model along the Cifalps line with independent geophysical data. (a) Bouguer gravity anomaly extracted from the AAGRG model (AlpArray Gravity Research Group; Zahorec et al., 2021). (b) Receiver-function CCP depth section migrated using our V_s model; The black plain lines are the 2.7, 3.2, 3.6, 3.8, 4.1 and 4.3 km/s contours of our V_s model; Locations of stations projected onto the profile are shown as black inverted triangles (station map shown in Fig. 2.9a).

We have seen in Fig. 2.6c that the probability of presence of an interface is a reliable marker of a strong velocity contrast. For instance, the probability is lower for the Adriatic Moho than for the European Moho, due to a lower velocity gradient on the Adriatic side (Fig. 2.7a and Fig. 2.7c). This correlation with the velocity gradient is however not valid everywhere, as for instance at the top of the Ivrea body anomaly where the probability is high while the gradient is rather smooth (Fig. 2.7b). Hence, the probability of presence of an interface is an accurate proxy not only for the base of sedimentary basins, but also for delineating the crust-mantle boundary of Adria and Europe, and highlighting interfaces with weak velocity gradient such as the top of the Ivrea body. However, Fig. 2.6c shows that the probability section is almost blind inside the subduction complex due to its very complex structure, which means that interface probability cannot be considered as a universal proxy for Moho. By contrast, the comparison between the V_s section and the *RF* section has confirmed that the 4.2 or 4.3 km/s iso-velocity contour is better suited to delineate deep discontinuities associated with the subduction of the European lithosphere. In future studies, we will therefore rather exploit the 4.3 km/s contour as a proxy of Moho to delineate its 3-D depth variations.

2.5.3 Crustal-scale geological interpretations

In Figure 2.9, we propose a geological interpretation of the shear-wave velocity section along the Cifalps profile that also builds on surface geological observation, on previous joint geophysical-geological works summarized in Malusà et al. (2021), on the *RF* section of Fig. 2.8b and on hypocenter locations by Eva et al. (2015) and Malusà et al (2017).

In the following subsections, we emphasize a number of first-order features related to the geometry of structures at crustal scale, to the deformation and thermicity of the lithosphere, and to the link between the lithospheric structure and the strain field.

2.5.3.1 Geometry of structures at lithospheric scale

The geology of the Western Alps (Fig. 9a) results from the convergence of two lithospheric plates (Polino et al., 1990; Dumont et al., 2012). To the west, the European margin corresponds to the lower plate, which subducted beneath the Adriatic upper plate to the east. Between these two continental domains, the subduction wedge developed by the juxtaposition of oceanic sediments and crustal fragments (Lardeaux et al., 2006; Schwartz et al., 2009; Agard et al., 2021) with units originating from the two continental margins (Fig. 2.9a). This prism is bounded by two major crustal-scale faults: to the west the Penninic Frontal Thrust (PFT) and to the east the dextral strike-slip Insubric Fault (IF). The European foreland accommodates the convergence through the propagation of a fold-and-thrust-belt system associated with the development of Cenozoic sedimentary basins (Ford et al., 1999). These basins are further deformed, uplifted and partially eroded during the westward propagation of compressional structures. This compressional deformation is localized at depth along crustal-scale thrusts leading to the exhumation of the External Crystalline Massifs in thick skin tectonic mode (e.g., Jourdon et al., 2014; Schwartz et al., 2017). To the East, the Po plain is affected by top-to-northeast back-thrusts allowing the uplift and erosion of Cenozoic basins (Mosca et al., 2010).

The V_s model documents the subduction of the European lithosphere towards the east below the Adria lithospheric mantle, marked by a continuous European continental crust down to a minimum depth of 100 km. This continental crust is featured by a progressive increase of V_s with depth from $3.4-3.5$ km/s at $20-30$ km to 4.2 km/s at 100 km interpreted as resulting from the densification of continental rocks during their progressive eclogitization.

Under the westernmost part of the European foreland, high crustal V_s values of $3.6-3.8$ km/s and a slight Moho uprise (iso-velocity contour $V_s = 4.3$ km/s) indicate crustal thinning beneath the Rhône valley consistently with the formation of the Western European Cenozoic Rift System (Ziegler, 1992).

One of the most striking features of the section is a standard crustal thickness of ~ 30 km below the frontal part of the External Massifs, increasing to ~ 50 km below the PFT. This observation is in line with other recent geophysical models along the Cifalps profile that exhibit very little crustal thickening of the External Alps (e.g., Malusà et al., 2021).

Beneath the Ivrea Gravity Anomaly (IGA in Fig. 2.9c), located along the Insubric Fault and extending southwards beneath the Internal Crystalline Massif of Dora Maira (Fig. 2.9a-b), the upper part of the subduction wedge is likely formed by stacking of crustal slices extracted from both the continental and oceanic crusts. This subduction wedge overlies the mantle wedge (MW, Fig. 2.9d) at a depth of about 10 km. This mantle wedge, documented by shear-wave velocities ranging between $\sim$ 3.8 and 4.0 km/s, may be composed of partially serpentinized mantle of Adriatic origin produced by hydration above the subducted oceanic units. Below the subduction wedge, a superposition of several mantle bodies with different geophysical signatures is observed, which suggests the superposition of two petrological Mohos: a first one characterized by a reverse V_s gradient with a negative polarity in the receiver function (RF) section (Fig. 2.9e). This 'inverted Moho' corresponds to the subduction interface between the European slab and the mantle wedge. The second, deeper Moho corresponds to the European Moho itself, steeply dipping due to subduction.

2.5.3.2 Deformation and thermicity

The deformation is dominated by compressive structures occurring in both forelands of the chain, with top-to-the-west thick-skinned propagation on the western side of the belt, rooted in the lower crust. A major thrust is well marked in the RF section as a set of positive-polarity signals down to 25 km depth that connects at the surface with the thrust (Fig. 2.9e). We name it the Alpine Frontal Thrust (AFT). Similar structures occur on the eastern side of the Alps, below the Po plain, which either do not outcrop or may merge with the frontal Po thrust system. The rooting of these peripheral thrusts appears to occur at different depth levels. We propose that the AFT becomes horizontal in the lower crust, where V_s has very low values < 3.4 km/s (Fig. 2.9d), which would be consistent with the more ductile rheology of the European lower crust. In contrast, the step-like shape of the V_s contours in the eastern side suggests that the Adriatic Moho and continental crust (ACC, Fig. 2.9d) are significantly offset by the main top-to-northeast thrusts. This difference in deformation style between the European crust and the Adria crust is in agreement with a different thermal state, revealed by different V_s layouts in the lithospheric mantle domains. The higher and more homogeneous shear-wave velocities observed in the Adria mantle may indicate a colder state leading to a more rigid behavior. In this context, the Adria lithospheric mantle behaves as a deep horizontal indentor (the Adria Lithospheric Indentor or ALI, Fig. 2.9d) buttressing the European slab along a 25 km-high vertical boundary.

As a result of this deep indentation, the mantle wedge is vertically indented by an intermediate, non-serpentinized rigid mantle body with $V_s \sim 4.2 - 4.4$ km/s that localizes most of the deep seismicity ($>$ 20 km) below the westernmost Po plain (pink open circles in Fig. 2.9a, b, d; Eva et al., 2015; Malusà et al., 2017). This rigid body is named Adria Seismic Body (ASB). We relate the vertical seismic swarm in the ASB to the rooting zone of the Insubric Fault.

2.5.3.3 Link between the geometry of lithospheric structures and the strain field

In the framework of plate tectonics and convergence between Europe and Adria, the observed split of the Adriatic lithospheric mantle into two units (ASB and ALI) would be responsible for the partitioning of the deformation at lithospheric scale. The deeper part of the Adria mantle (ALI) horizontally indents the European slab. This results both in lithospheric loading and in lithospheric shear deformation propagating westwards to reach the upper crust beneath the European foreland, corresponding to the activation of the Alpine Frontal Thrust (AFT). The upper part of the Adria mantle (ASB) was pushed upwards and maintained in a high structural position by the ALI horizontal indentation. In turn, the ASB acted as a vertical indentor responsible for the deformation and exhumation of the subduction wedge units.

This geometry leads to a partitioning of the active deformation on both sides of the Insubric Fault (Fig. 2.9d). To the east of the IF, the subduction wedge is backthrusted onto the Adria crust and the Adria lithosphere is significantly shortened (Mathey et al., 2020). In contrast, to the west of the IF, extensional deformation dominates in a crustal compartment bounded by the IF and the PFT (Mathey et al., 2020), as a result of vertical indentation. This latter thrust was reactivated since at least $3 - 4$ Ma, and it is still currently undergoing extensional deformation (Bilau et al., 2021).

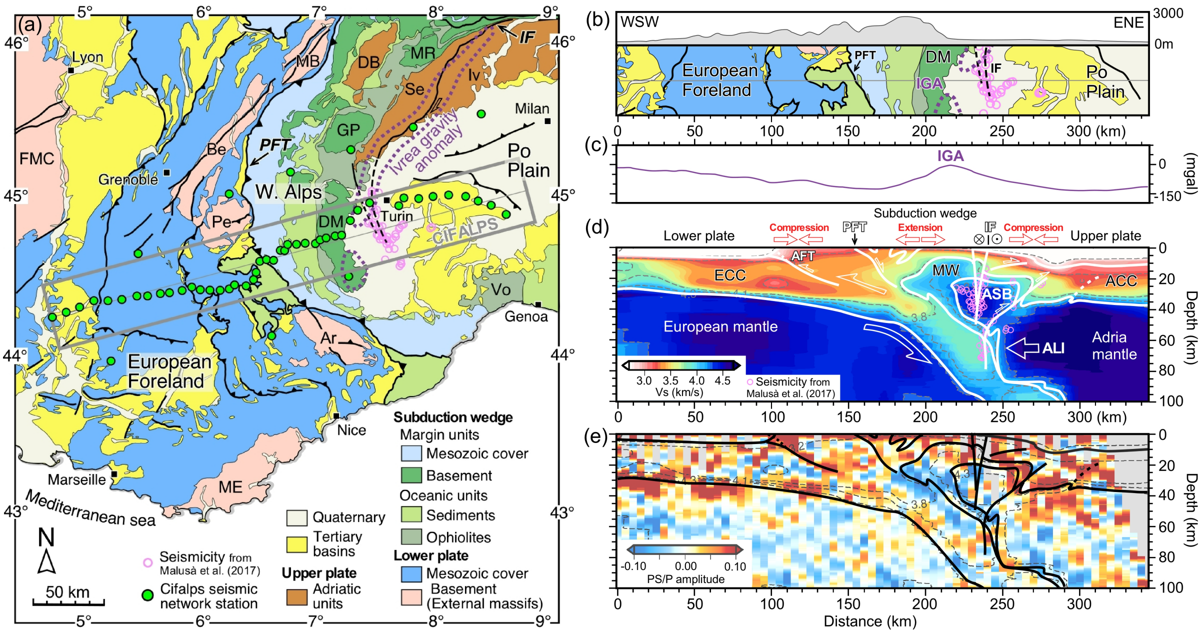

Figure 2.9: Geological and tectonic settings of the study area along the Cifalps transect. (a) Geological map of the W-Alps with location of the Cifalps seismic network (white rectangle in Fig. 2.1b). Earthquake epicenters with depth > 20 km beneath the westernmost Po plain are shown as pink open circles (after Eva et al., 2015 and Malusà et al., 2017). The Ivrea gravity anomaly is represented by the 0 mGal contour (dashed purple line) from Bigi et al. (1990). The continental crust units of the European plate (lower plate) are indicated by: Ar, Argentera; Be, Belledonne; MB, Mont-Blanc; Pe, Pelvoux; ME, Maures-Estérel; FMC, French Massif Central. The Adriatic units (upper plate) are indicated by: DB, Dent Blanche; Iv, Ivrea-Verbano; Se, Sesia. The internal crystalline massifs of the subduction wedge are indicated by: DM, Dora Maira; GP, Gran Paradiso; MR: Monte Rosa; Two major tectonic limits are also indicated: IF, Insubric Fault; PFT: Penninic Frontal Thrust. (b) Topographic profile and geological map (extracted from (a)) along the Cifalps transect. (c) Bouguer gravity anomaly extracted along the profile (same as Fig. 2.8a). IGA: Ivrea Gravity Anomaly. (d) Crustal-scale interpretation of the V_s depth section along the Cifalps transect. The main geological interfaces corresponding to lithological units and tectonic structures are underlined in white (see interpretation in text). This interpretation shows the subduction of the European lithosphere toward the East below the Adria lithospheric mantle. The European continental crust (ECC) is continuous down to 100 km depth. We observe separation of the Adria lithospheric mantle into two main bodies: (1) The deeper part ALI (Adria lithospheric indentor) acts as a horizontal indentor that deformed the European slab and enabled the activation of the Alpine Frontal Thrust (AFT). (2) The upper part ASB (Adria seismic body) acts as a vertical indentor controlling the exhumation of the mantle wedge (MW) and locating the deep seismicity along the Insubric Fault (IF) system. In this interpretation, the Adriatic continental crust (ACC) is deformed by top-to-northeast thrusts. In the global tectonic convergence, the crustal-scale geometry deduced from the V_s model controls the partitioning of the strain field (red arrows). The crustal compartment located between the IF and PFT tectonic structures records extension while the two other compartments record compression. (e) Crustal-scale interpretation plotted as black lines on the receiver-function CCP depth section of Fig. 2.8b.

2.6 Conclusion

The high density and rather homogeneous coverage of permanent European broadband networks complemented with the AlpArray temporary network and quasi-linear dense arrays such as Cifalps, Cifalps-2, and EASI were key in our derivation of a high-resolution shear-wave velocity model of the Alpine mountain belt and its forelands. We used four years of continuous seismic noise recorded by ~ 1550 broadband seismic stations, which led to 1.1 million cross-correlations of vertical noise records. Rayleigh-wave group-velocity dispersion curves were measured in the $4 - 150$ s period band and 2-D group-velocity maps and their uncertainties were computed using a data-driven transdimensional inversion that allows the local resolution to self-adapt to the path density and to the variability of information contained in group-velocity measurements. At each location of our $0.15° \times 0.15°$ grid, the local group-velocity dispersion curve and its associated uncertainties were inverted jointly in a Bayesian approach to derive a quasi-3-D probabilistic shear-wave velocity model. This model was further refined using a linear inversion.

The best-resolved part of our 3-D V_s model covers the Alpine range, its forelands and the Ligurian Sea. We showed on the Cifalps traverse of the South-Western Alps that the resolution of our model makes it possible to correlate features of the geophysical model with geological structures mapped at the surface. This enabled an integrated geological-geophysical interpretation that highlights first-order features related to the subduction of the European lithosphere under the Adriatic lithosphere in the South-Western Alps. One of these key features is the Ivrea geophysical body, which is likely made of a subduction wedge formed by stacking of crustal slices of continental and oceanic origin overlying a mantle wedge likely composed of partially serpentinized Adriatic mantle. Another key feature is the split of the Adriatic mantle lithosphere in two different units. This split could be responsible for the partitioning of the deformation at lithospheric scale.

Following the model verification at the location of the 2-D Cifalps cross-section, our velocity model makes it possible to construct a 3-D, lithospheric-scale geological models of the Alpine belt, extending the geological maps in depth. These models are expected to provide key constraints to conceptual geological-petrophysical models of subduction wedge systems, for example. Such interpretation work has already started for the Western Alps.

Our V_s model can also be used in further geophysical studies, including waveform modelling and full waveform inversion. Our next project is to use this model as an initial model to simultaneously build a 3-D V_p and V_s model of the Alpine lithosphere by joint inversion of surface-wave dispersion data from noise correlations and travel times of body waves emitted by local earthquakes using a 3-D wave-equation tomography. This combination of P-wave and s-wave velocities is required to establish the lithology of rocks buried at large depths.

2.7 Supporting information

Additional Figures (2.10-2.17) and information are presented as the Supplementary Material.
Figure 2.10. Distance-time plot of noise correlations.
Figure 2.11. Comparison of the 8-s and 25-s group-velocity maps with sedimentary basins and Moho depth maps.
Figure 2.12. Comparison with a matrix-based inversion.
Figure 2.13. Posterior distribution on the number of Voronoi cells.
Figure 2.14. Inversion misfit.
Figure 2.15. Checkerboard tests.
Figure 2.16. Depth sections through the V_s model along reference profiles.
Figure 2.17. Comparison with the V_s model by Zhao et al. (2020).

2.7.1 Distance-time plot of noise correlations

Fig. 2.10 shows a distance-time section of vertical-component seismic ambient noise cross-correlations computed in a region including most of the Western Alps. The dispersive Rayleigh wave emerges very clearly with a fairly good symmetry between the causal and acausal parts.

2.7.2 Comparison of the 8-s and 25-s group-velocity maps with sedimentary basins and Moho depth maps

Figure 2.11a shows the 8-s group-velocity map together with main sedimentary basins. Figure 2.11b shows the 25-s group-velocity map with contours of the reference Moho depth model of Spada et al. (2013), that is mainly derived from controlled-source seismology (CSS) and receiver-function data. The thick crust of the Alps and the Apennines mountain belts coincides with areas of low velocity ($<$ 3.0 km/s). Areas of thin crust such as the Liguro-Provençal basin and the Tyrrhenian Sea coincide with high velocity anomalies ($>$ 3.4 km/s).

2.7.3 Comparison with a matrix-based inversion

We compared results of the *rj-McMC* algorithm with a matrix-based linearized inversion (Boschi & Dziewonski., 1999) for the same dataset at 15 s period (Fig. 2.12). The linear problem is solved using an iterative *LSQR* algorithm (Paige and Saunders., 1982). The model solution is computed using an adaptive grid-based path density that remains fixed during inversion (Schaefer et al., 2011; Lu et al., 2018; Fig. 2.12a). Cell sizes of 0.15°, 0.3° and 0.6° were used depending on the path density (Fig. 2.12b). The regularization coefficients (damping, roughness) were set according to the maximum curvature of the *L-curve*. Fig. 2.12c shows the *rj-McMC* solution model computed by averaging the ensemble of models obtained from 64 Markov chains in parallel after 180×10^3 steps. The posterior map of velocity uncertainties is generated by computing the variance of this ensemble (Fig. 2.12d). The image resulting from the *rj-McMC* inversion is not as smooth as the one resulting from the linearized inversion, which is affected by the imposed degree of smoothing. On the other hand, a stronger velocity contrast is obtained using the trans-D inversion, with more focused anomalies that suggest a better resolution (see for example the low-velocity anomaly in the Po plain). In addition, the trans-D inversion highlights new features such as the high-velocity anomaly at 4° longitude and 43.5° latitude.

2.7.4 Posterior distribution on the number of Voronoi cells

Figure 2.13 shows the posterior probability distribution on the number of Voronoi cells used to describe the 2-D velocity field in the *rj-McMC* tomography shown in Fig. 2.12c. The small standard deviation of the Gaussian-shaped probability density curve shows that the algorithm has converged. The maximum model solution occurs for $760 - 770$ Voronoi cells.

2.7.5 Inversion misfit

Figure 2.14a shows the evolution of the normalized model misfit function with the number of iterations in the *rj-McMC* inversion shown in Fig. 2.12c. The misfit reduction reaches $\sim 90\%$. The posterior histogram of traveltime misfit between model predictions and observations is shown in Fig. 2.14b.

2.7.6 Checkerboard tests

In Figure 2.15, we check the resolution power of the *rj-McMC* inversion by synthetic checkerboard tests for cell sizes of 1° and 2°. Figures 2.15(1a)-(2a) show input models with square-shaped anomalies. Synthetic travel times were computed using the same source and receiver geometry as in observations at 15 s period, with added random Gaussian noise of 1 s standard deviation. Figures 2.15(1b)-(2b) show the average solution models obtained from the *rj-McMC* tomography. The Hierarchical Bayes reversible jump method is able to recover the velocity areas as defined in the synthetic models.

2.7.7 Depth sections through the V_s model along reference profiles

In Fig. 2.16, we present depth sections along three reference profiles across the Alpine mountain range: Cifalps and ECORS-CROP in the Western Alps and the alpine part of the EASI N-S transect in the Eastern Alps.

2.7.8 Comparison with the V_s model by Zhao et al. (2020)

Fig. 2.17 shows a comparison between our V_s model and the one by Zhao et al. (2020) on depth sections along the Cifalps and ECORS-CROP profiles. To facilitate the comparison between the results of the two models, we added on each depth section the reference Moho depth model of Spada et al. (2013) and the 4.3 km/s iso-velocity contour that we use as a proxy for the Moho (see discussion in section 5.2 of the main text). The middle and lower crust of the western parts of both profiles have higher velocities in our model than in Zhao et al. (2020). This difference is most probably due to the improved data coverage in our dataset with respect to the one of Lu et al. (2018) used in the inversion of Zhao et al. (2020), in particular in the westernmost part of the AlpArray network. In the alpine part of the Cifalps section, the model by Zhao et al. (2020) and our model exhibit similar first order features. In particular, they exhibit consistent geometries of the Ivrea body and similar Moho depths.

By contrast, these two models exhibit striking differences along the ECORS-CROP transect. The depth of the 4.3 km/s iso-velocity in our model is consistent with the Moho depth of Spada et al. (2013), but is deeper in Zhao et al. (2020). The 3.8 km/s V_s contour would better fit the Moho model of Spada et al. (2013), although 3.8 km/s is rather low for a Moho proxy.

Another striking difference is the velocity gradient at the Moho, which is strong in our model and smooth in Zhao et al. (2020). Our strong gradient is more in line with the results of receiver functions studies (Zhao et al., 2015) and seismic reflection profiling (e.g. ECORS-CROP Deep Seismic Sounding Group, 1989; Thouvenot et al., 2007) in the Western Alps, which documented a highly reflective Moho. This strong velocity gradient at Moho depth in our model is a direct consequence of the chosen parameterization and the 4-layer model assumption. By contrast, the reference model in the transdimensional inversion of Zhao et al. (2020) is a homogeneous half-space of 3.8 km/s velocity.

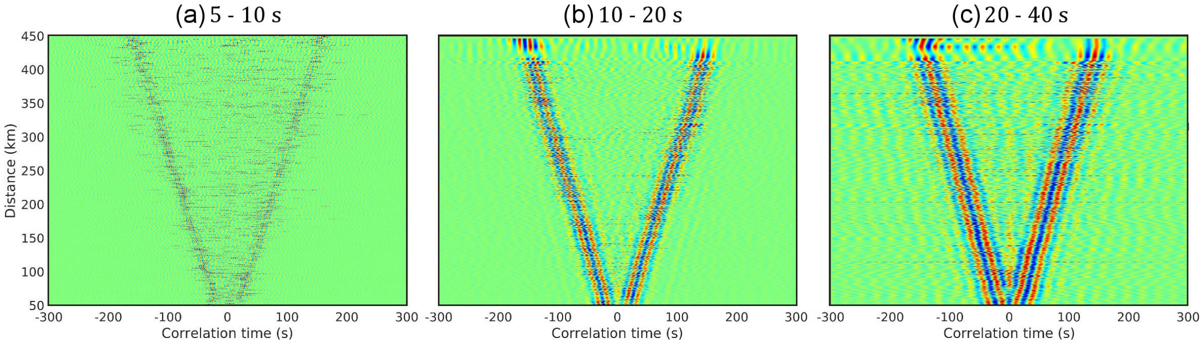

Figure 2.10: Sections of noise cross-correlation traces in the $5-10$ s, $10-20$ s and $20-40$ s period bands. The trace amplitudes are normalized to one. The causal part (positive times) corresponds to Rayleigh waves propagating eastwards while the acausal part (negative times) corresponds to Rayleigh waves propagating westwards.

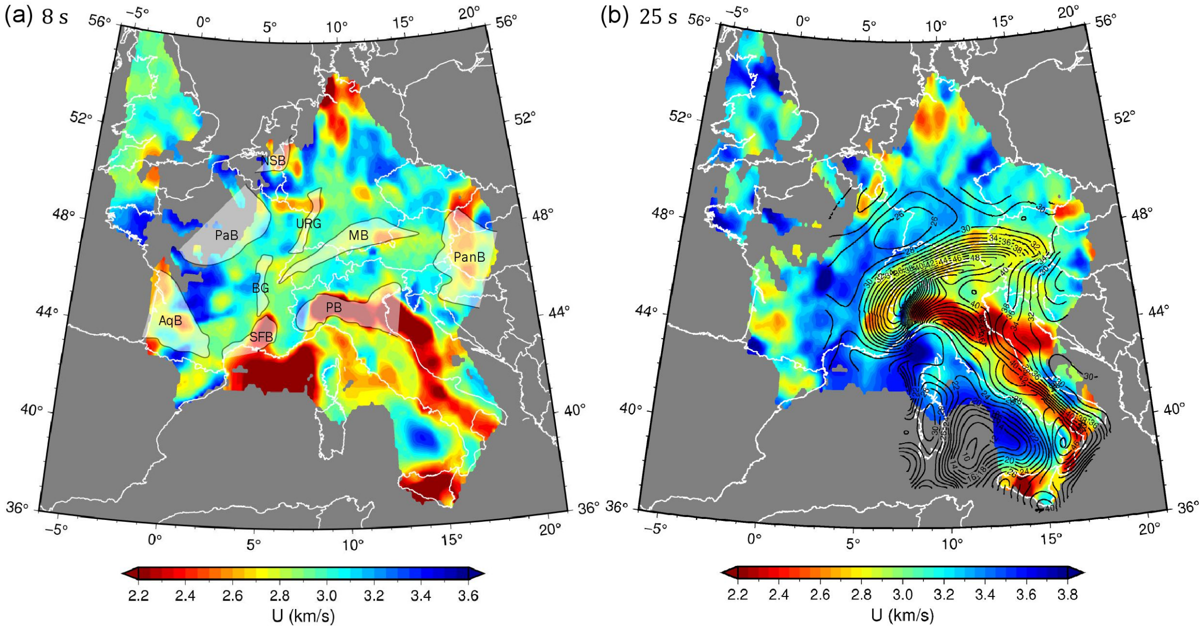

Figure 2.11: (a) Group-velocity map at 8 s period and Jurassic to Tertiary main sedimentary basins (shown as partially transparent areas). NSB: North-Sea basin, PB: Po basin, SFB: Southeast-France basin, AqB: Aquitaine basin, PaB: Paris basin, BG: Bresse Graben, URG: Upper Rhine Graben, MB: Molasse basin, PanB: Pannonian Basin. (b) Group-velocity map at 25 s period. Black lines are contours of the reference Moho depth map by Spada et al. (2013).

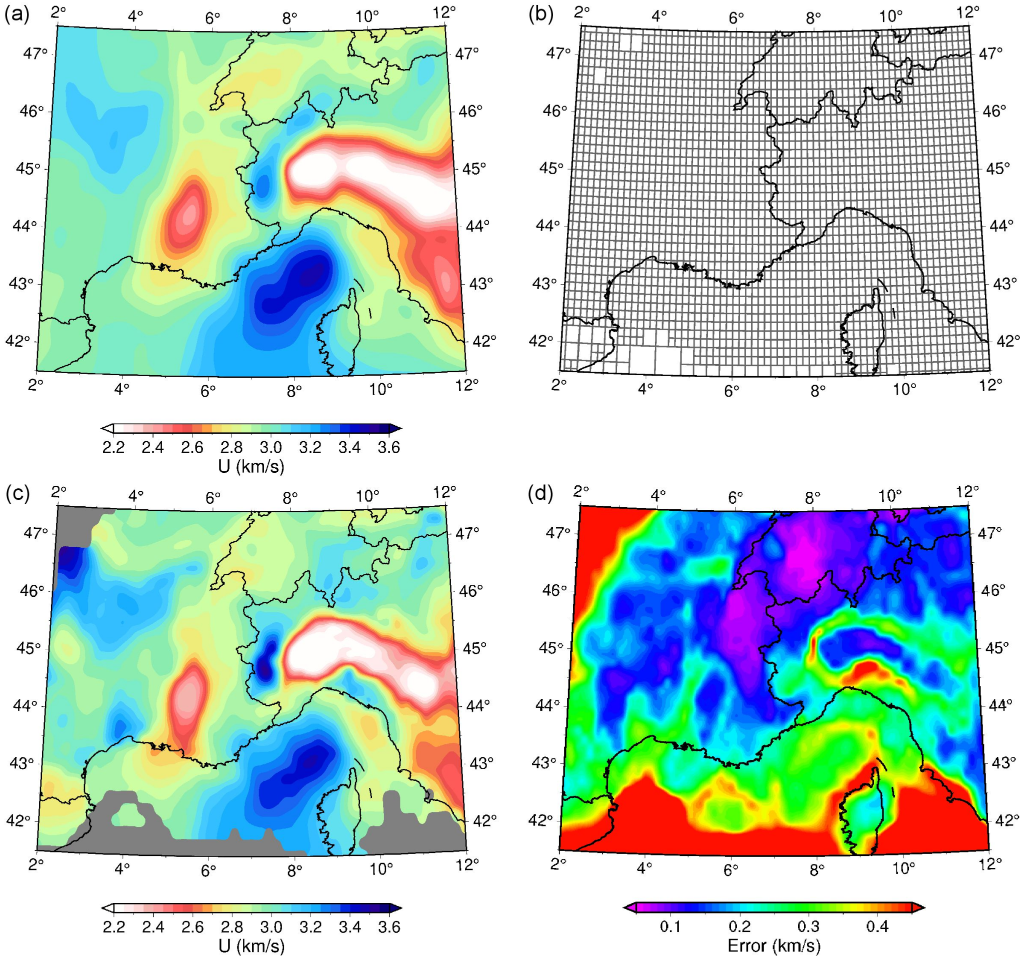

Figure 2.12: Comparison of the result of our Hierarchical Bayes inversion with the result of a matrix-based inversion at 15 *s* period. (a) Group-velocity map output of the regularized method. (b) Adaptive grid used to produce the regularized solution model. (c) Result of the Hierarchical Bayes reversible jump method. (d) Estimated error for the reversible jump tomography.

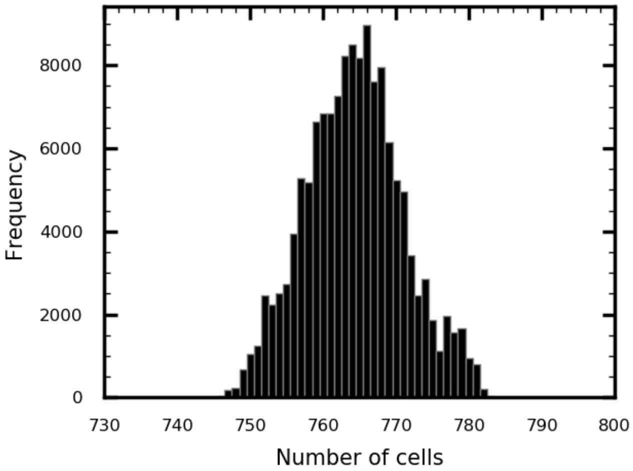

Figure 2.13: Posterior probability density for the number of Voronoi cells at 15 s period.

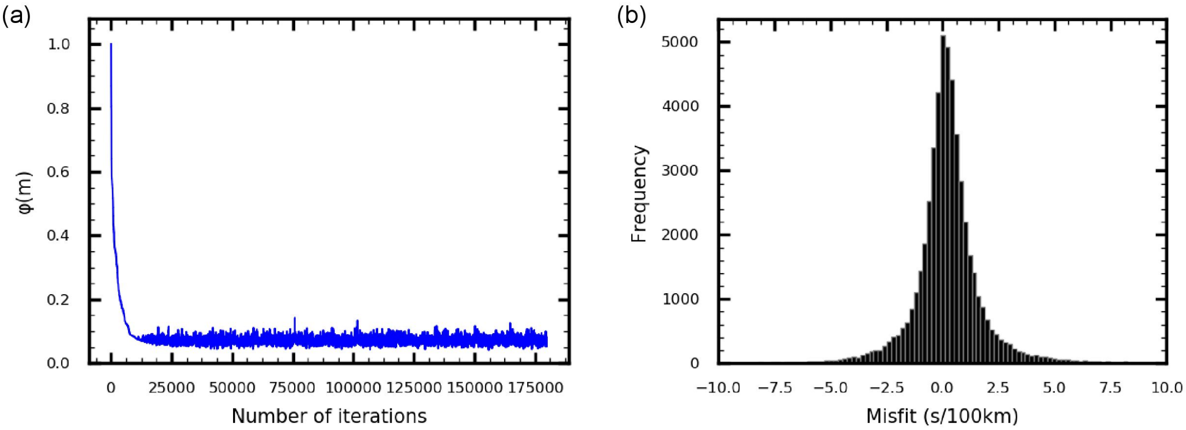

Figure 2.14: Misfit outputs at 15 s period from the reversible jump tomography. (a) Model misfit variation as a function of the number of iterations. (b) Histogram of traveltime misfit.

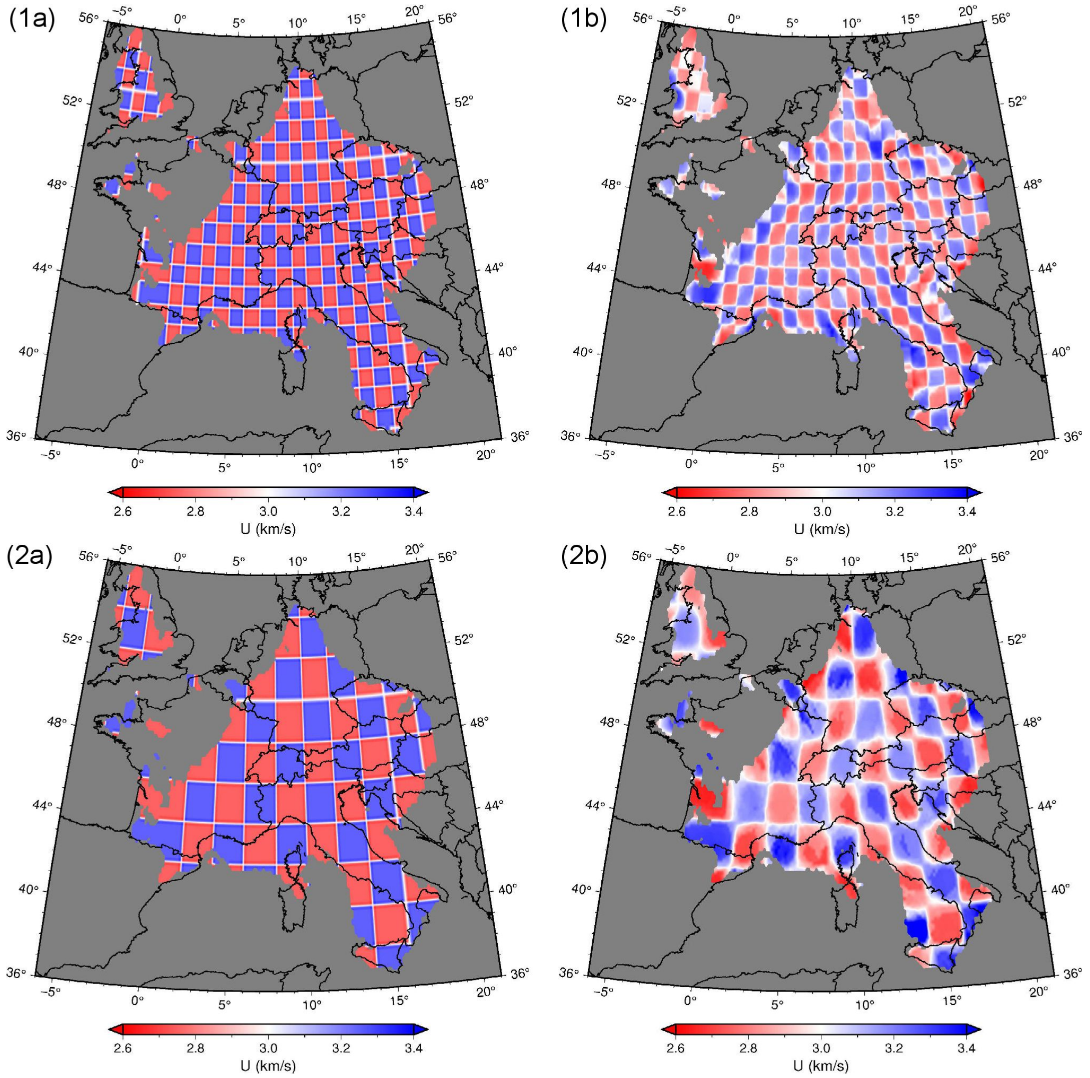

Figure 2.15: (1a) Input synthetic velocity model with a cell size of 1°. (1b) Average solution model of the Hierarchical Bayes reversible jump tomography. (2a) Input synthetic velocity model with a cell size of 2°. (2b) Average solution model of the Hierarchical Bayes reversible jump tomography.

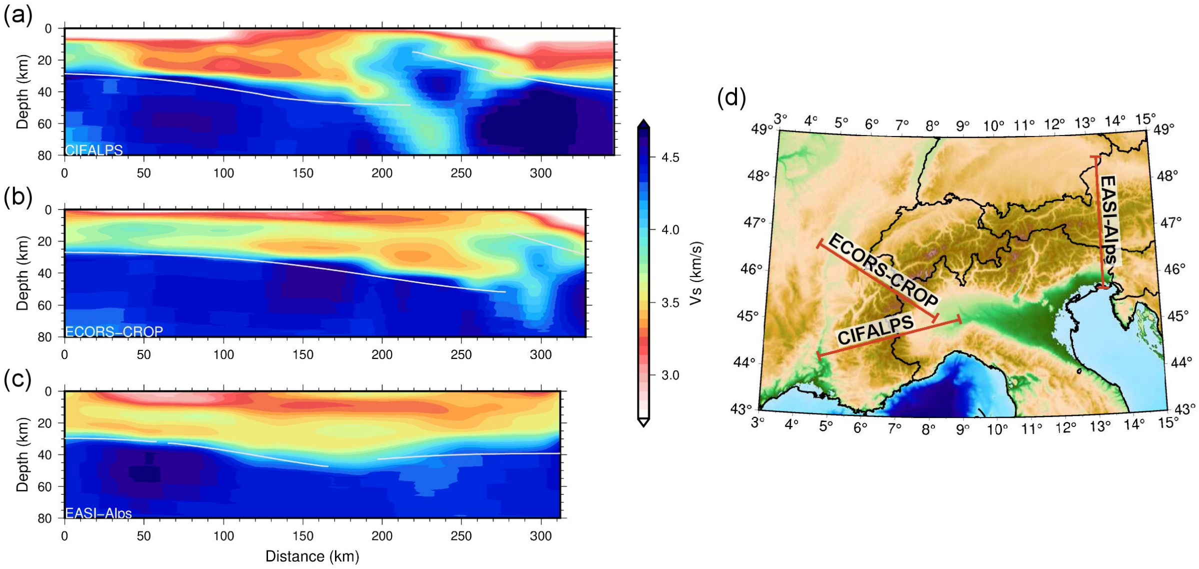

Figure 2.16: Cross sections in our V_s model along. (a) the CIFALPS profile, (b) the ECORS-CROP profile, and (c) the alpine part of the EASI profile (Hetényi et al., 2018). The white lines show Spada et al. (2013)'s Moho depth model. (d) Location map of the three profiles.

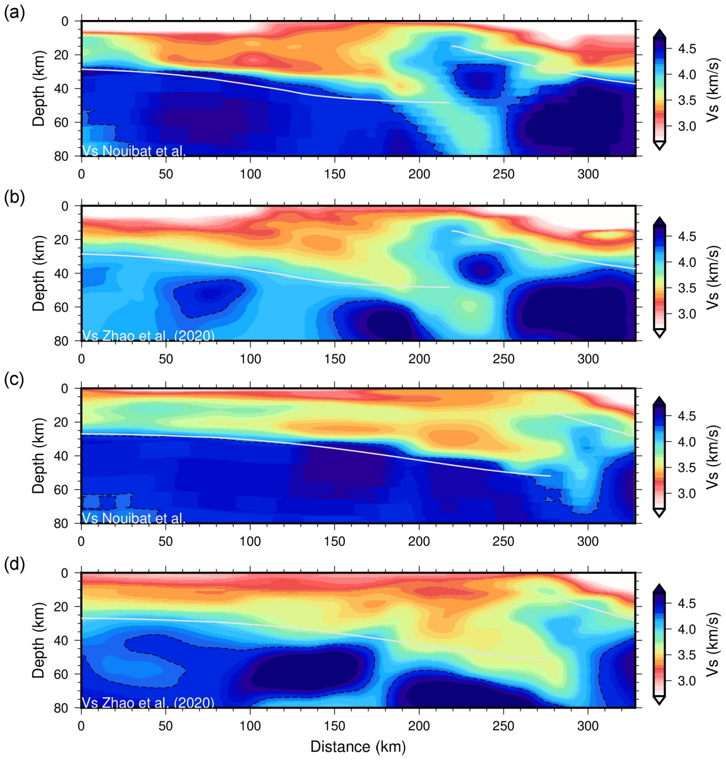

Figure 2.17: Cross sections in our V_s model and in the V_s model of Zhao et al. (2020), along the Cifalps (a, b) and ECORS-CROP (c, d) profiles. The dashed black lines correspond to the 4.3 km/s velocity contour. The thick white lines correspond to Spada et al. (2013)'s Moho depth.

Chapter 3

Model Validation with Receiver Functions of the Cifalps Experiments

This Chapter contains some parts of a published paper (Paul et al., 2022) in *Earth and Planetary Science Letters.* Citation: Paul, A., Malusà, M. G., Solarino, S., Salimbeni, S., Eva, E., Nouibat, A., Pondrelli, S., Aubert, C., Dumont, T., Guillot, S., Schwartz, S., and Zhao, L. (2022). Along-strike variations in the fossil subduction zone of the Western Alps revealed by the CIFALPS seismic experiments and their implications for exhumation of (ultra-) high-pressure rocks. *Earth and Planetary Science Letters*, 598, 117843, `https://doi.org/10.1016/j.epsl.2022.117843`.

This paper compares our ANT V_s model (Nouibat et al., 2022a), presented in Chapter 2, with series of new receiver function (RF) cross-sections across the northern western Alps based on new data from the CIFALPS2 experiment, and fully reprocessed data from the CIFALPS1 experiment. The striking fit between our V_s model and RFs, which are independent seismological data, validates our model in the western Alps, justifying its use to provide 3-D constraints on the deep crustal structure in-between the 2-D profiles. Indeed, Paul et al. (2022) use the 3-D Moho map from our V_s model to further document theses striking and rapid north-south variations in 3-D. Constraining theses variations in 3-D is of primary importance to set up conceptual and quantitative modelling of continental subduction and understand the exhumation mechanisms of (ultra-) high-pressure [(U)HP] rocks.

Contents

3.1 Abstract

In complex plate-boundary settings, a reliable 3-D geophysical characterization of the deep tectonic structure is a fundamental starting point for a breakthrough in the analysis of processes controlling plate subduction and (U)HP rock exhumation. The Western Alps host one of the best-studied fossil subduction zones worldwide, with a well-defined deep structure in 2-D based on recent geophysical experiments. However, a full 3-D characterization of its deep tectonic structure is still lacking. Here we present a series of new receiver function cross-sections across the northern and southern Western Alps, validated and complemented by a S-wave velocity model from ambient-noise tomography that provides additional constraints between the profiles. We document a marked change in Moho attitude from the northern Western Alps, where the eastward-dipping European Moho reaches $\sim$ 45 km depth beneath the Gran Paradiso dome, to the southern Western Alps, where the European Moho reaches $\sim$ 70 km depth beneath the equivalent Dora-Maira dome. This change in Moho attitude takes place over a few tens of kilometers and was likely emphasized by deformation of the slab during subduction. The Western Alps subduction wedge is much thicker in the south than in the north, and the mantle-wedge rocks are deeply involved in orogeny exclusively in the south, where coesite is found in continental (U)HP rocks at several locations. Our detailed information on the 3-D structure of the subduction wedge provides first-order constraints for the next-generation of thermo-mechanical numerical models and may help explain the lateral variations in exhumation style revealed by the geologic record.

Keywords: seismic tomography, continental subduction, exhumation, Western Alps

3.2 Data and Methods

The CIFALPS2 experiment (network code XT; Zhao et al., 2018) includes 55 broadband stations operating for 14 months in 2018–2019, that were roughly aligned along two segments: (i) a WNW-ESE segment from the eastern Massif Central (France) to the region of Ivrea (Italy) across the Bresse Graben, the Jura fold-and-thrust belt, and the northern Western Alps; and (ii) a NNW-SSE segment from the region of Ivrea to the Ligurian coast across the western Po Plain (Fig. 3.1). In this paper, we focus on the WNW-ESE segment of the transect, hereafter referred to as the CIFALPS2 main profile. The main profile is $\sim$ 330 km long and, with additions from the permanent networks (CH, Swiss Seismological Service (SED) At ETH Zurich, 1983; GU, University of Genoa, 1967; IV, INGV Seismological Data Centre, 2006; FR, RESIF, 1995) and AlpArray temporary network (Z3, AlpArray Seismic Network, 2015), includes 43 stations with a dense interstation spacing of 8 km on average. The CIFALPS2 experiment also includes two shorter complementary profiles across the Internal zone of the Western Alps, located to the north (ALP-N, 10 stations) and to the south (ALP-S, 9 stations) of the main profile (Fig. 3.1) (only the main profile is shown in this thesis manuscript).

To image the crustal structure and the Moho beneath the CIFALPS2 main profile, we used the receiver function analysis that enhances P-to-S converted phases at seismic discontinuities in three-component records of teleseismic earthquakes (Vinnik, 1977; Langston, 1979). We took advantage of the dense array of sensors to extract the scattered wavefield for each event, therefore enhancing the quality of receiver functions by applying the multichannel preprocessing approach (Rondenay, 2009; Millet et al., 2019). In regions with complex 3-D structure, this approach is more efficient than the conventional deconvolution of the vertical-component record from the radial-component record (e.g., Zhao et al., 2015). With respect to the conventional Z-R-T processing scheme, it also has the advantage to remove or strongly attenuate the direct P wave at 0 s lag time in the receiver functions, therefore enhancing the converted phases from shallow interfaces.

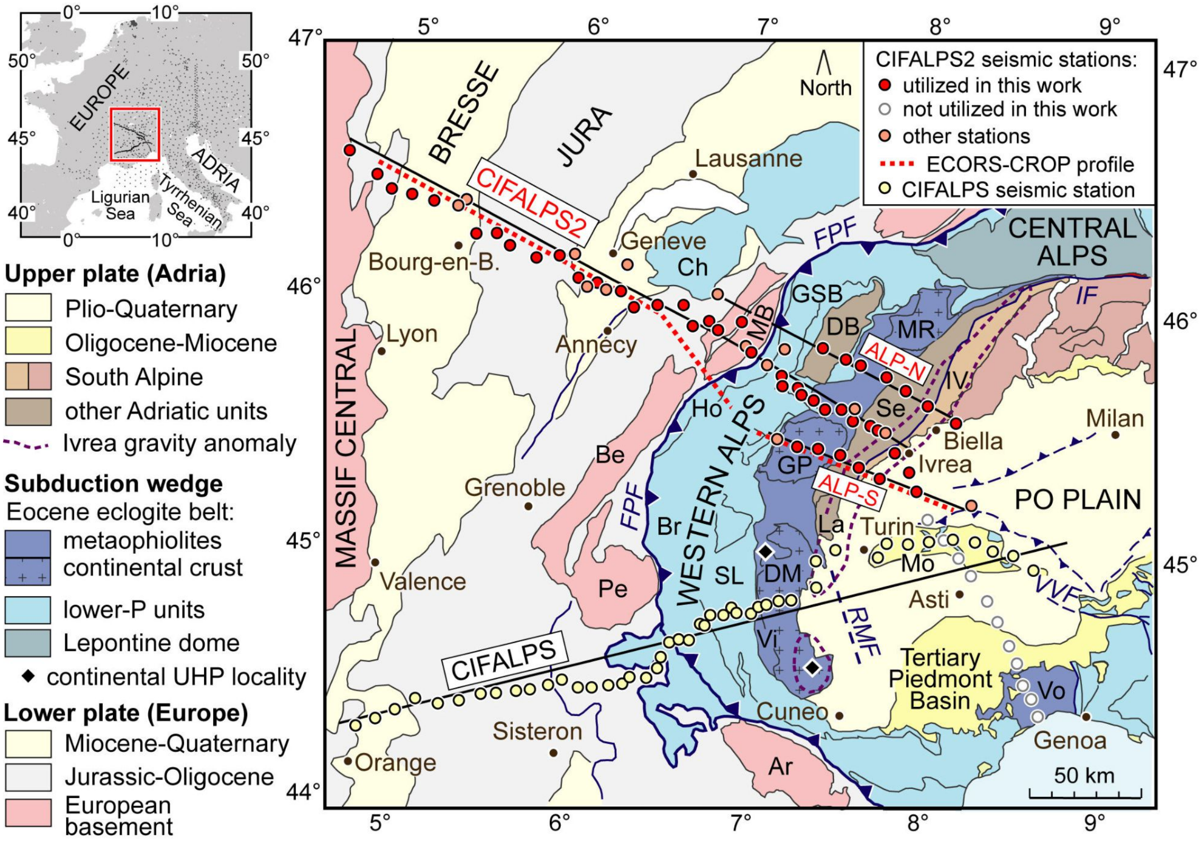

Figure 3.1: Locations of the CIFALPS temporary seismic experiments across the Western Alps. The thick black lines in the map (modified after Malusà et al., 2015) indicate the profiles of Figs. 3.2 and 3.3. The pink dots are seismic stations from other networks used in the receiver function study. The purple dashed line is the 0-mGal contour of the Ivrea gravity anomaly (from Bigi et al., 1990). The dotted red line shows the location of the ECORS-CROP deep seismic sounding reflection section. The grey dots in the top-left inset indicate the seismic stations used in the ambient-noise tomography of Nouibat et al. (2022a). Acronyms: Ar, Argentera; Be, Belledonne; Br, Briançonnais; Ch, Chablais; DB, Dent Blanche; DM, Dora-Maira; FPF, Frontal Pennine Fault; GP, Gran Paradiso; GSB, Grand St-Bernard; Ho, Houiller; IF, Insubric Fault; IV, Ivrea-Verbano; La, Lanzo; MB, Mont Blanc; MR, Monte Rosa; Pe, Pelvoux; RMF, Rivoli-Marene Fault; Se, Sesia-Lanzo; SL, Schistes lustrés; Vi, Viso; Vo, Voltri; VVF, Villalvernia-Varzi Fault. Continental UHP localities (black diamonds) after Chopin (1984) and Manzotti et al. (2022).

After this deconvolution step, we migrated the radial receiver functions to depth using, for each station, the 1-D shear-wave velocity model extracted from the 3-D ambient-noise tomography model of Nouibat et al. (2022a) and a constant V_p/V_s ratio for the crustal part, and the IASP91 Earth model for the mantle part (Kennett and Engdahl, 1991). Finally, we applied the classical common conversion point (CCP) stacking method (Dueker and Sheehan, 1997) to compute depth sections of stacked P-to-S converted phases beneath the main profile of 43 stations. Due to the complex 3-D structure of the Alpine crust, receiver function waveforms are highly variable with the back-azimuth of the incident P wave.

For the southern Western Alps, we re-processed the records of the CIFALPS experiment (Zhao et al., 2016b) using the same scheme, back-azimuth selection, and crustal S-wave velocity model for migration (Nouibat et al., 2022a) that we have adopted for the northern Western Alps (Fig. 3.1). The CCP stacks of the CIFALPS and CIFALPS2 experiments were validated by comparison with a recent ambient-noise tomography study by Nouibat et al. (2022a), a totally independent method that we use to test the reliability of the structural images delineated by receiver function analysis (see details in Figs. 3.2- 3.3 and Sect. 3.3). We consider this comparison between independent methods as a much better proof of reliability of the CCP stacks than any other type of test.

Finally, our receiver function images were interpreted jointly with the P-wave velocity depth sections by Solarino et al. (2018), with data provided by controlled-source seismology (e.g., Cassano et al., 1989; Sénéchal and Thouvenot, 1991), and with the S-wave velocity depth sections by Nouibat et al. (2022a), which also provide additional constraints on the deep structure in-between the profiles.

3.3 Results

3.3.1 CIFALPS2 main profile

Figure 3.2 shows, for the CIFALPS2 main profile and from top to bottom, the Bouguer anomaly from the new pan-Alpine gravity data base of Zahorec et al. (2021), the geological map around the main profile, the interpretive geologic cross-section resulting from the joint interpretation of geological and geophysical constraints (see next section), the CCP stack, the S-wave velocity section through the model of Nouibat et al. (2022a) and the P-wave velocity section through the model of Solarino et al. (2018). Since the ECORS-CROP normal-incidence deep seismic reflection profile (dashed red line in Fig. 3.1) was located close to the CIFALPS2 Alpine section, the interpretation also uses the depth migrated line drawing of ECORS-CROP (Sénéchal and Thouvenot, 1991).

On the lower-plate side of the CIFALPS2 main profile, the CCP stack displays laterally continuous P-to-S (Ps) converted phases of positive polarity and strong amplitude, labelled '1' in Fig. 3.2d. They correspond to the European Moho dipping gently from $\sim$ 25 km depth at the north-western end of the profile to $\sim$ 45 km depth at distance 260 km beneath the Gran Paradiso dome (GP in Fig. 3.2b) and the western tip of the Adriatic upper plate. To delineate the European Moho more precisely, we picked the 4.3 km/s S-wave velocity contour of Fig. 3.2e. This contour matches well the Ps phases of Fig. 3.2d even at depths between 55-65 km and distances between 260-300 km, where the quality of the CCP stack is poorer due to the higher seismic noise in the Po Plain and strong amplitude near-surface multiples (labelled M in Fig. 3.2d). Beneath the Mont Blanc Massif (MB in Fig. 3.2b), the V_s model of Nouibat et al. (2022a) displays the same Moho step as the ambient-noise tomography of Lu et al. (2018).

On the upper-plate side of the profile, the Adriatic Moho is more poorly detected by the receiver functions compared to the European Moho, due to the low signal-to-noise ratio and ringing waves in the poorly consolidated sediments of the Po Plain (label '2' in Fig. 3.2d). It is however clearly imaged by the high-frequency waves of the ECORS-CROP controlled-source seismic section, in close correspondence with the 4.3 km/s V_s contour. In the Adriatic crust, the S-wave velocity contour bounding the bedrock of the Po basin shows a vertical offset (Fig. 3.2d) consistent with backthrusting of the whole Adriatic crust as proposed by previous interpretations of the ECORS-CROP profile (e.g., Roure et al., 1990).

As in the CIFALPS profile (Zhao et al., 2015), the CCP stack shows a set of diffuse negative-polarity Ps converted phases in-between the shallow Adriatic Moho and the deep European Moho beneath the subduction wedge and the tip of the upper plate (label '3' in Fig. 3.2d). These negative-polarity signals outline a steeply southeast-dipping interface that intersects the surface at the Frontal Pennine Fault (FPF in Fig. 3.2b), which is the structural boundary separating the metamorphic units of the Alpine subduction wedge in the east from the unmetamorphosed rocks of the European lower plate in the west. The V_s model shows that this dipping boundary corresponds, in the 20-40 km depth range, to a 10-15 km thick zone of diffuse velocity decrease with depth, between the rather high seismic velocities of the subduction wedge and overlying serpentinized mantle wedge above ($\sim$ 3.7-3.8 km/s), and the weaker velocities of the European crust below ($\sim$ 3.5 km/s).

In the European crust, we recognized four sets of Ps converted phases labelled '4' to '7' in Fig. 3.2d. These interfaces closely correspond to velocity changes in the S-wave velocity section of Fig. 3.2e. The shallow positive-polarity conversion labelled '4' coincides with the strong velocity increase at the base of the Mesozoic cover of the Jura and Subalpine chains. The sharp positive and negative polarity converted phases labelled '5' and '6' bound a high-velocity body ($V_s \sim 3.7$ km/s) in the mid-crust (7-15 km depth) beneath the Bresse Graben, also extending beneath the western Jura fold-and-thrust belt to the east and the Massif Central to the west. The laterally discontinuous negative-polarity conversion labelled '7' is near-parallel to the European Moho and marks the top of two low-V_s anomalies (minimum 3.3 km/s) located in the European lower crust on both sides of the previously mentioned Moho step. The lateral change in polarity of converted phases in Fig. 3.2d coincides with the zone of slightly higher V_s that separates the two anomalies right above the Moho step.

3.3.2 Re-processed CIFALPS profile

Figure 3.3 shows the same information as Fig. 3.2 for the re-processed CIFALPS transect located farther south in the southern Western Alps. The improved CCP section of Fig. 3.3d enhances the converted phases from shallow interfaces and, when compared to the original analysis by Zhao et al. (2015), provides further information on the lithospheric structure of both the Adriatic and European plates, whereas no major improvement is introduced for the subduction wedge (Malusà et al., 2021). This information is consistent with indications provided by the V_s model of Fig. 3.3e and by controlled-source seismic data in the Po Plain (e.g., Cassano et al., 1989).

As shown in Fig. 3.3d-e, the European Moho along the CIFALPS profile (label '1') is better constrained at depth $>$ 45 km by the 4.3 km/s V_s contour (Fig. 3.3e) rather than by the low-amplitude Ps conversions of the CCP section (Fig. 3.3d), like what is observed in the ALP-S complementary profile. The Moho dip angle is steeper than in the CIFALPS2 section

(Fig. 3.2d-e) and, at depths > 60 km, is likely steeper than suggested by the previous CIFALPS studies (e.g., Zhao et al., 2015; Beller et al., 2018). The low amplitudes of the Ps conversions are coherent with the weak velocity gradient shown by the V_s section between the subducted, possibly eclogitized European lower crust and the underlying lithospheric mantle. The Ps conversions marking the Adriatic Moho (label '2' in Fig. 3.3d-e) are offset by faults already described in previous work (Zhao et al., 2015; Malusà et al., 2017; Solarino et al., 2018) and fully consistent with undulations of the S-wave velocity contours (Fig. 3.3e). Integration with information provided by the V_s model allows us to trace these faults at even greater depths in the Adriatic mantle lithosphere compared to previous studies. The set of negative-polarity Ps phases labelled '3' in Fig. 3.3d is more diffuse with weaker amplitudes than in Fig. 3.2d, probably due to the presence of a thicker subduction channel along the CIFALPS profile (Zhao et al., 2020) and a weak velocity contrast with the partly serpentinized Adriatic mantle on its top (Fig. 3.3e). Above this set of negative-polarity phases, the P-wave velocity contour 6.7 km/s in Fig. 3.3f was interpreted by Solarino et al. (2018) as marking the upper and western boundary of a serpentinized mantle body located underneath the (U)HP rocks of the Dora-Maira dome (DM in Fig. 3.3c). This velocity boundary crosscuts the V_s contours of Fig. 3.3e at a high angle, leaving out the western tip of a high-V_s body ($V_s = 3.8$-4.15 km/s) at 15-30 km depth (marked by a star in Fig. 3.3e-f) that shows rather low, more crust-like P-wave velocities ($V_p = 5.9$-6.4 km/s).

In the Adriatic crust, the base of the Oligocene-to-Quaternary sediments of the Tertiary Piedmont Basin and western Po Plain can be delineated as a set of positive-polarity Ps conversions (label '4' in Fig. 3.3d) that correspond to the V_s structure in Fig. 3.3e. Farther east, the Monferrato frontal thrust is marked by a set of south-dipping negative-polarity Ps conversions (label '5' in Fig. 3.3d) consistent with evidence from available seismic-reflection profiles (e.g., Cassano et al., 1989). These negative-polarity Ps conversions show a step along the Villalvernia-Varzi Fault (VVF in Fig. 3.3), consistent with the Neogene activity of the fault.

In the western side of the CIFALPS profile, the European crust includes, similar to CIFALPS2, a strong low-V_s anomaly (minimum 3.2 km/s) located beneath the Subalpine Chains, bounded on top by a set of sharp negative-polarity Ps conversions labelled '6' in Figs. 3.3d-e. The crust beneath the Rhône Valley shows rather high S-wave velocities, similar to the Bresse Graben in the CIFALPS2 section.

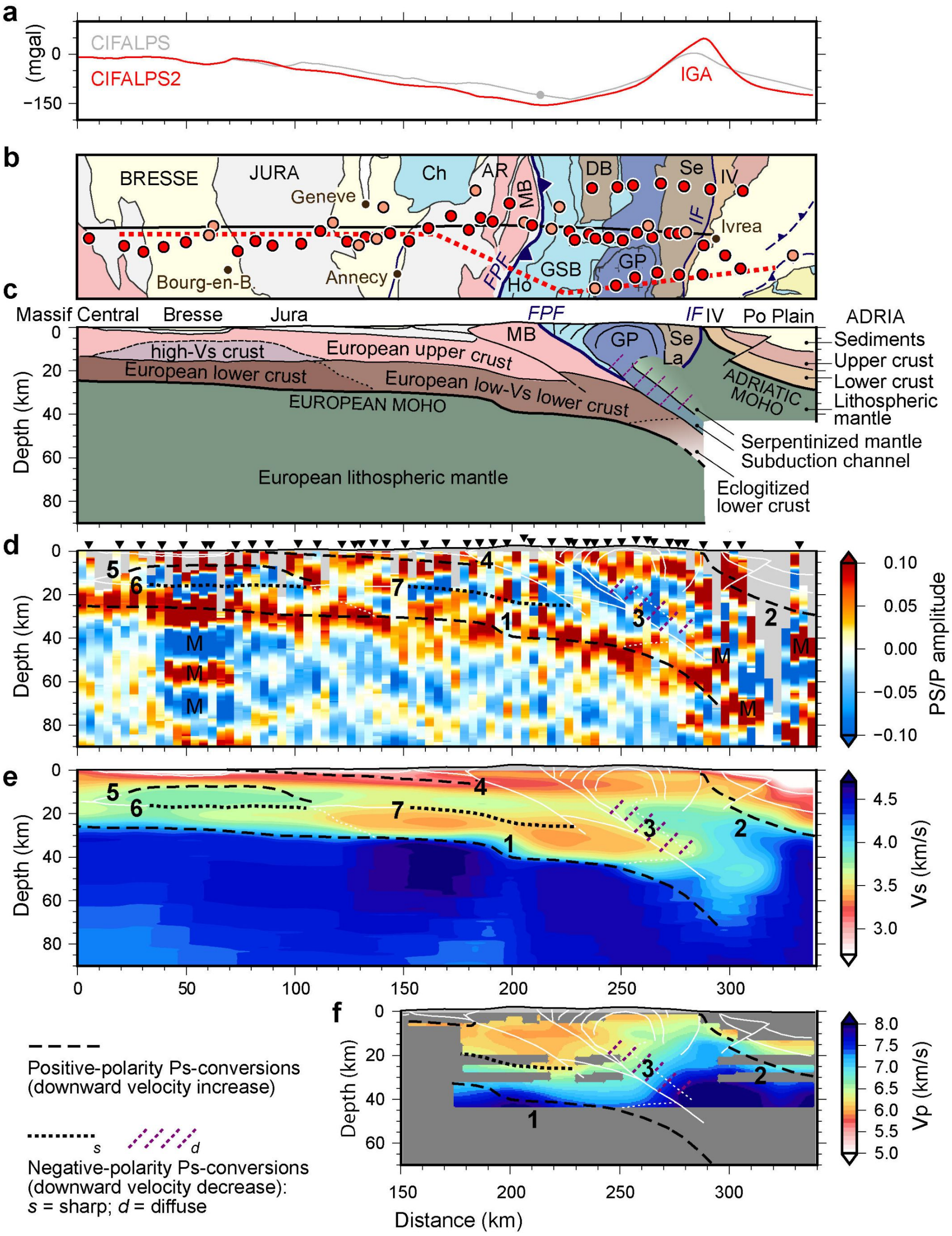

Figure 3.2: Depth sections along the CIFALPS2 main profile across the northern Western Alps. a: Bouguer anomaly from the gravity database of Zahorec et al. (2021) (in red); IGA: Ivrea gravity anomaly. The Bouguer anomaly along the CIFALPS profile is shown for comparison (in grey; the grey dot indicates the Frontal Pennine Fault). b: Geological map around the main profile (black line), see Fig. 3.1 for location and acronyms. c: Interpretive geologic cross-section. d: CCP stacked section for teleseismic earthquakes of 0-100° back-azimuth, with labels and dashed black lines (for positive-polarity Ps conversions and downward velocity decrease) or dotted black or purple lines (for negative-polarity Ps conversions and downward velocity increase) outlining the main features discussed in the text (labels 1-7). M: multiples. e: V_s section from Nouibat et al. (2022a) used for time-to-depth migration of the CCP stack ($V_p/V_s = 1.8$). f: V_p section from the local earthquake tomography of Solarino et al. (2018). Note the consistency between interfaces identified by independent methods in (d) and (e).

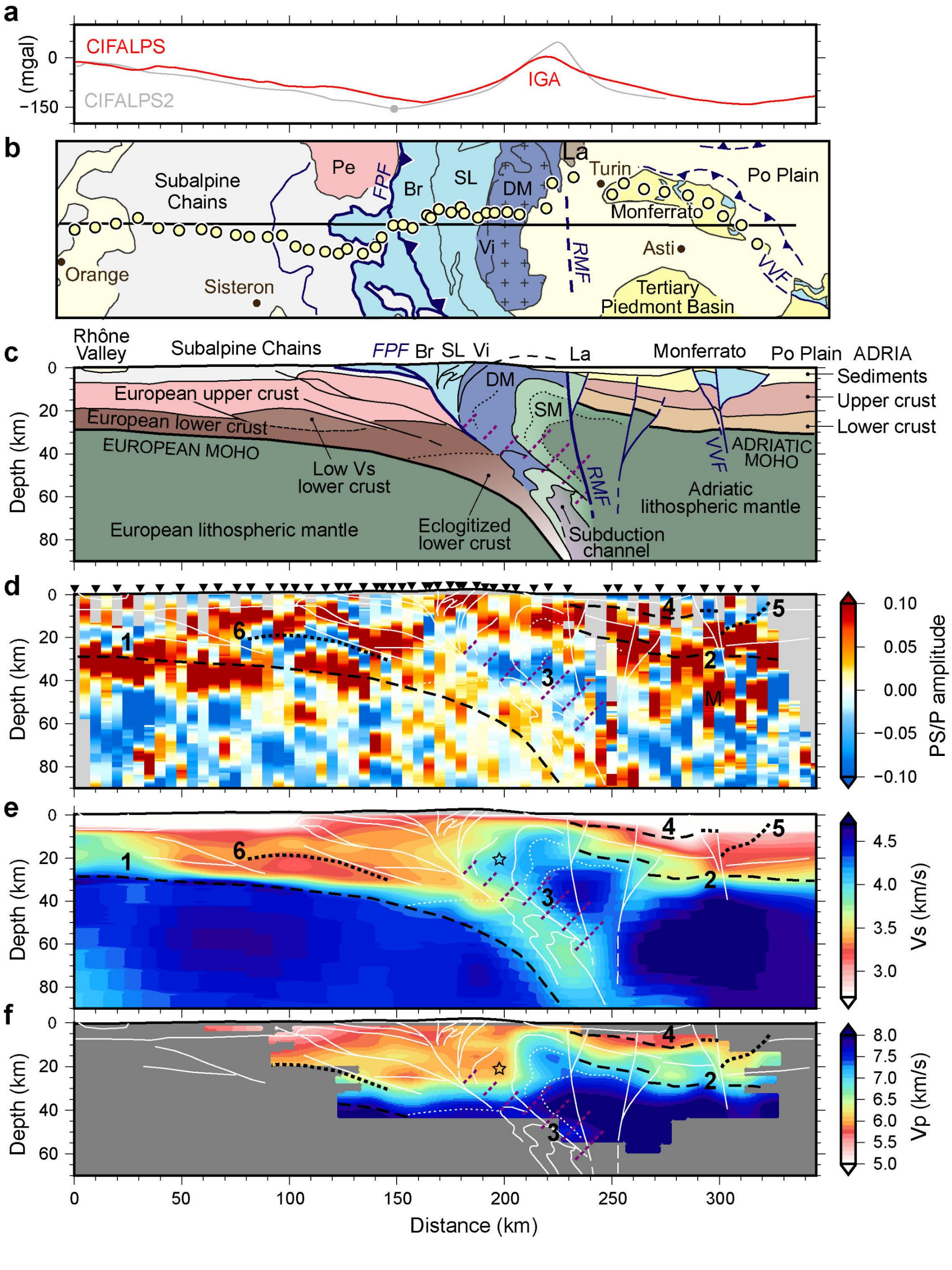

Figure 3.3: Depth sections along the CIFALPS profile across the southern Western Alps (same keys as Fig. 3.2). a: Bouguer anomaly (Zahorec et al., 2021) (in red). The Bouguer anomaly along the CIFALPS2 profile is shown for comparison (in grey; the grey dot indicates the Frontal Pennine Fault). b: Geological map. c: Interpretive geologic cross-section (modified after Malusà et al., 2021); d: CCP receiver-function stack (computed with $V_p/V_s = 1.7$). e: V_s section (Nouibat et al., 2022a). f: V_p section (Solarino et al., 2018). Labels 1-6 and the region marked by a star are discussed in the text. Note the consistency between interfaces identified by independent methods in (d) and (e).

3.4 Interpretation and discussion

3.4.1 CIFALPS2 vs CIFALPS geologic cross-sections

The new crustal-scale geological cross-section of the northern Western Alps along the CIFALPS2 main profile has some similarities with the previously proposed cross-section of the southern Western Alps (CIFALPS experiment, see Malusà et al., 2021), but also some major differences (cf. Fig. 3.2c and Fig. 3.3c). Along the CIFALPS2 profile, the uppermost 20-25 km of the European lower plate consists of a mainly granitic upper crust and associated sedimentary cover (Fig. 3.2c). To the east of the Jura fold-and-thrust belt, these upper crustal rocks rest on top of a relatively homogeneous lower crust with low S-wave velocities, reaching 3.3 km/s and detected as far east as underneath the Gran Paradiso dome. Such low S-wave velocities are not consistent with granulitic rocks of felsic to intermediate composition, which have been suggested for the European lower crust along the CIFALPS profile (Solarino et al., 2018). Instead, they are more consistent with V_s values expected for remnants of the Paleozoic Saxo-Turingian suture zone inherited from the Variscan orogeny (e.g., Guillot et al., 2009) and later involved in the Alpine orogeny. Notably, smaller volumes of low-V_s rocks at lower-crustal depths are also revealed along the CIFALPS section beneath the Subalpine Chains (Fig. 3.3e), to the west of a region characterized by felsic-intermediate granulitic rocks. This suggests that relics of this Variscan suture zone are also present to the west of the External massifs, where they were not previously detected because they are masked by Jurassic-Oligocene sedimentary successions. This Variscan suture zone was possibly involved obliquely into the Western Alps subduction zone, and to a greater extent in the north than in the south, which is consistent with the Variscan paleogeography (Guillot et al., 2009). Variscan inheritance is also evidenced by the presence of a Moho step detected beneath the Mont Blanc (Fig. 3.2c) and previously imaged by Lu et al. (2018) and Zhao et al. (2020) in their tomography models. The Moho step is parallel to the surface trace of the Eastern Variscan Shear Zone recognized as a major lithospheric fault active between 320 and 250 Ma (Guillot et al., 2009) and reactivated during the Alpine orogeny. However, no Variscan inheritance is expected deeper in the mantle.

At depths > 40 km beneath the Alpine subduction wedge, the European lower crust is likely eclogitized (Fig. 3.2c), in line with predicted pressures (> 1.2 GPa) and temperatures (> 400°C) in that region of the crust, but it is still seismically distinguishable from the underlying mantle lithosphere (Fig. 3.2d-e). No earthquake is associated to this eclogitized lower crust (Eva et al., 2020) because the subduction zone is fossil and has been inactive for a long time. On the western side of the profile, the high V_s (~ 3.7 km/s) crust detected from 7-15 km depth beneath the Bresse Graben, and also extending under the western Jura to the east and the Massif Central to the west (Fig. 3.2c), is likely related to the late Eocene-Oligocene activation of the Cenozoic Rift System of Central Europe (Ziegler, 1992; Sissingh, 2001), which mainly post-dates (U)HP rock exhumation in the Western Alps.

In the northern Western Alps, the eastward-dipping European Moho is located at 25-35 km depth beneath the External zone to the west of the Moho step, reaching $\sim$ 40 km depth underneath the Frontal Pennine Fault and $\sim$ 45 km depth beneath the centre of the Gran Paradiso dome. It is less steep than in the southern Western Alps, where the Moho shows a more continuous profile without steps from $\sim$ 40 km depth beneath the Frontal Pennine Fault to $\sim$ 70 km depth beneath the core of the Dora-Maira dome (Fig. 3.3c). A comparison between the CIFALPS2 main profile and the ALP-N and ALPS-S complementary profiles (Fig. 3.3), located $\sim$ 20 km to the north and south of the CIFALPS2 main profile, respectively, reveals that the change in European-Moho dip angle takes place over a distance of a few tens of kilometers around the city of Ivrea.

The eastward-dipping Adriatic Moho is located close to the Earth's surface near Ivrea, and at $\sim$ 30 km depth farther east, in front of the Monferrato (Fig. 3.2c). In the Ivrea region, the high-density peridotites of the Adriatic mantle, together with amphibolites of the Sesia-Lanzo unit and lower crustal rocks of the Ivrea-Verbano zone (Scarponi et al., 2020), induce a stronger and narrower Bouguer anomaly than in the south (IGA in Fig. 3.2a), where the lower but broader positive anomaly (IGA in Fig. 3.3a) is mostly induced by a deeper ($\sim$ 10 km depth) body of serpentinized mantle rocks located beneath the Dora-Maira dome (SM in Fig. 3.3c). These observations suggest that the Ivrea gravity anomaly probably has different causes in the northern Western Alps than in the southern Western Alps. The gravity anomalies documented by the pan-Alpine surface-gravity database of Zahorec et al. (2021) also show along-strike variations on the lower-plate side of the orogen (Figs. 3.2a and 3.4a). In the External zone of the Western Alps, the negative anomaly is more pronounced along the CIFALPS2 profile (red line in Fig. 3.2a) than along the CIFALPS profile (grey line in Fig. 3.2a), while the less steep European Moho would result in a less pronounced negative anomaly in the northern Western Alps than in the southern Western Alps. This negative anomaly matches and possibly reflects the distribution of low-V_s lower-crustal rocks of the previously mentioned Variscan suture zones. Further gravity modelling, which is beyond the aims of this paper, would help confirming such hypothesis and may provide further support to the geologic interpretation of the CIFALPS2 profile shown in Fig. 3.2c.

The high-velocity seismic body located above interface '3' in Fig. 3.3e and referred to as 'Adria seismic body' by Nouibat et al. (2022a), was already detected in the V_p model by Solarino et al. (2018) (Fig. 3.3f) and included in previous interpretations of the CIFALPS profile. However, the V_s model by Nouibat et al. (2022a) allows tracing near-vertical faults located to the east of the Rivoli-Marene Fault down to the lithospheric mantle. These strike-slip faults, like the thrust faults underneath the External massifs, were active for a long time after the exhumation of the subduction wedge (Malusà et al., 2017; Eva et al., 2020), and a reconstruction of their original structure should be applied for a proper analysis of the late Eocene dynamics of the subduction zone. The along-strike variations in European-Moho attitude revealed by the CIFALPS experiments have major implications for the structure and evolution of the overlying subduction wedge, which is much smaller in the northern Western Alps (Fig. 3.2c) than in the southern Western Alps (Fig. 3.3c). Also, mantle-wedge rocks are less involved in the orogeny in the north than in the south. Along the CIFALPS2 profile, we interpret the set of diffuse negative-polarity Ps converted phases beneath the Gran Paradiso dome as a progressive velocity change between subducted European crustal rocks and the overlying serpentinized mantle-wedge rocks (Fig. 3.2c). However, no large body of partly serpentinized mantle-wedge rocks is imaged beneath the Gran Paradiso dome, unlike beneath the Dora-Maira dome. Another major difference is highlighted at the level of the subduction channel, because a thick body of subduction-channel serpentinites and metasomatized mantle peridotites was suggested for the CIFALPS seismic images in the southern Western Alps (Zhao et al., 2020; Malusà et al., 2021), whereas no evidence of a thick and partly exhumed subduction channel has been imaged along the CIFALPS2 profile.

3.4.2 Lateral Moho variations and relations with the slab structure.

Our analysis reveals that the north-south change in the geometry of the subduction wedge is significant between profiles that are only ~ 20 km apart. We further investigate the sharpness of this change by mapping the depth of a Moho proxy, that is the iso-velocity surface $Vs =$ 4.3 km/s in Fig. 3.4a, taking benefit of the 3-D V_s model of Nouibat et al. (2022a). According to Figs. 3.2-3.3, this surface is a good proxy of the European Moho and a correct proxy for the Adriatic Moho at some distance from the subduction wedge. Close to the subduction wedge, the Adriatic Moho is shallower than the 4.3 km/s V_s contour, for example because of the serpentinization of upper-mantle peridotites (black dotted area in Fig. 3.4a). The western boundary of the Adriatic upper plate in the northern Western Alps is marked by the Ivrea gravity anomaly (red dashed line in Fig. 3.4a).

This Moho proxy depth map highlights the strong and sharp lateral changes in the deep structure of the Western Alps, confirming what is revealed by receiver function analysis (Figs. 3.2-3.3). The European Moho reaches very large depth (≥ 70 km, dark blue color in Fig. 3.4a) almost only in the region between our two profiles, from CIFALPS2 in the north to ~ 20 km south of CIFALPS in the south. The European Moho is affected by a major step, outlined by purple arrows in Fig. 3.4a, which is almost aligned with the Mont Blanc and Belledonne external massifs. The yellow arrows mark instead the region with the strongest along-strike change in European Moho attitude, which is located to the south of the Gran Paradiso dome and oriented ENE-WSW. The shallow body of $V_s > 4.3$ km/s (yellow star in Fig. 3.4a) that is crosscut by the CIFALPS profile and interpreted as dry Adriatic mantle in Fig. 3.3c, has a very small size of $\sim 20 \times 40$ km^2 and is exclusively located to the east of the Dora-Maira dome, within the region showing the deepest European Moho. This high-velocity body is clearly crosscut, in map view, by the Rivoli-Marene Fault (RMF in Fig. 3.4a), which marks the western boundary of the Adriatic upper plate in the southern Western Alps, in agreement with the interpretive geologic cross-section of Fig. 3.3c.

The ENE-WSW change in European Moho attitude shown in the map, when plotted on a 100-km depth slice of the P-wave velocity perturbation model of Zhao et al. (2016a) (black arrows in Fig. 3.4b) is aligned with a major bend in the high velocity anomaly interpreted as the European slab (dark blue colors in Fig. 3.4b). This suggests that the observed depression in the European Moho could be a response to slab bending, which was likely promoted by the Cenozoic northward motion and indentation of the Adriatic upper plate before (U)HP rock exhumation (Fig. 3.4c). We exclude any potential change in European Moho attitude due to European slab breakoff after (U)HP rock exhumation, because recent tomography models of the Alpine region (e.g., Zhao et al., 2016a; Rappisi et al., 2022) document a continuous and undetached slab beneath the Western Alps (see discussion in Malusà et al., 2021).

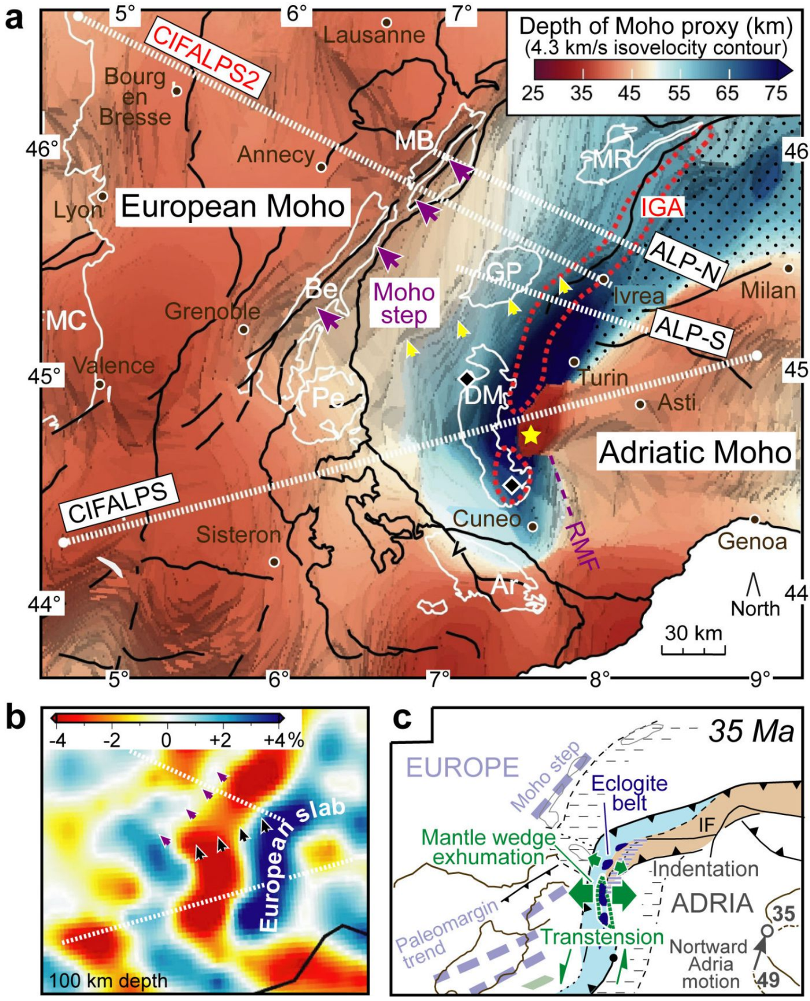

Figure 3.4: Along-strike Moho variations and relations with the slab structure. a: Analyzed profiles on a Moho-proxy depth map based on the S-wave velocity model by Nouibat et al. (2022a), where the iso-velocity surface $V_s = 4.3$ km/s is considered as the best proxy for the European Moho. Geologic boundaries (thin white lines) and major faults (black lines) are also shown for reference (same acronyms as Fig. 3.1; MC: Massif Central). Black dots mark the area where the Adriatic Moho lays at shallower levels than $V_s = 4.3$ km/s (e.g., due to serpentinization of the uppermost mantle, see main text and Figs. 3.2 and 3.3 for details). Purple arrows: inherited Moho step in the lower plate (Lu et al., 2018). Yellow arrows: region with the strongest along-strike change in Moho attitude. Yellow star: mantle-lithosphere dry peridotite at shallow depth. Black diamonds: continental UHP localities (Chopin, 1984; Manzotti et al., 2022). Dotted red line: 0-mGal contour of the Ivrea gravity anomaly (IGA, from Bigi et al., 1990). b: Upper mantle depth slice of the P-wave velocity perturbation model of Zhao et al. (2016a) (depth 100 km; same region as (a)). The strongest along-strike change in Moho attitude (black arrows) is aligned with a major bend in the European slab (dark blue colors in the model). c: Palinspastic reconstruction of the Alpine subduction zone at 35 Ma, showing the indentation of Adriatic lithosphere in the Central Alps and consequent transtension in the Western Alps leading to (U)HP rock and mantle-wedge exhumation. The exhumed mantle wedge of the southern Western Alps (in green) is juxtaposed against previously exhumed mantle rocks at the tip of the Adriatic upper plate (horizontal lilac lines). The grey arrow indicates Adria-Europe relative plate motion (after Malusà et al., 2021).

Chapter 4

Ambient Noise Tomography of the Ligurian-Provence Basin

This Chapter is a published paper in *Journal of Geophysical Research.* Citation: Nouibat, A., Stehly, L., Paul, A., Schwartz, S., Rolland, Y., Dumont, T., Crawford, W., Brossier, R., Team, C., and Group, A. W. (2022b). Ambient-noise tomography of the Ligurian-Provence basin using the AlpArray onshore-offshore network: Insights for the oceanic domain structure. *Journal of Geophysical Research*: Solid Earth, 127(8), e2022JB024228, `https://doi.org/10.1029/2022JB024228`.

In Chapter 2, we showed how high-quality ambient-noise correlations between onshore stations were used in a Bayesian inversion procedure to derive a large-scale V_s model, covering the Alpine belt (Nouibat et al., 2022a). The robustness of this model was emphasised in Chapter 3, through comparison with independent data in the western Alps (Paul et al., 2022). In the present Chapter, we aim to take use of the ocean-bottom-seismometers (OBSs) of AlpArray to extend the 3-D model to the Ligurian sea. However, the use of OBSs in ambient noise imaging is a challenging topic. OBS noise recordings are affected by different type of long-period noises – electronic transients (e.g., glitches) and infra-gravity waves, seafloor currents induced noises (compliance, tilt). Furthermore, OBS-OBS first order correlations (or C^1s) are of lower quality than onshore correlations, thus limiting the number of dispersion measurements to be used for the 2-D inversion and therefore the coverage of the V_s model a posteriori. Finally the water column above the OBSs – often not taken intro account in the inversion at depth for V_s – may have a considerable influence on the short-period component of the local dispersion curves.

We present a self-consistent ambient-noise tomography procedure for oceanic imaging with OBS data. This procedure includes a pre-processing step to correct the OBS continuous records from the transients and the seabed-induced noises. The second step consists on computing iterative correlations (or C^2s) between the OBSs to enhance the seismic coverage in the marine part. Then, similar to Nouibat et al. (2022a), the 3-D V_s model is derived using a transdimensionnal 2-D inversion for group-velocities followed by a probabilistic inversion for V_s at depth. In the inversion at depth, the water column is accounted for in the oceanic domain. This complete procedure is applied successfully in the Ligurian Sea by combining onshore stations and OBSs. The V_s model, validated by controlled-source seismic data, provides new insights into the 3-D architecture of the oceanic crust in the Ligurian-Provence basin.

Summary

The Ligurian-Provence basin (Northwestern Mediterranean Sea) is one of the Miocene-Pliocene back-arc basins that resulted from the retreat of the Adria subduction in the plate reorganization due to Africa-Europe convergence. The crustal structure of the basin is still debated, even though it has been probed by active seismic profiling. We derive a three-dimensional shear-wave velocity model of the Ligurian-Provence back-arc basin (Northwestern Mediterranean Sea) using ocean-bottom seismometers (AlpArray OBSs) and land stations from permanent and temporary seismic networks. The quality of OBS continuous records is enhanced by a specific processing that reduces instrumental and seabed-induced noises (transients, tilt, compliance). To further improve the resolution of ambient-noise tomography in the offshore area, we compute the Rayleigh-wave part of the Green functions for OBS-OBS pairs by using onshore stations as virtual sources. 2-D group-velocity maps and their uncertainties are computed in the 4 - 150 s period range by a transdimensional inversion of Rayleigh-wave travel times. The dispersion data and their uncertainties are inverted for a probabilistic 3-D shear-wave velocity model that includes probability densities for V_s and for the depth of layer interfaces. The probabilistic model is refined by a linearized inversion that accounts for the water layer in the Ligurian Sea. Our S-wave velocity and layer boundary probability models correspond well to a recent, high-resolution P-wave velocity cross-section derived from controlled-source seismic profiling along the Ligurian-Provence basin axis. A joint interpretation of the P- and S-wave velocity sections along this profile reveals a thin, anomalous oceanic crust of low P-wave velocities but high S-wave velocities, intruded by a gabbroic body. The illuminated part of the upper mantle appears to be devoid of serpentinization.

keypoints:

- Efficient processing scheme to remove transients and reduce tilt and compliance from continuous ambient noise recorded by OBSs
- Computation of iterative correlations between OBSs based on a virtual reconstruction of the Rayleigh waves
- Thin, anomalous oceanic crust with gabbroic intrusions evidenced in the basin axis from a joint interpretation of V_s and V_p models

Contents

4.1 Introduction

In the last two decades, the deployment of extensive and dense seismic networks of temporary broadband sensors (e.g., USArray, IberArray) has provided a better understanding of the deep structures of the crust and upper mantle, in particular through the emergence of increasingly more precise 3-D seismic imaging (e.g., Moschetti et al., 2010; Levander et al., 2011). However, many of these dense arrays included exclusively onshore sensors, thus preventing 3-D imaging of continent-ocean transitions and oceanic domains. The AlpArray seismic network (AASN) that covers the European Alps and their foreland, is one of the few dense seismic networks consisting of both onshore and offshore stations (Fig. 4.1; Hetényi et al., 2018). The onshore AASN has been used in ambient-noise imaging studies at the scale of the Alps and Apennines to construct 3-D models of shear-wave velocity (Lu et al., 2018, 2020), attenuation (coda-Q, Soergel et al., 2020), and radial anisotropy (Alder et al., 2021), as well as at the regional scale, e.g., Vienna basin (Schippkus et al., 2018), Western Alps (Zhao et al., 2020), Southeastern Alps (Sadeghi-Bagherabadi et al., 2021) and Bohemian Massif (Kvapil et al., 2021). The German-French ocean-bottom seismometers (OBS) of the AlpArray network have been deployed to gain insights into the 3-D structure of the lithosphere beneath the Ligurian-Provence basin and its margins, where major geological/geodynamical issues remain to be clarified. The OBS recordings have been used together with data of onshore permanent and temporary stations in the transdimensional ambient-noise tomography of Nouibat et al. (2022a) that covers a large part of Western Europe. In Nouibat et al. (2022a), we described the probabilistic inversion strategy for Rayleigh-wave group-velocity maps and their uncertainties, the injection of these uncertainties in the inversion for the V_s model, and the validity of the model in the southwestern Alps. The present paper is a complement to Nouibat et al. (2022a) that focuses on the Ligurian-Provence basin. We describe here the specific processing of OBS records and the use of iterative noise correlations that are required to improve ray coverage in the Ligurian Sea, hence improving the model resolution in the basin. We further explain how the water layer and its thickness changes are taken into account in the inversion for S-wave velocity. Finally, we compare our V_s model to a V_p section derived from controlled-source seismic profiling along the basin axis.

The geodynamic context of the western Mediterranean region is controlled by the northward motion of Africa (1 cm/yr) with respect to Europe since Late Cretaceous times (Fig. 4.1). This global convergence was accommodated by several collision episodes involving Europe with continental micro-plates (Iberia and Adria), leading to the formation of peri-mediterranean mountain belts (Alps, Apennines, Pyrenees, Dinarides and Betics; e.g., van Hinsbergen et al., 2020). During Miocene and Pliocene times, part of this convergence was accommodated by development of back-arc extensional basins behind the Adria northwest-dipping subduction zone (e.g., Gueguen et al., 1998; Jolivet et al., 2020). This extension started in the Ligurian-Provence basin, and has further spread from west to east, resulting in the opening of the Algerian basin, and later, of the Tyrrhenian basin (e.g., Séranne, 1999; Rollet et al., 2002). Crustal thinning in the central Ligurian basin resulted in the formation of a narrow oceanic domain mainly identified from geophysical data, including seismic reflection, refraction and wide-angle profiling (e.g., Egger et al., 1988; Déverchère and Beslier, 1995; Dannowski et al., 2020), altimetry data and magnetic data from aeromagnetic surveys and reduction to the pole (Sandwell et al., 1995). Although the crust of the central Ligurian basin is considered 'atypical' because it is thinner than normal oceanic crust and highlights non-linear magnetic anomalies and a concomitant low gravity anomaly (Bayer et al., 1973; Sandwell and Smith, 1997; Rollet et al., 2002), its petrological and lithological nature is poorly constrained and still debated. Several hypotheses have been considered: (1) thin oceanic crust with tholeitic volcanism overlying mantle rocks, similar to the Tyrrhenian sea (e.g., Mascle and Rehault, 1990; Bonatti et al., 1990); (2) partly serpentinized peridotites of exhumed upper mantle mostly devoid of volcanic crust (e.g., Boillot et al., 1989; Beslier et al., 1993; Jolivet et al., 2020); (3) thinned and stretched continental crust related to an hyper-extended margin (e.g., McKenzie, 1978; Pascal et al., 1993; Dannowski et al., 2020).

We combine the OBS records of the AlpArray network with those of 890 onshore stations from the AlpArray temporary network, the Cifalps-2 temporary experiment and European permanent networks (Fig. 4.1). Ambient-noise data recorded by OBSs have already been used to build shear-wave velocity and anisotropy models in different regions, e.g., South-central Pacific (Harmon et al., 2007), Southeast of Tahiti Island (Takeo et al., 2016) and Western Indian Ocean (Hable et al., 2019). The originality of our approach lies in the specific processing of OBS records and their use within an innovative tomographic framework based on data-driven Bayesian inversions, which has recently been successfully applied to image the lithosphere at the scale of Western Europe (Nouibat et al., 2022a). Specific and careful pre-processing of OBS records is compulsory because they are affected by noise sources at the seabed such as compliance and tilting, and they may also be impacted by intrinsic instrumental noise (Crawford et al., 1998; Crawford and Webb, 2000; Deen et al., 2017). Furthermore, OBSs are sensitive to local noise sources such as tides and currents, boat traffic, or marine animals, which are not recorded coherently over long distances (e.g., Batsi et al., 2019). Such noises are therefore unsuitable for ambient-noise tomography, and they even alter the signal-to-noise ratio of surface waves reconstructed by noise correlation. Finally, the water column above the seismometers (water depth of 1100 - 2800 m in our case) may have a significant impact on the quality of the Rayleigh-wave dispersion measurements between distant OBSs, particularly at periods shorter than 15 s. Wolf et al. (2021) have highlighted the difficulties in using the AASN OBSs to measure Rayleigh waves dispersion curves from noise correlations. These difficulties are partly related to the high level of sea-floor noises. To overcome these difficulties, we propose an innovative way of computing seismic noise correlations using OBS data that consist (1) in a pre-processing of the OBSs noise records that decrease efficiently the seabed noise, and (2) in computing iteratively noise correlations between OBS stations using onshore stations as virtual sources.

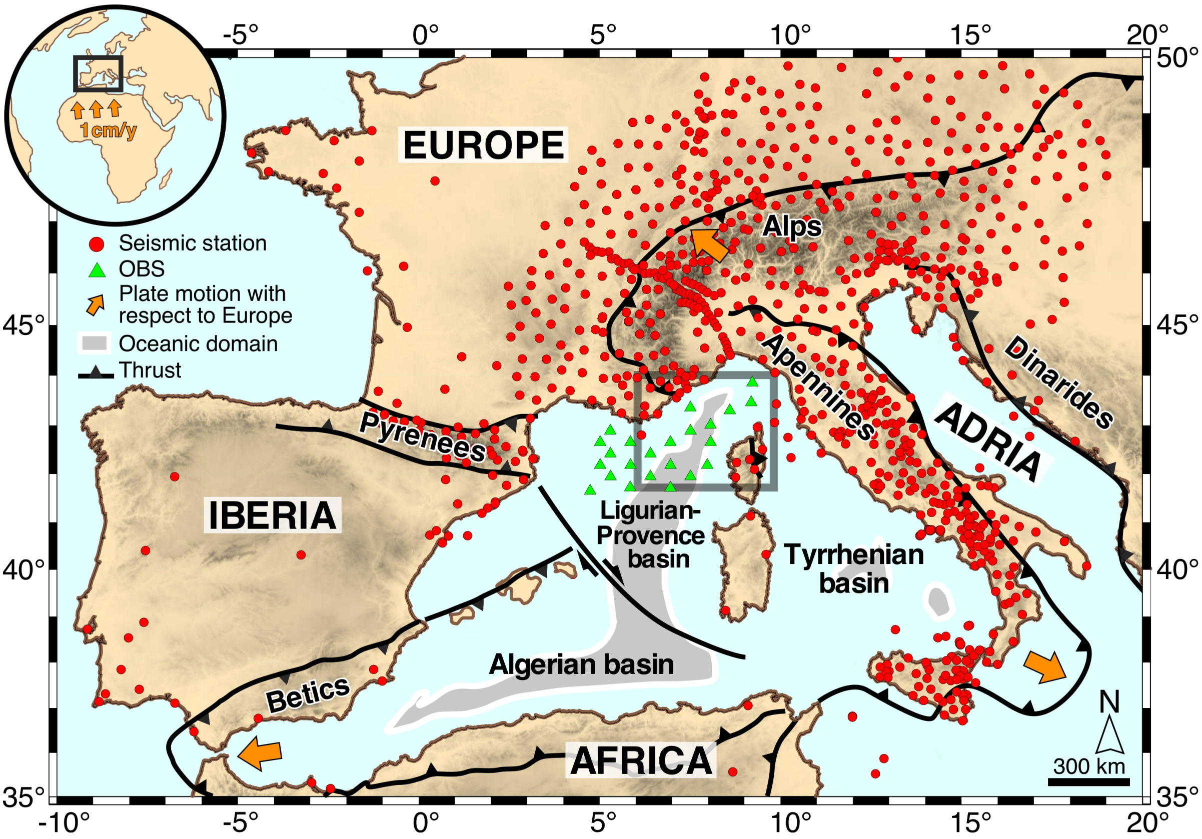

Figure 4.1: Tectonic map of the western Mediterranean region (modified from Faccenna et al., 2014; Jolivet et al., 2020) with locations of seismic stations used in this work (red circles: onshore sensors; green triangles: AASN OBS). The oceanic domains of the Ligurian-Provence, Algerian and Tyrrhenian back-arc basins are filled with gray color. The gray frame shows the location of the map in Figure 4.8a.

The overall methodology and its results are presented in sections 2 to 4. Section 2 is dedicated to the description of a specific pre-processing that aims at cleaning OBS daily noise records from instrumental transient glitches and seafloor noises. Section 3 presents how iterative noise correlations are computed between OBSs using onshore stations as virtual sources. In section 4, we show how noise correlations are used to build a 3-D S-wave velocity model of the Ligurian-Provence basin by computing 2-D probabilistic transdimensional Rayleigh wave group velocity maps and their uncertainties at different periods, and by inverting local dispersion curves to derive a probabilistic V_s model. The fifth and final section is dedicated firstly to a validation of the resulting 3-D V_s model through a comparison with a recent V_p model obtained along a linear refraction, wide-angle seismic profile in the center of the basin by Dannowski et al. (2020). Finally, we show how the combination of the V_p and V_s models along the same profile provides insightful clues to the structure and nature of the crust in the central Ligurian-Provence basin.

4.2 Data processing

4.2.1 Description of the AASN sea-bottom instruments

We processed ambient-noise records from 23 ocean-bottom-seismometers (OBS in Fig. 4.1) that were deployed for eight months in the northwestern Mediterranean Sea as the offshore part of the AlpArray temporary seismic network (AASN; network code Z3). All OBSs were deployed in June 2017 by the AlpArray-OBS cruise of the French R/V 'Pourquoi-Pas?' (Crawford, 2017), and recovered in February 2018 by the MSM71 cruise of the German R/V 'Maria S. Merian' (Kopp et al., 2018).

Sixteen LOBSTER instruments (Long-term Ocean Bottom Seismometer for Tsunami and Earthquake Research) belong to the GEOMAR and DEPAS pools (German instrument pool for amphibious seismology). Designed by K.U.M. Enviromental- and Marine Technology GmbH, these instruments were equipped with HTI-01-PCA hydrophones from High Tech Inc., Trillium compact velocimeters from Nanometrics and K.U.M., and with CMG-40T velocimeters from Güralp for four of them. Seven broadband OBS (BBOBS) belong to the French OBS pool of INSU-IPGP. Designed by the Scripps Institution of Oceanography, these instruments were equipped with deep-sea differential pressure gauges and Nanometrics Trillium-240 very broadband velocimeters.

The drift of the sensor clocks was measured before the deployment and after the recovery. Recordings were then corrected for clock drift in the RESIF and GEOFON datacenters that archive and distribute the dataset. Hable et al. (2018) has demonstrated that the assumption of a linear clock drift is adequate for the ocean-bottom instruments used here.

4.2.2 Glitch removal

The first step of the processing of OBS data is the removal of instrumental transient nearly-periodic impulsive noises (glitches) from continuous records of the 7 French broadband OBSs (BBOBS in section 2.1). Indeed, the vertical-component signals exhibit glitches of 1-hr period caused by the activation of the hourly-check of the internal mass centering of the sensor. The pressure component exhibits glitches with a period of 2.65 hrs, related to data writing on the hard disk. No glitch was detected on the horizontal components. Similar glitches have been observed in other datasets recorded with the same instruments (e.g., Deen et al., 2017).

Similarly to Deen et al. (2017), we remove glitches from the data using an average glitch waveform matching algorithm. Detailed explanation can be found in Text S1 of the supporting information. Supplementary Fig. 4.10 shows a vertical-component daily record of OBS A416A before and after removing the hourly glitches. It documents the efficiency of the processing by comparing the original signal (in blue), the synthetic glitch signal time series (in red), and the final, glitch-free signal (in black). Similarly, Supplementary Fig. 4.11 shows a daily record of the pressure component before and after removing the 2.65-hrs-period glitches. The power spectral density curves of an example of 1-day raw and pre-processed vertical component record displayed in Fig. 4.2a, show that removing the glitches reduces the noise level by up to 15 dB at frequencies lower than 10^{-1} Hz.

4.2.3 Seafloor-noise reduction

At frequencies below 5×10^{-2} Hz, the power spectral densities (PSD) of the three-component records of all OBSs are dominated by noise due to compliance and tilt (Fig. 4.2). The compliance is a long-period pressure signal generated by infra-gravity waves induced by pressure variations in the water column (Crawford et al., 1998). Tilting corresponds to displacements and rotations of the sensor induced by seafloor currents that also generate long-period noise. As documented by Fig. 4.2a, long-period noise is stronger on the horizontal components than on the vertical-component. Crawford and Webb (2000) have shown that noise on the vertical-component is lower when the instrument is better levelled. However, long-period noise on the vertical component strongly increases if the instrument is tilted, even slightly, since acceleration induced by seafloor currents on the horizontal components is projected onto the vertical component.

Tilt and compliance noises on the vertical-component records are reduced by using a frequency-dependent response function method (Crawford et al., 1998; Crawford and Webb, 2000). The horizontal components are firstly corrected for compliance noise by subtracting coherent signals derived from the pressure component. In a second step, tilt noise is reduced in the vertical-component by subtracting coherent signals derived from the compliance-corrected horizontal components (black to green in Fig. 4.2a). Finally, the resulting vertical-component signal is corrected for compliance by subtracting the coherent signal derived from the pressure-component signal (green to purple). Text S2 of the supporting information provides a detailed explanation of this procedure.

Figure 4.2a shows the power spectral density of a daily, vertical-component record of OBS A416A before any correction is applied (blue curve), after correcting from the hourly glitches (black), from the tilt (green) and from the compliance (purple). As shown in Fig. 4.2b, the coherence of the raw vertical-component with the horizontal components (black and blue curves) increases below 5×10^{-2} Hz (see also Supplementary Fig. 4.12a) while coherence with the pressure component increases around 1.2×10^{-2} Hz. Figure 4.2a shows that the reduction of the tilt noise (green curve) is maximum (10 dB) at 5×10^{-3} Hz, which is the frequency with the maximum coherence between the vertical component and the 2 horizontal components. The correction for the compliance noise is almost negligible for this record except around 1.2×10^{-2} Hz, where the coherence between the vertical and the pressure components increases (green area in Fig. 4.2b). Supplementary Fig. 4.12b confirms that the correction for compliance is maximized for this station around 1.2×10^{-2} Hz. In this specific case, the tilt noise is stronger than the compliance noise, which indicates that pressure variations generate less noise than sea-current induced tilt. This strong tilt noise may result from strong currents at the seabed and/or the presence of poorly consolidated sediments directly under the OBS. The lower compliance noise may be due to the large water depth of OBS A416A ($\sim$ 2630 m), damping the effect of pressure-induced infra-gravity waves.

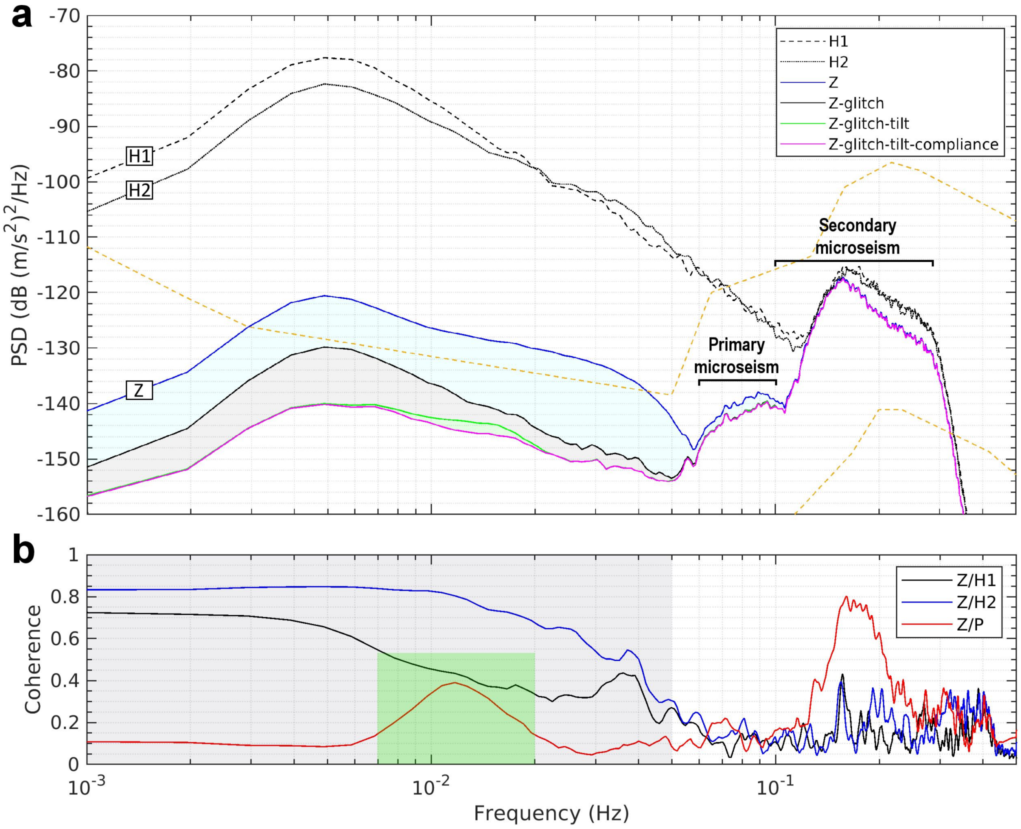

Figure 4.2: Effect of the different corrections for glitch and seafloor noises on the PSD of a 1-day vertical-component record of OBS A416A. Raw signals are band-pass filtered between 2.5 and 250 s, corrected from the instrumental response and decimated to 1 Hz sampling frequency. (a) PSDs before and after corrections; Orange dashed lines indicate the Peterson (1993) New Low and High Noise Model (NLNM & NHNM); Blue: PSD of the raw vertical-component record (blue signal in supplementary Fig. 4.10a); At frequencies $> 5 \times 10^{-2}$ Hz, the PSD is dominated by the primary (~ -140 dB) and secondary (~ -120 dB) microseisms. At longer periods, the PSD is dominated by the effect of the periodic glitches and the seafloor noises with levels similar to the secondary microseism and higher than the NHNM (in the 3×10^{-3} Hz - 4×10^{-2} Hz band) with a peak amplitude at 5×10^{-3} Hz; Black: PSD of the Z-component after correction for the 1-hr glitches (black signal in supplementary Fig. 4.10a); The -130 dB peak at 5×10^{-3} Hz remains, pointing to its oceanic origin; Its amplitude is weaker than the secondary microseism but still stronger than the primary microseism; Green: PSD of the Z-component after correction for the glitches and the tilt noise; Purple: PSD of the Z-component after correction for the glitches and seafloor noises; The maximum amplitude of the residual signal is now well below the primary microseism and the NHNM. The dotted and dashed black curves are the PSDs of the horizontal components. Colored areas show the reduction of the noise level after correcting from glitches (blue), from the tilt (gray), and from the compliance (green). (b) Coherence between the vertical channel and the horizontal (blue and black curves) and pressure (red curve) channels. The gray area shows the frequency domain where the Z-component is coherent with the horizontal components due to tilt noise. The green area shows the domain where the Z-component is coherent with the pressure component due to compliance noise. At frequencies higher than 5×10^{-2} Hz, the coherence is due to primary and secondary microseisms.

4.3 Computation of noise correlations and group-velocity measurements

Once OBS records have been corrected for glitches and seafloor noises, we apply the same pre-processing scheme described below to the records of all stations, onshore and offshore, in order to prepare the calculation of inter-station cross-correlations. As explained in Soergel et al. (2020) and Nouibat et al. (2022a), we first down-weight the contribution of earthquakes and other high-amplitude transients by removing all 4-hr segments with a peak amplitude 4 times greater than the standard deviation of the current daily record, and with a RMS greater than 1.5 times the daily mean RMS. Each daily record is then filtered into six period bands (3 - 5, 5 - 10, 10 - 20, 20 - 40, 40 - 80 and 80 - 200 s) and amplitudes are normalized by their envelope. Finally, the 6 filtered and normalized signals are stacked to obtain the 4-hr pre-processed broadband signal.

4.3.1 First-order correlations

As in Nouibat et al. (2022a), we compute seismic noise cross-correlations for all station pairs by segments of 4 hrs. The 4-hr correlations are normalized and stacked to obtain a single reference correlation per station pair. We use up to 4 years of continuous vertical records for on-land stations pairs, and up to 8 months data to compute correlations for OBS-OBS and OBS-land-station pairs.

As shown by Nouibat et al. (2022a) and supplementary Fig. 4.13a, Rayleigh waves are clearly visible in the correlations for on-land station pairs in a wide period band (5 - 150 s). The Rayleigh waves have an average signal-to-noise ratio (SNR) greater than 3.5 (Supplementary Table 4.2). Although correlations for OBS-land station pairs are computed from only 8 months of data, Rayleigh waves have a SNR > 3 in the 5 - 70 s period band, except in the 40 - 70 s band where the SNR is slightly lower (SNR $= 2.87$, see supplementary Fig. 4.13b and Table 4.2). These noise correlations can therefore be used for Rayleigh-wave tomography. Supplementary Figures 4.13b-c demonstrate the effectiveness of corrections for glitches and seafloor noise in enhancing the SNR of correlations between OBS and land-station records.

First-order correlations between raw OBS records are displayed in the Fig. 4.3a. They can be compared to correlations for land-land station pairs and OBS-land station pairs shown in Supplementary Fig. 4.13. The SNR of correlation signals for OBS pairs is poorer than for other types of pairs in all period bands (average SNR < 2.6, Table 4.1). Therefore, Rayleigh waves are hardly detectable at periods shorter than 40 s in OBS-OBS correlations, and undetectable at longer periods (SNR < 1.6, Table 4.1). This may be explained by several factors such as local noises generated around the sensors by seafloor currents, or seismic noises generated between the stations that induce signals around time 0 s of the correlations, masking the Rayleigh waves. Therefore, these first-order OBS-OBS correlations of raw records cannot be used for Rayleigh-wave tomography.

Figure 4.3b and Table 4.1 document once again the effectiveness of the corrections for glitches and seafloor noises applied to OBS records, which improve the inter-OBS correlation signals. The correlations have a better SNR and are more symmetrical than those obtained from uncorrected signals, particularly at periods shorter than 40 s (columns a-b of Fig. 4.3). However, correlation signals are still noisy, particularly at short lag times, and accurate measurements of Rayleigh-wave group velocities remain challenging. To further improve the quality of correlations for OBS pairs, we chose to virtually reconstruct the Rayleigh waves by computing iterative correlations.

SNR — % of retained paths			
Period band	1st order CC	Cleaned 1st order CC	2nd order CC
$10s - 20s$	2.52 — 2.45%	3.29 — 8.11%	5.77 — 39.6%
$20s - 40s$	2.32 — 1.52%	3.61 — 11.5%	5.62 — 23.4%
$40s - 70s$	1.57 — 0.03%	3.12 — 5.22%	4.52 — 14.3%
$70s - 150s$	1.13 — 0.01%	1.42 — 2.61%	4.37 — 7.31%

Table 4.1: Signal-to-noise ratio and percentage of selected paths for group-velocity tomography in different period bands using: (1) first-order cross-correlations of raw OBS vertical-component records, (2) first-order cross-correlations of pre-processed signals (corrected for glitches, and seafloor noises), and (3) second-order cross-correlations of pre-processed signals.

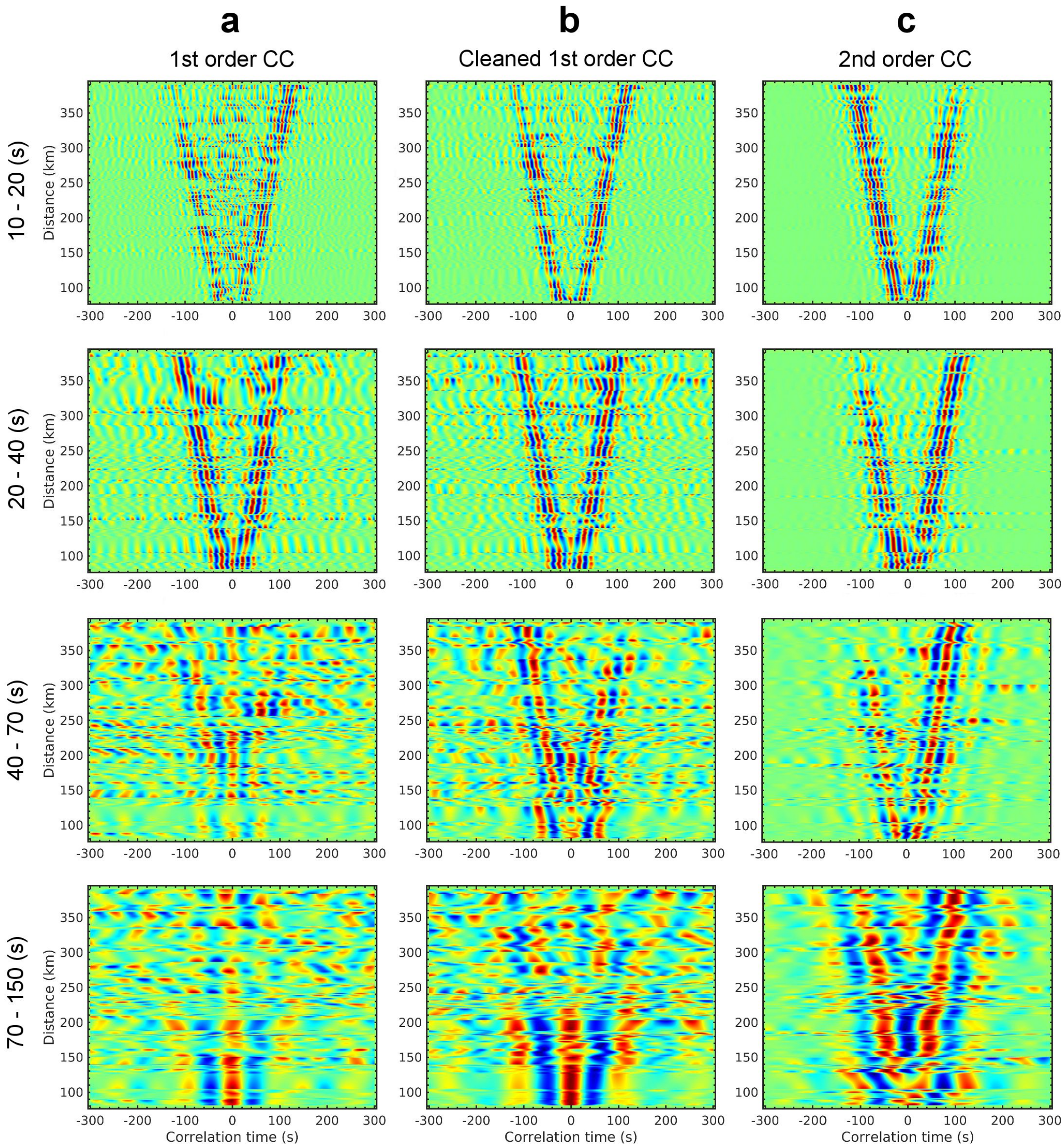

Figure 4.3: Time-distance plots of correlation signals for OBS-OBS pairs, obtained in different period bands at different steps of the processing. (a) First-order cross-correlations (C^1s) of raw signals. (b) C^1s of pre-processed signals (glitch removal & seafloor-noise reduction). (c) Second-order correlations (C^2s). The C^1s in (a) are generally of poor quality and poor symmetry, with strong signals at short lag times due to interferences even at short periods. These interferences become stronger with increasing period, and they progressively overshadow the Rayleigh wave-trains. In (b), the C^1 signals are strongly improved due to corrections for glitches and seafloor noises, in particular in the three short- and medium-period bands. The 70 - 150 s band is still affected by interferences that hide the Rayleigh wave-trains. In (c), the quality and the time-symmetry of correlation signals are significantly improved in all period bands by the calculation of C^2s. In particular, the Rayleigh wave-train emerges from the noise in the long-period band.

4.3.2 Iterative correlations for OBS-OBS paths

We have seen in the previous section that correlations for OBS pairs can hardly be used for Rayleigh-wave tomography. Since correlations computed between onshore stations and OBSs exhibit clear Rayleigh waves, we will use onshore stations as virtual sources in order to measure the travel time of Rayleigh waves between OBSs. Indeed, first-order correlations computed between onshore stations and OBSs contain the Rayleigh-wave part of the Green's function. It is thus possible to use them to mimic the case where Rayleigh waves are emitted on the continent and recorded by OBSs. By computing correlations of Rayleigh waves emitted by each virtual source and recorded by two OBSs (i.e., by computing a second-order correlation), it is possible, thanks to the stationary phase theorem, to isolate the Rayleigh-wave propagating between the two OBSs, and therefore to measure its travel time. We explain this with more detail in the following.

Let us consider any medium with a distribution of sources f. The wavefield recorded at a station A can be expressed using the Green's function G of the medium:

$$u(\vec{r_A}, t) = \int_\Omega \int_0^\infty G(\vec{r_s}, \vec{r_A}, t')\ f(\vec{r_s}, t - t')\ dt'\ d\vec{r_s} \tag{4.1}$$

It has been shown that the time-derivative of the first-order cross-correlation $C^1_{\vec{r_A},\vec{r_B}}(\tau)$ computed between wavefields recorded at two stations A and B is the Green's function $G_{\vec{r_A},\vec{r_B}}(t)$ of the medium, assuming for instance a perfectly homogeneous distribution of white noise everywhere in the medium (e.g., Lobkis and Weaver, 2001; Snieder, 2004; Wapenaar, 2004; Roux et al., 2005; Weaver, 2005; de Verdière, 2006):

$$\frac{d}{d\tau} C^1_{\vec{r_A},\vec{r_B}}(\tau) = G_{\vec{r_A},\vec{r_B}}(\tau) \tag{4.2}$$

In the case where all white noise sources are spatially uncorrelated, the correlation of wavefields recorded at A and B can be rewritten as the integral of correlations between $G(\vec{r}, \vec{r_A})$ and $G(\vec{r}, \vec{r_B})$:

$$\begin{aligned} C^1(\vec{r_A}, \vec{r_B}, \tau) &= \int_0^\infty u(\vec{r_A}, t)\ u(\vec{r_B}, t + \tau)\ dt \\ &= \int_\Omega \int_0^\infty G(\vec{r_s}, \vec{r_A}, t')\ f(\vec{r_s}, t - t')\ dt'\ d\vec{r_s} \otimes \int_\Omega \int_0^\infty G(\vec{r_s}, \vec{r_B}, t')\ f(\vec{r_s}, t - t')\ dt'\ d\vec{r_s} \\ &= \int_\Omega G(\vec{r_s}, \vec{r_A}, t) \otimes G(\vec{r_s}, \vec{r_B}, t)\ d\vec{r_s} \end{aligned} \tag{4.3}$$

where $\otimes$ denotes the cross-correlation operation. Since the time-derivative of correlations is similar to the Green's function of the medium, it follows immediately by substituting dC^1/dt to G in Eq. 4.3 that the first-order correlation is equivalent to a second-order correlation that we will note C^2:

$$C^1(\vec{r_A}, \vec{r_B}, \tau) = \int_\Omega \frac{d}{dt} C^1(\vec{r_s}, \vec{r_A}, t) \otimes \frac{d}{dt} C^1(\vec{r_s}, \vec{r_B}, t)\ d\vec{r_s} = C^2(\vec{r_A}, \vec{r_B}, \tau) \tag{4.4}$$

Equation 4 indicates that it is possible to reconstruct the Green's function of the medium between A and B by re-correlating the noise correlations computed between each point of the medium and stations A and B. However, this demonstration assumes that the time-derivative of correlations are the exact and complete Green's function of the medium. The assumption would be correct if stations that could be used as virtual sources would exist everywhere in the medium.

In practice, the seismic noise recorded at the Earth surface in the period band considered in this work (5 - 150 s) is dominated by Rayleigh waves. As a consequence, noise correlations computed between onshore stations and OBSs do not provide the full Green's function of the medium including all propagating modes, but they do provide robust estimates of the travel time of Rayleigh waves.

Rather than attempting to reconstruct the full Green's function, we will measure the travel time of the Rayleigh waves between OBSs A and B by using a simplified approach inspired by Eq. 4.4. It consists in re-correlating only the Rayleigh-wave parts of the correlations computed between onshore stations and OBSs A and B, that we consider as the Rayleigh-wave part of the Green's function:

$$\begin{aligned} \frac{d}{d\tau} C^{2,Ray}(\vec{r_A}, \vec{r_B}, \tau) &= \frac{d}{d\tau} \int_{\Omega} \frac{d}{dt} C^{1,Ray}(\vec{r_s}, \vec{r_A}, t) \otimes \frac{d}{dt} C^{1,Ray}(\vec{r_s}, \vec{r_B}, t)\ d\vec{r_s} \\ &\approx G^{Ray}(\vec{r_A}, \vec{r_B}, \tau) \end{aligned} \tag{4.5}$$

where superscript '*Ray*' indicates that we only correlate the fundamental mode of Rayleigh waves of first-order correlations. In that way, we only retrieve the fundamental mode of the Rayleigh-wave part of the Green's function.

In practice, the distribution of virtual sources is never homogeneous. Instead, we use land stations deployed all over Western Europe, while OBSs are located in the Ligurian Sea (Fig. 4.1). Therefore, the condition of the stationary phase theorem are not completely met. To circumvent this difficulty, we select virtual sources that are expected to contribute constructively to the correlations (Fig. 4.4). To that end, we design a virtual-source azimuthal-filter that only retains sources located in the end-fire lobe of the OBS couple, that is in azimuths at ± 20° with respect to the azimuth of the OBS pair. Moreover, we enhance the virtual source coverage by using separately the causal and anticausal parts of the first-order correlations to compute the second-order correlation.

Because onshore stations are well distributed and OBS-onshore correlations exhibit clear Rayleigh waves, the use of virtual sources in iterative correlations for OBS-OBS paths leads to a higher quality of Rayleigh waveforms (columns b-c of Fig. 4.3 and Table 4.1). This is achieved through: (1) separately recovering the causal and anticausal parts of the Green's function by using separately the causal and anticausal parts of the first-order correlations, thus avoiding interferences at long periods, and (2) controlling the distribution of virtual sources, thus guaranteeing a higher quality of the C^2s by contrast to OBS-OBS C^1s that exhibit low signal-to-noise ratio probably due to local noise sources. These local noise sources do not contribute significantly to OBS-onshore stations paths, and therefore neither to second-order correlations. Supplementary Fig. 4.14 shows that phases of the Rayleigh waveforms reconstructed from the C^1 and C^2 processes match. In the 5 - 10 s band, iterative correlations do not systematically improve the signal quality as compared to first-order correlations. Therefore, we select for each path the correlation of highest quality after checking that the C^1 and C^2 are coherent.

The strengths of the iterative correlations make it possible to substantially improve the path coverage in the Ligurian-Provence domain (Table 4.1). Our results demonstrate the efficiency of this method in providing robust group-velocity measurements. Further illustration and validation will be the subject of a future paper.

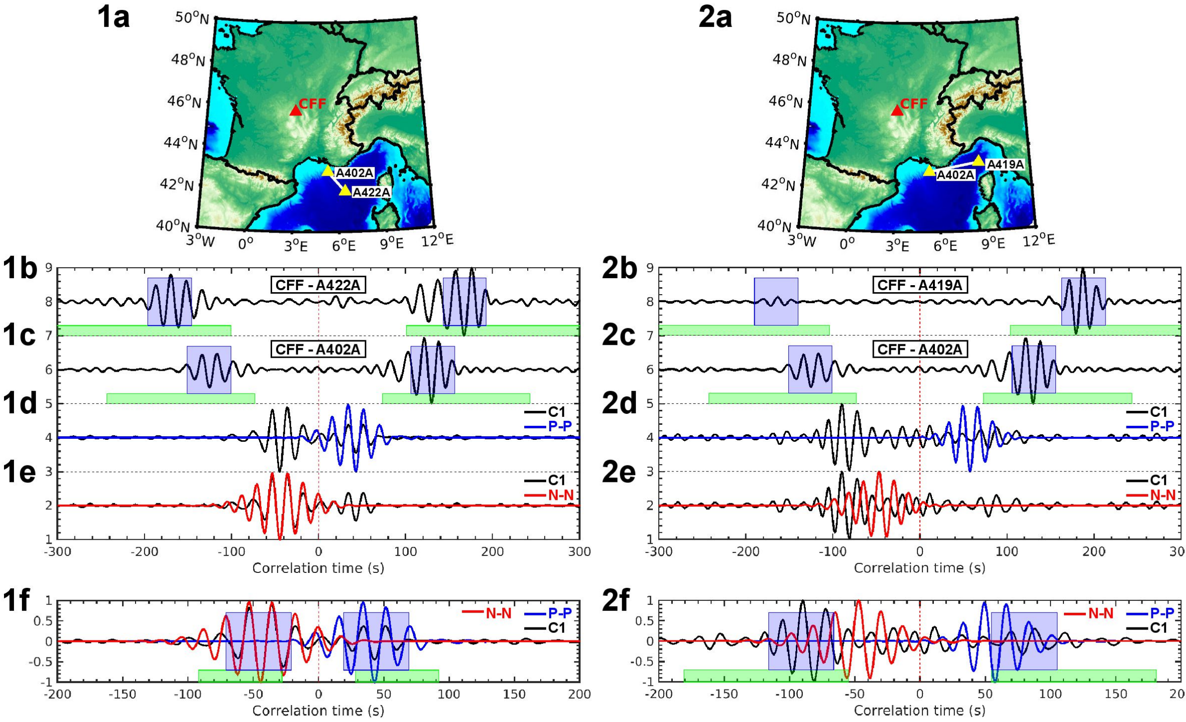

Figure 4.4: Details of the computation of second-order correlations for 2 examples of OBS-OBS pairs, using station CFF (FR network) as virtual source. (1-2a): Station location maps. In example (1), the virtual source is roughly aligned with the OBS pair, while in example (2), the azimuth of the virtual source is almost perpendicular to the pair. (1-2b, 1-2c): First-order correlation signals between CFF and each OBS. The green areas show the Rayleigh-wave search windows (wave propagation of 1 to 5 km/s over the inter-station distances). The blue areas show the Rayleigh-wave detection windows. (1-2d): First-order correlation of the OBS signals (C^1, in black), and correlation of the positive-time (causal) parts of the C^1s between CFF and the OBS couple (P-P, in blue). (1-2e): First-order correlation of the OBS signals (C^1, black), and correlation of the negative-time (acausal) parts of the C^1s between CFF and the OBS couple (N-N, red). (1-2f): Comparison of the causal (P-P, blue) and acausal (N-N, red) C^2s (that will be summed to obtain the final C^2), with the first-order correlation of the OBS signals (C^1, black). The C^2 and C^1 signals have similar phases in (1) where the virtual source is aligned with the OBS pair. They have incoherent phases in (2), since CFF is not located in the end-fire lobe of this OBS pair (see text).

4.3.3 Group-velocity measurements

Once first-order and iterative correlations have been computed for onshore and offshore stations respectively, we derive group-velocity dispersion curves of the causal and acausal parts of the correlations by using multiple filter analysis (MFA, Dziewonski et al., 1969b; Herrmann, 1973). As in Nouibat et al. (2022a), we adapt the width of the gaussian filter to the inter-station distance to accommodate the trade-off in resolution between the time and frequency domains (Levshin et al., 1989). We correct our group-velocity measurements from the biases that occur when the MFA method is applied on signals having a non-flat spectrum (Shapiro and Singh, 1999). This is especially important when measuring Rayleigh-wave velocities using noise correlations around the first and second microseismic peak, i.e., around 7 s and 14 s.

In order to build the group-velocity maps in the Ligurian-Provence domain, we maximize the path coverage over the Ligurian Sea by using simultaneously OBS-OBS, land-land, and land-OBS station pairs. A careful selection of group-velocity measurements is achieved to keep the most reliable ones and discard those that are biased by an unfavorable distribution of noise sources, or by interferences of causal and acausal Rayleigh waves for instance.

For first-order correlations (C^1s) computed between land-land and land-OBS stations, at each period, we keep measurements if: (1) the SNR defined as the ratio of the Raleigh-wave peak amplitude and the standard deviation of the following signal, is greater than 3 on the positive and negative correlation times, (2) group velocities measured in positive and negative correlation times differ by less than 0.2 km/s, and (3) the inter-station distance is greater than 2 wavelengths. For iterative correlations (C^2s) computed between OBS stations, we do not use the SNR criteria, since iterative correlations only exhibit the fundamental mode of the Rayleigh waves, owing to their construction. Nevertheless, for each C^2 satisfying the distance and symmetry criteria, we only keep the group-velocity measurement of the side of the correlation (positive or negative time) where the amplitude of the Rayleigh-wave is maximum (i.e., where we have more virtual sources contributing).

Table 4.1 shows that for OBS-OBS pairs, the selection procedure would reject more than 97% of Rayleigh waves velocity measurements performed on first-order correlations computed using OBS data that were not corrected from the compliance and tilt noises. This illustrates that these signals are obviously not usable for ambient-noise tomography. By contrast, we selected between 2.6% to 11.5% of the measurements performed on first-order correlations done using OBS data corrected from sea floor noises. This highlights the importance of the pre-processing scheme described in section 2. Moreover, we kept between 7.3% and 39.6% of group-velocity measurements performed on iterative correlations (C^2s) depending on the period-band considered. Second-order correlations provide a substantial gain over first-order correlations, leading to a significant improvement of the raypath coverage in the Ligurian-Provence basin with respect to the ANT of Wolf et al. (2021) based on first-order correlations.

4.4 3-D shear-wave velocity model

4.4.1 Inversion for 2-D group-velocity maps

We compute 2-D group-velocity maps and associated uncertainties using a 'data-driven' transdimensional approach at discrete periods from 4 s to 150 s. At each period, probabilistic group-velocity maps are derived by exploring millions of 2-D models using the reversible-jump Markov-chain Monte-Carlo method (rj-McMC, Bodin et al., 2012). The method used for the inversion and the spatial resolution of the resulting group-velocity maps are discussed in detail in Nouibat et al. (2022a). Uncertainty and path density maps at different periods are presented in Supplementary Figure 4.15.

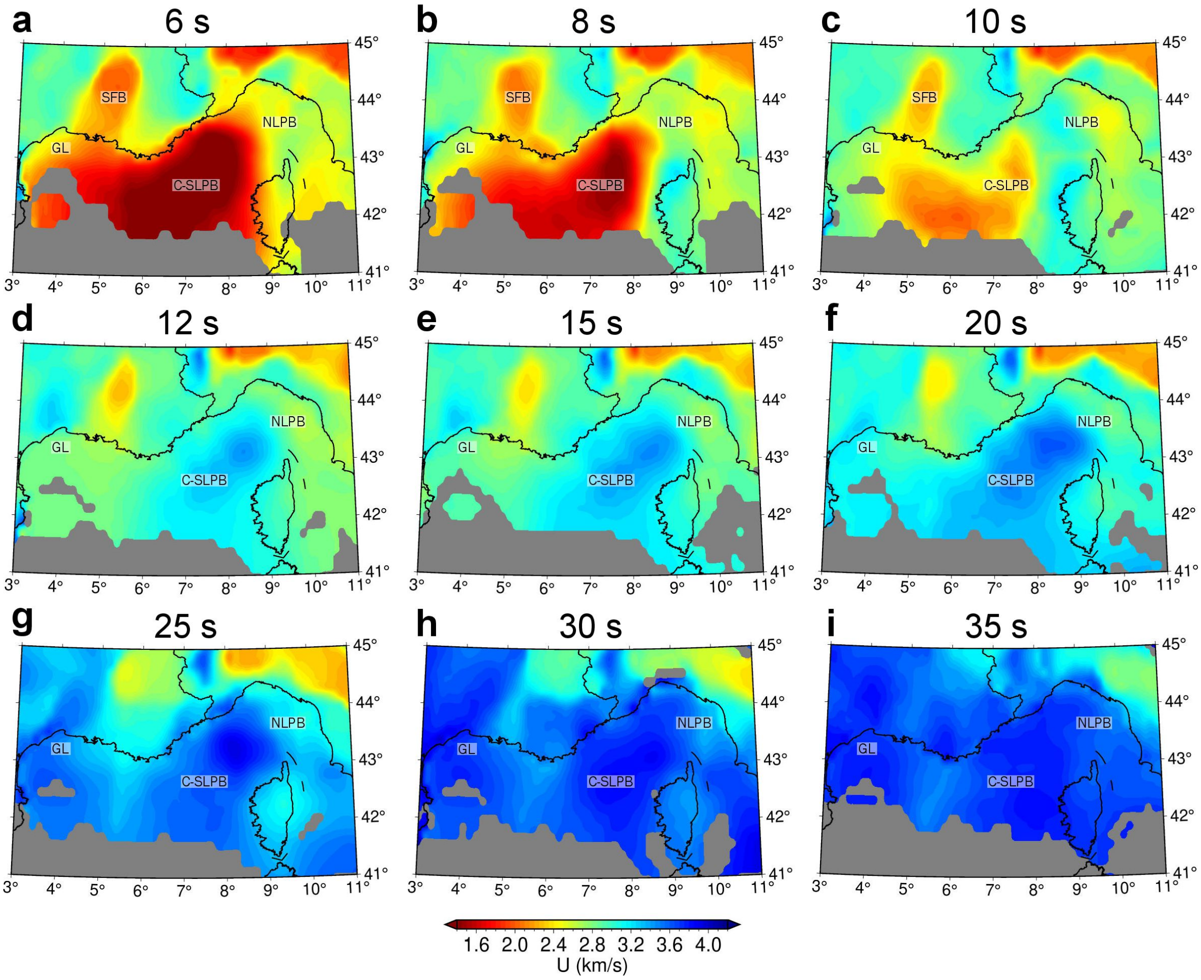

Figure 4.5: Group-velocity maps (average solutions) at 6 to 35 s periods, obtained with the Hierarchical Bayes reversible-jump algorithm. Only areas with uncertainty lower than 0.5 km/s are shown. C-SLPB: central and southwestern parts of the basin, GL: Gulf of Lion, NLPB: northeastern Ligurian-Provence basin, SFB: southeast-France basin.

Resulting group-velocity maps of the Ligurian-Provence basin and its margins are shown in Fig. 4.5 for periods from 6 s to 35 s. The 6 s and 8 s maps (sensitive to $\sim$ 4 - 8 km depth) highlight low-velocity anomalies ($U < 1.6$ km/s) in the central and southwestern parts of the basin (C-SLPB in Fig. 4.5), that are probably associated with thick sediment sequences. These velocities are lower than those of the southeast-France basin and the Gulf of Lion (respectively SFB and GL in Fig. 4.5). The northeastern Ligurian-Provence basin (NLPB), its northern, Provence coast margin and its southern margin in Corsica have larger velocities ($U \geq 2.4$ km/s). From simulations of Rayleigh-wave dispersion in synthetic 1-D models, we show that such periods are also highly sensitive to the presence and thickness of the water column (Supplementary Figure 4.16). The 10 s map still shows velocities lower than 2.5 km/s in the central and southwestern Ligurian-Provence basin. The 12 s and 15 s maps (sensitive to $\sim 10-15$ km depths) highlight velocities larger than 3.5 km/s associated with the thin crust of the Ligurian basin. However, the northeastern basin has lower velocities indicative of a deeper Moho in the Gulf of Genova. Velocities lower than 3.2 km/s correspond to thick crust under Corsica and the Provence coast. At 25 s period (sensitive to $\sim 15-30$ km depth), velocities are still lower along the western coast of the Gulf of Genova than in the basin, indicative of a thicker crust, as in Corsica. At 30 s and 35 s periods, group velocities are homogeneous and exhibit large velocities ($U > 3.5$ km/s) in most of the study region.

4.4.2 Inversion for shear-wave velocity

The group-velocity maps and their uncertainties are used to derive a 3-D V_s model. For this, we perform a two-step data-driven inversion to tackle the non-unicity of the inverse problem. The main part of this process is described in detail in Nouibat et al. (2022a), so we will only summarize it here. We will rather focus on the specificity of the inversion for the offshore region, which is the consideration of the water layer. A result of the inversion for V_s at an offshore location in the Ligurian Sea is shown in Supplementary Fig. 4.17.

Firstly, a 3-D probabilistic solution is computed that gives at each location the probability distribution of V_s and the probability of having an interface as a function of depth. This is achieved using an exhaustive grid search on a set of $\sim$ 130 million synthetic four-layer models, which include a sedimentary layer, the upper crust, the lower crust and a half-space representing the upper mantle. The strength of this first-step Bayesian framework lies in constraining the structural complexity of the crust (i.e., of the short-period part of the dispersion curve) by means of an ensemble of models, fitting the dispersion curve to the degree required by its uncertainties. However, due to the four-layer model assumption, this procedure is not sufficient to fully describe the complexity of the model structure, particularly in the mantle part, that is in the long-period part of the dispersion curve. Hence, we use an iterative linear least-square inversion (Herrmann, 2013) as a complement to update the mantle part of the model and further refine the fit to the local dispersion curve for the crustal part (Supplementary Fig. 4.17).

The initial model for the linear inversion (second step) at a given location is the average of all selected probabilistic solutions of the first inversion step, weighted by their likelihood values. We discretize the crustal and mantle parts at intervals of 1 and 5 km, respectively, and assume a gradual increase of V_s below Moho according to the global model PREM (Dziewonski and Anderson, 1981). For offshore locations, we incorporate on top of this initial model an additional layer of thickness equal to water depth at the given location. The parameters of this water layer are kept fixed during the linear least-square inversion (thickness, $V_s = 0$ km/s, $V_p = 1.5$ km/s, $\rho = 1 \times 10^3$ kg/m^3). Since we invert for short periods as well, an appropriate parameterisation of the water column is crucial. Indeed, we highlight its influence by computing group-velocity dispersion curves for synthetic 3-layer crustal models representative of the oceanic crust of the Ligurian-Provence basin, and different water levels from 0 to 3.1 km (Supplementary Fig. 4.16). This shows that the effect of the water layer on the dispersion curve is substantial at periods shorter than 15 - 20 s, where the water depth changes impact: (1) the absolute group velocities, and (2) the shape of the dispersion curve, particularly in the vicinity of the Airy phase.

Figure 4.6 shows depth slices in the 3-D shear-wave velocity model at 3 to 30 km depth. The sediment layer is clearly visible at 3 - 7 km depth in the central and southwestern Ligurian-Provence basin, with low velocities of 2 - 3.2 km/s. The transition from crustal (3.5 - 4.1 km/s) to mantle velocities (4.1 - 4.5 km/s) is located between 10 km and 12 - 15 km in the parts of the basin with thinnest crust. Between 20 and 30 km, areas of strong velocities corresponding to the mantle extend westward from the Ligurian-Provence basin to the Gulf of Lion across a nearly N-S transition of slower velocities at $\sim 5.5°$ E.

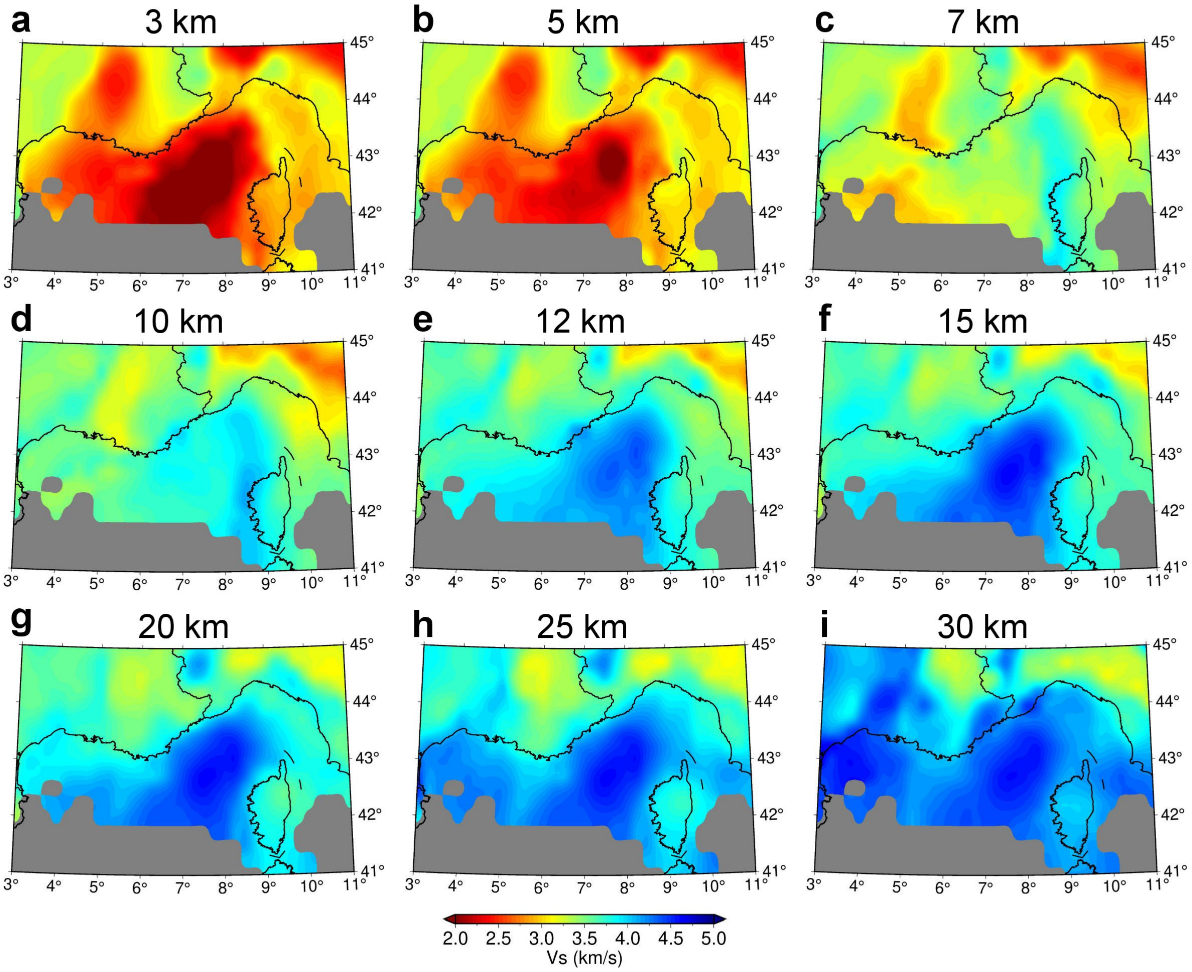

Figure 4.6: Depth slices in the final V_s model at 3 to 30 km depths. Only regions with 1σ error < 8 % are shown.

4.4.3 Comparison with the $\mathrm{V_s}$ model by Wolf et al. (2021)

Figure 4.7 shows a comparison of our V_s model and the model by Wolf et al. (2021), which was the first published ambient-noise tomography using data of AlpArray OBSs in the Ligurian basin. Our V_s model covers a wider area as part of the large-scale model by Nouibat et al. (2022a) that uses all available broadband stations in Western Europe.

At 3-km depth, our model (Fig. 4.7-1a) highlights: (1) the sedimentary cover in the central and southwestern basin (1.8 - 2.2 km/s), where Wolf et al's model (Fig. 4.7-1b) exhibits patches of very low velocities ($V_s \leq 1.4$ km/s), and (2) gradual increasing of velocity from the central basin towards the conjugate margins, which is not clearly visible in Wolf et al's model where velocities fluctuate from very low ($V_s \leq 1.8$ km/s) to high values (2.4 - 2.5 km/s). At 5-km depth, we still observe typical sediment velocities (Fig. 4.7-2a), while Wolf et al's model (Fig. 4.7-2b) exhibits higher velocities ($V_s > 3.5$ km/s). At 13-km depth, our model (Fig. 4.7-3a) shows almost homogeneous mantle velocities in the basin ($V_s \geq 4.1$ km/s) while Wolf et al's model (Fig. 4.7-3b) exhibits numerous small-size velocity anomalies, fluctuating between mantle-like ($V_s \geq 4.1$ km/s) and crust-like velocities ($V_s \leq 3.7$ km/s). These heterogeneities suggest a much more irregular Moho surface than in our model. At 20-km depth, our model (Fig. 4.7-4a) documents crustal thinning towards the basin axis with V_s increasing across the conjugate margins. Again, velocities in the central basin are more heterogeneous in Wolf et al's model (Fig. 4.7-4b), with localized small-size anomalies. Although the transition domain has an irregular shape in Wolf et al's model, it remains to first order similar to that shown in our model.

We think that such strong differences between the two V_s models are mostly due to differences in coverage and quality of Rayleigh-wave dispersion data. Indeed, we greatly enhanced the path coverage in the Ligurian basin by using iterative correlations for OBS-OBS paths. In addition, the use of all broadband stations in Western Europe provides long ray paths across the Ligurian sea, allowing us to improve path coverage to the west and southeast and make use of Rayleigh-wave dispersion measurements up to 150 s. On the other hand, Wolf et al. (2021) used only 23 onshore stations nearby the basin, thus a limited aperture. Therefore, they used earthquake records for periods greater than 20 s. To a lesser extent, the differences between the two models may also be explained by the different strategies used to invert Rayleigh-wave dispersion measurements. Wolf et al. (2021) computed their 2-D dispersion maps using a linear inversion that depends on an explicit regularization, while our transdimensional approach does not. Moreover, our 1-D Bayesian inversion for V_s take uncertainties on dispersion measurements into account, which is key for controlling model complexity.

As we will see in the following section, our V_s model is more coherent with current knowledge on the crustal structure of the Ligurian-Provence basin than the one by Wolf et al. (2021). In particular, the thickness of the sedimentary cover and Moho depth and geometry estimated from our V_s model are coherent with the V_p model by Dannowski et al. (2020) along the basin axis and with the stratigraphic log after Leprêtre et al. (2013).

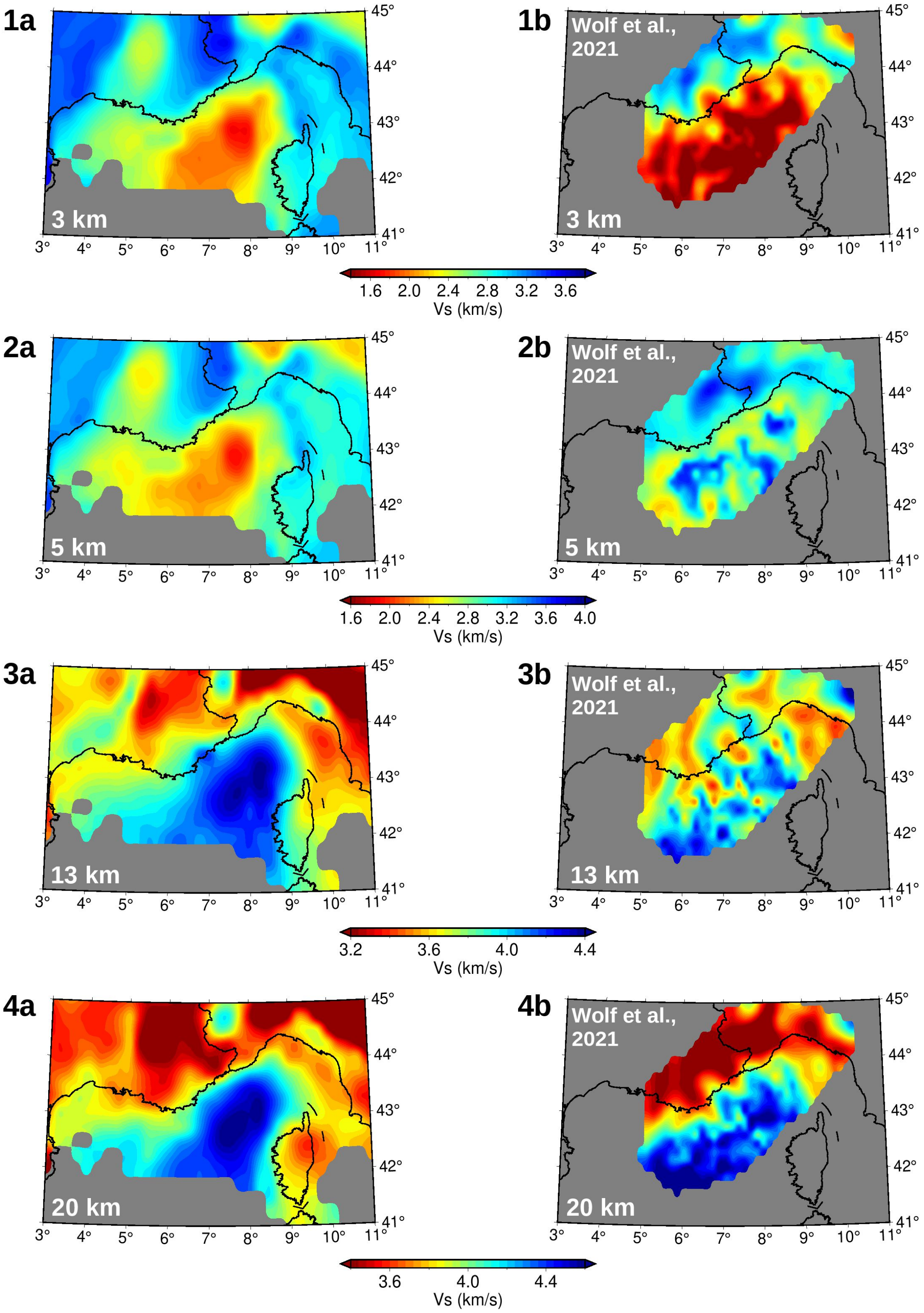

Figure 4.7: Comparison between our V_s model (left panel) and the V_s model by Wolf et al. (2021) (right panel) at four depths.

4.5 Discussion

We now focus on the oceanic domain of the Ligurian-Provence basin (Fig. 4.8a), in particular on the comparison of our S-wave velocity model with a recent P-wave velocity model derived by Dannowski et al. (2020) from a controlled-source seismic profile recorded along the basin axis (thick black line in Fig. 4.8a). The availability of this high-resolution V_p section provides a unique opportunity to assess the accuracy and validate our V_s model against an independent dataset. Moreover, the existence of V_p and V_s models along the same profile may provide clues on the petrological structure of the crust in the oceanic domain of the basin, which is still debated. Indeed, it has been proposed that the oceanic domain is made of an oceanic crust with a thin basaltic layer (e.g., Mascle and Rehault, 1990; Bonatti et al., 1990), or an exhumed and serpentinized mantle devoid of any volcanic upper layer (e.g., Boillot et al., 1989; Beslier et al., 1993; Jolivet et al., 2020), or even an hyper-extended continental crust (e.g., McKenzie, 1978; Pascal et al., 1993; Dannowski et al., 2020).

4.5.1 Geological setting of the Ligurian-Provence basin

The basin opening initiated at 30 Ma by a rifting phase between Europe and the Corsica-Sardinia block, as a result of back-arc extension above the Adria oceanic micro-plate, initially subducting north-westward (e.g., Faccenna et al., 1997). The progressive south-eastward roll-back and retreat of the Adria slab below the Corsica-Sardinia domain led to stretching of the continental crust followed by continental break-up during the early Miocene, and to the genesis of an oceanic crust between 20 and 15 Ma (Séranne, 1999). As a result, the Ligurian-Provence basin includes two thinned conjugate continental passive margins separated by an oceanic domain (Fig. 4.8a). According to Rollet et al. (2002), the entire region is characterized by magnetic anomalies, and by the presence of magmatic bodies identified from acoustic facies in seismic reflection profiles. The area between the margins and the oceanic domain is described as a transitional domain, likely made up of a very thin continental crust overlying a thick rift-related corner of magmatic underplating (e.g., Séranne, 1999). This limit is marked by an abrupt change in the amplitude of magnetic anomalies with a transition from mostly positive values in the deep basin (i.e., oceanic domain) to negative values at the continent-ocean transition, and by a change in acoustic facies on seismic reflection profiles (e.g., Réhault et al., 1984; Déverchère and Beslier, 1995; Rollet et al., 2002). While the magmatism occurring in the margins has been associated to back-arc magmatic activity strongly influenced by subduction (e.g., Coulon, 1977; Bellon, 1981; Réhault et al., 2012), the nature of magmatism observed in the oceanic domain remains unknown. It could not be investigated by direct geochemical analysis due to the presence of a sedimentary cover several kilometres thick.

Figure 4.8b shows a stratigraphic log representative of Western Mediterranean oceanic basins that includes P-wave velocity estimates. It is derived from the results of joint seismic wide-angle and reflection profiling in the Algerian and Western Sardinia basins Klingelhoefer et al. (2008); Gailler et al. (2009); Leprêtre et al. (2013). The sedimentary layer of 5-km average thickness and 1.9 - 5 km/s P-wave velocities is made up of Plio-quaternary sediments, Messinian and pre-salt units (Fig. 4.8b). The transition from Plio-quaternary to Messinian units occurs at $V_p \approx 2.5$ km/s. The Messinian sequence exhibits strong thickness variations ascribed to salt diapirism. It is separated from the pre-salt unit by the 4.2 km/s velocity boundary. The deepest sediments overlay an oceanic basement that starts at $V_p > 5$ km/s. The oceanic crust is relatively thin with an average thickness of 4.5 km. Its P-wave velocities range from 5 to 7.2 - 7.3 km/s at $\sim$ 12 km depth, which corresponds to the Moho depth ($V_p > 7.3$ km/s in the upper mantle). Controlled-source seismic data are useful to constrain the layer thicknesses and the depths of major interfaces (intra-sedimentary, sediment-crust and Moho), but their interpretation in terms of petrology only rely on P-wave velocity estimates. The interpretation is ambiguous as two lithologies of different petrological natures may have similar V_p (or V_s) signatures. However, P- and S-wave velocities can be used jointly to yield information on lithologies and their hydration degree (e.g., Grevemeyer et al., 2018; Malusà et al., 2021). For instance, the V_p/V_s ratio is commonly used to assess the degree of serpentinization in oceanic domains and margins (e.g., Bullock and Minshull, 2005; Reynard, 2013; Grevemeyer et al., 2018). We will take advantage of the availability of the V_p cross-section by Dannowski et al. (2020) and our V_s section along the same profile to further constrain the petrological nature of the crust in the central Ligurian-Provence basin.

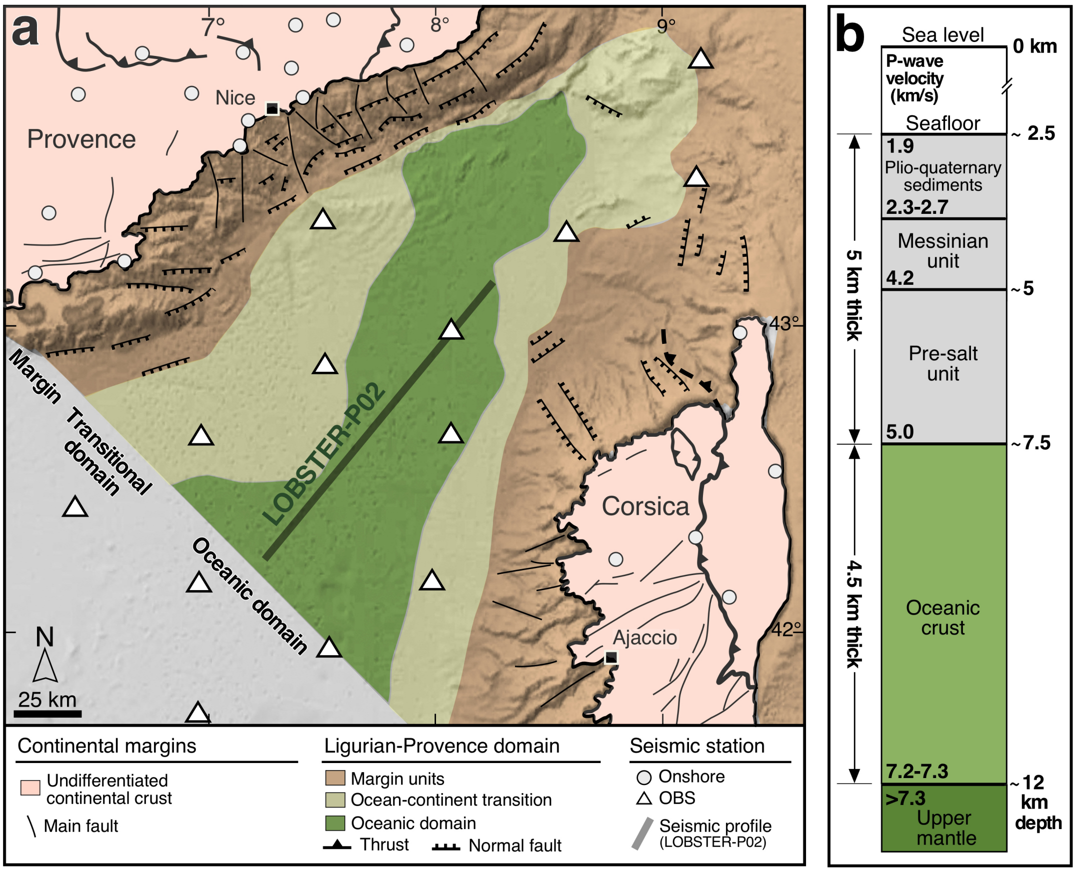

Figure 4.8: (a) Geological and tectonic setting of the Ligurian-Provence basin and European domains of southeast France and Corsica, showing: (1) continental margins, (2) transitional domains, and (3) the central oceanic domain. Gray line: trace of the seismic profile used in the discussion (Dannowski et al., 2020). Seismic stations are indicated by white triangles (AASN OBSs) and white circles (onshore stations). (b) stratigraphic log showing P-wave velocity and thickness of geological units observed in Western Mediterranean oceanic basins (after Leprêtre et al., 2013).

4.5.2 Seismic velocity cross-sections in the central oceanic domain

Figures 4.9a-b show vertical sections through our 3-D V_s model and probability of presence of interfaces along the SW-NE transect investigated by Dannowski et al. (2020). The P-wave velocity section of Dannowski et al. (2020) is shown in Fig. 4.9c.

Figure 4.9b shows two major layer boundaries at $\sim$ 5 and $\sim$ 12 km depth with rather high probabilities of presence, and a third one of weaker probability at $\sim$ 7.5 km depth. The good correspondence of the shallowest boundary with the velocity contour $V_s = 2.5$ km/s suggests that it is probably an intra-sedimentary interface. This boundary also coincides with the 4.2 km/s P-wave velocity contour (Fig. 4.9c), which corresponds to the base of the Messinian salt unit according to Fig. 4.8b. This interpretation is consistent with S- and P-wave velocities, typical of salt (e.g., Yan et al., 2016). The intermediate interface at $\sim$ 7.5 km depth, which is slightly less pronounced that the Moho boundary (Fig. 4.9b) coincides with the velocity contours $V_s = 3.5$ km/s (Fig. 4.9b) and $V_p = 5$ km/s (Fig. 4.9c), which may support its interpretation as the sediment-crust boundary, in agreement with Fig. 4.8b. However, this interface does not correspond to a marked change in seismic velocity in the final model of Fig. 4.9a. Therefore, we cannot detect unambiguously the depth of the sediment-crust transition. We will use the proxy $V_s = 3.5$ km/s (or $V_p = 5$ km/s) for the sediment-crust boundary.

In the northeastern part of the transect ($x > 70$ km), the lower crust has higher, but still crustal P-wave velocities (6.0 - 7.2 km/s, in green in Fig. 4.9c), hence a weaker P-wave velocity gradient at the Moho than in the southwestern part. By contrast, S-wave velocities are high and almost mantle-like (4.0 - 4.4 km/s), with a low S-wave velocity gradient at Moho depth, in particular at the northeastern end of the profile ($x > 90$ km in Fig. 4.9a). These P- and S-wave velocities are typical of gabbro (Grevemeyer et al., 2018), which suggests a gabbro intrusive body within the oceanic crust. Our interpretation is at odd with Dannowski et al. (2020) who interpreted the high V_p part of the deep crust as hyper-extended continental crust based on gravity modeling. The observed high S-wave velocity rules out the continental crust hypothesis.

As outlined by Dannowski et al. (2020), the $V_p = 7.2$ km/s is a good Moho proxy because it coincides with a very strong velocity gradient. In the southwestern part of the profile ($x <$ 70 km), the $V_p = 7.2$ km/s contour closely corresponds to the $V_s = 4.1$ km/s contour while it corresponds to the $V_s = 4.4$ km/s contour for $x > 70$ km, that is beneath the gabbroic intrusion (Fig. 4.9c). Owing to the presence of the gabbro intrusion, a single S-wave velocity contour cannot be used as proxy for the petrological Moho in the Ligurian-Provence basin, unlike in continental areas (Nouibat et al., 2022a).

In the southwestern part of the profile, the depths of the V_s (4.1 km/s) and V_p (7.2 km/s) Moho proxies differ by less than 1 km. Such a small discrepancy is remarkable, given that the two models are totally independent. The depth profiles of the two shallower layer boundaries are also remarkably similar to those of the V_p contours that define lithological layering in the western Mediterranean basins (Fig. 4.8b). Such similarity to the P-wave velocity model of Dannowski et al. (2020) validates the offshore part of our shear-wave velocity model, as similarity to the receiver function section of the Cifalps profile validated its onshore part (Nouibat et al., 2022a).

In the few locations where information on P-wave velocity is available, the uppermost mantle has the seismic signature of a dry peridotite, with $V_p > 7.2$ km/s and $V_s > 4.0$ km/s

(Grevemeyer et al., 2018). We find no evidence of serpentinized mantle, which would show much lower P- and S-wave velocities. Dannowski et al. (2020) and Wolf et al. (2021) also concluded on low mantle serpentinization in this part of the basin axis.

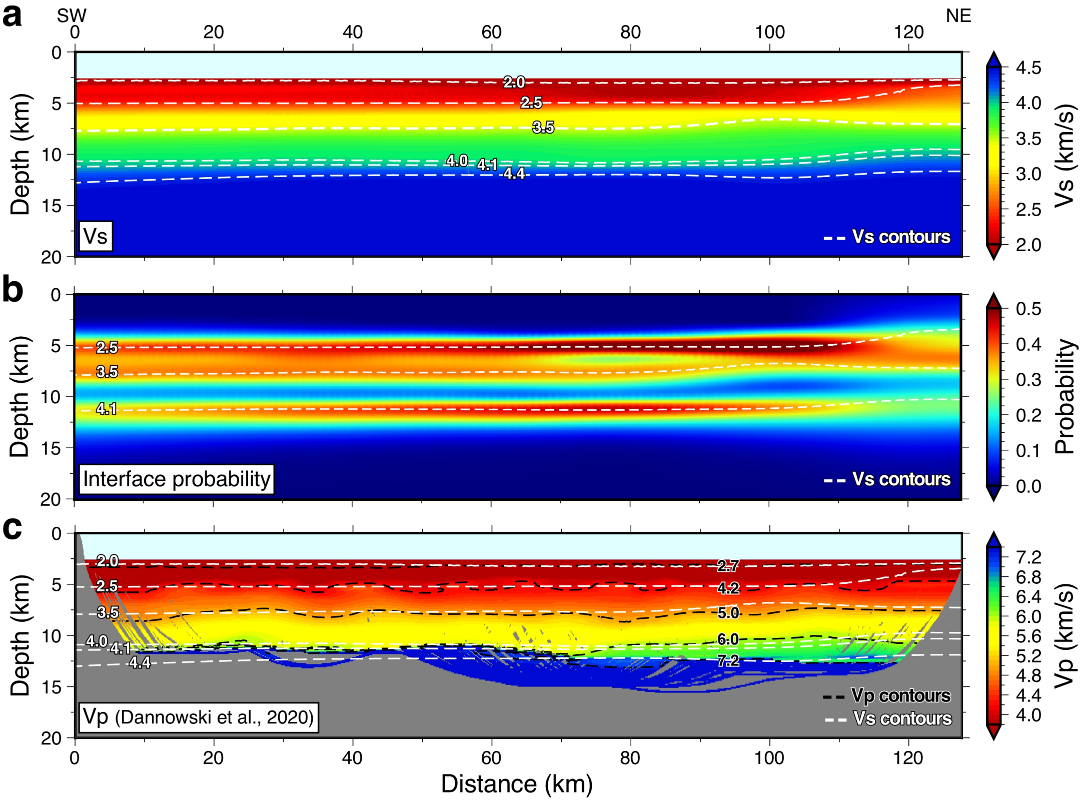

Figure 4.9: Depth sections along the LOBSTER-P02 transect (location shown in Fig. 4.8a). (a) Shear-wave velocities from our final model. The 2, 2.5, 3.5, 4, 4.1, and 4.4 km/s V_s contours are shown as white dashed lines. The water column is in sky blue. (b) Posterior probability densities of presence of a layer boundary obtained from the Bayesian inversion. White dashed lines indicate the 2.5, 3.5 and 4.1 km/s V_s contours. (c) P-wave velocities from Dannowski et al. (2020). Black dashed lines indicate the 2.7, 4.2, 5, 6, and 7.2 km/s V_p contours; white dashed lines as in (a).

4.6 Conclusion

Using data of 23 ocean-bottom seismometers of the AlpArray network with those of 890 temporary and permanent onshore stations, we have derived a 3-D high-resolution shear-wave velocity model encompassing the Ligurian-Provence basin and its conjugate margins. The OBS continuous records could be fully exploited after a careful, specific pre-processing scheme including removal of instrument noises (glitches) and reduction of seabed-induced compliance and tilt noises. We enhanced the quality of correlations between OBSs and maximized the path coverage in the Ligurian-Provence basin by involving correlations with onshore stations to virtually reconstruct Rayleigh waves propagating between OBSs. As in Nouibat et al. (2022a), we computed 2-D group-velocity maps and their uncertainties using a data-driven transdimensional inversion of Rayleigh-wave group-velocity measurements. The dispersion data and their uncertainties have then been used jointly in a Bayesian probabilistic approach to derive a 3-D probabilistic shear-wave velocity model. The output average model was further refined using a linear inversion that accounts for the presence of the water column.

The comparison with the high-resolution P-wave velocity section derived by Dannowski et al. (2020) from traveltime inversion of controlled-source seismic data along the basin axis validates our 3-D ANT model. Layer boundaries revealed by high probabilities of presence of an interface and V_s contours are remarkably consistent with V_p contours. The joint interpretation of the V_p and V_s models highlights a relatively thin anomalous oceanic crust of low P-wave velocities but rather high S-wave velocities. In the NE part of the profile, the lower part of the crust exhibits a gabbroic intrusive body. The underlying mantle is anhydrous and shows no evidence of serpentinisation. These results show the potential of a joint interpretation of V_p and V_s models since they provide reliable answers to a number of debated questions on the petrological nature of the crust and uppermost mantle of the Ligurian-Provence basin, at least along the LOBSTER-P02 seismic profile. They also warrant the same type of study on the SEFASILS controlled-source seismic profile that crosses the northern margin of the basin (Dessa et al., 2020).

The use of OBS recordings in ambient-noise tomography is more challenging than with onshore stations due to shorter recording times, a higher potential of technical problems, sea-floor noises and generally a poorer signal-to-noise ratio in the frequency bands of microseismic noise that are key for ambient-noise tomography. Parts of these problems have been solved here by a specific pre-processing of OBS records that reduces instrument and sea-floor generated noises such as tilt and compliance. When available, land stations can be used in combination with OBSs to provide higher quality surface-wave signals between offshore and onshore stations than for OBS pairs, therefore improving interstation path coverage of ANT in particular at the ocean-continent transition. We went a step further by showing how to take full benefit of onshore stations to enhance the quality of correlations for OBS pairs. Our Rayleigh-wave reconstruction scheme for OBS pairs based on second-order correlations between OBSs and land stations has proven to be effective in improving the coverage of the offshore domain. Finally, the transdimensional inversion of the enhanced set of Rayleigh-wave group-velocity observations for group-velocity maps and their uncertainties and the following hybrid inversion for V_s that accounts for the water layer have lead to a high-quality 3-D V_s model of the study region. We have therefore set up a complete, efficient and reliable ambient-noise imaging methodology of oceanic domains and their margins using OBSs and land stations that opens new perspectives for the processing of similar datasets.

4.7 Supporting information

Additional Figures and information are presented as the Supplementary Material. Text S1 provides details on the processing applied to remove glitches of instrumental origin from vertical and pressure component records of seven AlpArray seismic network broadband ocean-bottom seismometers (AASN BBOBSs). Text S2 describes how coherent signals are detected and used to reduce tilt- and compliance-induced noises in vertical-component records of the 23 AASN OBSs used in this work. Table 4.2 and Figures 4.10 to 4.17 complement sections 2 to 4 of the main text.

4.7.1 Text S1: Glitch removal

After detrending and demeaning the daily records, we perform a global analysis of the vertical and pressure components to check that the glitches are continuously present and that their periodicity is stable with time. At this stage, we measure the average glitch periodicity on both components. Since the periodicity fluctuates slightly from day to day, we measure the deviation from the average periodicity for each daily record and design a Dirac comb signal of the same periodicity for each record.

This Dirac comb signal is firstly used to extract an average glitch signal by cross-correlation with the corresponding daily record. A synthetic glitch time series is created by convolving the average glitch signal with the Dirac comb. The peak amplitude of the glitches is reduced by subtracting this synthetic glitch time series from the daily records. Then, we further reduce the residual artifacts by matching each glitch individually. This is achieved by searching the combination of time shift and amplitude with respect to average that best fits each residual glitch. In that aim, we compute the least-square solution of the linear system:

$$GA = r \longmapsto \begin{bmatrix} g_-(t) & g_+(t) \end{bmatrix} \begin{bmatrix} A_- \\ A_+ \end{bmatrix} = r(t) \tag{4.6}$$

where g_-, g_+ are one left-shifted and one right-shifted average glitch and A_-, A_+ their amplitudes adjustment factor. r is the residual signal that we want to erase. Finally, we subtract from r the matrix product of G and the least-square solution (A_{LSQR}).

4.7.2 Text S2: Seafloor noise reduction

We use transfer functions to correct the vertical-component record by removing coherent signals derived from the three other components:

$$\tilde{Z}(f) = Z(f) - T^*_{\mathbf{z},\mathbf{r}}(f)R(f) \tag{4.7}$$

Z and R are Fourier transforms of the vertical channel $\mathbf{z}$ and the component $\mathbf{r} = \{\mathbf{h1}, \mathbf{h2}, \mathbf{p}\}$, which is either the pressure channel $\mathbf{p}$, or one of the two horizontal channels $\mathbf{h1}$, $\mathbf{h2}$. $\tilde{Z}$ is the Fourier transform of the clean signal $\tilde{z}$. T^* is the conjugate of the transfer function between $\mathbf{z}$ and $\mathbf{r}$ and T^*R is the coherent signal between the two components. f is the frequency.

The transfer function T is computed in the frequency domain by quantifying the coherent function C between $\mathbf{z}$ and $\mathbf{r}$:

$$\begin{aligned} T_{\mathbf{z},\mathbf{r}}(f) &= C_{\mathbf{z},\mathbf{r}}(f)\sqrt{\frac{D_{\mathbf{z},\mathbf{z}}(f)}{D_{\mathbf{r},\mathbf{r}}(f)}}, \\ C_{\mathbf{z},\mathbf{r}}(f) &= \frac{D_{\mathbf{z},\mathbf{r}}(f)}{\sqrt{D_{\mathbf{z},\mathbf{z}}(f)D_{\mathbf{r},\mathbf{r}}(f)}} \end{aligned} \tag{4.8}$$

where $D_{\mathbf{z},\mathbf{z}}$ and $D_{\mathbf{r},\mathbf{r}}$ are the auto-spectral density functions of $\mathbf{z}$ and $\mathbf{r}$, and $D_{\mathbf{z},\mathbf{r}}$ is the cross-spectral density function.

4.7.3 Table and Figures

Period band	Land-Land	Land-OBS	Land-Cleaned OBS
$5s - 10s$	3.85	3.03	3.54
$10s - 20s$	4.32	3.57	4.21
$20s - 40s$	4.03	3.18	3.56
$40s - 70s$	3.58	2.87	3.11

Table 4.2: Signal-to-noise ratio in different period bands for: (1) correlations between land-land stations pairs, (2) correlations between land stations and OBSs raw signals, and (3) correlations between land stations and OBSs pre-processed signals.

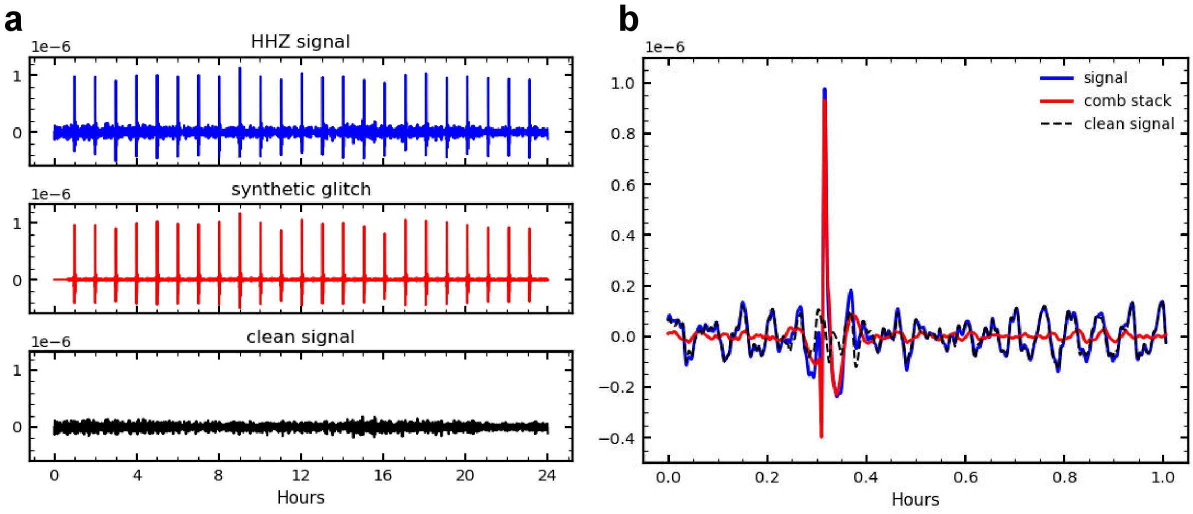

Figure 4.10: Example of result of the glitch removal process applied to a vertical-component 1-day record of the sea-bottom station A416A. (a) Blue: initial record band-pass filtered between 2 and 30 mHz to reduce the micro-seismic peaks and enhance the 1-hr period glitches; Red: synthetic glitch time series used to clean the signal; Black: cleaned record. (b) Blue: 1-hr length slice containing waveform of the first glitch; Red: waveform of the average glitch used to construct the synthetic glitch time series (red trace in a); Black: signal after correcting for the glitch wavelet. Note that: (1) the initial and cleaned signals are quite coherent on both sides of the glitch peak amplitude; (2) phase and amplitude are stable in the vicinity of the removed glitch. This illustrates the efficiency of the glitch removal processing.

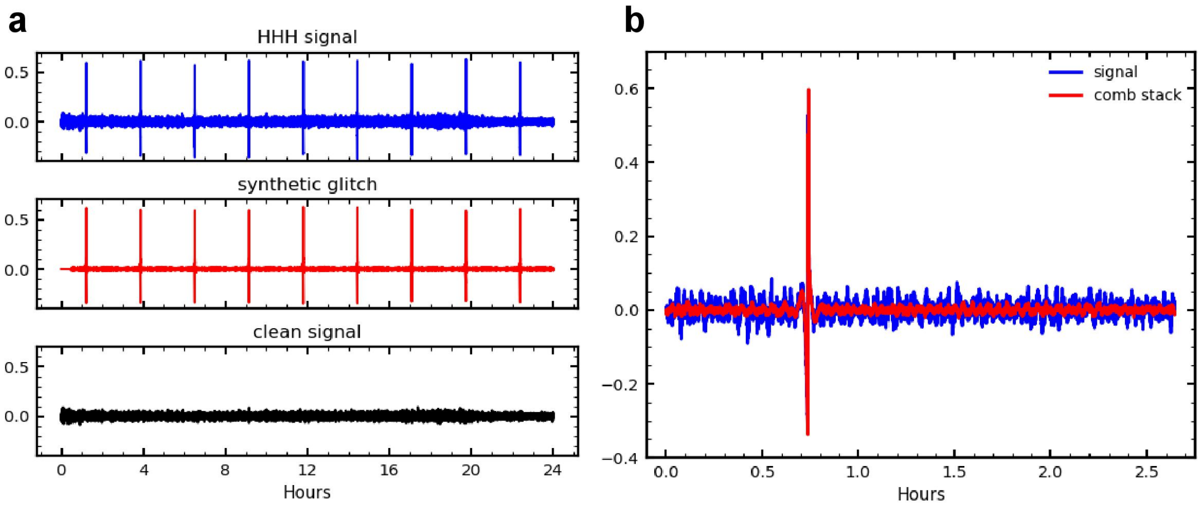

Figure 4.11: Example of result of the glitch removal process applied to a pressure-component 1-day record of the sea-bottom station A416A. (a) Blue: initial record band-pass filtered between 2 and 30 mHz to reduce the micro-seismic peaks and enhance the 2.65-hr period glitches; Red: synthetic glitch time series used to clean the signal; Black: cleaned record. (b) Blue: 2.65-hr length slice containing waveform of the first glitch; Red: waveform of the average glitch used to construct the synthetic glitch time series (red trace in a).

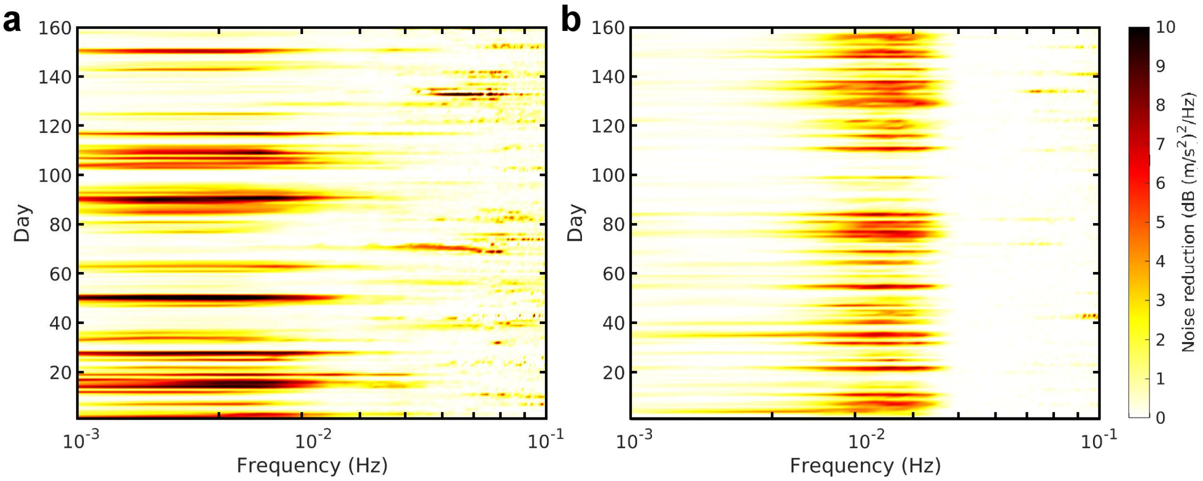

Figure 4.12: Reduction of the noise level after correction from the tilt- (a) and the compliance- (b) induced noises of a 5-month vertical-component record of OBS A416A. For each 1-day record, the amplitude of the reduction is computed from the difference between power spectral densities (PSDs) before and after correction. The frequency range that is most impacted by the noise reduction due to tilt correction (a) is indicated by the gray area in the example of Fig 4.2b in the main text. The frequency band most impacted by the correction for compliance (b) is shown as the green area in the example of Fig 4.2b in the main text. Note that the tilt affects signals over a wide band (below 5×10^{-2} Hz) while the compliance effect is more focused around 1.2×10^{-2} Hz. The noise reduction due to compliance correction is weaker than for tilt correction. However, we observe that tilt is maximum when compliance is minimum and vice versa. During periods of strong tilt (i.e., strong seabed currents), the tilted vertical sensor is less sensitive to signals induced by pressure variations in the vertical direction (i.e., lower compliance effect).

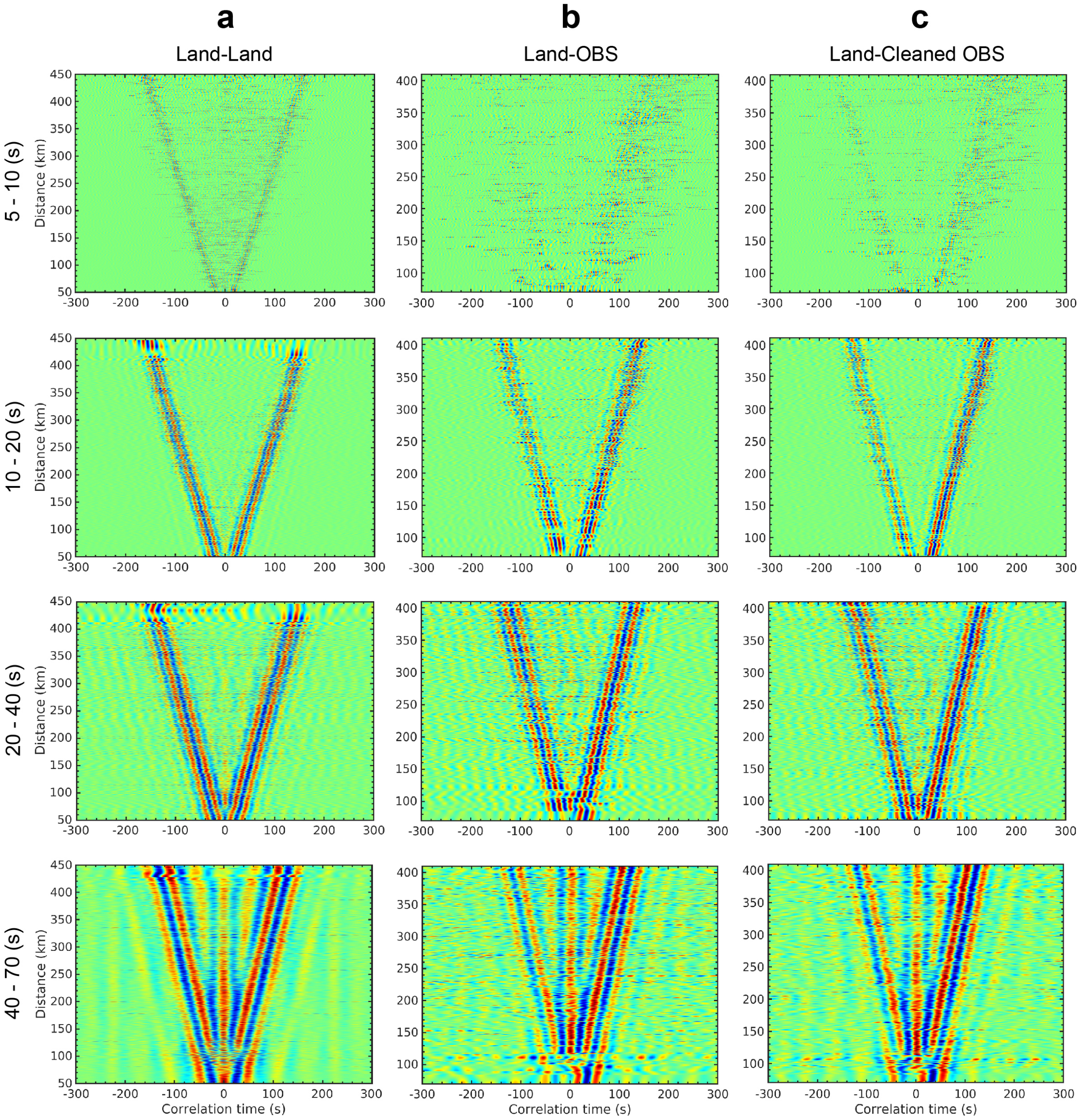

Figure 4.13: Time-distance plots of correlation signals obtained in different period bands. (a) Correlations between land-land stations pairs. (b) Correlations between land stations and OBSs raw signals. (c) Correlations between land stations and OBSs pre-processed signals (glitch removal & seafloor-noise reduction).

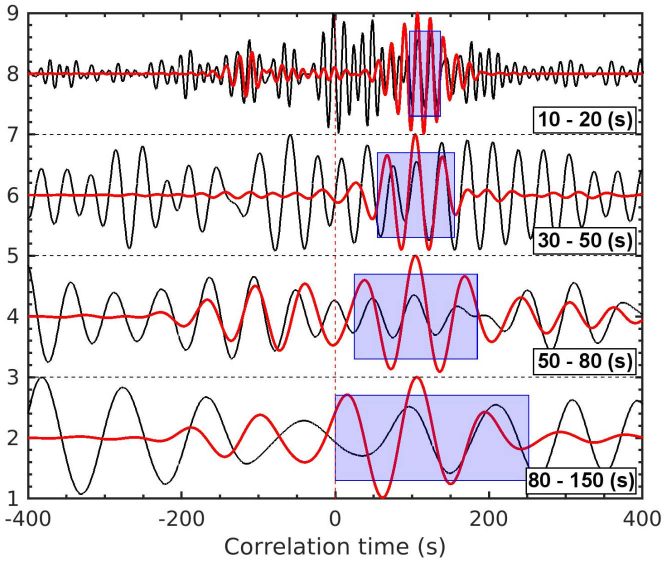

Figure 4.14: Example of comparison between Rayleigh waveforms reconstructed from the first order correlation or 'C^1' (in black) and the iterative correlation or 'C^2' (in red). Signals are normalized and filtered in four different period bands.

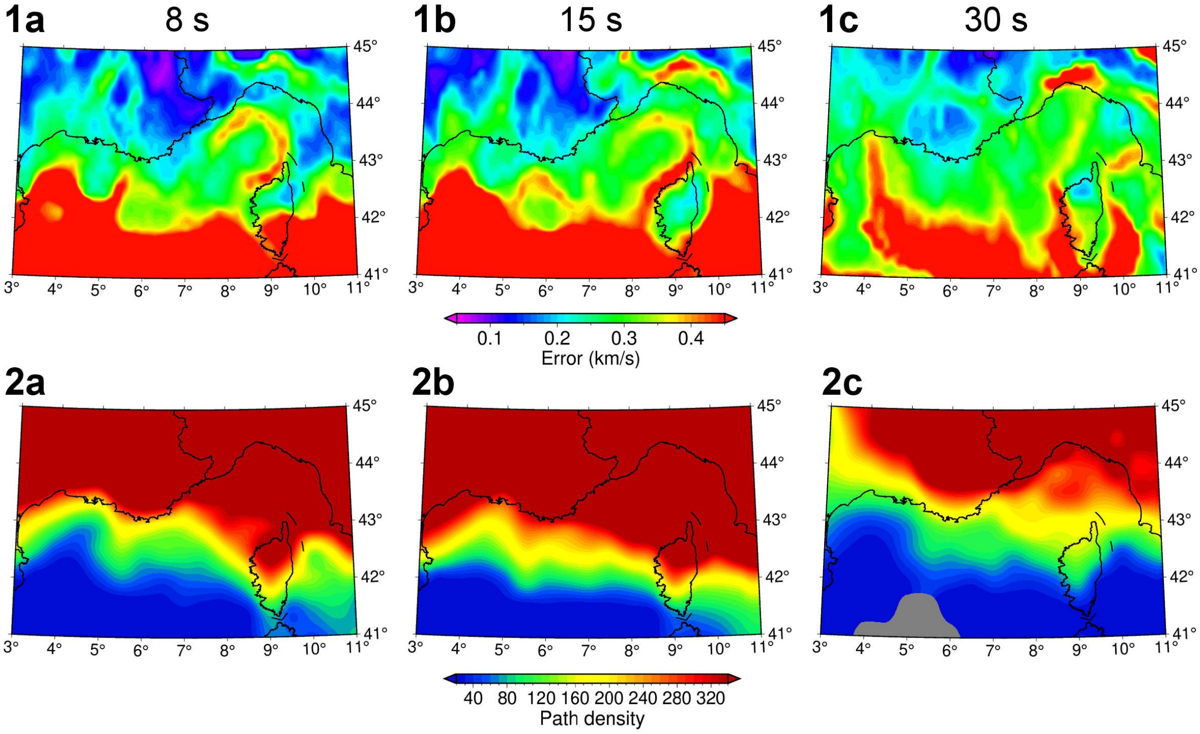

Figure 4.15: Maps of: (1) estimated error of the group-velocity estimates (standard deviation of the ensemble of sampled velocities) at (1a) 8 s, (1b) 15 s and (1c) 30 s; (2) path density (number of paths crossing each 0.15° × 0.15° cell) at (2a) 8 s, (2b) 15 s and (2c) 30 s. Except for regions with strong velocity contrast (see Fig. 4.5 of the main text), uncertainty is generally low where ray coverage is high. Note that the Ligurian-Provence basin is covered by no less than 40 - 50 paths per cell, and that coverage increases in the northwestern part of the basin.

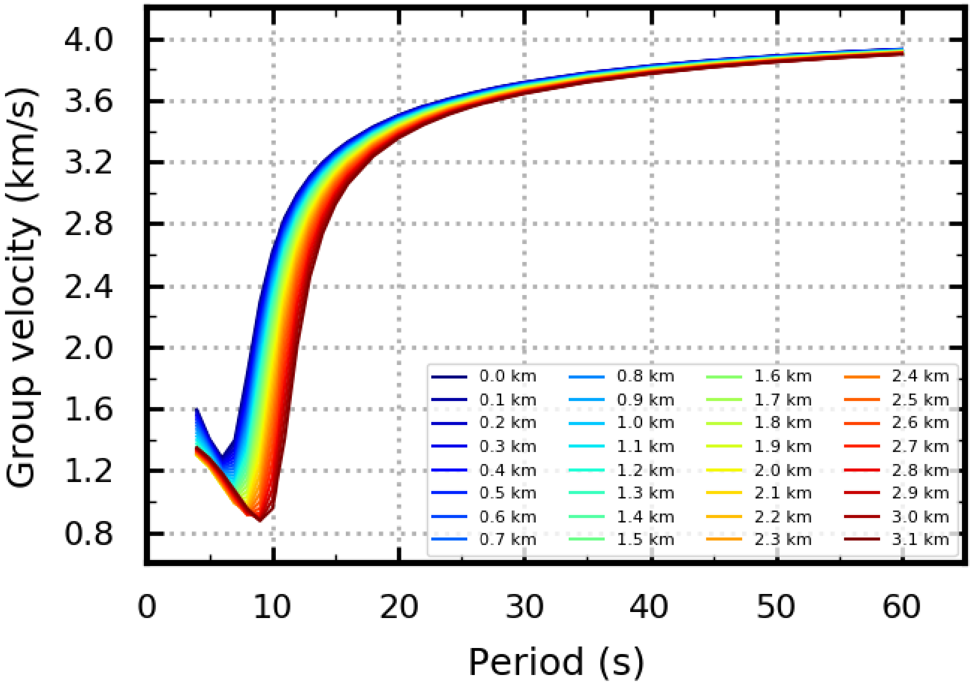

Figure 4.16: Influence of the water layer thickness on a synthetic Rayleigh-wave group-velocity dispersion curve at an offshore location. Dispersion curves are computed for a 3-layer crustal model consistent with a typical oceanic crust of the Ligurian-Provence basin. The underlying uppermost mantle is represented by a half space. Colors indicate dispersion curves computed with different water levels, from 0 to 3.1 km. The presence of the water layer and its thickness variations influence absolute group velocities and the shape of the dispersion curve, particularly at periods shorter than 15 - 20 s. These changes are for instance strong in the vicinity of the Airy phase (minimum of the dispersion curve).

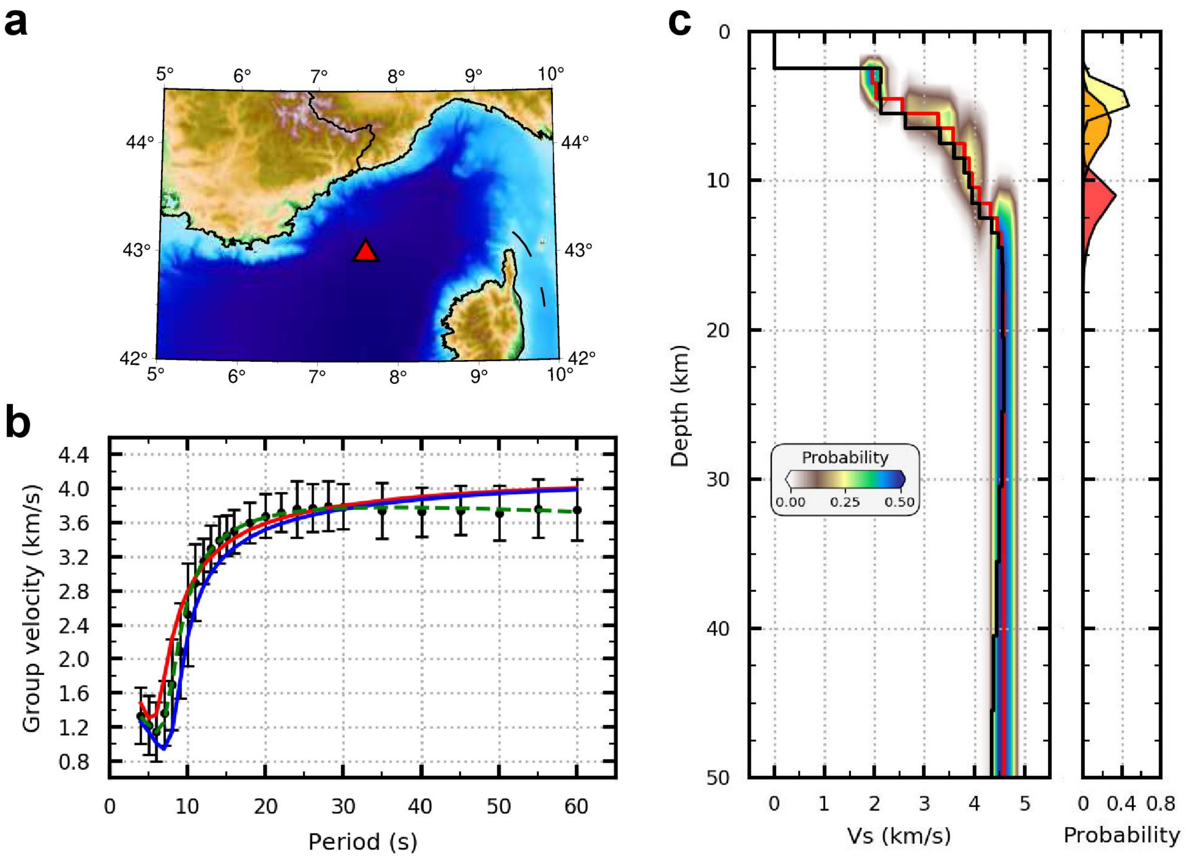

Figure 4.17: Example of the inversion process for V_s at an offshore location in the Ligurian sea. (a) Location map of the selected grid point (red triangle). (b) Group-velocity dispersion curve of Rayleigh-wave for the selected grid point; Black: observed dispersion curve with its uncertainties; Red: predicted dispersion curve for the average Bayesian model; Blue: predicted dispersion curve for the average Bayesian model with water layer on top; Green: predicted dispersion curve after the linear inversion. Note that the average Bayesian model does not fit well the long-period part of the dispersion curve (periods $>$ 30 s) because of the half-space mantle assumption used in the grid search. The fit is further improved after the linear inversion. (c) Resulting velocity models; Left: posterior probability distribution on shear-wave velocity from the Bayesian inversion (background colors), weighted average solution model (posterior mean) predicted from the probabilistic scheme (red line) and final solution model predicted from the linear inversion (black line). Right: posterior probability distribution on layer boundaries resulting from the Bayesian inversion. Three maxima at $\sim$ 5 km, $\sim$ 6.5 km and $\sim$ 11 km depths correspond respectively to the base of the Messinian salt unit, to the base of the sediment layer and to the Moho.

Chapter 5

Wave-Equation Tomography of the Alps and Ligurian-Provence Basin

As seen in Chapters 2 and 4, by combining temporary and permanent, onshore and offshore European seismological stations, we derived a data-driven probabilistic ANT V_s model of the Alps and the Ligurian sea (Nouibat et al., 2022a,b). In Chapters 2, 3 and 4, we validated both its onshore and offshore parts by comparison with independent seismological data available in the western Alps and in the Ligurian-Provence basin (Nouibat et al., 2022a,b; Paul et al., 2022). To build the V_s model, we applied the 'classical' ambient-noise tomography workflow, that is a two-step procedure – a 2-D traveltime inversion for dispersion maps, followed by a 1-D depth inversion for V_s. Our probabilistic procedure allows to explore a large number of possible model solutions for the two steps of the model construction. However, the 'classical' two-step procedures present two main limitations related to simplifying assumptions used in the inversions: (i) the use of ray theory in the 2-D inversion, stating that travel times are only sensitive to the zero-width source-receiver paths, and (ii) the point-by-point inversion at depth for V_s based on 1-D sensitivity kernels of the Rayleigh-wave – valid in a laterally homogeneous media. The last implies that only the vertical fluid-solid interaction is accounted for in the oceanic domain and its margins, neglecting the effect of the lateral interactions.

The present Chapter contains an article (Nouibat et al., in prep) to be submitted soon to *Journal of Geophysical Research*. In this Chapter, we show how the ANT limitations can be addressed with the use of a wave-equation based tomography. The principle objective is to further refine the crust and upper-mantle parts of the ANT V_s model in the western Alps and the Ligurian-Provence basin. We present the methodology of our onshore-offshore wave-equation tomography and its application to the study area. The specificity of this study is to highlight the effect of the water layer on the 3-D propagation of surface waves in oceanic domains and their margins. In particular, we show that ignoring this effect in the 5-20 s may result in wrong physics of the surface-wave propagation and therefore bias in the velocity model. The wave equation tomography improves the contrast and shape of the velocity structures of the initial model (ANT model) by correcting bias related to the assumptions used in the two steps of the ANT inversion. We obtain the highest-resolution V_s model of the Alps and Ligurian-Provence basin to date. This model provides a high-resolution image of the 3-D geometry of the subduction of the European lithosphere beneath the western Alps and further constrain the 3-D structure of Moho in the Ligurian-Provence basin and its conjugate margins.

5.1 Summary

Taking benefit of the entire AlpArray and all available permanent seismic networks in Western Europe, we construct a 3-D onshore-offshore shear-wave velocity model of the crust and upper mantle using ambient noise wave-equation tomography. We use a frequency-dependent phase traveltime misfit function in an iterative procedure to refine a recent 3-D Vs model computed from a Bayesian-based two-step ambient noise tomography. Observed waveforms consist in vertical-component ambient-noise correlations from 600 high-quality broadband stations in the Alpine region and surroundings, including ocean-bottom seismometers (OBS) in the Ligurian Sea. We perform 3-D elastic waveform simulations in the period range 20-85 s. In the 5-20 s period band, we account for the effect of the water layer in the Ligurian Sea by applying solid-fluid coupling for acoustic-elastic waveform simulations. The resulting shear-wave velocity model enhances the velocity structures shape and contrast, accounting for 3-D and finite-frequency effects. It emphasizes the deep sediments of the Ligurian Basin and the Corsica variscan domain and focuses the low-velocity anomalies of the crust beneath the Alps. We obtain a high-resolution 3-D depth map of Moho proxy covering the Alps and Ligurian Sea. In the western Alps, this map confirms the deepening of the European crust following the subduction beneath Adria and validates major structures such as the Moho jump beneath the external crystalline massifs and the Adria Seismic Body (ASB). It provides further constraint on the 3-D architecture of the deep structure beneath the Ligurian basin, regarding the lateral and alog-strike crustal-thickness variations from the oceanic domain to the conjugate margins.

keypoints:

- An improved S-wave velocity model of the crust and upper mantle beneath the western European region, based on wave equation tomography
- 3-D acoustic-elastic coupled modelling of Rayleigh-Scholte wave propagation in the North-western Mediterranean Sea
- High-resolution 3-D depth map of Moho proxy beneath the Alps and Ligurian-Provnce basin

Contents

5.2 Introduction

In the northwestern Mediterranean region, convergence between African and European plates was accommodated by an Oligocene collision leading to the subduction of the European margin beneath Adria micro-plate and the formation of the Alps (e.g., Schmid et al., 2004; Handy et al., 2010; Faccenna et al., 2014), followed by a Miocene-Pliocene opening of the Ligurian-Provence back-arc basin as a result of Adria subduction roll-back (e.g., Gueguen et al., 1998; Séranne, 1999; Jolivet et al., 2020). Hence, a better constraint on the 3-D heterogeneous structure beneath the Alpine and Ligurian-Provence continental and oceanic domains and their transition is crucial to describe the geodynamics of the western Mediterranean region in a global context. Surface geology of the Alpine domain is described by two continental domains that are European foreland to the west (lower plate units) and Adriatic foreland to the east (upper plate units), and in between a subduction wedge of metamorphic units (accretionary prism) delimited by two major crustal-scale accidents that are the Penninic Frontal Thrust (PFT) to the West and the strike-slip Insubric Fault (IF) to the East (Figure 1; e.g., Lardeaux et al., 2006; Schwartz et al., 2009; Agard, 2021). The Ligurian-Provence domain is composed by two conjugate continental margins, Ligurian-Provence margin to the North and Corsica margin to the South, separated by transitional and oceanic domains (Figure 1; Rollet et al., 2002).

With the deployment of the AlpArray temporary seismic network (AASN, Hetényi et al., 2018), the Western European region has become one of the most densely covered areas. More specifically, the region consisting of the Alps and the Ligurian Sea, which includes, in addition to the onshore part of AlpArray, other temporary experiments such as Cifalps-2 in the northwestern Alps (Zhao et al., 2018) and the marine part of AlpArray in the Ligurian-Provence basin. These dense and high-quality surveys provide ideal set up to use ambient seismic noise to resolve the crust and upper mantle, as well as major interfaces such as Moho. Several traditional ambient noise tomography (ANT) were conducted in the region; based on a two-step workflow: (1) 2-D traveltime inversion for group velocity maps, and (2) 1-D depth inversion for Vs based on the local dispersion curve. Following on from the large-scale ANT by Lu et al. (2018), which used a part of the land component of AlpArray, the recent ANT by Nouibat et al. (2022a,b) was the first study to use the entire AlpArray, resulting in a land-sea model covering the Alps and the northwestern Mediterranean. These large-scale models combined with other more regional ANT models, e.g, in the western Alps, Zhao et al. (2020); in the southeastern Alps, Sadeghi-Bagherabadi et al. (2021); in the Vienna basin, Schippkus et al. (2020); in the Bohemian massif, Kvapil et al. (2021); in the Ligurian sea, Wolf et al. (2021) and Magrini et al. (2022), have substantially improved existing knowledge and provided new insights into the complex deep structure of the region: Moho jumps beneath the external crystalline massifs (Lu et al., 2018; Nouibat et al., 2022a), subduction of the European continental crust beneath Adria (Zhao et al., 2020; Nouibat et al., 2022a), and the structure of the crust beneath the Ligurian Basin (Wolf et al., 2021; Nouibat et al., 2022b), etc. However, these two-step inversion based models suffer from two major limitations that may bias geological interpretations: (1)

the ray theory assumption in the first step, which is only valid in the high-frequency case (e.g., Snieder, 1986; Cerveny, 2003), and (2) the local 1-D nature of the depth inversion in the second step, which does not account for the 3-D lateral heterogeneity of the medium, thus limiting the velocity model to be pseudo-3-D by construction.

Tomographic methods based on the wave equation are an alternative of choice to overcome such simplifying assumptions, as they naturally accommodate for 3-D heterogeneity and finite-frequency effects, thus providing more realistic sensitivity kernel for surface waves. These approaches consist in iteratively updating the velocity model by minimising a misfit function between observed and synthetic waveforms obtained through 3-D numerical modelling of seismic wave propagation. Although full waveform inversion (FWI), which relates to waveform differences (i.e. phase and amplitude), has been widely used for crust and uppermost mantle scales using earthquake body waves (e.g., Tape et al., 2010; Zhu et al., 2012; Yuan et al., 2014; Fichtner and Villaseñor, 2015; Beller et al., 2018), its applications for ambient noise cross-correlations is still challenging because of the sensitivity to the anisotropic distribution of noise sources. However, wave-equation tomography (WET) using traveltime differences from noise correlations has recently demonstrated its potential in resolving small-scale structures and refining velocity models of the crust and upper-mantle (e.g., Chen et al., 2014; Liu et al., 2017). Using ambient-noise cross-correlations from the data set of Lu et al. (2018), Lu et al. (2020) applied WET to the Alpine region in the 10-50 s period band in order to improve the crustal part of the ANT model by Lu et al. (2018). They computed forward simulation and misfit gradient using 3-D elastic wavefield modelling for a uniform distribution of virtual sources consisting in 64 stations. Although this model confirmed the presence of the Moho jump observed in their initial model under the external crystalline massifs in the northwestern Alps and increases the resolution of other existing features (e.g., Ivrea body), it failed in mapping subduction of the European continental crust although it is evidenced by receiver functions (Zhao et al., 2015; Paul et al., 2022) and a recent ANT model (Nouibat et al., 2022a). Indeed, there was no substantial change in the structure of the crust in the resulting WET model beyond the change in magnitude and contrast of the anomalies in response to the correction for a systematic velocity shift for periods lower than 25 s resulting from a bias in their initial model. Moreover, this model only covers the onshore part as Lu et al. (2020) only used a part of the terrestrial component of AlpArray, while its offshore part was not yet available.

In this study, we present an improved WET methodology to that used by Lu et al. (2020). Theses improvements consist in: (i) perform an acoustic-elastic coupled wave equation tomography to achieve a more realistic constrain on velocity structure in the oceanic domain of the Ligurian basin and along the continental margins; (ii) invert seismic data in a broader band (5-85 s) in order to constrain the shallow part of the crust as well as the deeper part of the mantle, and employ a hierarchical inversion strategy that avoids possible cycle-skipping issues; (iii) using a random sub-sampling scheme over 185 virtual sources rather than a fixed number of virtual sources. Similar to Lu et al. (2020), we minimize the frequency-dependent phase traveltime differences of surface waveforms and tackle the inversion using the SEISCOPE SEM46 code originally developed for exploration scales (Trinh et al., 2019). Taking advantage of the densest seismological coverage to date, including the entire AlpArray network, we perform this methodology at the scale of Western Europe in order to refine the land-sea model by Nouibat et al. (2022a) from conventional ANT. This model is the most up-to-date and constrained model of the crust and upper-mantle beneath the Alpine region. It has notably confirmed in 3-D the subduction of European lithosphere beneath Adria. The offshore part of this model represents the best 3-D Vs model of the crust beneath the Ligurian sea to date.

The combination of the availability of offshore, onshore-offshore and onshore-onshore cross-correlation data throughout the Ligurian sea, the offshore extension of the ANT model, and the recent implementation work to deal with coupled acoustic-solid media in SEM46 (Cao et al., 2022), motivated us to go further in the improvement of wave equation-based ambient noise imaging by considering the effect of the water layer on the 3-D propagation of surface waves from ambient noise correlations. In a oceanic domain, two types of surface waves of different properties in terms of amplitude intensity and velocity propagation can be superimposed: Scholte waves (fluid-solid interface waves) and the long-period content of the dispersion of Rayleigh waves which are free surface solid waves. The distinction between the two types of waves, the conversion from one to the other or their superposition, is not generally addressed in marine ambient noise imaging. Scholte waves are generally treated as Rayleigh waves by neglecting the presence of the water layer. Nevertheless, methodological efforts to address this issue have been mainly dedicated to improvements of traditional ANT by considering the effect of the water column on the local dispersion in the 1-D depth inversion framework (e.g., Mordret et al., 2014; Guerin et al., 2020; Wolf et al., 2021; Nouibat et al., 2022b; Carvalho et al., 2022), assuming only the effect of a vertical coupling. Nouibat et al (2022b) have shown that a water layer thicker than 0.5 km may have a significant effect on the local dispersion curve (at periods ≤ 20 s) and thus should be taken into account in the 1-D inversion for V_s in the conventional ANT workflow. However, this is not sufficient as it implies a strictly 1-D coupling in a laterally homogeneous medium. Furthermore, the dispersion maps used to extract the local dispersion curve are derived without accounting for the effect of the water since the 2-D inversion step assumes surface-wave ray paths in elastic medium. This biases the physics in the local dispersion curve, even if the 1-D effect of the water layer is taken into account in its inversion for V_s. To fully recover the effect of the water layer, the 3-D fluid-solid interaction needs to be addressed. An accurate modeling of surface-wave propagation through/along a rough seafloor such as in the Ligurian Sea is therefore important to that end. For this purpose, we apply a fluid-solid coupling for acoustic-elastic 3-D simulations and compare with observed data. The objective is twofold. Firstly, to investigate the influence of the water layer on the propagation of surface waves between onshore and sea-bottom stations, more specifically, the Rayleigh-Scholte waves. To our knowledge, this is the first study to document the influence of the water layer on the 3-D propagation of ambient noise surface waves. The second goal is to incorporate the fluid-solid coupling in the inversion framework, which makes this study the first ambient noise wave equation tomography to account for the effect of 3-D coupling for deep imaging including marine environment.

The objective of this study is to build a self-consistent high-resolution onshore-offshore 3-D V_s model. This model is intended to better constrain the geometry of the European Moho and refine the imaging of subduction wedge and assess the pertinence of other major features shown by Nouibat et al. (2022a) in the continental part, such as the low-velocity anomalies at the base of the lower crust and the Adria seismic body (ASB). Its offshore part is designed to improve the 3-D velocity structure in the marine environment of the ANT model, in particular by correcting for any bias deriving from ignoring the 3-D effect of the water layer. Finally, we will use this 3-D model to derive an homogeneous 3-D Moho depth map, covering the Alps and the Ligurian-Provence basin.

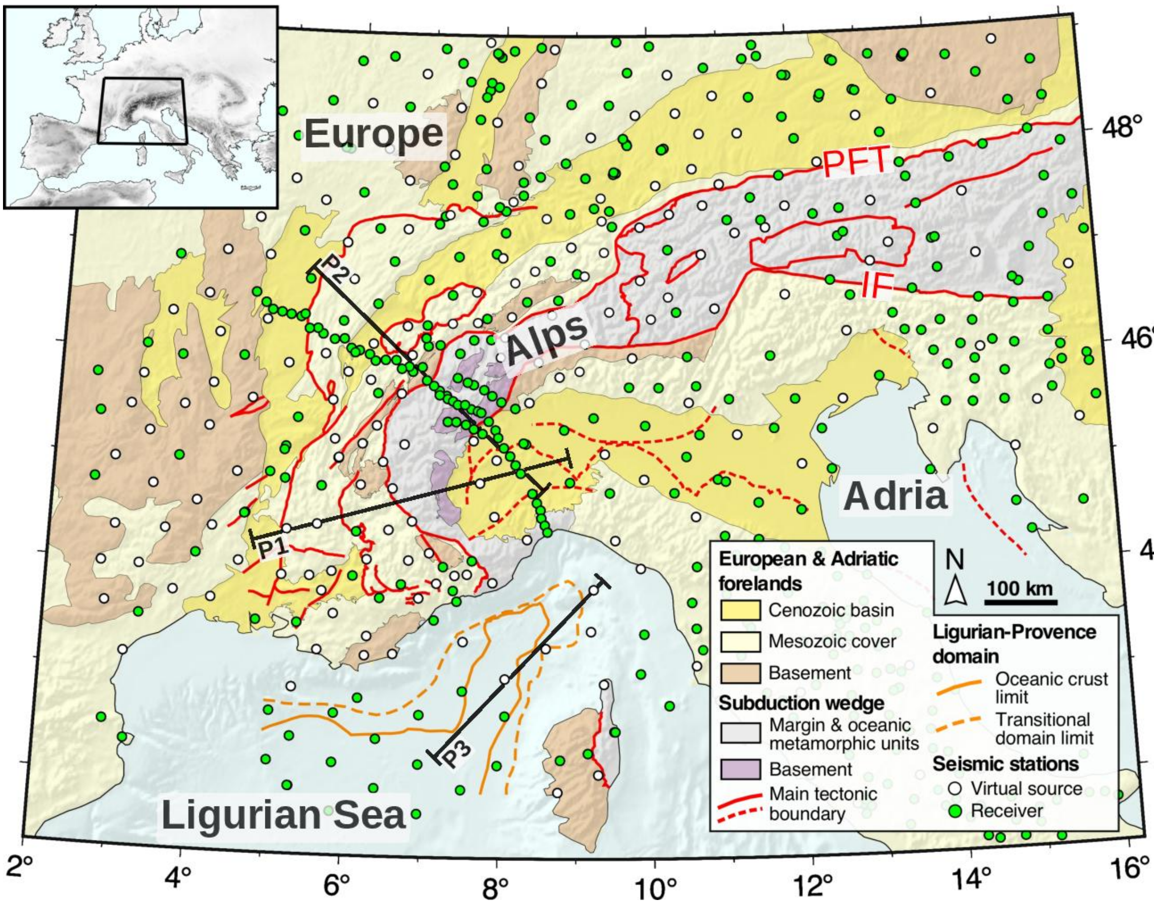

Figure 5.1: Geological and tectonic setting of the study area modified from Handy et al. (2010) in the Alpine domain and from Rollet et al. (2002) in the Ligurian Sea, with locations of seismic stations used in this work (white circles: virtual sources; green circles: receivers). Black lines show locations of the seismic profiles discussed in the text.

Section 2 describes the dataset of ambient-noise correlations and the initial velocity model used in the wave equation tomography. The overall methodology is presented in Sections 3–4. Section 3 introduces the iterative process of the WET workflow, while Section 4 is dedicated to 3-D modelling of surface waves, with emphasis on the acoustic-elastic case. In the light of the specific case of the Ligurian-Provence basin, we document the importance of the fluid-solid coupling for marine crustal imaging based on ambient noise data. In Section 5, we assess the robustness of the resulting 3-D V_s model. Section 6 presents tomography results and related discussions; depth slices, 2-D transects, and a proxy of the 3-D depth map of Moho.

5.3 Data

5.3.1 Ambient noise processing

We use cross-correlations of vertical-component seismic noise records from the dataset of Nouibat et al. (2022a,b). It involves 600 broadband stations from all available temporary and permanent networks in Western Europe between 2015 and 2019, including the entire AlpArray Seismic Network (AASN) and the Cifalps-2 experiment (Fig. 5.1). Correlations between onshore stations are computed after a standard comb-filter processing of noise records. Nouibat et al. (2022b) applied a specific processing to remove transients and reduce seafloor-induced noises from records of the AASN OBSs, and used an iterative approach to compute correlations between OBSs by involving onshore station records. All stations in Figure 1 serve as virtual receivers, out of which 185 stations are selected as virtual sources. Waveforms are filtered in four period bands: 5-10 s, 10-20 s, 20-40 s, and 40-85 s with frequency corners adjusted to those used in the pre-processing of ambient-noise waveforms to avoid overlap problems. We keep only reliable cross-correlations by applying the following criteria: (1) signal-to-noise ratio (SNR) greater than 5, (2) inter-station distance larger than one wavelength for the maximum period considered in each period-band. The final dataset includes 10000-35000 high-quality cross-correlations depending on the period band.

5.3.2 Initial model

The initial model is the 3-D onshore-offshore V_s model by Nouibat et al. (2022a) computed by ambient-noise tomography using all available permanent and temporary seismic networks in Western Europe from 2015 to 2019. This model is derived from a hybrid data-driven tomography involving a 2-D transdimensional Bayesian inversion for group-velocity maps and their uncertainties, and a 1-D probabilistic inversion for V_s at depth. The onshore part of this model has been validated in the western Alps by comparison with other available geophysical studies, e.g, receiver functions, controlled-source seismic experiments, Bouguer anomaly along the Cifalps & Cifalps-2 profiles (Nouibat et al., 2022a; Paul et al., 2022). The offshore part has been validated by comparison with a high-resolution V_p cross-section derived from refraction and wide-angle seismic profiling along the axis of the Ligurian basin (Nouibat et al., 2022b). Based on the extensive land-sea coverage of the seismic array and the improved ANT methodology that were used, this model is so far the best resolved model at the scale of Western Europe. However, it remains limited by the assumptions made in the two steps of the inversion, in particular the high-frequency assumption for Rayleigh-wave propagation in the 2-D inversion, and the 1-D assumption in the inversion for V_s. Furthermore, even if Nouibat et al. (2022b) considered the water column in the oceanic part, they assumed Rayleigh-mode dispersion, which might be problematic in the case of Rayleigh-Scholte mode conversion or pure Scholte-mode dispersion. The objective of the present study is to overcome these limitations and improve the resolution of the V_s model by performing wave-equation tomography.

5.4 Iterative inversion scheme

Similar to Lu et al. (2020), we formulate the inverse problem as the minimization of the misfit function (ξ) defined by the differences of frequency-dependent phase traveltime between observed and synthetic vertical-component waveforms of ambient-noise Rayleigh waves

$$\min_{\mathbf{m}} \xi(\mathbf{m}) = \frac{1}{2} \sum_{i} \sum_{\omega} \Delta T_i(\omega, \mathbf{m})^2, \tag{5.1}$$

where $\Delta T_i(\omega, \mathbf{m})$ is the phase traveltime residual for the ith station pair at frequency ω, given the model parameters ($\mathbf{m}$). We measure ΔT using a multi-taper technique (Tape et al., 2010). We tackle the minimization of (ξ) using a quasi-Newton local optimization method, with the following iterative scheme:

$$\mathbf{m}_{k+1} = \mathbf{m}_k + \alpha_k \delta \mathbf{m}_k \tag{5.2}$$

where α_k is the step length estimated by line search strategy and $\delta \mathbf{m}_k = -B_k \nabla \xi(\mathbf{m}_k)$ is the model update in which B_k is an approximation of the inverse of the Hessian H matrix (i.e. the second-order derivative of ξ with respect to model parameters). We use the limited memory version of quasi-Newton methods (l-BFGS) to estimate B_k using gradients at few previous iterations. We update the velocity model by inverting from low to high frequencies, in four narrow period bands: 5-10 s, 10-20 s, 20-40 s, and 40-85 s. Given the dispersive character and depth sensitivity of the Rayleigh-wave phase velocity at these periods, such a hierarchical approach is useful to prevent cycle skipping issue. This approach first constrains large-scale anomalies in the upper mantle part of the model using the long-period content, then it constrains small-scale anomalies in its crustal part using the short-period content.

We reconstruct simultaneously V_s and V_p to account for the sensitivity of the Rayleigh-wave to V_p, which becomes non-negligible at short periods (e.g., Eddy and Ekström, 2014; Qiao et al., 2018). Therefore, the relative perturbation of the misfit function (ξ) to perturbations of the two parameters is given by the linear relation: $\delta\xi(\mathbf{m}) = K_{V_s}(\mathbf{m})\delta \ln V_s + K_{V_p}(\mathbf{m})\delta \ln V_p$, where K_{V_s} and K_{V_p} are the sensitivity kernels for V_s and V_p respectively (i.e. misfit gradients with respect to V_s and V_p). Due to the computational cost of modelling for multiple sources, we employ a randomized sub-sampling strategy of the ensemble of virtual sources over iterations in order to achieve optimal path coverage without compromising the quality of the inversion results. The general workflow of the inversion is summarized in the following:

(1) Perform the forward modelling for subsets of 64 virtual sources.

(2) Measure phase traveltime misfits between observed and simulated waveforms and compute the adjoint sources.

(3) Perform the adjoint modelling and extract gradients from cross-correlations of incident and adjoint fields.

(4) Gradients are summed and smoothed using a 2nd-order Bessel filter with coherent lengths computed from the local wavelength associated with model velocity, at the maximum frequency considered (Trinh et al., 2017).

(5) Estimate the step length and update the current velocity model.

(6) At each 3 iterations, another subset is selected. The inversion at the current period-band is stopped after 9 iterations and the output model is used for the next shorter period-band following the same iterative procedure. The density model is updated accordingly using empirical formulas (Brocher, 2005).

5.5 3-D simulations of surface-wave propagation

We perform forward and adjoint simulations using the time-domain wave-equation modelling of the SEM46 spectral-element-based code. We simulate the propagation of the vertical component of Rayleigh waves by applying a point-force at the location of virtual sources whith a filtered Dirac delta as source-time function. Therefore, the synthetic waveform (u_{syn}) at a receiver position for model ($\mathbf{m}$) is the convolution product between the source time function (s) and the synthetic Green's function (G_{syn}) for the source–receiver pair (e.g., Lu et al., 2020): $u_{syn}(\mathbf{m}, t) = s(t) \ * \ G_{syn}(\mathbf{m}, t)$. To compare with synthetic waveforms, we convolve the source time function (s) with the time derivative of the noise cross-correlation (C) for the source–receiver pair, which is a good approximation of the Green's function (G) of the target medium (e.g., Lobkis and Weaver, 2001; Snieder, 2004; Wapenaar, 2004; Roux et al., 2005; Weaver, 2005): $u(t) = s(t) \ * \ -\partial_t C(t) \approx s(t) \ * \ G(t)$. The time sampling of simulation varies from 0.04 to 0.0015 s, with the CFL condition satisfied. Surface waves are extracted in a time window with $min[d/5, t_{max} - 1.5T]$ and $max[d/2, t_{max} + 1.5T]$ as lower and upper limits in the 10-20 s, 20-40 s, and 40-85 s, and a time window with $min[d/1.5, t_{max} - 2T]$ and $max[d/4, t_{max} + 2T]$ as lower and upper limits in the 5-10 s, where d is the interstation distance (in km), t_{max} is the arrival time of the maximum of the envelope of synthetic waveform, and T is the maximum period of the considered band.

5.5.1 Elastic modelling of Rayleigh waves

We simulate the incident wavefield in the 20-85 s period band by solving the second-order elastic wave equation:

$$\rho_s \partial_{tt} \mathbf{u} = \nabla \cdot \boldsymbol{\sigma} + \mathbf{f}_s, \quad \boldsymbol{\sigma} = \mathbf{C} \boldsymbol{\varepsilon} \tag{5.3}$$

where $\mathbf{u}$ is the displacement field, $\mathbf{f}_s$ is the force vector, $\boldsymbol{\sigma}$ and $\boldsymbol{\varepsilon}$ are the second-order stress and strain tensors respectively, ρ_s is the solid density and $\mathbf{C}$ is the fourth-order elastic stiffness tensor. The velocity model is discretized based on a flexible 3-D Cartesian-based hexahedral mesh, with element size in the solid domain varying from 15 to 6 km and from 10 to 4 km in the horizontal and vertical directions, respectively. We parameterize Gauss–Lobatto–Legendre (GLL) points by isotropic P-, S-wave velocities and density, starting from the S-wave velocity model described in section 2, and the (V_p, ρ) computed from V_s by empirical formulas (Brocher, 2005).

Misfit elementary gradients with respect to the medium parameters are obtained from the zero-lag correlation of adjoint and incident wavefields, based on the adjoint-state method (Plessix, 2006). Adjoint wavefields are obtained by injecting the adjoint sources at receiver locations in the adjoint wave equations. The adjoint source for the multi-taper method is given by the derivative of synthetic waveforms weighted by the frequency-dependent phase difference measurements (Tape et al., 2010). Gradients of (ξ) with respect to the solid parameters (ρ_s, C_{IJ}) are obtained by the zero-lag cross-correlations

$$\frac{\partial \xi\left(\mathbf{m}\right)}{\partial \rho_s} = \left(\bar{\mathbf{u}}, \partial_{tt} \mathbf{u}\right)_{\Omega_s, t}; \quad \frac{\partial \xi\left(\mathbf{m}\right)}{\partial C_{IJ}} = \left(\bar{\boldsymbol{\varepsilon}}, \frac{\partial \mathbf{C}}{\partial C_{IJ}} \boldsymbol{\varepsilon}\right)_{\Omega_s, t} \tag{5.4}$$

where $\bar{\mathbf{u}}$ is the adjoint wavefield vector associated with $\mathbf{u}$, and $\bar{\boldsymbol{\varepsilon}}$ is the adjoint of the strain field $\boldsymbol{\varepsilon}$ for model sets Ω_s.

5.5.2 Acoustic-elastic modelling of Scholte-Rayleigh waves

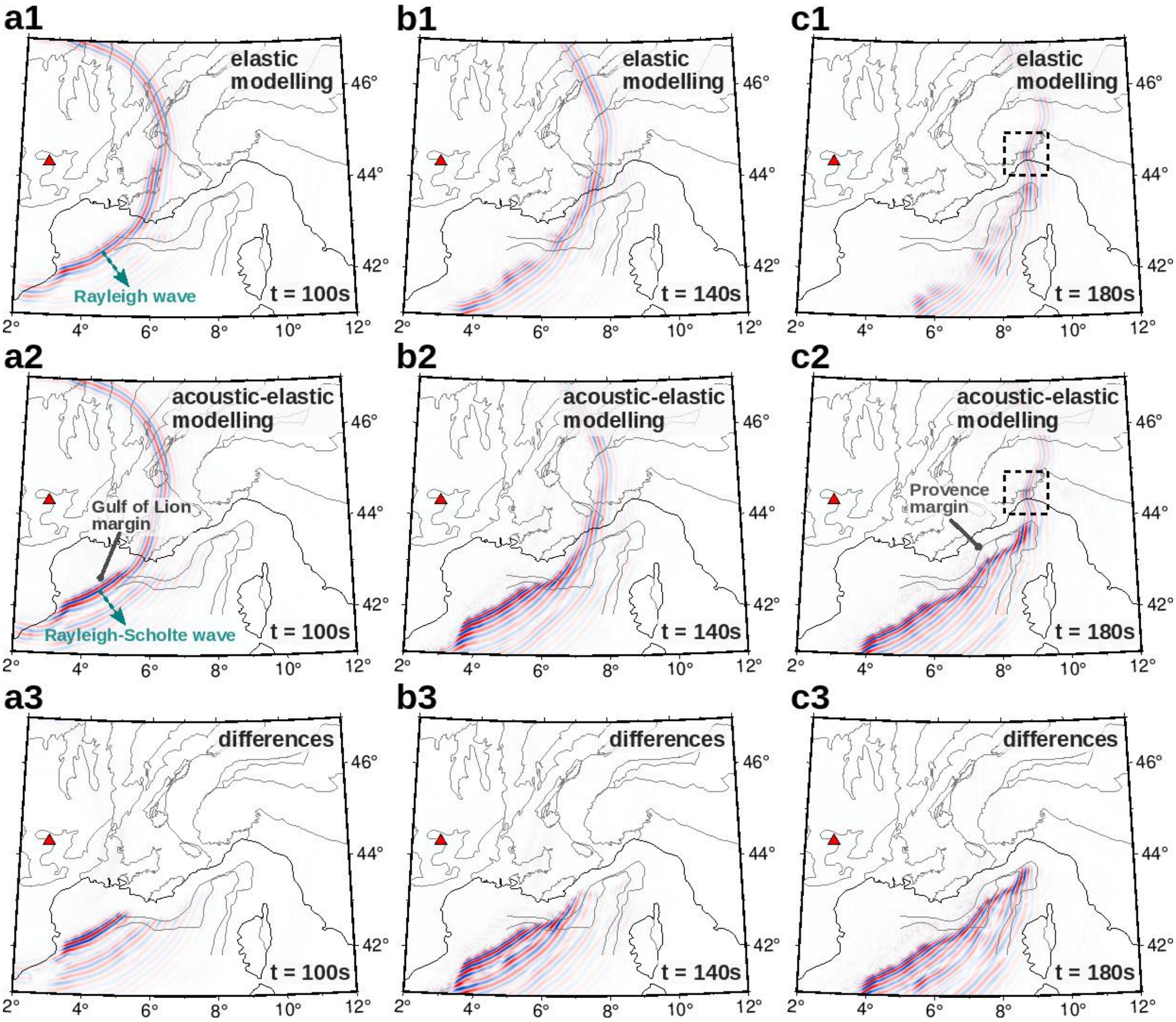

Figure 5.2: Comparison of snapshots of the vertical displacement wavefield in the 5-10 s period-band simulated using (a1-c1) the elastic wave equation, (a2-c2) the acoustic-elastic coupled wave equation for the source station indicated by the red triangle. (a3-c3) show the differences between the elastic and acoustic-elastics wavefields. The wave fields are extracted on a 3-D surface corresponding to the topography in the onshore part and to the bathymetry of the sea floor in the marine part. Black dashed frames show scattered Rayleigh-wave packets. The thin black lines are geological and tectonic boundaries (Fig. 5.1).

Since we also invert phase dispersion data for S-wave velocities in the Ligurian-Provence basin, we have to consider the influence of the seafloor topography on the propagation of surface waves in the 5-20 s period band. Indeed, Scholte waves can be excited as a result of the fluid-solid interaction (e.g., Zheng et al., 2013; Zhu et al., 2004). Scholte waves can also be generated from Rayleigh-Scholte mode conversion at the continent-ocean transitions. To further investigate this influence, we account for the effect of the water layer by considering fluid-solid coupling in the 3-D wave equation through the second-order equation system (Cao et al., 2022):

$$\begin{aligned}
&\rho_s \partial_{tt}\mathbf{u} = \nabla\cdot\boldsymbol{\sigma} + \mathbf{f}_s, \quad \boldsymbol{\sigma} = \mathbf{C}\boldsymbol{\varepsilon}, && \text{in } \Omega_s,\\
&\frac{1}{\kappa}\partial_{tt}\varphi - \nabla\cdot\left(\frac{1}{\rho_f}\nabla\varphi\right) = \frac{1}{\kappa}\iint -P_f dt dt, && \text{in } \Omega_f,\\
&\mathbf{u}\cdot\mathbf{n} = \frac{1}{\rho_f}\nabla\varphi\cdot\mathbf{n}, \quad \boldsymbol{\sigma}\cdot\mathbf{n} = \partial_{tt}\varphi\mathbf{n}, && \text{on } \Gamma_{fs}.
\end{aligned} \tag{5.5}$$

where the first equation describes the elastic wave propagation in the solid domain (Ω_s) in terms of displacement vector $\mathbf{u}$ (same as Eq. 3), the second equation describes the acoustic wave propagation in the fluid domain (Ω_f) in terms of scalar displacement potential φ, P_f is the pressure source associated with a force vector $\mathbf{f}_f$, ρ_s is the fluid density and κ is the bulk modulus of the fluid. The third system gives the boundary conditions along the fluid–solid interface (Γ_{fs}), describing the interaction between the two domains. Our implementation considers a staircase fluid-solid coupling to handle the meshing of the seafloor and consider a minimum vertical size of 200 m for elements in the water column, ensuring proper sampling of waves in water. Misfit gradients in the solid domain are given by expressions (4). In the fluid domain, gradient building is performed following the hybrid approach proposed by Cao et al. (2022). Gradients of (ξ) with respect to the fluid parameters (ρ_f, κ) are then obtained by the zero-lag cross-correlations:

$$\frac{\partial\xi(\mathbf{m})}{\partial\rho_f} = \left(\nabla\bar{P}, \frac{1}{\rho_f^2}\nabla P\right)_{\Omega_f,t}; \quad \frac{\partial\xi(\mathbf{m})}{\partial\kappa} = \left(\bar{P}, \frac{1}{\kappa^2}\partial_{tt}P\right)_{\Omega_f,t} \tag{5.6}$$

The gradients on V_p and V_s are estimated using elementary gradients (4) and (6) based on chain rule.

Figure 5.2 shows snapshots of the simulated vertical displacement at the surface in the 5-10 s period band for an onshore source station located in southern France. We performed elastic (Fig. 5.2a1-c1) and acoustic-elastic modelling (Fig. 5.2a2-c2) in the initial model and computed their differences (Fig. 5.2 a3-c3). Figure 5.3 shows synthetic surface waveform fits to data at an OBS located in the central Ligurian-Provence basin at a depth of $\sim$ 2700 m (location in Fig. 5.3a). Figures 3b1,b2;c1,c2 and d1,d2 show simulations in the initial model and Figures. 3b3,c3,d3 show simulations in the final model. In the elastic modelling case, the source–OBS pair is assumed to be located on the free surface. We therefore observe the propagation of a Rayleigh wave everywhere in the oceanic part (Fig. 5.2a1,c1). In the acousitc-elastic case, we account for the fluid-solid coupling by considering the presence of the water layer in the basin. In this case, we detect a mode conversion from Rayleigh to Rayleigh-Scholte wave at the Gulf of Lion margin. The resulting wave packet is characterized by stronger amplitude and slower propagation velocity inducing strong wavefront distortion (Fig. 5.2a2,c2). However, we notice in both modeling cases a dissipation within the Ligurian-Provence basin and almost the same wavefield in the continental part, as expected. For instance, both simulations evidence a scattering of the wave packet to the north of the Ligurian sea (dashed black frame in Fig. 5.2c1,c2). As highlighted in Fig. 5.2a3,c3, the discrepancies in amplitude and travel time, mostly in the oceanic part, are significant. Indeed, the arrival time of the Rayleigh-wave envelope from elastic modelling in the 5-10 s band is $\sim$ 35 s earlier than that of the Rayleigh-Scholte wave from acoustic-elastic modelling (Fig. 5.3b1). The arrival time of the observed surface wave is much closer to the arrival time of the simulated signal with fluid-solid coupling (Fig. 5.3b2). This fit is further improved after inversion as shown in Fig. 5.3b3. Differences between the two modeling results are also visible in the 10-20 s period band with a lower but still significant misfit due to the free-surface boundary condition (Fig. 5.3c1-c3). As illustrated in Figures 3d1-d3, the differences between elastic and acoustic-elastic simulations are negligible in the 20-40 s period band, showing that the surface wave in these period ranges becomes insensitive to the coupling effect. Furthermore, the waveform computed from elastic modelling in the final model fits very well the observed signal, indicating that the elastic assumption is efficient at long periods. Finally, even though amplitude differences are not built into the misfit function, the fits of the observed waveforms are quite good, and they are improved by the WET, which points to the robustness of the initial model and the inversion. This example illustrates that neglecting the effect of the water layer in this context would lead to significant phase shifts, biasing the robustness of the velocity model and inducing cycle skipping issues.

Figure 5.4 shows snapshots extracted at the solid surface (topography and seafloor) and at 10 km depth, in the 5-10 s period band for an OBS source located in the northeastern part of the basin. A significant amplitude attenuation of the wave propagating in the Ligurian-Provence and Tyrrhenian basins is observed at 10 km depth. This is consistent with the trapping of the Rayleigh-Scholte wave in the vicinity of the elastic-acoustic interface (Nayfeh, 1995). Hence, we detect the long-period dispersion of the elastic wave at 10 km depth, and a undistorted wavefront. Finally, Figure 5.4 shows that wave packets are dissipated in the oceanic part (Ligurian-Provence and Tyrrhenian basins) or through the sharp Provence margin towards the continental part. This example suggests that considering the fluid-solid interaction would help to recover the shallow 3-D velocity structures, as it will be illustrated in the next section.

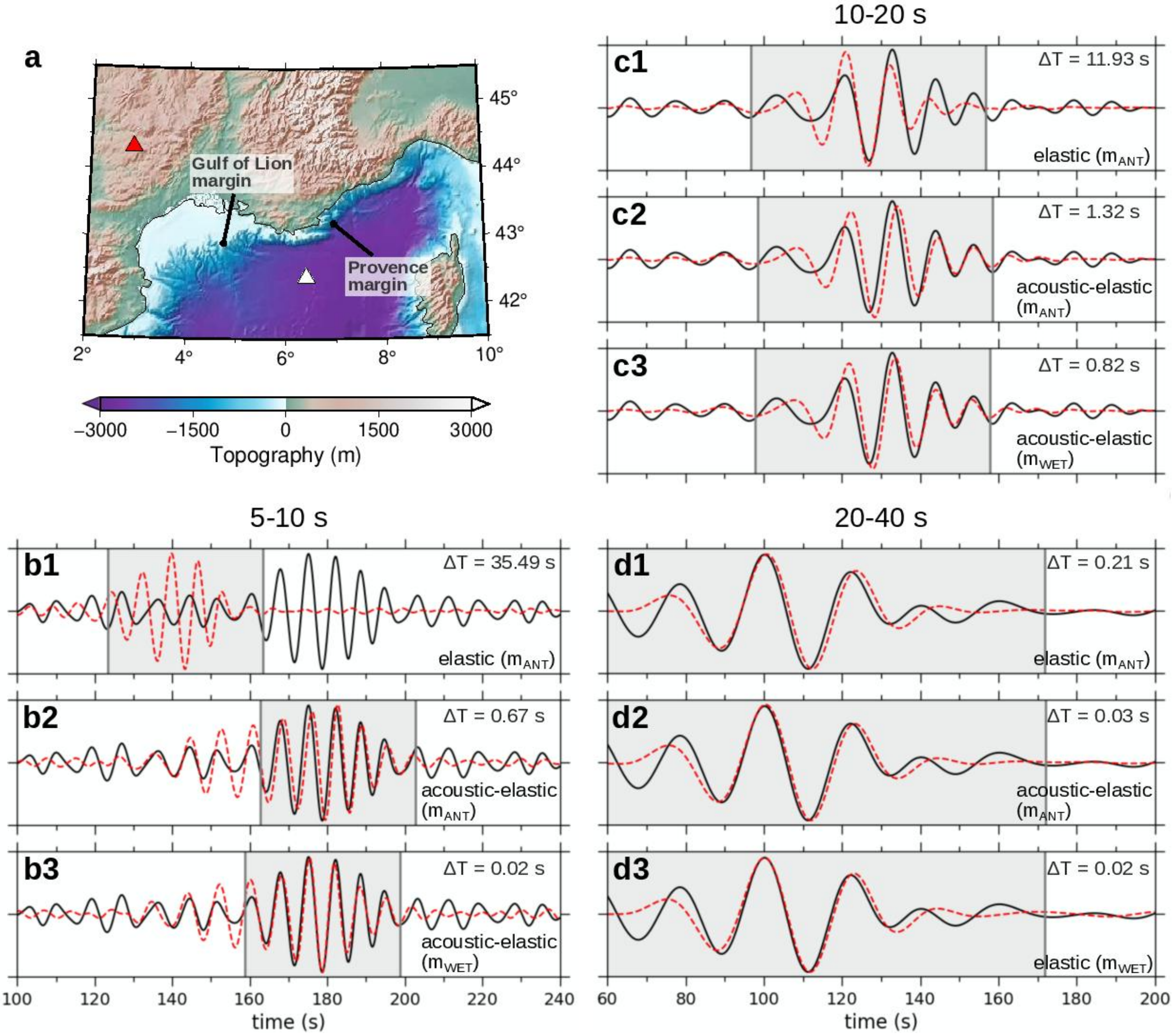

Figure 5.3: Comparisons between simulated vertical-component seismograms (red) and observed noise correlation waveforms (black) filtered in the 5-10 s, 10-20 s and 20-40 s period bands for the source-receiver pair in (a) (red: station source, white: receiver). Elastic and acoustic-elastic simulations in the initial model (labeled 'm$_{ANT}$') are shown in b1, c1, d1 and b2, c2, d2 respectively. Seismograms in b3, c3 are computed from acoustic-elastic modelling in the final model (labeled 'm$_{WET}$') while d3 is computed from elastic modelling. The gray areas indicate the surface-wave window and ΔT corresponds to the cross-correlation-based time shift between observed and synthetic windowed waveforms.

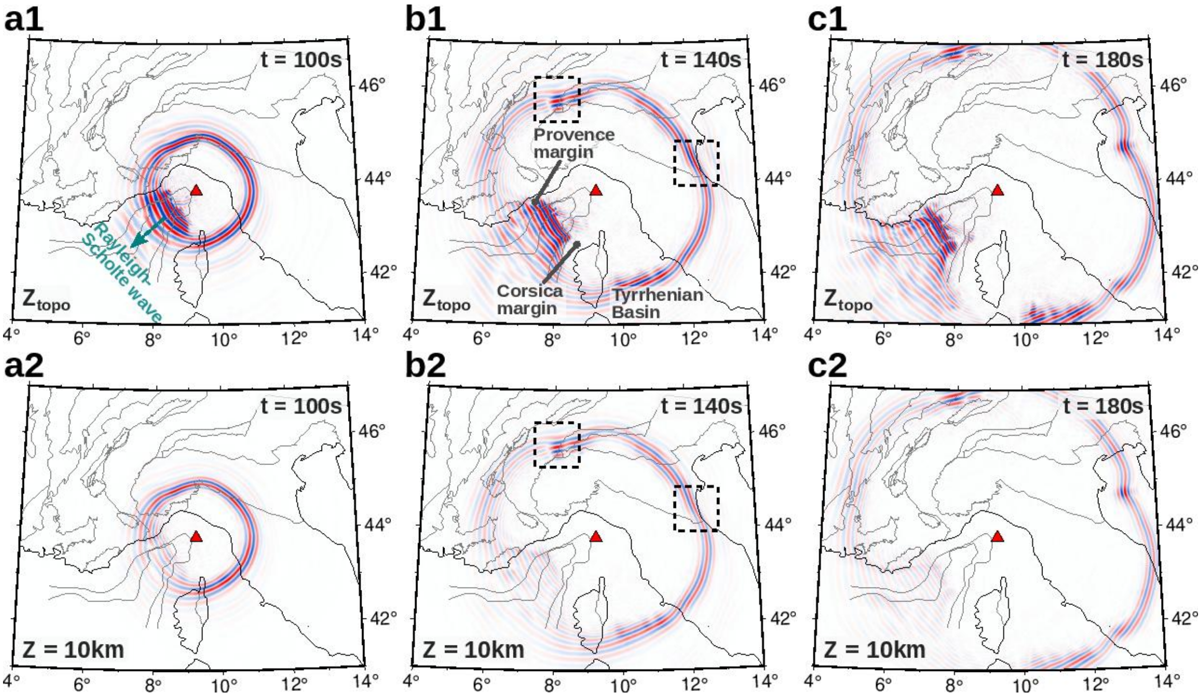

Figure 5.4: Snapshots of the wavefield computed from the acoustic-elastic coupled wave equation in the 5-10 s period-band, showing the depth attenuation of the Rayleigh-Scholte wave generated by an offshore source (red triangle). Wavefields are extracted (a1-c1) at the surface (Z_{topo}, same definition as in Fig. 5.2) and (a2-c2) at 10 km depth. Black dashed frames show scattered Rayleigh-wave packets.

5.6 Model robustness

We document the model robustness by analyzing histograms of misfit for the initial and final model and their spatial and azimuthal distributions. The misfit is expressed as traveltime delay for waves propagating on 100-km distance (s/100 km) in order to avoid biases related to long inter-station distances. Figure 5.5 shows histograms of traveltime misfits for the initial (in gray) and final models (in blue) at 8, 20, 35 and 35 s. The indication of mean and standard deviation values allows a quantitative comparison. The initial histograms are rather narrow and globally centred around zero misfit value (absolute misfit $\leq$ 0.2 s/100 km). Similarly to Lu et al. (2020), the initial standard deviation increases with period (0.3 s/100 km at 8 s to 0.73 s/100 km at 55 s). However, we do not observe a significant positive shift of the mean value at periods lower than 20 s as in Lu et al. (2020), which illustrates the consistency of our ANT model. The final model fits the data significantly better than the initial model, with overall smaller average misfits and standard deviations.

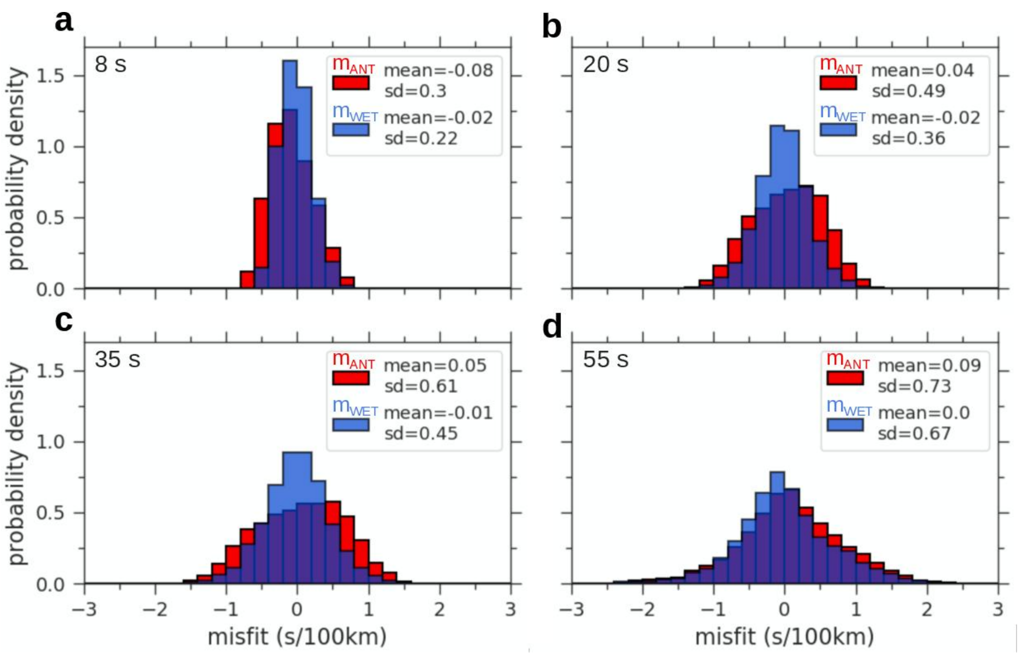

Figure 5.5: Comparison of histograms of misfit (in s/100 km interstation distance) for the initial (m_{ANT}, red) and final (m_{WET}, blue) velocity models at 8, 20, 35 and 55 s periods. Labels 'mean' and 'sd' refer respectively to the mean value and standard deviation of the misfit distribution.

Figure 5.6 displays the azimuthal distribution of misfit for the initial (red) and final (blue) models at 8, 20, 35 and 35 s. In Lu et al. (2020), the main difference between the initial and final distributions was an overall correction towards zero for the final model in particular at long periods as a result of the shift of the mean misfit. Our initial distributions do not show such a bias, which is in line with the mean value of initial histograms of misfits at the same periods. However, we observe an increase of the average misfit with period as in Lu et al. (2020). The final model improve the fit to the data, with overall smaller average misfits and standard deviations. However, the residual variations, even if small, may be related to anisotropy.

Furthermore, the variations presented here are averaged over the whole study region, which may encompass local variations of anisotropy. Indeed, recent studies on azimuthal anisotropy reveal significant variations in the Alpine region (Kästle et al., 2022; Soergel et al., 2022). Further analysis of anisotropy variations would require computing the distribution of misfits by clusters on specific locations. This could be the topic of a future article.

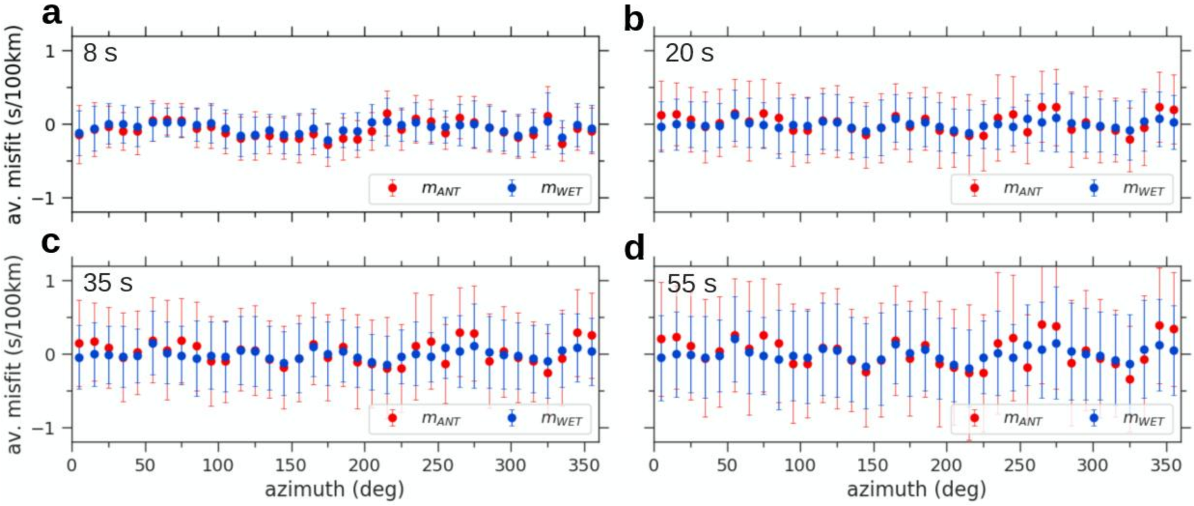

Figure 5.6: Comparison of the azimuthal distributions of misfit for the initial (red) and final (blue) velocity models at 8, 20, 35 and 55 s periods. Misfits are averaged over uniform azimuth bins of 10°. Error bars represent the standard deviation of the misfits inside bins.

The spatial distribution of misfit can also be used to document the quality of the final model. Figure 5.7 displays misfit maps for the initial and final models at 8, 20, 35 and 35 s. In the initial model, the misfit patterns tend to coincide with geological structures due to imperfection in the isotropic initial velocity model. The 8 s map (Fig. 5.7a1) highlights low misfit anomalies along the central and eastern Alps, west Po basin, southeastern french foreland and the central Ligurian-Provence basin. A strong low anomaly is observed in the Adriatic Sea. Positive anomalies are observed in the northeast french foreland, north and south Apennines and south Ligurian-Provence basin. The 20 and 35 s misfit maps (Fig. 5.7b1-c1) evidence positive misfits all around the Alpine belt, while negative misfits are observed along the Alpine arc and Po basin. Note that the western foreland of the Alps has rather low positive misfit values (<0.5 s/100 km) which indicates that the 1-D inversion in the ANT model is sufficiently robust to recover such structural changes at depth. We will further document this point along cross-sections in the next section. The transition to 55 s is marked by an inversion of polarity: the European foreland and central Ligurian-Provence basin evidence negative anomalies, while the central and eastern Alps and Apennines display positive anomalies. Strong negative anomalies are observed in the western Ligurian-Provence basin and central Adriatic Sea. Most of these regionally organized misfit patterns are corrected after WET inversion (Fig. 5.7a2-d2). Although strong misfits in the South of the study region are significantly smaller, some residuals remain, in particular along boundaries of the study region where path coverage is poorer (e.g., southern Corsica, in the 20 and 35 s maps, or in the eastern Ligurian-Provence basin at 55 s).

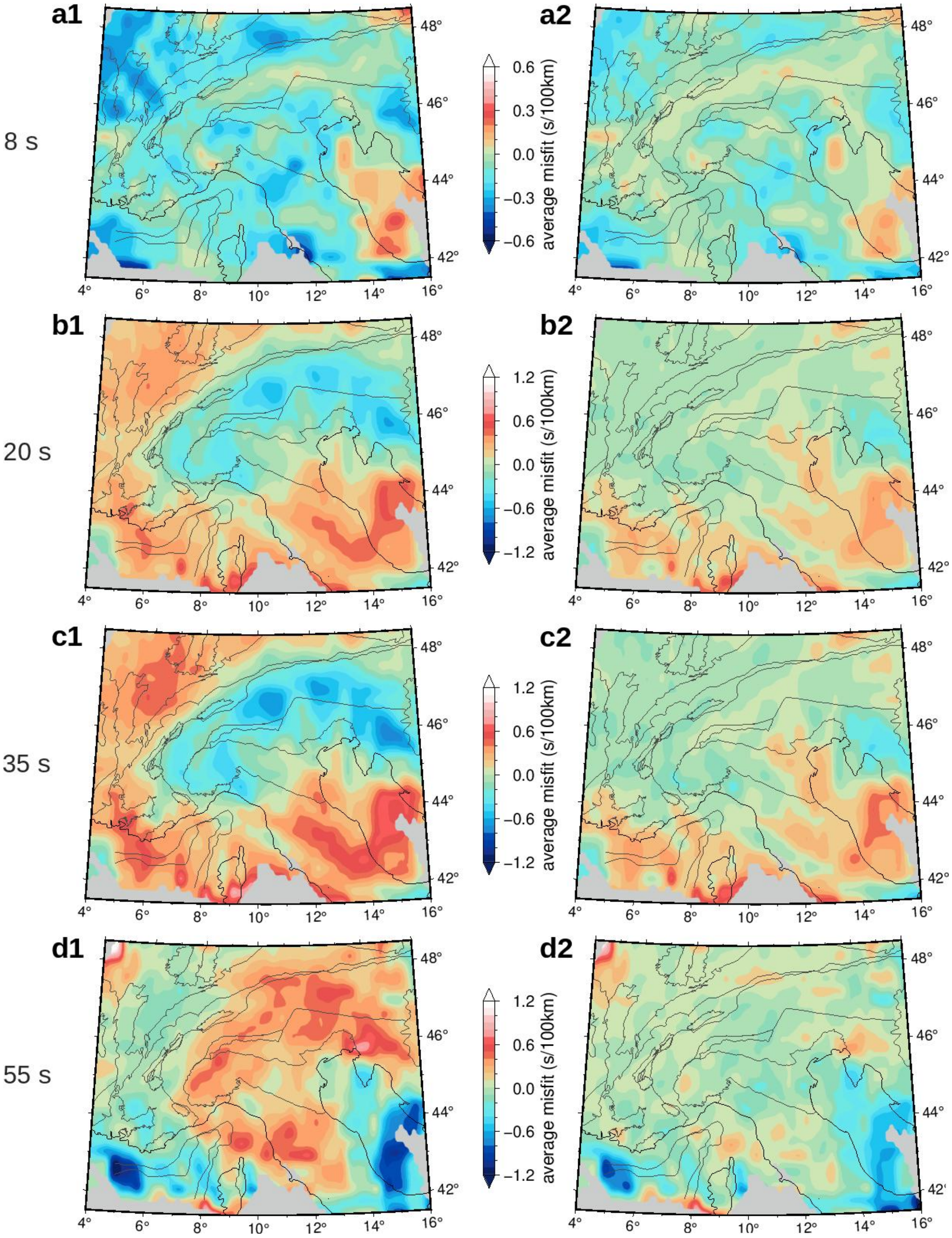

Figure 5.7: Comparison of the spatial distributions of misfit for the initial (left-hand side: a1-d1) and final (right-hand side: a2-d2) velocity models at 8, 20, 35 and 55 s periods. Misfits are averaged over cells of 0.2° × 0.2° assuming great circle ray paths. The gray area hides regions where the initial model is unconstrained.

5.7 Results and discussion

5.7.1 Depth slices

Figure 5.8 shows the shear-wave velocity depth slices at 6 and 26 km in the initial and final models and the relative variations to the initial model. The geometry of V_s heterogeneities is roughly preserved, but the velocity are different, as shown by Fig. 5.8a3,b3. At 6 km-depth (Fig. 5.8a1-a3), the final model exhibits lower velocities (≤ 2.5 km/s) with strong negative velocity variations (≤ -8 %) in the Ligurian-Provence basin. This low velocity anomaly arises from the slower velocity of the Rayleigh-Scholte waves. Another new pattern appears in Corsica where the western Variscan Corsica exhibits high V_s while northeastern Alpine Corsica exhibits lower velocities. Such changer in the oceanic part of the velocity model and in Corsica are likely due to the incorporation of fluid-solid coupling in the 3-D inversion. This coupling is important, not only for sea-sea paths but also for land-sea or land-land paths (e.g., in and around Corsica). On the onshore domain, relative variations roughly coincide with geological structures, with a velocity decrease in the western and eastern parts of the subduction wedge and an increase in the forelands.

The 26-km maps (Fig. 5.8b1-b3) display two striking features: (1) a velocity decrease in velocity (to -8 %) in the subduction wedge and the Ligurian-Provence basin, and (2) a velocity increase (up to 8 %) in the crust beneath the Alpine forelands and the Apennines. In particular, we point out two strong and nearby velocity changes of reversed polarities in the European crust: the fast anomaly (labelled '1') and the low anomaly (labelled '2') in Figure b3, that will be discussed in more detail in the next section.

Transitions between the main domains exhibit small variations from the initial model. This is consistent with the low average misfit observed along the main tectonic boundaries (e.g., the subduction wedge-European foreland boundary, see Fig. 5.1). This again shows the robustness of the ANT model that deals with such sharp transitions. However, strong velocity changes between the ANT and the WET models show that the WET overcomes imperfections in the ANT model and the high-frequency approximation in the inversion for group velocity maps or the 1-D assumption in the inversion for V_s.

Figure 5.9 shows that important differences are observed between our V_s model and the WET V_s model by Lu et al. (2020). We observe an overall change in amplitude of velocity anomalies and their contrast, in the European crust along the Alpine arc, and in the Adriatic crust as well. Our velocity model is obviously higher resolution as illustrates the 46-km depth slice (lower crust to upper-mantle, Fig. 5.9c1-c2), where the western Alpine lower-crust and the Adriatic upper-mantle appear more differentiated in our model. These discrepancies are due to differences in the initial models' seismic coverage and robustness, as well as to differences in the inversion methodology, since we invert hierarchically in four narrow period bands instead of one broad band as Lu et al. (2020) did.

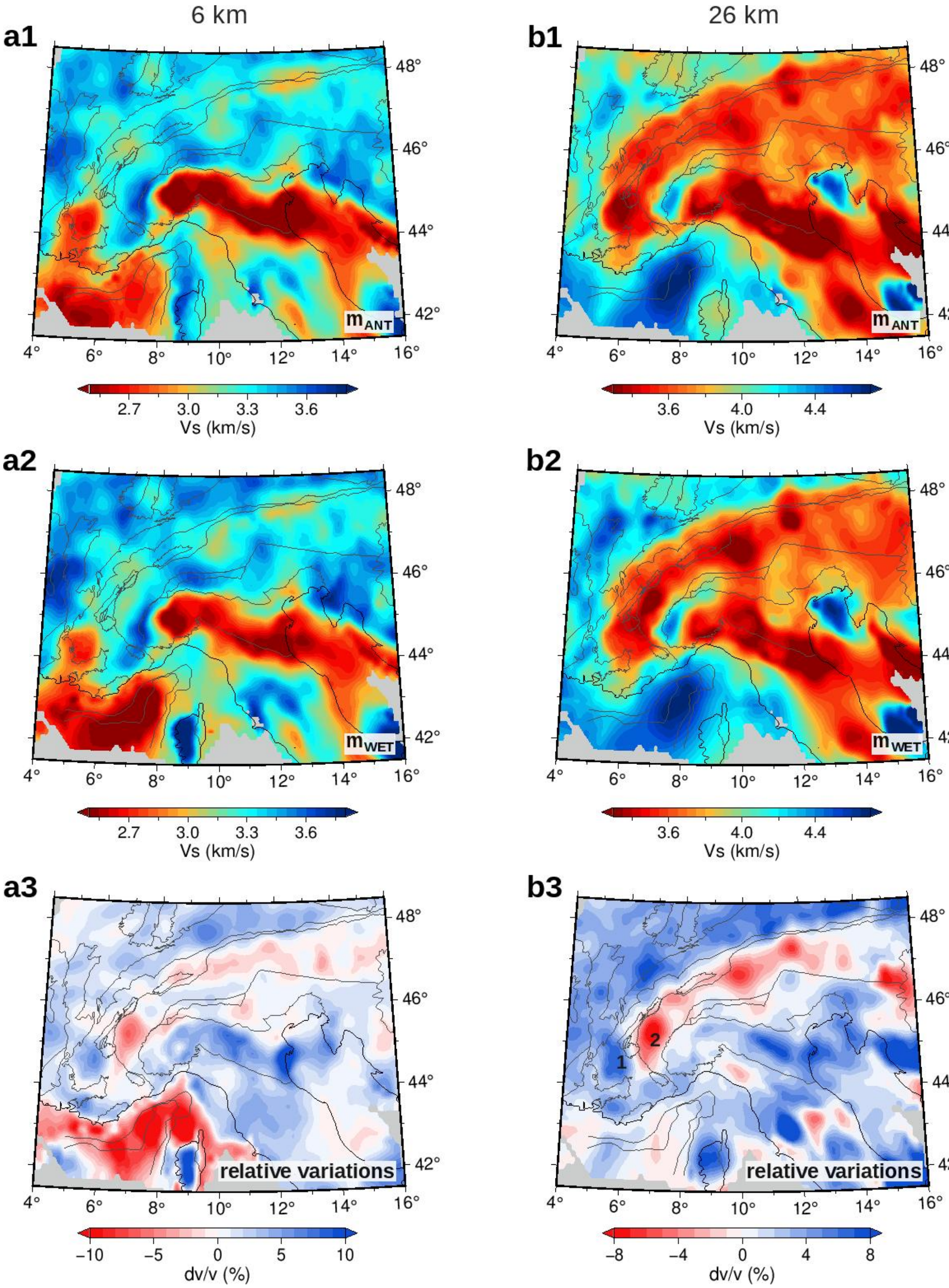

Figure 5.8: Depth slices in the initial (a1-b1) and final (a2-b2) shear-wave velocity models and the relative variations to the initial model (a3-b3), at 6 (a1-a3) and 26 km (b1-b3) depths. Labels 1 and 2 refer to velocity structures discussed in the text.

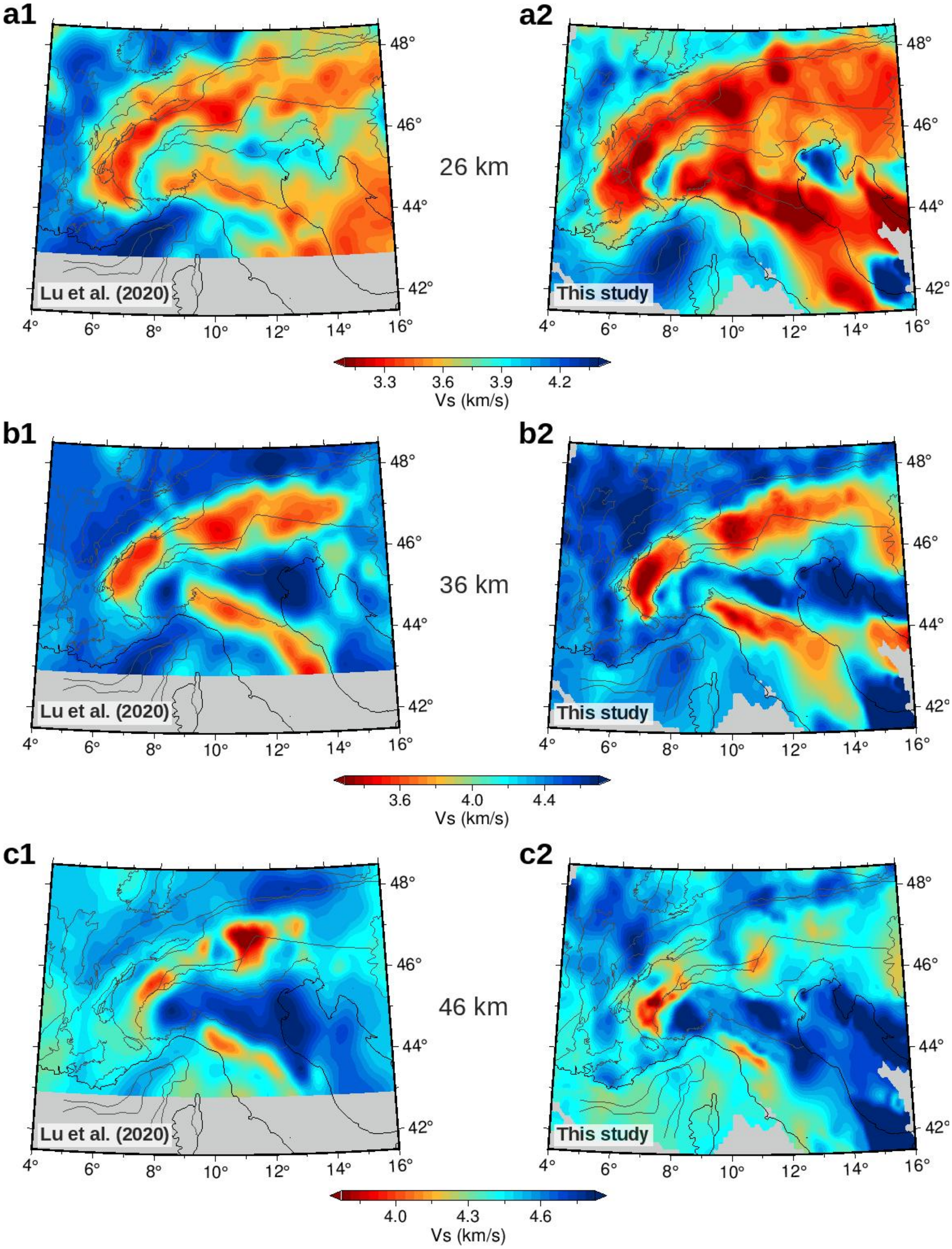

Figure 5.9: Comparison of depth slices of shear-wave velocities in the WET model of Lu et al. (2020) (a1-c1), the WET model of this study (a2-c2), at 26 (a1-a2), 36 (b1-b2) and 46 km (c1-c2) depths. The gray areas hide regions where the velocity models are unconstrained.

5.7.2 Vertical cross-sections

To further point out the improvements bought by wave-equation tomography, we now compare V_s crustal-scale depth sections in the initial and final models along three representative profiles, P1, P2 in the southwest Alps and P3 in the Ligurian-Provence basin (see locations in Fig. 5.1).

5.7.2.1 Cross-sections in the western Alps

Profile P1 coincides with the Cifalps transect, which was extensively investigated in a number of tomography studies (Malusà et al., 2021, and references herein). It was also used by Nouibat et al. (2022a) to validate the onshore part of the ANT model, by comparison to a migrated receiver function stack. Profile P2 is located close to the ECORS-CROP controlled-source seismic profile (Nicolas et al., 1990) and the Cifalps-2 profile (Fig. 5.1; Paul et al., 2022). Both transects cross the mountain belt from the European foreland (subducted lower plate) to the Adriatic foreland (upper plate) and the subduction wedge bounded by the Penninic Frontal Thrust (PFT) to the west and the Insubric Fault (IF) to the est.

Figure 5.10 shows the two velocity models along P1 and P2 profiles and the relative velocity changes. The final model displays lower velocities in the European mantle and higher velocities in the Adria mantle along the two transects (±2 %). This indicates a non-negligible contribution of misfit enhancement at long periods in the model update. The European crust (labeled ECC) shows three main patterns: (i) an attenuation ($dv/v \geq +5$ % in P1) of the LVZ in the lower crust of the foreland (label '1'); (ii) a strengthening ($dv/v \leq -3$ to -4 %) of the lower crustal LVZ located beneath the surface trace of the PFT (label '2'). These two velocity changes are also visible in the Fig. 5.8b3 which shows a shift of the LVZ1 towards the north-east. This shift is likely the result of correcting for the seismic ray deviation bias that is not considered in the ANT model due to the high frequency approximation. It also reflects the higher resolution of the final model; (iii) a progressive increasing of velocities beneath the SW, as highlighted by positive-velocity variations from 40 km depth and 180 km offset. The final model shows almost no change in the Adria crust, which is less structurally complex than the European crust, indicating that the ACC is indeed well constrained at depth by the ANT.

Similarly to the receiver function Moho (dashed yellow line), the 4.2 km/s contour of the final model dips continuously following the subduction of the European lithosphere beneath the westernmost Po plain, and reaches a maximum depth of $\sim$ 80 km. We can therefore define this iso-velocity as a proxy for Moho. The European Moho proxy reaches only 55 km maximum depth in the north (profile P2), Two major changes of the Moho proxy may be noticed: (i) a change of geometry underneath the subduction wedge in profile P1, at location 3, where the shape of the 4.2 km/s contour is much more consistent than the one of the ANT model that goes down deeper as a result of anomalous low velocities ($>$ 4.2 km/s) at depths $>$ 80 km. Indeed, the final model displays a velocity increase in this zone. Similar changes in the north (P2) underline a decrease in the maximum depth reached by the Moho proxy (55 km instead of 70 km), which is more coherent with the ECORS-CROP wide-angle reflection profile (Nicolas et al., 1990); (ii) strong changes in the V_s gradient at Moho depth, particularly in the north (P2) with positive variations ($dv/v \geq +5$ %). In P1, the European Moho shows a decrease in velocity under the Rhone valley, then a strong increase (under the LVZ labelled '1'). The Moho jump in P2 is well preserved in the final model which indicate that this structure is well constrained by the ANT and therefore not an artefact. The crust-sediment interface, which can be roughly approximated by 2.8 km/s contour, shows a velocity decrease below the Po plain and below the Rhone valley. These variations along the main interfaces are possibly due to the correction of the bias associated with the 1-D layer model assumption in the construction of the ANT model. Moreover, their sharpness undoubtedly demonstrates the resolving capacity of our tomography. The comparison with Lu et al. (2020)'s model along the two transects (Fig. 5.10a5,b5) shows first-order discrepancies, particularly in the lower crust and the upper mantle. These differences are more important in the P1 profile, reflected for instance by the absence of the European Moho deepening in the model of Lu et al. (2020). Nevertheless, there are similar first-order lateral structures, such as the Moho jump in the P2 profile. It is worth remembering that these differences are most likely due to differences in the resolution and robustness of the two initial models. However, this comparison is meaningful since the model of Lu et al. (2020) is the only WET model in the Alpine region.

5.7.2.2 Cross-section in the Ligurian-Provence basin

We now focus on the offshore part of the study area, on profile P3 along the axis of the Ligurian-Provence back-arc basin (location in Fig. 5.1). This transect crosses the three main domains involved in the genesis of oceanic crust as a result of the roll-back of the Apenninic slab and the opening of the basin (Séranne, 1999): (1) the oceanic domain, described as an atypical oceanic crust by Rollet et al. (2002); (2) the transitional domain which includes a thin continental crust overlying a thick rift-related corner of magmatic underplating (e.g., Séranne, 1999); (3) the Ligurian margin made of stretched continental crust units. The oceanic southwestern part of the transect coincides with the seismic refraction and wide-angle reflection line by Dannowski et al. (2020), which has been used by Nouibat et al. (2022b) to validate the offshore part of the ANT model. The northeastern part of the profile coincides with the marine part of the wide-angle reflection line by Makris et al. (1999).

Figure 5.11 shows that the final model displays major changes with the ANT model: (i) a strong velocity decrease in the sediments and oceanic crust of the oceanic domain ($dv/v \geq -8$ %); (ii) a strong increase in velocity of sediments followed by a decrease in velocity of the crust in the transitional domain; (iii) a decrease in sediments velocity followed by an increase in velocity of the crust in the margin domain. These changes at shallow depths are likely related to the consideration of 3-D fluid-solid coupling. Conversely, the uppermost mantle displays lower velocity changes with an overall decrease in the oceanic domain and an increase in the transitional and continental domains. Similarly to the onshore part, we define the Moho proxy as the 4.2 km/s contour. This contour is consistent with the V_p Moho proxy defined as the 7.3 km/s V_p contour by Dannowski et al. (2020) (dashed yellow line in Fig. 5.11). Depth and geometry of the Moho proxy is almost unchanged in the oceanic part between the two models. However, we see a significant increase in velocity reflecting a stronger gradient at this interface, similar to the Moho in the continental part. The most important change is in the margin part where the Moho proxy is shallower indicating a gradual thickening of the continental crust towards the northeast, to a maximum depth of 27 km.

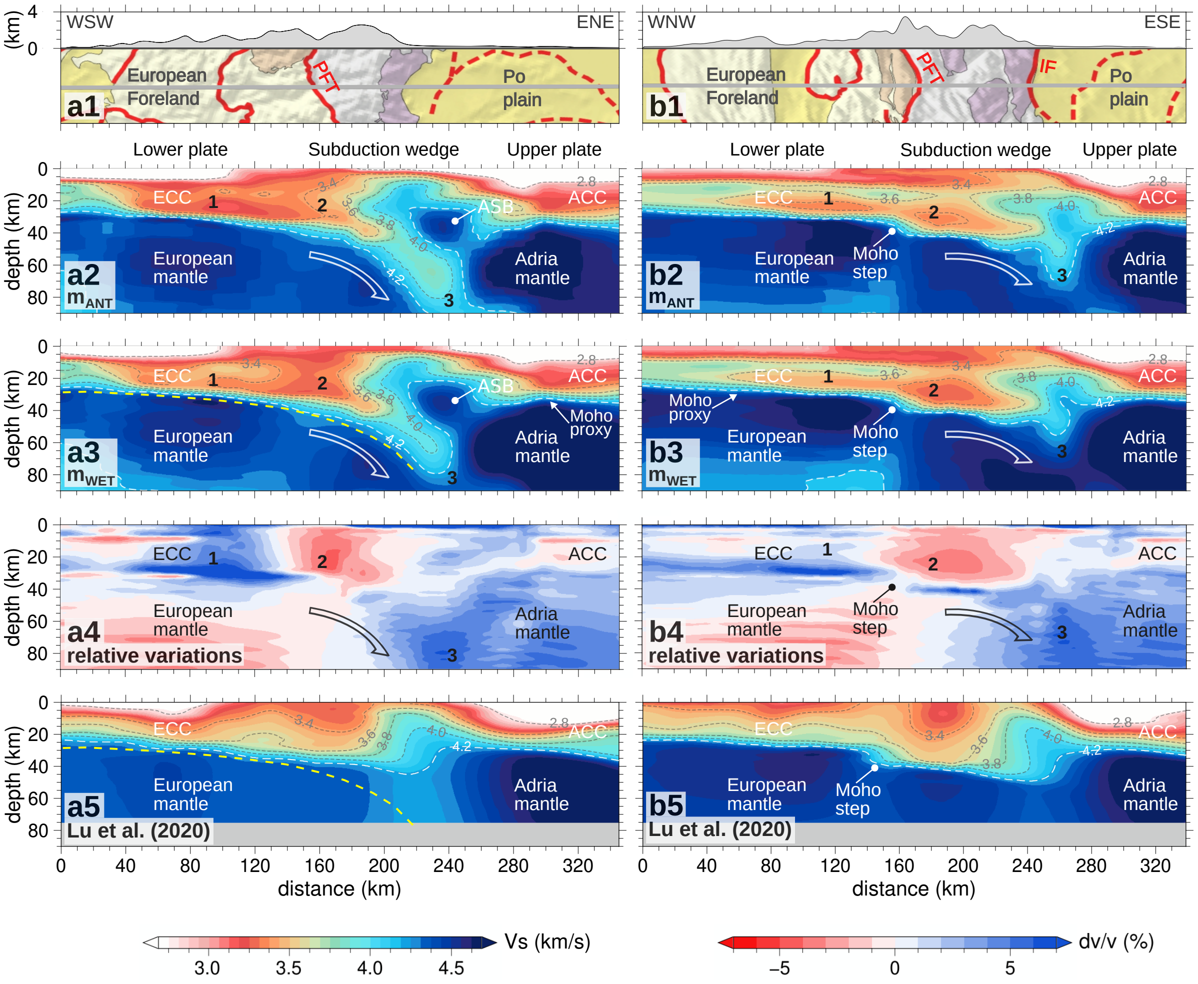

Figure 5.10: Comparison of depth sections for the initial and final models and the model by Lu et al. (2020) along the WSW-ENE transect P1 (left-hand side) and the WNW-ESE transect P2 (right-hand side). Locations of P1 and P2 are indicated in Figure 5.1. (a1,b1) Topographic profile and geological map (extracted from Fig. 5.1). (a2-b2) Shear-wave velocities from the ANT initial model ('m_{ANT}'). (a3-b3) Shear-wave velocities from the WET final model 'm_{WET}'). (a4-b4) Relative variations to the initial model. The white and black curved arrow highlight the subduction of the European lithosphere beneath Adria. The dashed yellow line in (a3) and (a5) show the European Moho picked from a receiver function section (Zhao et al., 2015; Paul et al., 2022). Note the remarkable agreement with the V_s Moho proxy in (a3). Acronyms: ECC, European Continental Crust; ACC, Adriatic Continental crust; ASB, Adria seismic body. Labels 1, 2 and 3 indicate structures discussed in the text.

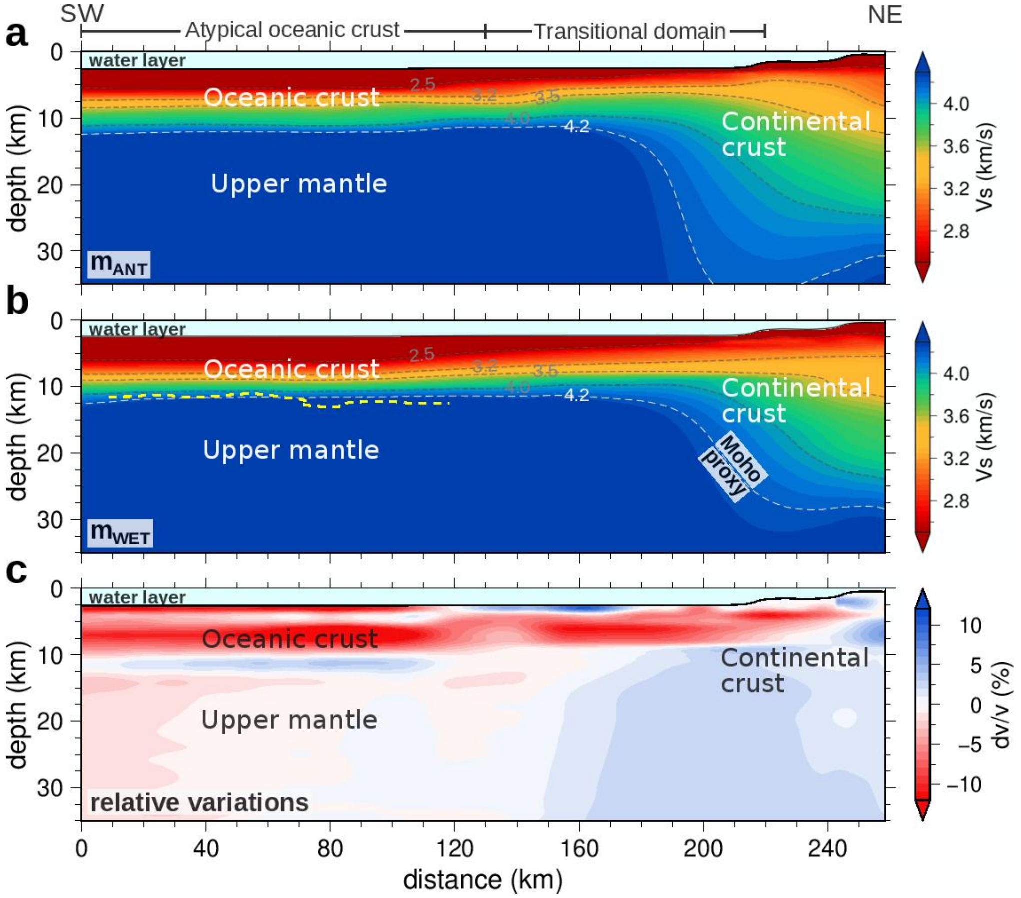

Figure 5.11: Comparison of depth sections for the initial and final models along the SW-NE offshore transect P3 (see location in Fig. 5.1). (a) Shear-wave velocities from the ANT initial model. (b) Shear-wave velocities from the WET final model. The black dashed line represent the Moho proxy from the active seismic P-wave velocity section of Dannowski et al. (2020). (c) Relative variations to the initial model.

5.7.3 New large-scale map of Moho depth

The Moho depth cartography in the western Mediterranean region has been the target of a variety of seismic experiments but is so far still not enough well constrained in 3-D to answer first-order questions regarding the deep 3-D geodynamics. We discuss the 3-D structure of the Moho in the Alpine region by comparing with the Spada et al. (2013)'s reference Moho map and the recent Moho map from the WET by Lu et al. (2020). We further discuss the topography of Moho in the Ligurian Sea by comparing with depth iso-contours from the recent conventional ANT by Magrini et al. (2022).

In a tectonically complex setting as in the western Mediterranean region, a precise definition of the three-dimensional Moho structure is fundamental to understanding the link between mantle dynamics and the geological setting. Thus, numerous large-scale Moho maps have been constructed from different seismological methods. By interpolating data from CSS, RF and LET (e.g., Waldhauser et al., 1998; Lombardi et al., 2008; Piana Agostinetti and Amato, 2009; Diehl et al., 2009; Di Stefano et al., 2009), Spada et al. (2013) derived a first 3-D Moho map in three blocks: a European Moho, an Adriatic Moho, and a Ligurian–Sardinia–Corsica–Tyrrhenian Moho (Fig. 5.12a). This smooth Moho shows crustal thickening beneath the Alps and Apennines and thinning beneath the Ligurian and Tyrrhenian oceanic domains. However, this Moho is limited by the quality of the CSS and RF measurements, limited coverage of the 2-D profiles, and finally by the resolution and coverage of the LET model by Diehl et al. (2009). The densification of permanent seismic networks in Western Europe and the expansion of conventional ANT have made it possible to derive finer versions of the Moho structure as a V_s Moho proxy (e.g., Molinari and Morelli, 2011; Kästle et al., 2018; Lu et al., 2018; Nouibat et al., 2022a). These models have provided significant constraints on geological models, confirming 2-D observations by other methods such as CSS and RF. However, although these models are spatially continuous, they are not truly 3-D as all of them are based on a point-by-point depth inversion for V_s, which is problematic for lateral consistency.

The recent Moho depth map of the Alpine region by Lu et al. (2020), estimated from the depth of the V_s=4.2 km/s iso-velocity surface from their WET, is up-to-now the highest resolution depth map of Moho proxy (Fig. 5.12b). This Moho map is truly 3-D as the WET relies on the physics of wave propagation. This model is consistent with the geometry of the large ensembles in Spada et al. (2013)'s model with far higher resolution. It shows changes in maximum crustal thickening along the Alpine arc from Western Alps ($\sim$ 50 km) to Central-Eastern Alps (50-55 km), marked by a maximum depth between Tauern and Engadin windows in the the Eastern Alps and $\sim$ 40 km shallower depths beneath the Lepontine Dome. The European foreland exhibits a crustal thickness of 35 km while larger thicknesses are observed in the Adriatic side, beneath the Po basin. This model exhibits a SW-NE oriented Moho step that roughly follows the boundary of the external crystalline massifs in the western Alps. The recovery of such sharp features reveals the strength and resolving capability of the wave-equation tomography of Lu et al. (2020). However, this Moho map has two major deficiencies: (i) it does not highlight the subduction of the European continental crust, in disagreement with the RF Moho (see Fig. 5.10). Indeed, this major structure was not recovered in the ANT by Lu et al. (2018) used as an a priori model in their WET; (ii) it does not cover the Ligurian-Provence basin due to the low ray coverage in this area before the deployment of AASN OBSs.

Figure 5.12c shows the Moho depth map estimated from the iso-velocity surface V_s=4.2 km/s in our WET V_s. This Moho map covers a wider area than that of Lu et al. (2020), notably the oceanic domain of the Ligurian-Provence basin and Corsica. In the area covered by the Moho of Lu et al. (2020), our depth map is overall similar to that of Lu et al. (2020), with a few important discrepancies. First, our map exhibits higher resolution, as illustrated by the Moho beneath the Po basin which appears more differentiated. In the Western Alps, the European Moho deepens to significantly larger depths ($>$ 60 km). The area of maximum Moho depth is overlain by a small-size anomaly at 20-25 depth located in the subduction wedge (dashed white line). This shallow high-velocity is already visible in the initial ANT model and is discussed in Nouibat et al. (2022a). The strong along-strike variations in Moho depth from north to south are in line wih RF observations between the northwestern and southern Alps (Paul et al., 2022), indicating a non-cylindricity of the deep structure of the Western Alps. Besides this differences, we confirm structures outlined by Lu et al. (2020), such as the Moho jump below the external crystalline massifs that appears more linear and better aligned with the Variscan Accident than the one in Lu et al. (2020) which presents a shift to the east from theses faults, likely due to poorer station coverage in the western part of their covered area.

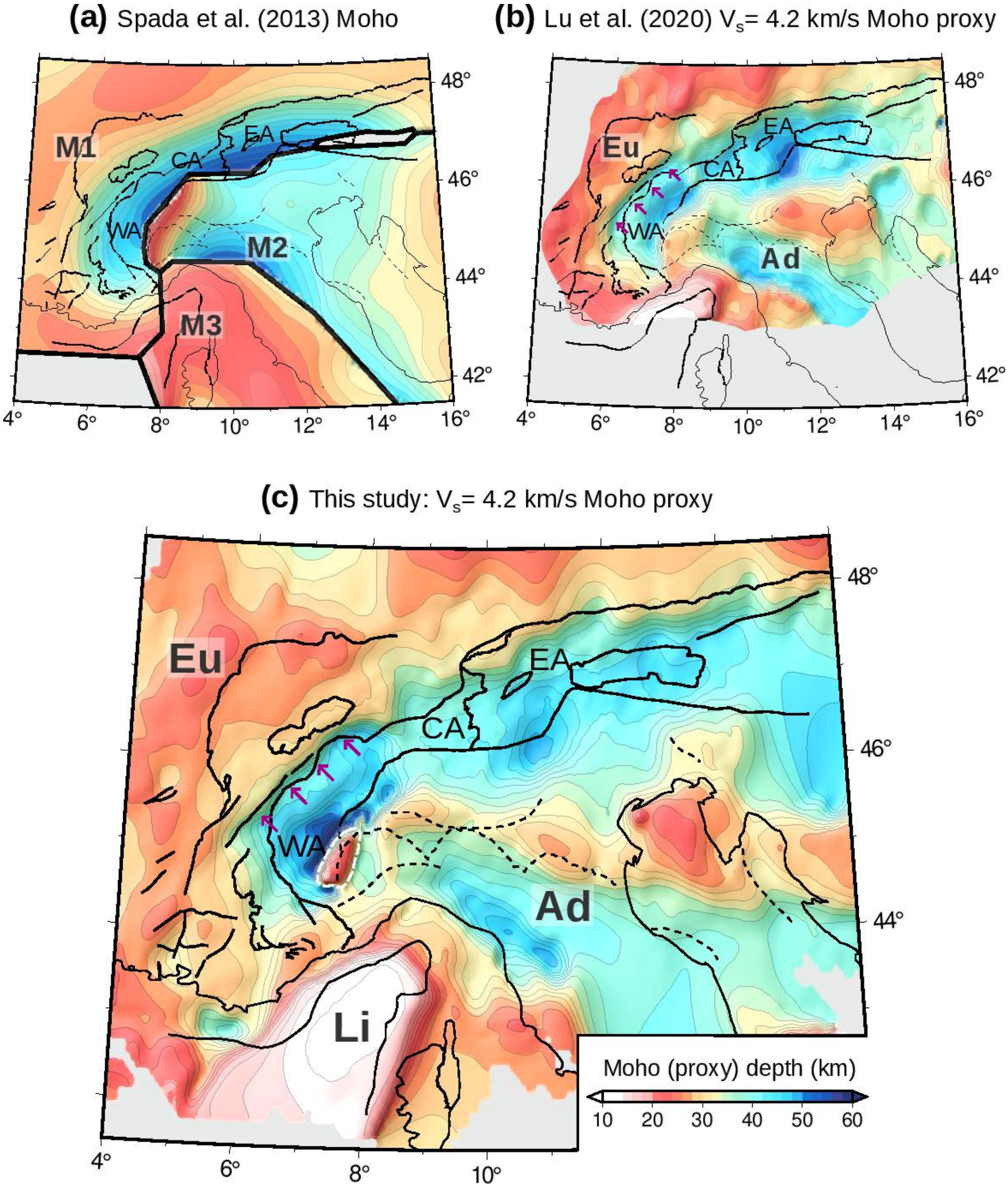

Figure 5.12: Depth maps of Moho and Moho proxy in the western Mediterranean region. (a) Spada et al. (2013)'s map composed of three blocks: European Moho (M1), Adriatic Moho (M2) and Ligurian–Sardinia–Corsica–Tyrrhenian Moho (M3). (b) Lu et al. (2020)'s depth map of the $V_s = 4.2$ km/s iso-velocity surface from their WET model. (c) Depth map of the $V_s = 4.2$ km/s iso-velocity surface from our WET model. Acronyms: Eu, European Moho; Ad, Adriatic Moho; Li, Ligurian Moho; WA, Western Alps; CA, Central Alps; EA, Eastern Alps. Arrows in purple: Moho step beneath the external crystalline massifs (Lu et al., 2018). Dashed white line: boundary of the Adria seismic body (ASB; Nouibat et al., 2022a). The black lines correspond to geological and tectonic boundaries of Figure 5.1. The gray areas hide regions where Moho maps are unconstrained.

5.7.4 Moho architecture beneath the Ligurian Sea

3-D crustal imaging of back-arc basins with continental margins based on surface waves is a challenging topic due to the difficulty of accounting for the effect of complex topography on the wave propagation physics, as illustrated in this study. One of the main objectives of this study is to produce an homogeneous 3-D map of the Ligurian Moho structure in line with the physics of surface wave propagation in a hybrid medium.

Unlike the Alpine region, the 3-D structure of Moho in the Ligurian Sea is poorly constrained by 3-D velocity models. In this region, the few constraints on the Moho depth are mainly provided by CSS data (e.g., Makris et al., 1999; Rollet et al., 2002; Contrucci et al., 2001; Dannowski et al., 2020). This gap is partly due to the poor coverage of seismological stations in this area before the deployment of AlpArray OBSs, making it difficult to achieve 3-D high-resolution imaging with tomography methods such as ANT or LET for instance. Figure 5.13 shows the Moho proxy depth map in the Ligurian-Provence basin. This Moho map shows strong lateral variations with depths ranging from 12 km between Provence and Corsica to ∼40 km along the margins and Provence margin. In the oceanic domain, the Moho gradually deepens along the axis of the basin, from 12 km between the Ligurian-Provence and Corsica margins to 18 km in the southern part. The transition to the Ligurian-Provence and Corsica margins is characterised by a strong gradient in Moho depth while the transition to the Ligurian margin is smoother. A strong crustal thickening reaching 40 km in is visible in the Provence margin. Red dashed show depth contours of the Moho surface recently published by Magrini et al. (2022) from conventional ANT. This model shows smoother depth variations than ours within the basin and at transitions to the conjugate margins. Along the basin axis, it shows depths increase from the southern part of the (15 km) to the northern part (18 km). While our Moho has a depth of about 12 km in the oceanic domain traversed by the active seismic profile of Dannowski et al. (2020), the Magrini et al. (2022)'s Moho is 15-18 km deep in the northern portion of the profile and more than 18 km deep in the southern portion. However, Dannowski et al. (2020) detected a Moho of ∼ 12 km depth, which is more consistent with the depths displayed by our model (see Figure 5.11). These comparisons demonstrate that our Moho model provides a better resolution of the crustal thinning beneath the Ligurian-Provence basin.

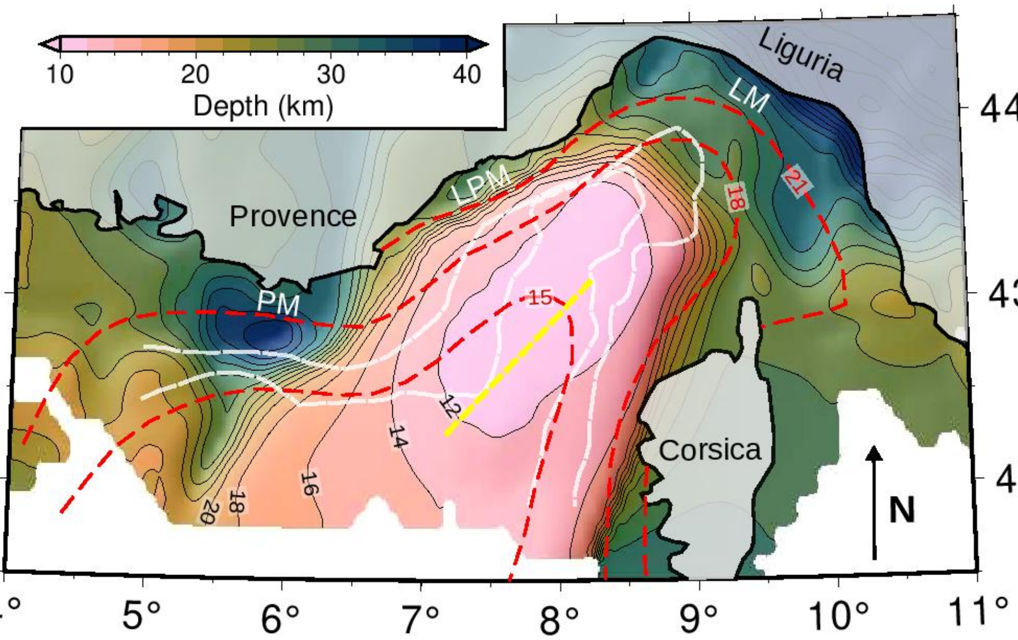

Figure 5.13: Depth map of the $V_s = 4.2$ km/s iso-velocity surface from our WET model as a proxy of Moho in the northwestern Mediterranean Sea. Black lines are iso-depth contours from our Moho proxy. Red lines: iso-depth contours from Magrini et al. (2022)'s Moho depth map. Dashed yellow line shows the trace of Dannowski et al. (2020)'s CSS profile. Dashed white lines are limits of the main geological domains in the Ligurian-Provence basin from Rollet et al. (2002). Acronyms: PM, Provence margin; LPM, Ligurian-Provence margin; LM, Ligurian margin.

5.8 Conclusion

Using ambient noise data from exhaustive coverage of permanent and temporary arrays in the western European region, we derive a 3-D high-resolution onshore-offshore S-wave velocity model of the Alps and Ligurian-Provence basin from wave equation tomography. We iteratively refine the recent ANT model of Nouibat et al. (2022a) by minimizing the phase travel time differences between observed and simulated waveforms in the 5-85 s period band. Observed signals are obtained from ambient noise cross-correlations and synthetics are computed from SEM-based 3-D elastic and acoustic-elastic modelling of surface waves. Taking the Ligurian Sea domain as an illustration, the specificity of this study is to highlight the effect of the water layer on the 3-D propagation of Rayleigh waves by applying a fluid-solid coupling for 3-D acoustic-elastic simulations. We demonstrate that the elastic propagation assumption is no longer valid at short periods (5-20 s), since the surface-wave packet is dominated by a composite Rayleigh-Scholte mode propagation with lower velocities. Finally, we incorporate the fluid-solid coupling in the inversion framework of the WET.

In line with the true physics of surface-wave propagation, the ANT corrects for the biases in the ANT model related to the high-frequency assumption and the 1-D inversion. The resulting model has a better resolution, with significant intra-crustal changes. In the superficial part, the WET better emphasizes the deep sediments of the Ligurian-Provence domain and a high-velocity anomaly beneath the Variscan part of Corsica. This improvement is partly due to accounting for Rayleigh-Scholte wave 3-D sensitivity kernels at short periods. In the crust, the WET mainly change the velocity contrast and focus the LVZ in the W-Alps with an overall velocity decreasing in the subduction wedge and increasing in the two forelands. In addition, the WET validates major structures already present in the initial model, such as the subduction of the European crust down to 70-75 km beneath Adria in the southwestern Alps, and the slow anomalies at the base of the crust in the northwestern Alps, thus validating recent first-order interpretations on the deep structure in this area (e.g., Nouibat et al., 2022a; Paul et al., 2022). Significant changes are observed in the oceanic crust of the Ligurian-Provence domain, where intra-crustal velocities decrease significantly with up to 10 % variations from the initial model along the axis of the basin.

The resulting model is so far the highest resolution S-wave velocity model of Western Europe. We present a new depth map of the Moho proxy of Western Europe. In the Western Alps, this map shows the deepening of the European crust and confirms the Moho jump under the outer crystalline massifs (Lu et al., 2020) and the ASB (Adria seismic body Nouibat et al., 2022a). This proxy is the first truly 3-D representation of the land-sea Moho in the western Mediterranean region. We show a strong deepening of the Moho towards the Ligurian-Provence and Corsica conjugate margins, and a smoother deepening towards the Ligurian margin with depths ranging from 10-12 km at the oceanic domain axis to 40 km at the Provence margin. In a future perspective, this final model can be used as the initial model in earthquake-based FWI to better constrain the P-wave velocity of Western Alps and Ligurian Sea.

Chapter 6

Conclusion and Perspectives

Conclusion

The objective of this thesis was to set up a new generation of 3-D large-scale seismological models, to be used as self-consistent input for geological and tectonic interpretation for a better understanding of the deep geodynamics in the western Mediterranean region. To achieve this, we have deployed innovative ambient noise-based imaging methodologies and applied them for the crust and upper-mantle beneath the Alps and the Ligurian sea, taking advantage of the densest database in Western Europe to date.

With this manuscript, we provide two shear-wave velocity models that cover the Alpine belt and the Ligurian-Provence basin. First, a probabilistic quasi-3-D model derived from a two-step ambient noise group velocity tomography (ANT), presented in Chapters 2 and 4. This model provides at each location, at each depth, the probability density on V_s and on the presence of interfaces. This ANT V_s model was used as an initial model in wave equation tomography (WET) to construct a higher resolution 3-D V_s model in the western Alps and the Ligurian-Provence basin, as seen in Chapter 5.

In terms of methodological development, we first set up a full data-driven Bayesian approach to derive the ANT V_s model. This approach, designed to address the issue of data and model uncertainties, allowed the construction of both V_s and their uncertainties at depth, and both group velocities and their uncertainties at period, while realistically quantifying the errors in the source-receiver group-velocity measurements. In the framework of this Bayesian ANT methodology, we set up a dedicated procedure for 3-D imaging of oceanic crust with ocean-bottom-seismometers (OBS). This involves a specific processing sequence that deals with electronic and seabed-induced noise in the OBS raw recordings, and an iterative scheme that improves the quality of the OBS-OBS first-order correlations. We have successfully applied this procedure to the Ligurian-Provence basin, thereby complementing the onshore part of the V_s model. In a second step, we deployed a wave-equation-based inversion procedure that naturally deals with the limitations of the 'classical' two-step ANT, which are the use of the ray theory and the point-by-point inversion at depth. The specificity of our WET is that it accounts for the effect of the water layer on the 3-D propagation of the surface waves, by incorporating an efficient 3-D fluid-solid coupling for the acoustic-elastic numerical simulations. We have successfully applied this procedure to the crust and upper-mantle beneath the western Alps and the Ligurian-Provence basin, thus improving both the onshore and offshore parts of the ANT V_s model.

The ANT V_s model is so far the highest resolution model of the Alps and the Ligurian sea, from the conventional two-step tomography. We validated both the onshore and offshore parts of this model by comparing with recent receiver function (RF) and controlled-source seismic (CSS) cross-sections across the western Alps and the Ligurian-Provence basin, as seen in Chapters 2-4. Our V_s model provided new insights on the 3-D geometry and along-strike variations of the crust and upper-mantle structures beneath the western Alps (Moho steps in the French External Massifs and the subduction wedge, LVZ in the European lower crust, Adria seismic body, etc.). It also provided new insights into the thickness and petrological-lithological nature of the oceanic crust and the underlying upper-mantle beneath the Ligurian-Provence basin (gabbro intrusive bodies, no evidence of serpentinization, etc.). Finally, we achieved an even finer resolution and better robustness of the model with the use of the WET, which enhanced the contrast of the velocity structures and corrected their spatial location, especially in the marine part (as seen in Chapter 5). We extracted from this model, a high-resolution large-scale 3-D Moho map that covers the Alps and the Ligrurian sea. The obtained WET model is, to-date, the highest resolution shear-wave velocity model of the Alps and the Ligurian-Provence basin.

Perspectives

Improvement of the ANT and WET

In view of its robustness and simplicity, the classical two-step ANT is still required to derive robust preliminary 3-D velocity models for use in seismic imaging methods based on numerical modelling of wave propagation, such as the WET. The full Bayesian approach we have proposed, allowing the exploration of large sets of models, both for group velocity maps and for Vs depth, is a significant step forward in improving existing ANT methodologies. However, this method can be further improved. For instance, our 2-D traveltime inversion for the dispersion maps, still relies on the ray theory, which is the case in almost all classical ANT methods. A potential methodological effort to be made on this issue is considering finite-frequency kernels, already used in the framework of local earthquake tomography (LET). With regards to our 1-D inversion for V_s, it would be useful to perform the grid search over 1-D V_s model composed of larger number of sub-layers for a better description of complex geological lithologies. Finally, another possible improvement is to accompany the velocity models with a meaningful estimate of the resolution by considering it as a part of the inversion problem.

A possible improvement of our wave equation tomography might be the consideration of the anisotropy effect, which is non negligible in the Alpine region as shown be recent studies (e.g., Alder et al., 2021; Soergel et al., 2022). In our WET, we used only the vertical-component of Rayleigh waves and compared with the correlation signals of vertical-component noise records. Considering both Rayleigh and Love waves by using multi-component ambient-noise correlations would be useful to further constrain the 3-D shear-wave velocity model. Besides that, other types of misfit functions can be used for the WET, based on group traveltime differences or on cross-correlation time delays. In contrast to the multi-taper misfit function we used, these misfit functions are not phase-based and hence less resolving. However, they can be useful in preventing cycle skipping, which would potentially make initial model building by the ANT no longer necessary. It may also be useful to consider the issue of quantifying the model uncertainties in the context of WET, by employing techniques that have been already developed for the FWI problem, such as statistical-oriented approaches (e.g., Biswas and Sen, 2017; Fichtner et al., 2019), or ensemble Kalman filter (EnKF) approaches (e.g., Thurin et al., 2019, Hoffmann et al., in prep). Finally, the numerical modelling of wave propagation in the ocean and on its margins can be further improved with a finer meshing of the seabed than the staircase approximation we used. This could be useful at higher frequencies, especially for subsurface marine imaging with ambient noise.

Towards 3-D V_p, V_s models from FWI of earthquake body waves

Our next objective is to construct V_p, V_s models of the crust beneath the western Alps and the Ligurian-Provence basin using body waves from regional earthquakes. Our ANT and WET V_s models rely on surface waves, which are more sensitive to lateral variations than the intracrustal variations and structural interfaces, in contrast to the body waves. However, these models are high-quality starting models for full-waveform inversion (FWI) of body waves – a natural extension of the wave equation tomography based on ambient noise.

We aim to perform the FWI using body waves records from all available seismological stations in the period 2015-2022, the AlpArray network included. All available body-wave-based 3-D V_p, V_s models in our study area were derived from conventional local earthquake tomography (LET) – based on the arrival time information of the body-wave. As none of these models used the temporary AlpArray network (deployed only from 2016), they do not recover the 3-D velocity structures beneath the Ligurian-Provence basin. By performing the FWI, including the amplitude and waveform of body waves, and using the AlpArray stations in complement to permanent stations, we would further improve the resolution and coverage of the previous LET models. Since the earthquake parameters (origin time, hypocentre, focal mechanism) depend on the physical parameters of the medium, we will consider jointly inverting for the velocity and source parameters to achieve a better model robustness. Finally, to constrain both the structural interfaces and lateral velocity variations, we will consider alternating FWI and WET to invert both earthquake body waves and ambient-noise surface waves.

Applying FWI based on local-earthquake body waves for 3-D large-scale crustal imaging would involve the use of higher frequency content (up to 1 Hz), which is challenging both in terms of technical aspects and computational costs (rough estimates of the computational cost is shown in Appendix A). Nevertheless, we will take advantage of the same 3-D numerical simulation tools used for the WET, developed as part of the SEM46 package of the Seiscope consortium. The principal differences with respect to the WET, beyond the change in the seismic-wave type, will be the choice of the misfit function and the account of focal mechanisms of the earthquakes. As far as the computational time is at issue, the use of the WET model as an initial model, which is moreover the most reliable model to date, would be beneficial to achieve a reasonable convergence time. In addition, we will deploy the same source subsampling algorithm used in the WET this time for earthquakes, so that we can ensure a more thorough coverage while keeping the same total number of iterations.

The 3-D FWI model is intended to provide a high-resolution image of the crustal structures beneath the western Alps and the Ligurian sea, and key information on their lithological-petrological nature (with the V_p/V_s ratios). For instance, further constraining the complex 3-D structure of the subduction wedge – crucial in the understating of the strong lateral variations recorded at the surface and of the deep processes involved in the subduction of the European lithosphere. In the Ligurian-Provence basin, this model could provide key insights into the still debated nature and composition of the oceanic crust and underlying mantle.

The 3-D velocity models as input for other studies

Our 3-D velocity models can be used for other studies, either as 3-D self-consistent observations for geological and tectonic interpretations, or as input data for geophysical studies. Our ANT V_s model is already used to set up an integrated geological-geophysical 3-D model of the lithosphere beneath the western Alps and the Ligurian sea in the framework of the RGF (French Geological Referential) program. In this 3-D geomodel, the main geological formations (sediments, upper and lower crust, mantle) and their boundaries (basement, Moho, etc.) are constrained at depth by a series of geologically interpreted V_s cross-sections, together with 3-D iso-velocity surfaces, extracted from our model. Other ongoing studies use our ANT V_s model, for instance, as a seismological reference model for detection of clustered seismicity beneath the southwestern Alps and the Ligurian-Provence basin (Beaucé et al., in prep), for assessing chemical and mineralogical properties of the Alpine slab (Sonnet et al., in prep), and for describing the kinematic evolution of the Alpine orogeny since 35 Ma, in combination with geo-thermochronological, tectonic and sedimentological data (Bellahsen et al., in prep).

Appendix A

Computing resources required

I present here an overview of the computing resources required for the main tasks of this Ph.D. work.

We have used the regional High Performance Computing infrastructure of the GRICAD/CIMENT project, hosted by Univ. Grenoble Alpes (`https://gricad.univ-grenoble-alpes.fr`) and the national HPC clusters of the TGCC infrastructure (`https://www-hpc.cea.fr/fr/complexe/tgcc.htm`), available through the GENCI annual calls.

Main tasks	Computing time (CPU-scalar hours)	Machine - center	CPU architecture
Data download, processing and tests	~ 80 000	Dahu - GRICAD CIMENT	2×24c & 2×32c Intel Xeon Skylake @2.30 GHz
ANT (2-step inversion and tests)	~ 1 100 000	Dahu - GRICAD CIMENT	2×24c & 2×32c Intel Xeon Skylake @2.30 GHz
WET (inversion in 4 period bands and tests)	~ 970 000	Irene - TGCC	2×64c AMD Rome @2.60 GHz

Appendix B

Origin of data

The waveforms data used in this manuscript belong to the permanent seismological networks with codes AC, BE (Royal Observatory of Belgium, 1985), CA (Institut Cartogràfic i Geològic de Catalunya-Institut d'Estudis Catalans, 1984), CH [Swiss Seismological Service (SED) at ETH Zürich, 1983], CR (University Of Zagreb, International Federation of Digital Seismograph Networks, 2001), CZ (Institute of Geophysics, Academy of Sciences of the Czech Republic, 1973), ES (Instituto Geografico Nacional, Spain, 1999), FR (RESIF, 1995), G [Institut de Physique du Globe de Paris (IPGP) and Ecole et Observatoire des Sciences de la Terre de Strasbourg (EOST), 1982], GB [GEOFON Data Centre, 1993], GR [Federal Institute For Geosciences And Natural Resources (BGR), 1976], IV (INGV Seismological Data Centre, 2006), NL (KNMI, 1993), OE (ZAMG— Zentralanstalt für Meterologie und Geodynamik, 1987), SL (Slovenian Environment Agency, 2001), and UP (SNSN, 1904). We also used data of the temporary AlpArray network (Z3 network, AlpArray Seismic Network, 2015), Cifalps (YP network, Zhao et al., 2016b, and XT network, Zhao et al., 2018) and EASI experiments (XT network, AlpArray seismic network, 2014).

Acknowledgments

This study was partly funded by the SEISCOPE consortium (https://seiscope2.osug.fr), sponsored by AKERBP, CGG, CHEVRON, EQUINOR, EXXON-MOBIL, JGI, SHELL, SINOPEC, SISPROBE and TOTAL, and by the RGF program (Référentiel Géologique de la France, (http://rgf.brgm.fr/). It is part of the AlpArray-FR project funded by Agence Nationale de la Recherche (contract ANR-15-CE31-0015) and by Labex OSUG@2020 (Investissements d'Avenir, ANR-10-LABX-56).

This study was granted access to the HPC resources of the Dahu platform of the CIMENT infrastructure (https://gricad.univ-grenoble-alpes.fr/), which is supported by the Auvergne-Rhône-Alpes region (grant CPER07-13CIRA), the Labex OSUG@2020 (reference ANR10 LABX56) and the Equip@Meso project (reference ANR-10-EQPX-29-01) of the program 'Investissements d'Avenir' supervised by the Agence Nationale de la Recherche and the HPC resources of CINES/IDRIS/TGCC under allocation 046091 by GENCI.

We warmly thank Thomas Bodin, Yang Lu and Wayne Crawford for having shared their tools and for their constructive feedback on our ANT inversion methodology (TB, YL) and on OBS data processing (WC). We warmly thank Anke Dannowski for providing us the P-wave velocity model of LOBSTER-P02 transect.

We are grateful to the operators of European permanent seismic networks who make their data available through EIDA (http://www.orfeus-eu.org/data/eida/). We are grateful to the captains and crews of R.V. Pourquoi Pas? (France) and R.V. Maria S. Merian (Germany) for their work during the AlpArray-Leg-1 deployment cruise (doi:10.17600/17000400) and the MSM71-LOBSTER recovery cruise (doi:10.3289/GEOMAR_REP_NS_41_2018). We also thank all members of the scientific crews, in particular C. Aubert, S. Besançon and R. Daniel. The DEPAS pool provided 16 sea-bottom instruments used in his work, while the INSU-IPGP pool provided 7 broadband OBSs. The CIFALPS Team includes Coralie AUBERT, Elena EVA, Stéphane GUILLOT, Marco G. MALUSA, Silvia PONDRELLI, Simone SALIMBENI, Stefano SOLARINO, and Liang ZHAO. The Z3 network was operated by the AlpArray Seismic Network Team: György HETÉNYI, Rafael ABREU, Ivo ALLEGRETTI, Maria-Theresia APOLONER, Coralie AUBERT, Simon BESANÇON, Maxime BÈS DE BERC, Götz BOKELMANN, Didier BRUNEL, Marco CAPELLO, Martina ČARMAN, Adriano CAVALIERE, Jérôme CHÈZE, Claudio CHIARABBA, John CLINTON, Glenn COUGOULAT, Wayne C. CRAWFORD, Luigia CRISTIANO, Tibor CZIFRA, Ezio D'ALEMA, Stefania DANESI, Romuald DANIEL, Anke DANNOWSKI, Iva DASOVIĆ, Anne DESCHAMPS, Jean-Xavier DESSA, Cécile DOUBRE, Sven EGDORF, ETHZ-SED Electronics Lab, Tomislav FIKET, Kasper FISCHER, Wolfgang FRIEDERICH, Florian FUCHS, Sigward FUNKE, Domenico GIARDINI, Aladino GOVONI, Zoltán GRÁCZER, Gidera GRÖSCHL, Stefan HEIMERS, Ben HEIT, Davorka HERAK, Marijan HERAK, Johann HUBER, Dejan

JARIĆ, Petr JEDLIČKA, Yan JIA, Hélène JUND, Edi KISSLING, Stefan KLINGEN, Bernhard KLOTZ, Petr KOLÍNSKÝ, Heidrun KOPP, Michael KORN, Josef KOTEK, Lothar KÜHNE, Krešo KUK, Dietrich LANGE, Jürgen LOOS, Sara LOVATI, Deny MALENGROS, Lucia MARGHERITI, Christophe MARON, Xavier MARTIN, Marco MASSA, Francesco MAZZARINI, Thomas MEIER, Laurent MÉTRAL, Irene MOLINARI, Milena MORETTI, Anna NARDI, Jurij PAHOR, Anne PAUL, Catherine PÉQUEGNAT, Daniel PETERSEN, Damiano PESARESI, Davide PICCININI, Claudia PIROMALLO, Thomas PLENEFISCH, Jaroslava PLOMEROVÁ, Silvia PONDRELLI, Snježan PREVOLNIK, Roman RACINE, Marc RÉGNIER, Miriam REISS, Joachim RITTER, Georg RÜMPKER, Simone SALIMBENI, Marco SANTULIN, Werner SCHERER, Sven SCHIPPKUS, Detlef SCHULTE-KORTNACK, Vesna ŠIPKA, Stefano SOLARINO, Daniele SPALLAROSSA, Kathrin SPIEKER, Josip STIPČEVIĆ, Angelo STROLLO, Bálint SÜLE, Gyöngyvér SZANYI, Eszter SZŰCS, Christine THOMAS, Martin THORWART, Frederik TILMANN, Stefan UEDING, Massimiliano VALLOCCHIA, Luděk VECSEY, René VOIGT, Joachim WASSERMANN, Zoltán WÉBER, Christian WEIDLE, Viktor WESZTERGOM, Gauthier WEYLAND, Stefan WIEMER, Felix WOLF, David WOLYNIEC, Thomas ZIEKE, Mladen ŽIVČIĆ, Helena ŽLEBČÍKOVÁ.

Bibliography

Agard, P. (2021). Subduction of oceanic lithosphere in the Alps: Selective and archetypal from (slow-spreading) oceans. *Earth-Science Reviews*, 214:103517.

Aki, K., Christoffersson, A., and Husebye, E. S. (1977). Determination of the three-dimensional seismic structure of the lithosphere. *Journal of Geophysical Research*, 82(2):277–296.

Aki, K. and Lee, W. H. K. (1976). Determination of three-dimensional velocity anomalies under a seismic array using first p arrival times from local earthquakes: 1. a homogeneous initial model. *Journal of Geophysical Research (1896-1977)*, 81(23):4381–4399.

Alder, C., Debayle, E., Bodin, T., Paul, A., Stehly, L., Pedersen, H., and the AlpArray Working Group (2021). Evidence for radial anisotropy in the lower crust of the Apennines from Bayesian ambient noise tomography in Europe. *Geophysical Journal International*, 226(2):941–967.

AlpArray Seismic Network (2014). Eastern Alpine Seismic Investigation (EASI) - AlpArray Complimentary Experiment.

AlpArray Seismic Network (2015). AlpArray Seismic Network (AASN) temporary component.

Batsi, E., Tsang-Hin-Sun, E., Klingelhoefer, F., Bayrakci, G., Chang, E. T., Lin, J.-Y., Dellong, D., Monteil, C., and Géli, L. (2019). Nonseismic signals in the ocean: Indicators of deep sea and seafloor processes on ocean-bottom seismometer data. *Geochemistry, Geophysics, Geosystems*, 20(8):3882–3900.

Bayer, R., Le Mouel, J., and Le Pichon, X. (1973). Magnetic anomaly pattern in the western mediterranean: Earth and planetary sci. *Letters*, 19(2):168–176.

Beller, S., Monteiller, V., Operto, S., Nolet, G., Paul, A., and Zhao, L. (2018). Lithospheric architecture of the South-Western Alps revealed by multiparameter teleseismic full-waveform inversion. *Geophysical Journal International*, 212:1369–1388.

Bellon, H. (1981). Chronologie radiométrique (k-ar) des manifestations magmatiques autour de la méditerranée occidentale entre 33 et 1 ma. In *Consiglio nazionale delle ricerche. International conference*, pages 341–360.

Beslier, M.-O., Ask, M., and Boillot, G. (1993). Ocean-continent boundary in the iberia abyssal plain from multichannel seismic data. *Tectonophysics*, 218(4):383–393.

Bigi, G., Cosentino, D., Parotto, M., Sartori, R., and Scandone, P. (1990). Structural model of Italy and gravity map. *Quad. Ric. Sci.*, 114.

Bilau, A., Rolland, Y., Schwartz, S., Godeau, N., Guihou, A., Deschamps, P., Brigaud, B., Noret, A., Dumont, T., and Gautheron, C. (2021). Extensional reactivation of the Penninic frontal thrust 3 Myr ago as evidenced by U–Pb dating on calcite in fault zone cataclasite. *Solid Earth*, 12(1):237–251.

Biswas, R. and Sen, M. (2017). 2d full-waveform inversion and uncertainty estimation using the reversible jump hamiltonian monte carlo. In *2017 SEG International Exposition and Annual Meeting*. OnePetro.

Bodin, T., Sambridge, M., Rawlinson, N., and Arroucau, P. (2012). Transdimensional tomography with unknown data noise. *Geophysical Journal International*, 189(3):1536–1556.

Boillot, G., Féraud, G., Recq, M., and Girardeau, J. (1989). Undercrusting by serpentinite beneath rifted margins. *Nature*, 341(6242):523–525.

Bonatti, E., Seyler, M., Channell, J., Girardeau, J., and Mascle, G. (1990). Peridotites drilled from the tyrrhenian sea, odp leg 107. In *Proc. Ocean Drill. Program Sci. Results*, volume 107, pages 37–47.

Boschi, L. and Dziewonski, A. M. (1999). High- and low-resolution images of the Earth's mantle: Implications of different approaches to tomographic modeling. *Journal of Geophysical Research: Solid Earth*, 104(B11):25567–25594.

Boué, P., Roux, P., Campillo, M., and Briand, X. (2014). Phase velocity tomography of surface waves using ambient noise cross correlation and array processing. *Journal of Geophysical Research: Solid Earth*, 119(1):519–529.

Brives, J. (2020). *Tomographie des Pyrénées par corrélation de bruit d'ordre supérieur. Application multi-échelle.* PhD thesis, Université Grenoble Alpes.

Brocher, T. (2005). Empirical Relations between Elastic Wavespeeds and Density in the Earth's Crust. *Bulletin of the Seismological Society of America*, 95:2081–2092.

Bullock, A. D. and Minshull, T. A. (2005). From continental extension to seafloor spreading: crustal structure of the Goban Spur rifted margin, southwest of the UK. *Geophysical Journal International*, 163(2):527–546.

Burov, E., Francois, T., Yamato, P., and Wolf, S. (2014). Mechanisms of continental subduction and exhumation of HP and UHP rocks. *Gondwana Research*, 25(2):464–493.

Byrd, R. H., Lu, P., Nocedal, J., and Zhu, C. (1995). A limited memory algorithm for bound constrained optimization. *SIAM Journal on scientific computing*, 16(5):1190–1208.

Campillo, M. and Paul, A. (2003). Long-Range Correlations in the Diffuse Seismic Coda. *Science*, 299(5606):547–549.

Campillo, M., Roux, P., Romanowicz, B., and Dziewonski, A. (2014). Seismic imaging and monitoring with ambient noise correlations. *Treatise on geophysics*, 1:256–271.

Cao, J., Brossier, R., Górszczyk, A., Métivier, L., and Virieux, J. (2022). 3-d multiparameter full-waveform inversion for ocean-bottom seismic data using an efficient fluid–solid coupled spectral-element solver. *Geophysical Journal International*, 229(1):671–703.

Carvalho, J., Silveira, G., Kiselev, S., Custódio, S., Ramalho, R. S., Stutzmann, E., and Schimmel, M. (2022). Crustal and uppermost mantle structure of Cape Verde from ambient noise tomography. *Geophysical Journal International*, 231(2):1421–1433.

Cassano, E., Anelli, L., Fichera, R., and Cappelli, V. (1989). Pianura padana, interpretazione integrata di dati geofisici e geologici, agip servizi centrali per l'esplorazione, metodologie e appl. geofisiche, milano, 28.

Cerveny, V. (2003). Seismic ray theory.

Cerveny, V., Klimeš, L., and Pšenčík, I. (2007). Seismic ray method: Recent developments. *Advances in Geophysics*, 48:1–126.

Chauris, H. (2021). *Chapter 5 Full waveform inversion*, pages 123–146. EDP Sciences, Les Ulis.

Chen, M., Huang, H., Yao, H., van der Hilst, R., and Niu, F. (2014). Low wave speed zones in the crust beneath se tibet revealed by ambient noise adjoint tomography. *Geophysical Research Letters*, 41(2):334–340.

Chopin, C. (1984). Coesite and pure pyrope in high-grade blueschists of the Western Alps: a first record and some consequences. *Contributions to Mineralogy and Petrology*, 86(2):107–118.

Closs, H. and Labrouste, Y. (1963). Recherches séismologiques dans les alpes occidentales au moyen des grandes explosions en 1956, 1958 et 1960: Année géophysique internationale. *CNRS, 12e série, fasc. II.*

Contrucci, I., Nercessian, A., Béthoux, N., Mauffret, A., and Pascal, G. (2001). A ligurian (western mediterranean sea) geophysical transect revisited. *Geophysical Journal International*, 146(1):74–97.

Coulon, C. (1977). Le volcanisme calco-alcalin cénozoique de sardaigne (italie): Pétrologie, géochimie et genese des laves andésitiques et des ignimbrites: Signification géodynamique, these de doctorat. *Univ. d'Aix-Marseille III, Aix en Provence, France.*

Cox, H. (1973). Spatial correlation in arbitrary noise fields with application to ambient sea noise. *The Journal of the Acoustical Society of America*, 54(5):1289–1301.

Crawford, W. (2017). AlpArray LEG1 cruise, RV Pourquoi pas ?

Crawford, W. and Webb, S. (2000). Identifying and Removing Tilt Noise from Low-Frequency (<0.1 Hz) Seafloor Vertical Seismic Data. *The Bulletin of the Seismological Society of America*, 90:952–963.

Crawford, W., Webb, S., and Hildebrand, J. (1998). Estimating shear velocities in the oceanic crust from compliance measurements by two-dimensional finite difference modeling. *Journal of Geophysical Research: Solid Earth*, 103(B5):9895–9916.

Curtis, A. and Snieder, R. (1997). Reconditioning inverse problems using the genetic algorithm and revised parameterization. *Geophysics*, 62(5):1524–1532.

Dahlen, F. and Zhou, Y. (2006). Surface-wave group-delay and attenuation kernels. *Geophysical Journal International*, 165(2):545–554.

Dannowski, A., Kopp, H., Grevemeyer, I., Lange, D., Thorwart, M., Bialas, J., and Wollatz-Vogt, M. (2020). Seismic evidence for failed rifting in the ligurian basin, western alpine domain. *Solid Earth*, 11(3):873–887.

Davis, J. (1987). Local eigenfrequency and its uncertainty inferred from fundamental spheroidal mode frequency shifts. *Geophysical Journal International*, 88(3):693–722.

de Verdière, Y. C. (2006). Mathematical models for passive imaging i: general background. *arXiv: Mathematical Physics*.

Deen, M., Wielandt, E., Stutzmann, E., Crawford, W., Barruol, G., and Sigloch, K. (2017). First Observation of the Earth's Permanent Free Oscillations on Ocean Bottom Seismometers. *Geophysical Research Letters*, 44(21):10,988–10,996.

Derode, A., Larose, E., Campillo, M., and Fink, M. (2003a). How to estimate the green's function of a heterogeneous medium between two passive sensors? application to acoustic waves. *Applied Physics Letters*, 83(15):3054–3056.

Derode, A., Larose, E., Tanter, M., De Rosny, J., Tourin, A., Campillo, M., and Fink, M. (2003b). Recovering the green's function from field-field correlations in an open scattering medium (l). *The Journal of the Acoustical Society of America*, 113(6):2973–2976.

Dessa, J.-X., Beslier, M.-O., Schenini, L., Chamot-Rooke, N., Corradi, N., Delescluse, M., Déverchère, J., Larroque, C., Sambolian, S., Canva, A., et al. (2020). Seismic exploration of the deep structure and seismogenic faults in the ligurian sea by joint multi channel and ocean bottom seismic acquisitions: Preliminary results of the sefasils cruise. *Geosciences*, 10(3):108.

Di Stefano, R., Kissling, E., Chiarabba, C., Amato, A., and Giardini, D. (2009). Shallow subduction beneath italy: Three-dimensional images of the adriatic-european-tyrrhenian lithosphere system based on high-quality p wave arrival times. *Journal of Geophysical Research: Solid Earth*, 114(B5).

Diehl, T., Husen, S., Kissling, E., and Deichmann, N. (2009). High-resolution 3-D P-wave model of the Alpine crust. *Geophysical Journal International*, 179(2):1133–1147.

Duchêne, S., Blichert-Toft, J., Luais, B., Télouk, P., Lardeaux, J.-M., and Albarede, F. (1997). The Lu–Hf dating of garnets and the ages of the alpine high-pressure metamorphism. *Nature*, 387(6633):586–589.

Dueker, K. G. and Sheehan, A. F. (1997). Mantle discontinuity structure from midpoint stacks of converted p to s waves across the yellowstone hotspot track. *Journal of Geophysical Research*, 102:8313–8327.

Dumont, T., Schwartz, S., Guillot, S., Simon-Labric, T., Tricart, P., and Jourdan, S. (2012). Structural and sedimentary records of the oligocene revolution in the western alpine arc. *Journal of Geodynamics*, 56:18–38.

Dziewonski, A. and Anderson, L. (1981). Preliminary reference earth model. *Physics of the earth and planetary interiors*, 25(4):297–356.

Dziewonski, A., Bloch, S., and Landisman, M. (1969a). A technique for the analysis of transient seismic signals. *Bulletin of the Seismological Society of America*, 59(1):427–444.

Dziewonski, A., Bloch, S., and Landisman, M. (1969b). A technique for the analysis of transient seismic signals. *Bulletin of the Seismological Society of America*, 59(1):427–444.

Dziewonski, A., Hales, A., and Lapwood, E. (1975). Parametrically simple earth models consistent with geophysical data. *Physics of the Earth and Planetary Interiors*, 10(1):12–48.

Déverchère, J. and Beslier, M.-O. (1995). Malis cruise, rv le nadir.

Eddy, C. L. and Ekström, G. (2014). Local amplification of rayleigh waves in the continental united states observed on the usarray. *Earth and Planetary Science Letters*, 402:50–57.

Egger, A., Demartin, M., Ansorge, J., Banda, E., and Maistrello, M. (1988). The gross structure of the crust under corsica and sardinia. *Tectonophysics*, 150:363–389.

Eva, E., Malusà, M. G., and Solarino, S. (2015). A seismotectonic picture of the inner southern Western Alps based on the analysis of anomalously deep earthquakes. *Tectonophysics*, 661:190–199.

Eva, E., Malusà, M. G., and Solarino, S. (2020). Seismotectonics at the Transition Between Opposite-Dipping Slabs (Western Alpine Region). *Tectonics*, 39(9):e2020TC006086.

Faccenna, C., Becker, T. W., Auer, L., Billi, A., Boschi, L., Brun, J. P., Capitanio, F. A., Funiciello, F., Horvàth, F., Jolivet, L., Piromallo, C., Royden, L., Rossetti, F., and Serpelloni, E. (2014). Mantle dynamics in the mediterranean. *Reviews of Geophysics*, 52(3):283–332.

Faccenna, C., Mattei, M., Funiciello, R., and Jolivet, L. (1997). Styles of back-arc extension in the central mediterranean. *Terra Nova*, 9(3):126–130.

Federal Institute for Geosciences and Natural Resources (BGR) (1976). German Regional Seismic Network (GRSN). Publisher: Federal Institute for Geosciences and Natural Resources (BGR).

Fichtner, A., Kennett, B. L., Igel, H., and Bunge, H.-P. (2009). Full seismic waveform tomography for upper-mantle structure in the australasian region using adjoint methods. *Geophysical Journal International*, 179(3):1703–1725.

Fichtner, A. and Villaseñor, A. (2015). Crust and upper mantle of the western mediterranean–constraints from full-waveform inversion. *Earth and Planetary Science Letters*, 428:52–62.

Fichtner, A., Zunino, A., and Gebraad, L. (2019). Hamiltonian monte carlo solution of tomographic inverse problems. *Geophysical Journal International*, 216(2):1344–1363.

Ford, Lickorish, and Kusznir (1999). Tertiary foreland sedimentation in the Southern Subalpine Chains, SE France: a geodynamic appraisal. *Basin Research*, 11:315–336.

Gailler, A., Klingelhoefer, F., Olivet, J.-L., Aslanian, D., Technical, O., et al. (2009). Crustal structure of a young margin pair: New results across the liguro–provencal basin from wide-angle seismic tomography. *Earth and Planetary Science Letters*, 286(1-2):333–345.

Galetti, E., Curtis, A., Meles, G. A., and Baptie, B. (2015). Uncertainty Loops in Travel-Time Tomography from Nonlinear Wave Physics. *Phys. Rev. Lett.*, 114:148501.

GEOFON Data Centre (1993). GEOFON seismic network. Publisher: Deutsches GeoForschungsZentrum GFZ.

Gouedard, P., Stehly, L., Brenguier, F., Campillo, M., De Verdière, Y. C., Larose, E., Margerin, L., Roux, P., Sánchez-Sesma, F. J., Shapiro, N., et al. (2008). Cross-correlation of random fields: Mathematical approach and applications. *Geophysical prospecting*, 56(3):375–393.

Grand, S. P. (1987). Tomographic inversion for shear velocity beneath the north american plate. *Journal of Geophysical Research: Solid Earth*, 92(B13):14065–14090.

Graves, R. W. (1996). Simulating seismic wave propagation in 3d elastic media using staggered-grid finite differences. *Bulletin of the seismological society of America*, 86(4):1091–1106.

Grevemeyer, I., Hayman, N. W., Peirce, C., Schwardt, M., Van Avendonk, H. J., Dannowski, A., and Papenberg, C. (2018). Episodic magmatism and serpentinized mantle exhumation at an ultraslow-spreading centre. *Nature Geoscience*, 11(6):444–448.

Gueguen, E., Doglioni, C., and Fernandez, M. (1998). On the post-25 ma geodynamic evolution of the western mediterranean. *Tectonophysics*, 298(1):259–269.

Guerin, G., Rivet, D., Deschamps, A., Larroque, C., Mordret, A., Dessa, J.-X., and Martin, X. (2020). High resolution ambient noise tomography of the southwestern alps and the ligurian margin. *Geophysical Journal International*, 220(2):806–820.

Guillot, S., Hattori, K., Agard, P., Schwartz, S., and Vidal, O. (2009). Exhumation Processes in Oceanic and Continental Subduction Contexts: A Review. In Lallemand, S. and Funiciello, F., editors, *Subduction Zone Geodynamics*, pages 175–205, Berlin, Heidelberg. Springer Berlin Heidelberg.

Gutenberg, B. (1914). Ueber erdbebenwellen. vii a. beobachtungen an registrierungen von fernbeben in göttingen und folgerung über die konstitution des erdkörpers (mit tafel). *Nachrichten von der Gesellschaft der Wissenschaften zu Göttingen, Mathematisch-Physikalische Klasse*, 1914:125–176.

Gutenberg, B. (1926). Untersuchungen zur frage, bis zu welcher tiefe die erde kristallin ist. *Zeitschrift für Geophysik*, 2:24–29.

Hable, S., Sigloch, K., Barruol, G., Stähler, S. C., and Hadziioannou, C. (2018). Clock errors in land and ocean bottom seismograms: high-accuracy estimates from multiple-component noise cross-correlations. *Geophysical Journal International*, 214(3):2014–2034.

Hable, S., Sigloch, K., Stutzmann, E., Kiselev, S., and Barruol, G. (2019). Tomography of crust and lithosphere in the western Indian Ocean from noise cross-correlations of land and ocean bottom seismometers. *Geophysical Journal International*, 219(2):924–944.

Handy, M. R., Schmid, S. M., Bousquet, R., Kissling, E., and Bernoulli, D. (2010). Reconciling plate-tectonic reconstructions of alpine tethys with the geological–geophysical record of spreading and subduction in the alps. *Earth-Science Reviews*, 102(3-4):121–158.

Harmon, N., Forsyth, D., and Webb, S. (2007). Using ambient seismic noise to determine short-period phase velocities and shallow shear velocities in young oceanic lithosphere. *Bulletin of the Seismological Society of America*, 97(6):2009–2023.

Herak, M. (2005). *Andrija Mohorovičić memorial rooms*. http://www.gfz.hr/sobe-en/andrija.htm.

Herrmann, R. B. (1973). Some aspects of band-pass filtering of surface waves. *Bulletin of the Seismological Society of America*, 63(2):663–671.

Herrmann, R. B. (2013). Computer Programs in Seismology: An Evolving Tool for Instruction and Research. *Seismological Research Letters*, 84(6):1081–1088.

Hetényi, G., Molinari, I., and Clinton, J. (2018). The AlpArray Seismic Network: A Large-Scale European Experiment to Image the Alpine Orogen. *Surveys in Geophysics*, 39.

Hetényi, G., Plomerová, J., Bianchi, I., Kampfová Exnerová, H., Bokelmann, G., Handy, M. R., and Babuška, V. (2018). From mountain summits to roots: Crustal structure of the eastern alps and bohemian massif along longitude 13.3°E. *Tectonophysics*, 744:239–255.

Hirn, A., Nadir, S., Thouvenot, F., Nicolich, R., Pellis, G., Scarascia, S., Tabacco, I., Castellano, M., and Merlantip, F. (1989). A new picture of the Moho under the western Alps. *Nature*, 337:249–251.

INGV Seismological Data Centre (2006). Rete Sismica Nazionale (RSN). Publisher: Istituto Nazionale di Geofisica e Vulcanologia (INGV), Italy.

Institut Cartogràfic I Geològic De Catalunya - Institut D'Estudis Catalans (1984). Catalan Seismic Network. Publisher: International Federation of Digital Seismograph Networks.

Institut de Physique du Globe de Paris (IPGP) and Ecole et Observatoire des Sciences de la Terre de Strasbourg (EOST) (1982). GEOSCOPE, French Global Network of broad band seismic stations. Publisher: Institut de Physique du Globe de Paris (IPGP).

Institute Of Geophysics Of The Academy Of Sciences Of The Czech Republic (1973). Czech Regional Seismic Network. Publisher: International Federation of Digital Seismograph Networks.

Instituto Geografico Nacional, Spain (1999). Spanish Digital Seismic Network. Publisher: International Federation of Digital Seismograph Networks.

Jolivet, L. and Faccenna, C. (2000). Mediterranean extension and the africa-eurasia collision. *Tectonics*, 19(6):1095–1106.

Jolivet, L., Romagny, A., Gorini, C., Maillard, A., Thinon, I., Couëffé, R., Ducoux, M., and Séranne, M. (2020). Fast dismantling of a mountain belt by mantle flow: Late-orogenic evolution of pyrenees and liguro-provençal rifting. *Tectonophysics*, 776:228312.

Jourdon, A., Rolland, Y., Petit, C., and Bellahsen, N. (2014). Style of Alpine tectonic deformation in the Castellane fold-and-thrust belt (SW Alps, France): Insights from balanced cross-sections. *Tectonophysics*, 633:143–155.

Kästle, E., Molinari, I., Boschi, L., Kissling, E., and Group, A. W. (2022). Azimuthal anisotropy from eikonal tomography: example from ambient-noise measurements in the alparray network. *Geophysical Journal International*, 229(1):151–170.

Kennett, B. L. N. and Engdahl, E. R. (1991). Traveltimes for global earthquake location and phase identification. *Geophysical Journal International*, 105(2):429–465.

Kirkpatrick, S., Gelatt Jr, C. D., and Vecchi, M. P. (1983). Optimization by simulated annealing. *science*, 220(4598):671–680.

Klingelhoefer, F., Olivet, J., Aslanian, D., Bache, F., Moulin, M., Matias, L., Afilhado, A., Nouze, H., Bellier, M., and Gailler, A. (2008). Preliminary results from the sardinia deep seismic cruise on the western sardinia and gulf of lions conjugate margin pair. In *EGU meeting april 2008*.

KNMI (1993). Netherlands Seismic and Acoustic Network. Publisher: Royal Netherlands Meteorological Institute (KNMI).

Komatitsch, D. and Tromp, J. (1999). Introduction to the spectral element method for three-dimensional seismic wave propagation. *Geophysical journal international*, 139(3):806–822.

Komatitsch, D. and Vilotte, J.-P. (1998). The spectral element method: an efficient tool to simulate the seismic response of 2d and 3d geological structures. *Bulletin of the seismological society of America*, 88(2):368–392.

Kopp, H., Lange, D., Thorwart, M., Paul, A., Dannowski, A., Petersen, F., Aubert, C., Beek, F., Beniest, A., Besançon, S., Brotzer, A., Caielli, G., Crawford, W. C., Deen, M., Lehmann, C., Marquardt, K., Neckel, M., Papanagnou, L., Schramm, B., Schröder, P., Steffen, K.-P., Wolf, F. N., and Xia, Y. (2018). Rv maria s. merian fahrtbericht / cruise report msm71 lobster: Ligurian ocean bottom seismology and tectonics research, las palmas (spain) – heraklion (greece) 07.02.-27.02.2018.

Kustowski, B., Ekström, G., and Dziewoński, A. (2008). Anisotropic shear-wave velocity structure of the earth's mantle: A global model. *Journal of Geophysical Research: Solid Earth*, 113(B6).

Kvapil, J., Plomerová, J., Kampfová Exnerová, H., Babuška, V., Hetényi, G., and Group, A. W. (2021). Transversely isotropic lower crust of variscan central europe imaged by ambient noise tomography of the bohemian massif. *Solid Earth*, 12(5):1051–1074.

Kästle, E. D., El-Sharkawy, A., Boschi, L., Meier, T., Rosenberg, C., Bellahsen, N., Cristiano, L., and Weidle, C. (2018). Surface Wave Tomography of the Alps Using Ambient-Noise and Earthquake Phase Velocity Measurements. *Journal of Geophysical Research: Solid Earth*, 123(2):1770–1792.

Lailly, P. and Bednar, J. (1983). The seismic inverse problem as a sequence of before stack migrations.

Langston, C. A. (1979). Structure under mount rainier, washington, inferred from teleseismic body waves. *Journal of Geophysical Research: Solid Earth*, 84(B9):4749–4762.

Lardeaux, J.-M., Schwartz, S., Tricart, P., Paul, A., Guillot, S., Béthoux, N., and Masson, F. (2006). A crustal-scale cross-section of the south-western Alps combining geophysical and geological imagery. *Terra Nova*, 18:412–422.

Lehmann, I. (1936). " p'". *Bur. Ctr. Seism. Int. A*, 14:3–31.

Leprêtre, A., Klingelhoefer, F., Graindorge, D., Schnurle, P., Beslier, M.-O., Yelles, K., Déverchère, J., and Bracene, R. (2013). Multiphased tectonic evolution of the central algerian margin from combined wide-angle and reflection seismic data off tipaza, algeria. *Journal of Geophysical Research: Solid Earth*, 118(8):3899–3916.

Levander, A., Schmandt, B., Miller, M. S., Liu, K., Karlstrom, K. E., Crow, R. S., Lee, C.-T. A., and Humphreys, E. D. (2011). Continuing colorado plateau uplift by delamination-style convective lithospheric downwelling. *Nature*, 472(7344):461–465.

Levshin, A., Yanovskaya, T., Lander, A., Bukchin, B., Barmin, M., Its, E., and Ratnikova, L. (1989). *Seismic Surface Waves in a Laterally Inhomogeneous Earth*. Kluwer Publ, Dordrecht, pp 129–182.

Liao, J., Malusà, M. G., Zhao, L., Baldwin, S. L., Fitzgerald, P. G., and Gerya, T. (2018). Divergent plate motion drives rapid exhumation of (ultra)high pressure rocks. *Earth and Planetary Science Letters*, 491:67–80.

Liu, D., Zhao, L., Paul, A., Yuan, H., Solarino, S., Aubert, C., Pondrelli, S., Salimbeni, S., Eva, E., Malusà, M. G., and Guillot, S. (2022). Receiver function mapping of the mantle transition zone beneath the western alps: New constraints on slab subduction and mantle upwelling. *Earth and Planetary Science Letters*, 577:117267.

Liu, Y., Niu, F., Chen, M., and Yang, W. (2017). 3-d crustal and uppermost mantle structure beneath ne china revealed by ambient noise adjoint tomography. *Earth and Planetary Science Letters*, 461:20–29.

Lobkis, O. I. and Weaver, R. L. (2001). On the emergence of the green's function in the correlations of a diffuse field. *The Journal of the Acoustical Society of America*, 110(6):3011–3017.

Lombardi, D., Braunmiller, J., Kissling, E., and Giardini, D. (2008). Moho depth and poisson's ratio in the western-central alps from receiver functions. *Geophysical Journal International*, 173(1):249–264.

Lu, Y., Stehly, L., Brossier, R., Paul, A., and AlpArray Working Group (2020). Imaging Alpine crust using ambient noise wave-equation tomography. *Geophysical Journal International*, 222(1):69–85.

Lu, Y., Stehly, L., Paul, A., and AlpArray Working Group (2018). High-resolution surface wave tomography of the European crust and uppermost mantle from ambient seismic noise. *Geophysical Journal International*, 214(2):1136–1150.

Luo, Y. and Schuster, G. T. (1991). Wave-equation traveltime inversion. *Geophysics*, 56(5):645–653.

Macchiavelli, C., Vergés, J., Schettino, A., Fernàndez, M., Turco, E., Casciello, E., Torne, M., Pierantoni, P. P., and Tunini, L. (2017). A new southern north atlantic isochron map: Insights into the drift of the iberian plate since the late cretaceous. *Journal of Geophysical Research: Solid Earth*, 122(12):9603–9626.

Macquet, M., Paul, A., Pedersen, H. A., Villaseñor, A., Chevrot, S., Sylvander, M., Wolyniec, D., and Pyrope Working Group (2014). Ambient noise tomography of the Pyrenees and the surrounding regions: inversion for a 3-D Vs model in the presence of a very heterogeneous crust. *Geophysical Journal International*, 199(1):402–415.

Magrini, F., Diaferia, G., El-Sharkawy, A., Cammarano, F., van der Meijde, M., Meier, T., and Boschi, L. (2022). Surface-wave tomography of the central-western mediterranean: New insights into the liguro-provençal and tyrrhenian basins. *Journal of Geophysical Research: Solid Earth*, 127(3):e2021JB023267.

Makris, J., Egloff, F., Nicolich, R., and Rihm, R. (1999). Crustal structure from the ligurian sea to the northern apennines—a wide angle seismic transect. *Tectonophysics*, 301(3-4):305–319.

Malinverno, A. and Briggs, V. (2004). Expanded uncertainty quantification in inverse problems: Hierarchical Bayes and empirical Bayes. *Geophysics*, 69:1005–1016.

Malusà, M. G., Faccenna, C., Baldwin, S. L., Fitzgerald, P. G., Rossetti, F., Balestrieri, M. L., Danišík, M., Ellero, A., Ottria, G., and Piromallo, C. (2015). Contrasting styles of (u)hp rock exhumation along the cenozoic adria-europe plate boundary (western alps, calabria, corsica). *Geochemistry, Geophysics, Geosystems*, 16(6):1786–1824.

Malusà, M. G., Guillot, S., Zhao, L., Paul, A., Solarino, S., Dumont, T., Schwartz, S., Aubert, C., Baccheschi, P., Eva, E., Lu, Y., Lyu, C., Pondrelli, S., Salimbeni, S., Sun, W., and Yuan, H. (2021). The deep structure of the alps based on the cifalps seismic experiment: A synthesis. *Geochemistry, Geophysics, Geosystems*, 22(3):e2020GC009466. e2020GC009466 2020GC009466.

Malusà, M. G., Zhao, L., Eva, E., Solarino, S., Paul, A., Guillot, S., Schwartz, S., Dumont, T., Aubert, C., Salimbeni, S., Pondrelli, S., Wang, Q., and Zhu, R. (2017). Earthquakes in the western Alpine mantle wedge. *Gondwana Research*, 44:89–95.

Manzotti, P., Schiavi, F., Nosenzo, F., Pitra, P., and Ballèvre, M. (2022). A journey towards the forbidden zone: a new, cold, UHP unit in the Dora-Maira Massif (Western Alps). *Contributions to Mineralogy and Petrology*, 177(6):59.

Mascle, J. and Rehault, J.-P. (1990). A revised seismic stratigraphy of the tyrrhenian sea: implications for the basin evolution. pages 617–637.

Masters, G., Jordan, T. H., Silver, P. G., and Gilbert, F. (1982). Aspherical earth structure from fundamental spheroidal-mode data. *Nature*, 298(5875):609–613.

Mathey, M., Sue, C., Pagani, C., Baize, S., Walpersdorf, A., Bodin, T., Husson, L., Hannouz, E., and Potin, B. (2020). Present-day geodynamics of the Western Alps: new insights from earthquake mechanisms. *Solid Earth Discussions*, 2020:1–38.

McKenzie, D. (1978). Some remarks on the development of sedimentary basins. *Earth and Planetary science letters*, 40(1):25–32.

Metropolis, N. and Ulam, S. (1949). The monte carlo method. *Journal of the American statistical association*, 44(247):335–341.

Millet, F., Bodin, T., and Rondenay, S. (2019). Multimode 3-d kirchhoff migration of receiver functions at continental scale. *Journal of Geophysical Research: Solid Earth*, 124(8):8953–8980.

Mohorovičić, A. (1909). Das beben vom 8. x. 1909. *Jb. Met. Obs. Zagreb (Agram)*, (9):1–63.

Molinari, I. and Morelli, A. (2011). Epcrust: a reference crustal model for the european plate. *Geophysical Journal International*, 185(1):352–364.

Molinari, I., Verbeke, J., Boschi, L., Kissling, E., and Morelli, A. (2015). Italian and Alpine three-dimensional crustal structure imaged by ambient-noise surface-wave dispersion. *Geochemistry, Geophysics, Geosystems*, 16(12):4405–4421.

Mordret, A., Landès, M., Shapiro, N., Singh, S., and Roux, P. (2014). Ambient noise surface wave tomography to determine the shallow shear velocity structure at valhall: depth inversion with a neighbourhood algorithm. *Geophysical Journal International*, 198(3):1514–1525.

Mosca, P., Riccardo, P., Rogledi, S., and Rossi, M. (2010). New data for the kinematic interpretation of the Alps–Apennines junction (Northwestern Italy). *International Journal of Earth Sciences*, 99:833–849.

Moschetti, M. P., Ritzwoller, M. H., Lin, F., and Yang, Y. (2010). Seismic evidence for widespread western-us deep-crustal deformation caused by extension. *Nature*, 464(7290):885–889.

Nataf, H.-C., Nakanishi, I., and Anderson, D. L. (1986). Measurements of mantle wave velocities and inversion for lateral heterogeneities and anisotropy: 3. inversion. *Journal of Geophysical Research: Solid Earth*, 91(B7):7261–7307.

Nayfeh, A. H. (1995). *Wave propagation in layered anisotropic media: With application to composites*. Elsevier.

Nicolas, A., Hirn, A., Nicolich, R., and Polino, R. (1990). Lithospheric wedging in the western Alps inferred from the ECORS-CROP traverse. *Geology*, 18(7):587–590.

Nocedal, J. (1980). Updating quasi-newton matrices with limited storage. *Mathematics of computation*, 35(151):773–782.

Nocedal, J. and Wright, S. J. (2006). Numerical optimization 2nd edition.

Nouibat, A., Stehly, L., Paul, A., Schwartz, S., Bodin, T., Dumont, T., Rolland, Y., Brossier, R., Team, C., and AlpArray Working Group (2022a). Lithospheric transdimensional ambient-noise tomography of W-Europe: implications for crustal-scale geometry of the W-Alps. *Geophysical Journal International*. ggab520.

Nouibat, A., Stehly, L., Paul, A., Schwartz, S., Rolland, Y., Dumont, T., Crawford, W., Brossier, R., Team, C., and Group, A. W. (2022b). Ambient-noise tomography of the ligurian-provence basin using the alparray onshore-offshore network: Insights for the oceanic domain structure. *Journal of Geophysical Research: Solid Earth*, 127(8):e2022JB024228.

of Genova, U. (1967). Regional seismic network of north western italy. *International Federation of Digital Seismograph Networks*.

Operto, S., Virieux, J., Amestoy, P., L'Excellent, J.-Y., Giraud, L., and Ali, H. B. H. (2007). 3d finite-difference frequency-domain modeling of visco-acoustic wave propagation using a massively parallel direct solver: A feasibility study. *Geophysics*, 72(5):SM195–SM211.

Paige, C. C. and Saunders, M. A. (1982). Lsqr: An algorithm for sparse linear equations and sparse least squares. *ACM Transactions on Mathematical Software (TOMS)*, 8(1):43–71.

Pascal, G., Mauffret, A., and Patriat, P. (1993). The ocean-continent boundary in the gulf of lion from analysis of expanding spread profiles and gravity modelling. *Geophysical Journal International*, 113(3):701–726.

Paul, A. (2022). What we (possibly) know about the 3-d structure of crust and mantle beneath the alpine chain.

Paul, A., Cattaneo, M., Thouvenot, F., Spallarossa, D., Béthoux, N., and Fréchet, J. (2001). A three-dimensional crustal velocity model of the southwestern Alps from local earthquake tomography. *Journal of Geophysical Research: Solid Earth*, 106(B9):19367–19389.

Paul, A., Malusà, M. G., Solarino, S., Salimbeni, S., Eva, E., Nouibat, A., Pondrelli, S., Aubert, C., Dumont, T., Guillot, S., Schwartz, S., and Zhao, L. (2022). Along-strike variations in the fossil subduction zone of the western alps revealed by the cifalps seismic experiments and their implications for exhumation of (ultra-) high-pressure rocks. *Earth and Planetary Science Letters*, 598:117843.

Peterson, J. R. (1993). Observations and modeling of seismic background noise. Technical report, US Geological Survey.

Piana Agostinetti, N. and Amato, A. (2009). Moho depth and vp/vs ratio in peninsular italy from teleseismic receiver functions. *Journal of Geophysical Research: Solid Earth*, 114(B6).

Pladys, A., Brossier, R., Li, Y., and Métivier, L. (2021). On cycle-skipping and misfit function modification for full-wave inversion: Comparison of five recent approaches. *Geophysics*, 86(4):R563–R587.

Plessix, R.-E. (2006). A review of the adjoint-state method for computing the gradient of a functional with geophysical applications. *Geophysical Journal International*, 167(2):495–503.

Polino, R., Dal Piaz, G. V., and Gosso, G. (1990). Tectonic erosion at the adria margin and accretionary processes for the cretaceous orogeny of the alps. *Mémoires de la Société géologique de France (1833)*, 156:345–367.

Potin, B. (2016). *Les Alpes occidentales: tomographie, localisation de séismes et topographie du Moho*. Université Grenoble Alpes.

Qiao, L., Yao, H., Lai, Y.-C., Huang, B.-S., and Zhang, P. (2018). Crustal structure of southwest china and northern vietnam from ambient noise tomography: Implication for the large-scale material transport model in se tibet. *Tectonics*, 37(5):1492–1506.

Rappisi, F., VanderBeek, B., Faccenda, M., Morelli, A., and Molinari, I. (2022). Slab geometry and upper mantle flow patterns in the central mediterranean from 3d anisotropic p-wave tomography. *Journal of Geophysical Research: Solid Earth*, 127(5):e2021JB023488.

Rawlinson, N. and Sambridge, M. (2004). Wave front evolution in strongly heterogeneous layered media using the fast marching method. *Geophysical Journal International*, 156(3):631–647.

Réhault, J.-P., Boillot, G., and Mauffret, A. (1984). The western mediterranean basin geological evolution. *Marine Geology*, 55(3):447–477. Geological and Geodynamical Aspects on the Mediterranean.

Réhault, J.-P., Honthaas, C., Guennoc, P., Bellon, H., Ruffet, G., Cotten, J., Sosson, M., and Maury, R. (2012). Offshore oligo-miocene volcanic fields within the corsica-liguria basin: Magmatic diversity and slab evolution in the western mediterranean sea. *Journal of Geodynamics*, 58:73–95.

Ren, Y., Grecu, B., Stuart, G., Houseman, G., Hegedüs, E., and Group, S. C. P. W. (2013). Crustal structure of the carpathian–pannonian region from ambient noise tomography. *Geophysical Journal International*, 195(2):1351–1369.

RESIF (1995). RESIF-RLBP French Broad-band network, RESIF-RAP strong motion network and other seismic stations in metropolitan France. Publisher: RESIF - Réseau Sismologique et géodésique Français.

Reynard, B. (2013). Serpentine in active subduction zones. *Lithos*, 178:171–185.

Ritzwoller, M. H. and Lavely, E. M. (1995). Three-dimensional seismic models of the earth's mantle. *Reviews of Geophysics*, 33(1):1–66.

Rollet, N., Déverchère, J., Beslier, M.-O., Guennoc, P., Réhault, J.-P., Sosson, M., and Truffert, C. (2002). Back arc extension, tectonic inheritance, and volcanism in the ligurian sea, western mediterranean. *Tectonics*, 21(3):6–1–6–23.

Romanowicz, B. (1991). Seismic tomography of the earth's mantle. *Annual Review of Earth and Planetary Sciences*, 19:77.

Rondenay, S. (2009). Upper mantle imaging with array recordings of converted and scattered teleseismic waves. *Surveys in geophysics*, 30(4):377–405.

Roure, F., Polino, R., and Nicolich, R. (1990). Early neogene deformation beneath the po plain: constraints on the post-collisional alpine evolution. *Mémoires de la Société géologique de France (1833)*, 156:309–321.

Roux, P., Sabra, K. G., Gerstoft, P., Kuperman, W., and Fehler, M. C. (2005). P-waves from cross-correlation of seismic noise. *Geophysical Research Letters*, 32(19).

Royal Observatory Of Belgium (1985). Belgian Seismic Network. Publisher: International Federation of Digital Seismograph Networks.

Sadeghi-Bagherabadi, A., Vuan, A., Aoudia, A., Parolai, S., , T. A., Group, A.-S.-D. W., Heit, B., Weber, M., Haberland, C., and Tilmann, F. (2021). High-resolution crustal s-wave velocity model and moho geometry beneath the southeastern alps: New insights from the swath-d experiment. *Frontiers in Earth Science*, 9:188.

Sambridge, M. (1999). Geophysical inversion with a neighbourhood algorithm—i. searching a parameter space. *Geophysical journal international*, 138(2):479–494.

Sambridge, M., Rawlinson, N., Levander, A., and Nolet, G. (2005). Seismic tomography with irregular meshes. *GEOPHYSICAL MONOGRAPH-AMERICAN GEOPHYSICAL UNION*, 157:49.

Sandwell, D. T. and Smith, W. H. (1997). Marine gravity anomaly from geosat and ers 1 satellite altimetry. *Journal of Geophysical Research: Solid Earth*, 102(B5):10039–10054.

Sandwell, D. T., Yale, M., and Smith, W. (1995). Gravity anomaly profiles from ers-1, topex and geosat altimetry. *Eos Trans. AGU*, 76(17):S89.

Scarponi, M., Hetényi, G., Berthet, T., Baron, L., Manzotti, P., Petri, B., Pistone, M., and Müntener, O. (2020). New gravity data and 3-d density model constraints on the ivrea geophysical body (western alps). *Geophysical Journal International*, 222(3):1977–1991.

Schaefer, J. F., Boschi, L., and Kissling, E. (2011). Adaptively parametrized surface wave tomography: methodology and a new model of the European upper mantle. *Geophysical Journal International*, 186(3):1431–1453.

Schippkus, S., Zigone, D., and Bokelmann, G. (2020). Azimuthal anisotropy in the wider vienna basin region: a proxy for the present-day stress field and deformation. *Geophysical Journal International*, 220(3):2056–2067.

Schippkus, S., Zigone, D., Bokelmann, G., and the AlpArray Working Group (2018). Ambient-noise tomography of the wider Vienna Basin region. *Geophysical Journal International*, 215(1):102–117.

Schmid, S. M., Fügenschuh, B., Kissling, E., and Schuster, R. (2004). Tectonic map and overall architecture of the alpine orogen. *Eclogae Geologicae Helvetiae*, 97(1):93–117.

Schmid, S. M., Kissling, E., Diehl, T., van Hinsbergen, D. J., and Molli, G. (2017). Ivrea mantle wedge, arc of the Western Alps, and kinematic evolution of the Alps–Apennines orogenic system. *Swiss Journal of Geosciences*, 110(2):581–612.

Schwartz, S., Allemand, P., and Guillot, S. (2001). Numerical model of the effect of serpentinites on the exhumation of eclogitic rocks: insights from the Monviso ophiolitic massif (Western Alps). *Tectonophysics*, 342(1):193–206.

Schwartz, S., Gautheron, C., Audin, L., Dumont, T., Nomade, J., Barbarand, J., Pinna Jamme, R., and van der Beek, P. (2017). Foreland exhumation controlled by crustal thickening in the Western Alps. *Geology*, 45:139–142.

Schwartz, S., Tricart, P., Lardeaux, J.-M., Guillot, S., and Vidal, O. (2009). Late tectonic and metamorphic evolution of the Piedmont accretionary wedge (Queyras Schistes lustrés, Western Alps): Evidences for tilting during Alpine collision. *Geological Society of America Bulletin*, 121(3-4):502–518.

Sen, M. and Stoffa, P. (1995). Global optimization method in geophysical inversion: Elsvier sci. *Publ. Co., The Netherlands.*

Sénéchal, G. and Thouvenot, F. (1991). Geometrical migration of line-drawings: A simplified method applied to ecors data. *Continental Lithosphere: Deep Seismic Reflections*, 22:401–407.

Séranne, M. (1999). The gulf of lion continental margin (nw mediterranean) revisited by ibs: an overview. *Geological Society, London, Special Publications*, 156(1):15–36.

Shapiro, N. M. and Campillo, M. (2004). Emergence of broadband Rayleigh waves from correlations of the ambient seismic noise. *Geophysical Research Letters*, 31(7).

Shapiro, N. M., Campillo, M., Stehly, L., and Ritzwoller, M. H. (2005). High-resolution surface-wave tomography from ambient seismic noise. *Science*, 307(5715):1615–1618.

Shapiro, N. M. and Singh, S. K. (1999). A systematic error in estimating surface-wave group-velocity dispersion curves and a procedure for its correction. *Bulletin of the Seismological Society of America*, 89(4):1138–1142.

Simon-Labric, T., Rolland, Y., Dumont, T., Heymes, T., Authemayou, C., Corsini, M., and Fornari, M. (2009). 40Ar/ 39Ar dating of Penninic Front tectonic displacement (W Alps) during the Lower Oligocene (31–34 Ma). *Terra Nova*, 21(2):127–136.

Sissingh, W. (2001). Tectonostratigraphy of the west alpine foreland: correlation of tertiary sedimentary sequences, changes in eustatic sea-level and stress regimes. *Tectonophysics*, 333(3-4):361–400.

Slovenian Environment Agency (2001). Seismic Network of the Republic of Slovenia. Publisher: International Federation of Digital Seismograph Networks.

Snieder, R. (1986). 3-d linearized scattering of surface waves and a formalism for surface wave holography. *Geophysical Journal International*, 84(3):581–605.

Snieder, R. (2004). Extracting the green's function from the correlation of coda waves: A derivation based on stationary phase. *Physical Review E*, 69(4):046610.

SNSN (1904). Swedish National Seismic Network. Publisher: Uppsala University, Uppsala, Sweden.

Soergel, D., Pedersen, H. A., Bodin, T., Paul, A., Stehly, L., et al. (2022). Bayesian analysis of azimuthal anisotropy in the alpine lithosphere from beamforming of ambient noise cross-correlations. *Geophysical Journal International.*

Soergel, D., Pedersen, H. A., Stehly, L., Margerin, L., Paul, A., and AlpArray Working Group (2020). Coda-Q in the 2.5–20 s period band from seismic noise: application to the greater Alpine area. *Geophysical Journal International*, 220(1):202–217.

Solarino, S., Malusà, M. G., Eva, E., Guillot, S., Paul, A., Schwartz, S., Zhao, L., Aubert, C., Dumont, T., Pondrelli, S., et al. (2018). Mantle wedge exhumation beneath the dora-maira (u) hp dome unravelled by local earthquake tomography (western alps). *Lithos*, 296:623–636.

Spada, M., Bianchi, I., Kissling, E., Agostinetti, N. P., and Wiemer, S. (2013). Combining controlled-source seismology and receiver function information to derive 3-D Moho topography for Italy. *Geophysical Journal International*, 194(2):1050–1068.

Spakman, W. (1986). Subduction beneath eurasia in connection with the mesozoic tethys. *Geol. Mijnbouw*, (65):145–53.

Spakman, W. (1988). *PhD thesis*. University of Utrecht Utrecht, The Netherlands.

Spakman, W. and Bijwaard, H. (1998). Irregular cell parameterization of tomographic problems. *Ann. Geophys*, 16:18.

Stehly, L., Campillo, M., Froment, B., and Weaver, R. L. (2008). Reconstructing Green's function by correlation of the coda of the correlation (C3) of ambient seismic noise. *Journal of Geophysical Research: Solid Earth*, 113(B11).

Stehly, L., Fry, B., Campillo, M., Shapiro, N. M., Guilbert, J., Boschi, L., and Giardini, D. (2009). Tomography of the Alpine region from observations of seismic ambient noise. *Geophysical Journal International*, 178(1):338–350.

Swiss Seismological Service (SED) At ETH Zurich (1983). National Seismic Networks of Switzerland. Publisher: ETH Zürich.

Takeo, A., Kawakatsu, H., Isse, T., Nishida, K., Sugioka, H., Ito, A., Shiobara, H., and Suetsugu, D. (2016). Seismic azimuthal anisotropy in the oceanic lithosphere and asthenosphere from broadband surface wave analysis of obs array records at 60 ma seafloor. *Journal of Geophysical Research: Solid Earth*, 121(3):1927–1947.

Tape, C., Liu, Q., Maggi, A., and Tromp, J. (2010). Seismic tomography of the southern california crust based on spectral-element and adjoint methods. *Geophysical Journal International*, 180(1):433–462.

Tarantola, A. (1984). Inversion of seismic reflection data in the acoustic approximation. *Geophysics*, 49(8):1259–1266.

Thouvenot, F., Paul, A., Fréchet, J., Béthoux, N., Jenatton, L., and Guiguet, R. (2007). Are there really superposed Mohos in the southwestern Alps? New seismic data from fan-profiling reflections. *Geophysical Journal International*, 170(3):1180–1194.

Thurin, J., Brossier, R., and Métivier, L. (2019). Ensemble-based uncertainty estimation in full waveform inversion. *Geophysical Journal International*, 219(3):1613–1635.

Trefethen, L. N. and Bau, D. (1997). *Numerical linear algebra*, volume 50. Siam.

Trinh, P.-T., Brossier, R., Métivier, L., Tavard, L., and Virieux, J. (2019). Efficient time-domain 3d elastic and viscoelastic full-waveform inversion using a spectral-element method on flexible cartesian-based mesh. *Geophysics*, 84(1):R75–R97.

Trinh, P.-T., Brossier, R., Métivier, L., Virieux, J., and Wellington, P. (2017). Bessel smoothing filter for spectral-element mesh. *Geophysical Journal International*, 209(3):1489–1512.

University Of Zagreb (2001). Croatian Seismograph Network. Publisher: International Federation of Digital Seismograph Networks.

Van der Hilst, R. D. et al. (1990). *Tomography with P, PP and pP delay-time data and the three-dimensional mantle structure below the Caribbean region.* Faculteit Aardwetenschappen.

van Hinsbergen, D. J., Torsvik, T. H., Schmid, S. M., Maţenco, L. C., Maffione, M., Vissers, R. L., Gürer, D., and Spakman, W. (2020). Orogenic architecture of the mediterranean region and kinematic reconstruction of its tectonic evolution since the triassic. *Gondwana Research*, 81:79–229.

Verbeke, J., Boschi, L., Stehly, L., Kissling, E., and Michelini, A. (2012). High-resolution Rayleigh-wave velocity maps of central Europe from a dense ambient-noise data set. *Geophysical Journal International*, 188(3):1173–1187.

Vinnik, L. (1977). Detection of waves converted from P to SV in the mantle. *Physics of the Earth and Planetary Interiors*, 15(1):39–45.

Virieux, J. and Operto, S. (2009). An overview of full-waveform inversion in exploration geophysics. *Geophysics*, 74(6):WCC1–WCC26.

Waldhauser, F., Kissling, E., Ansorge, J., and Mueller, S. (1998). Three dimensional interface modelling with two-dimensional seismic data: the alpine crust-mantle boundary. *Geophysical Journal International*, 135(1):264–278.

Wang, K., Yang, Y., Jiang, C., Wang, Y., Tong, P., Liu, T., and Liu, Q. (2021). Adjoint tomography of ambient noise data and teleseismic p waves: Methodology and applications to central california. *Journal of Geophysical Research: Solid Earth*, 126(6):e2021JB021648.

Wapenaar, K. (2004). Retrieving the elastodynamic green's function of an arbitrary inhomogeneous medium by cross correlation. *Phys. Rev. Lett.*, 93:254301.

Wathelet, M. (2008). An improved neighborhood algorithm: parameter conditions and dynamic scaling. *Geophysical Research Letters*, 35(9).

Weaver, R. L. (2005). Information from seismic noise. *Science*, 307:1568 – 1569.

Wolf, F. N., Lange, D., Dannowski, A., Thorwart, M., Crawford, W., Wiesenberg, L., Grevemeyer, I., Kopp, H., and the AlpArray Working Group (2021). 3D crustal structure of the Ligurian Basin revealed by surface wave tomography using ocean bottom seismometer data. *Solid Earth*, 12(11):2597–2613.

Yan, F., Han, D.-h., Yao, Q., and Chen, X.-L. (2016). Seismic velocities of halite salt: Anisotropy, heterogeneity, dispersion, temperature, and pressure effects. *Geophysics*, 81(4):D293–D301.

Yuan, H. and Bodin, T. (2018). A probabilistic shear wave velocity model of the crust in the central west australian craton constrained by transdimensional inversion of ambient noise dispersion. *Tectonics*, 37(7):1994–2012.

Yuan, H., French, S., Cupillard, P., and Romanowicz, B. (2014). Lithospheric expression of geological units in central and eastern north america from full waveform tomography. *Earth and Planetary Science Letters*, 402:176–186.

Zahorec, P., Papčo, J., Pašteka, R., Bielik, M., Bonvalot, S., Braitenberg, C., Ebbing, J., Gabriel, G., Gosar, A., Grand, A., et al. (2021). The first pan-alpine surface-gravity database, a modern compilation that crosses frontiers. *Earth System Science Data*, 13(5):2165–2209.

ZAMG-Zentralanstalt Für Meterologie Und Geodynamik (1987). Austrian Seismic Network. Publisher: International Federation of Digital Seismograph Networks.

Zhao, L., Malusà, M. G., Yuan, H., Paul, A., Guillot, S., Lu, Y., Stehly, L., Solarino, S., Eva, E., Lu, G., and Bodin, T. (2020). Evidence for a serpentinized plate interface favouring continental subduction. *Nature Communications*, 11:2171.

Zhao, L., Paul, A., Guillot, S., Solarino, S., Malusà, M., Zheng, T., Salimbeni, S., Dumont, T., Schwartz, S., Zhu, R., and Wang, Q. (2015). First Seismic Evidence for Continental Subduction beneath the Western Alps. *Geology*, 43:815–818.

Zhao, L., Paul, A., Malusà, M. G., Xu, X., Zheng, T., Solarino, S., Guillot, S., Schwartz, S., Dumont, T., Salimbeni, S., et al. (2016a). Continuity of the alpine slab unraveled by high-resolution p wave tomography. *Journal of Geophysical Research: Solid Earth*, 121(12):8720–8737.

Zhao, L., Paul, A., Solarino, S., and RESIF (2016b). Seismic network YP: CIFALPS temporary experiment (China-Italy-France Alps seismic transect).

Zhao, L., Paul, A., Solarino, S., and RESIF (2018). Seismic network XT: CIFALPS temporary experiment (China-Italy-France Alps seismic transect).

Zheng, Y., Fang, X., Liu, J., and Fehler, M. C. (2013). Scholte waves generated by seafloor topography. *arXiv preprint arXiv:1306.4383*.

Zhu, H., Bozdağ, E., Peter, D., and Tromp, J. (2012). Structure of the european upper mantle revealed by adjoint tomography. *Nature Geoscience*, 5(7):493–498.

Zhu, J., Popovics, J. S., and Schubert, F. (2004). Leaky rayleigh and scholte waves at the fluid–solid interface subjected to transient point loading. *The Journal of the Acoustical Society of America*, 116(4):2101–2110.

Zhu, L. (2000). Crustal structure across the San Andreas Fault, southern California from teleseismic converted waves. *Earth and Planetary Science Letters*, 179(1):183–190.

Ziegler, P. A. (1992). European cenozoic rift system. *Tectonophysics*, 208(1-3):91–111.